University of Bath

PHD

Structural and electronic properties of oxide solid solutions containing transition metal ions.

Arean, C. Otero

Award date:
1976

Awarding institution:
University of Bath

Link to publication

Alternative formats
If you require this document in an alternative format, please contact:
openaccess@bath.ac.uk

General rights
Copyright and moral rights for the publications made accessible in the public portal are retained by the authors and/or other copyright owners and it is a condition of accessing publications that users recognise and abide by the legal requirements associated with these rights.

- Users may download and print one copy of any publication from the public portal for the purpose of private study or research.
- You may not further distribute the material or use it for any profit-making activity or commercial gain
- You may freely distribute the URL identifying the publication in the public portal ?

Take down policy
If you believe that this document breaches copyright please contact us providing details, and we will remove access to the work immediately and investigate your claim.

Download date: 18. Sep. 2021

75-12141

STRUCTURAL AND ELECTRONIC PROPERTIES OF OXIDE SOLID SOLUTIONS CONTAINING TRANSITION METAL IONS

Submitted by C. Otero Arean

for the degree of Ph.D. of the

University of Bath

1976

Attention is drawn to the fact that copyright of this thesis rests with its author. This copy of the thesis has been supplied on condition that anyone who consults it is understood to recognise that its copyright rests with its author and that no quotation from the thesis and no information derived from it may be published without prior written consent of the author.

This thesis may be made available for consultation within the University Library and may be photocopied or lent to other libraries for the purposes of consultation.

C. Otero Arean

ProQuest Number: U641700

All rights reserved

INFORMATION TO ALL USERS
The quality of this reproduction is dependent upon the quality of the copy submitted.

In the unlikely event that the author did not send a complete manuscript
and there are missing pages, these will be noted. Also, if material had to be removed,
a note will indicate the deletion.

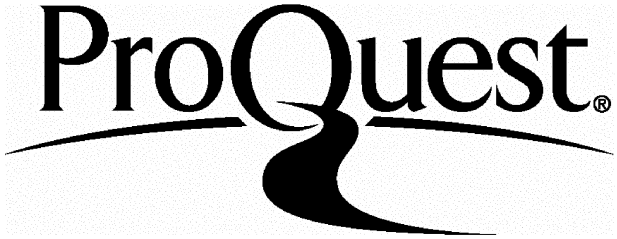

ProQuest U641700

Published by ProQuest LLC(2015). Copyright of the Dissertation is held by the Author.

All rights reserved.
This work is protected against unauthorized copying under Title 17, United States Code.
Microform Edition © ProQuest LLC.

ProQuest LLC
789 East Eisenhower Parkway
P.O. Box 1346
Ann Arbor, MI 48106-1346

Meis parentibus et meis magistris

ACKNOWLEDGMENTS

The author is indebted to the following for their help in the development of this thesis:

Professor F.S. Stone, my supervisor, for his continued advice and encouragement.

Dr. J.N. Andrews for many helpful discussions.

Dr. V.D. Scott for advice on the electron diffraction work.

Dr. A.P. Hagan who obtained most of the UV-vis spectra.

Mr. M.R. Lock, a most skilful glassblower, for his invaluable assistance.

Mr. M.A. Trevethan for some help and discussions on the UV-vis work.

Miss G.A. Gibbs for her care in typing the thesis.

Messrs. B. Chapman, C. Cryer, R. Draper, N. Park, H. Perrot and C. Wilson for their technical assistance.

Professors E. Gutierrez Rios and A. Mata Arjona who first aroused my interest in Solid State Chemistry.

The Spanish C.S.I.C. for a grant under the Plan de Formacion de Personal Investigador.

MEMORANDUM

The work described in this thesis was conducted in the Department of Physical Chemistry of the University of Bath during the period January 1973 to July 1975 and has not been submitted for any other degree. All the work described is the original work of the author except where specially acknowledged.

SUMMARY

Studies have been made on the formation of oxide solid solutions, and on their structural and electronic properties. Three different oxide systems have been investigated: CoO-MgO, MnO-CaO and $CuIn_2O_4$-$CdIn_2O_4$

CoO-MgO (0-10 mol % Co) has been prepared in low, medium and high surface area (LSA, MSA and HSA) forms. The lattice parameter, a_o, was determined by X-ray diffraction (XRD) for LSA and MSA specimens, and by electron diffraction for HSA specimens where severe line broadening precludes accurate determination of a_o by XRD. The increase in a_o with [Co] was found to be identical in all cases, which implies that solid solution is maintained even at very small particle size ($\bar{D}$ < 500 Å). However, reflectance spectra of MSA ($\bar{D}$ = 500 - 1.000 Å) and HSA ($\bar{D}$ = 200 - 500 Å) oxides show that some Co in the surface layers of finely-divided outgassed CoO-MgO is not in octahedral coordination.

MnO-CaO, prepared by heating coprecipitated carbonates at 1273 K in vacuo, has been shown to form a solid solution over the whole composition range in spite of the large difference (22%) in cation radius. ESR studies showed the site symmetry of Mn^{2+}

to be accurately cubic. The onset of magnetic interactions between manganese ions takes place when [Mn] ≈ 1% for the dipole interaction and when [Mn] ≈ 3% for the exchange interaction. By co-addition of Na^+ ions small amounts of Mn^{3+} can be incorporated in solid solution in CaO.

$CuIn_2O_4$-$CdIn_2O_4$ specimens have been prepared by solid state reaction between CuO, CdO and In_2O_3 at three different temperatures (1173, 1223 and 1323 K) and, by X-ray analysis, solubility limits have been found at 2.4, 2.9 and 5.2 mol % Cu respectively. A study has also been made on the crystal structure of $CdIn_2O_4$.

CONTENTS

1. INTRODUCTION

2. EXPERIMENTAL TECHNIQUES

Page

4. DISCUSSION AND CONCLUSIONS

CHAPTER I

INTRODUCTION

1.1. The Sodium Chloride Structure

Sodium chloride (natural halite) presents a close-packed structure which is common to a vast series of ionic compounds of the type MX, where M stands for the cationic and X for the anionic species. The NaCl lattice has a cubic symmetry, space group $Fm3m$,[1,2] and can be considered to be made up of two interpenetrating face-centred cubic sub-lattices, corresponding to the chlorine and sodium ions respectively.

Inspection of fig. 1.1a shows that the unit cell contains sodium ions at 000, $\frac{1}{2}\frac{1}{2}0$, $\frac{1}{2}0\frac{1}{2}$, $0\frac{1}{2}\frac{1}{2}$, and chlorine ions at $\frac{1}{2}\frac{1}{2}\frac{1}{2}$, $\frac{1}{2}00$, $0\frac{1}{2}0$, $00\frac{1}{2}$ respectively. Each unit cell contains four cations and four anions, being equivalent to four "formula units" of NaCl.

In terms of coordination polyhedra the sodium chloride lattice displays a coordination number 6:6 with each cation surrounded by six anions and vice versa. All edges of each $NaCl_6$ octahedron are shared with neighbouring octahedra, as shown in fig. 1.1b. All the octahedra are exactly alike. If it is assumed that in the NaCl structure ions are spherical, and if one takes into account that the stability of an ionic structure is increased by contact between ions of opposite charge, it is possible to calculate from a knowledge of ionic radii the range of substances MX

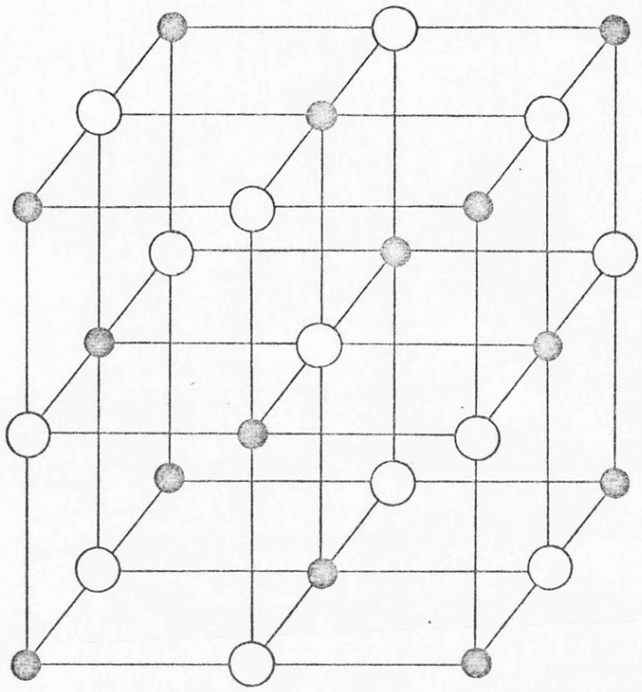

a

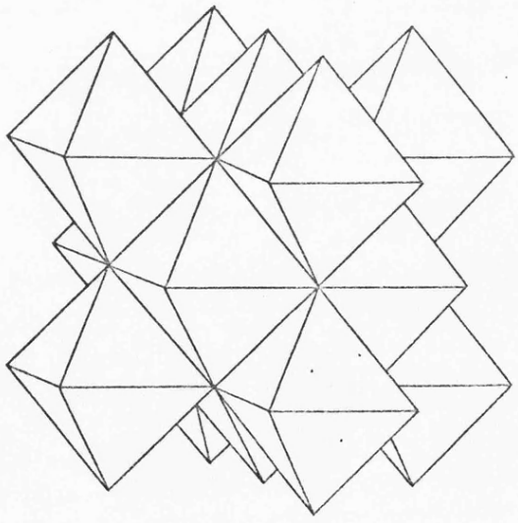

b

Fig. 1.1

The sodium chloride structure
a) Unit cell
b) Stacking of coordination octahedra

which may be expected to have the NaCl atomic arrangement. Born and Mayer[3] have shown that the sodium chloride structure is the most stable one for ionic compounds of the type MX with a cation/anion radius ratio $0.73 > r(M)/r(X) > 0.41$. Although this relation prevails in general, there are some examples of compounds which possess the NaCl structure in spite of the fact that the radius ratio falls outside the above figures. The explanation for this can be found in terms of an extra stabilization of the structure due to factors such as polarization and covalency. The NaCl lattice is ideal for the formation of covalent bonds by overlap of p_x-, p_y- and p_z-orbitals which have lobes aligned with the orthogonal MX directions.

Compounds possessing the sodium chloride structure include, among others, most of the alkali halides (except CsCl, CsBr and CsI); alkaline earth chalcogenides (except Be-salts and MgTe); first row transition metal monoxides (except CuO) and many intermetallic compounds. The structure is also frequently stable when the number of metallic ions is less than the number of non-metallic ions. An example is the compound $Mg_6Mn\square O_8$,[4,5] where $\square$ signifies a cation vacancy; the vacancies and the tetravalent manganese, however, bring about a slight displacement of the positions of the oxygen ions.

1.2. The Spinel Structure

Magnesium aluminate ($MgAl_2O_4$), found in nature as the mineral spinel, is the representative of a wide

family of isostructural compounds known collectively as "spinels"; these compounds have the general formula XY_2Z_4 where X and Y are cations and Z is an anion, most typically O^{2-}, but it may also be S^{2-}, Se^{2-}, Te^{2-}, F^-, Cl^-, CN^-. The old view on the chemical structure was that the formula of the spinels should be expressed as $XZ \cdot Y_2Z_3$, but X-ray analysis of the spinel structure does not reveal any differentiation of the anion arrangement in the lattice. All anions are equivalent, forming a close-packed cubic structure.

The structure of the mineral spinel was determined in 1915 by Bragg [6,7] and independently by Nishikawa[8], using X-ray diffraction. Between 1915 and 1932 the structures of many spinels were determined, but little attention was paid to the study of the relative intensities of the diffracted X-ray beams. In 1932 Barth and Posnjak[9] made a more detailed study of the X-ray diffraction patterns of several spinels and related the intensities of certain lines to the cation distribution in the spinel lattice. Many subsequent studies have been involved with a comprehensive explanation of the cation distribution as found experimentally. This section will be devoted to a description of the lattice geometry of the spinels whilst the cation distribution will be discussed in sections 1.3 and 1.4.

The spinel structure may be regarded as a cubic close-packed (or nearly close-packed) array of anions

held together by the cations. If the anions are considered to be spheres, such a packing will not fill space completely, but leaves voids totalling 26% of the whole volume[10]. These voids are called tetrahedral or octahedral holes according to the geometrical arrangement of the surrounding anions. The former are surrounded by four anions in tetrahedral arrangement whilst the latter are surrounded by six anions in octahedral arrangement. For every N anions there are N octahedral holes and 2N tetrahedral holes.

In the spinel lattice a unit cell is taken as containing 8 formula units (XY_2Z_4) that is, 32 anions, making available 64 tetrahedral holes and 32 octahedral holes. The cations, distributed among these positions of four-fold and six-fold anion coordination, occupy 8 of the 64 tetrahedral sites and 16 of the 32 octahedral sites available. The occupied sites are regularly disposed in order to minimize cationic repulsion. Tetrahedra share corners only with octahedra and the octahedra share edges with one another.

Fig. 1.2b shows a unit cell of the spinel lattice and the sites of the various ions. The structure can be thought of as eight octants of alternating XZ_4 tetrahedra and Y_4Z_4 cubes; the four anions making up a tetrahedron have the same arrangement and the same orientation in all eight octants, their positions being

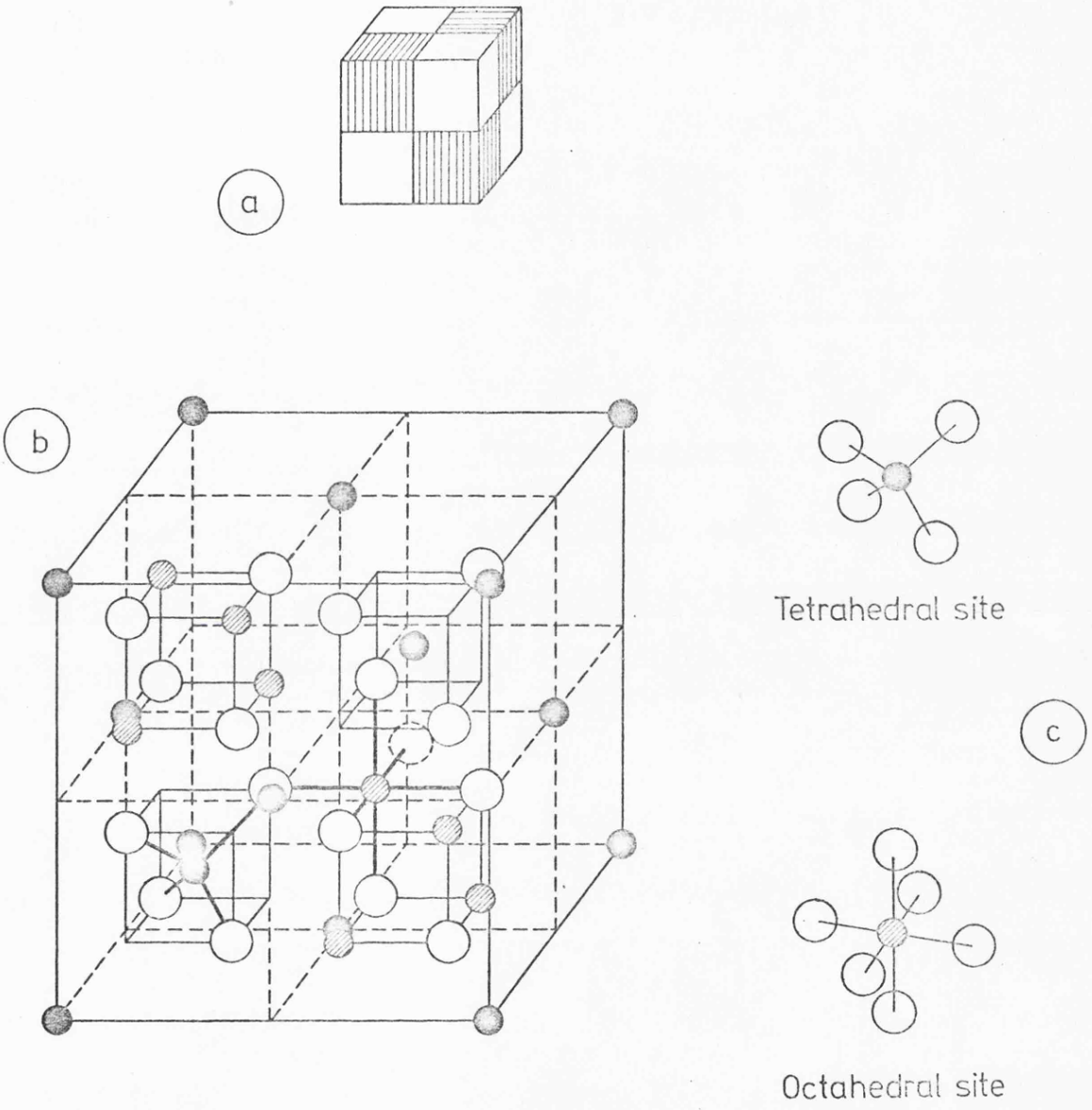

Fig. 1.2

The unit cell of the spinel structure
a) Division in octants
b) Ionic sites (only the four front octants are drawn completely)
c) Anion coordination around tetrahedral and octahedral sites

○ Tetrahedral cation

○ Octahedral cation

◯ Anion

defined by four alternating corners of small cubes. In the octants corresponding to the shaded parts of the small diagram, the remaining corners of the small cube are occupied by cations with six-fold anion coordination. In alternate octants these corners are not occupied; instead there is a cation with four-fold anion coordination in the centre of the octant.

The spinel structure consists, therefore, of a number of interlaced face-centred cubic sub-lattices with an overall symmetry corresponding to the space group Fd3m.[11,1] The most obvious of these face-centred cubic sub-lattices in fig. 1.2b is that formed by the tetrahedral cations on the cell corners and face centres. The remaining tetrahedral cations (octant centres) form another face-centred cubic lattice displaced from the first along the cube diagonal. All the black spheres in fig. 1.2b are in the same tetrahedral coordination, although this is not obvious when considering only one isolated unit cell. The positions of the anions also define a set of interlaced face-centred cubic lattices. Any anion may be taken as occupying a corner of a face-centred cube having the same dimensions as the unit cell; all other sites in this face-centred cube are also occupied by anions. Likewise, the six-fold coordinated cations

occupy sites on four face-centred cubic lattices, each of them having the same dimensions as the unit cell and being displaced from one another along the edges of the smaller cube in the shaded octants.

The coordinates of the ionic positions are the following:[12]

8 positions of four-fold anion coordination at:

$$\left\{ 000;\tfrac{1}{4}\tfrac{1}{4}\tfrac{1}{4} \right\} \qquad \text{(face-centred)}$$

16 positions of six-fold anion coordination at:

$$\left\{ \begin{array}{l} \tfrac{5}{8}\tfrac{5}{8}\tfrac{5}{8};\tfrac{5}{8}\tfrac{7}{8}\tfrac{7}{8}; \\ \tfrac{7}{8}\tfrac{5}{8}\tfrac{7}{8};\tfrac{7}{8}\tfrac{7}{8}\tfrac{5}{8} \end{array} \right\} \qquad \text{(face-centred)}$$

32 anionic positions at:

$$\left\{ \begin{array}{l} uuu;u\bar{u}\bar{u};\bar{u}u\bar{u};\bar{u}\bar{u}u \\ \tfrac{1}{4}-u,\tfrac{1}{4}-u,\tfrac{1}{4}-u;\tfrac{1}{4}-u,\tfrac{1}{4}+u,\tfrac{1}{4}+u \\ \tfrac{1}{4}+u,\tfrac{1}{4}-u,\tfrac{1}{4}+u;\tfrac{1}{4}+u,\tfrac{1}{4}+u,\tfrac{1}{4}-u \end{array} \right\} \text{(face-centred)}$$

u being a parameter to which further reference will be made in section 1.2.1.

Fig. 1.2b also shows that each anion has four near neighbour cations; three of these are in octahedral positions orthogonally arranged with respect to the anion, while the fourth cation lies in a tetrahedral position along the {111} direction away from the octant defined by the three octahedral neighbours.

The importance of this arrangement in relation to covalent bonding in spinels will be discussed in section 1.4.4. If the centres of all the occupied and unoccupied interstices surrounding an anion are joined, the polyhedron shown in fig. 1.3 results, with the cations located at some corners. The spinel structure can be built by stacking these polyhedra together. Such "space filling blocks" were first discussed for the spinel lattice by Gorter,[13] and the concept has proved to be fruitful in the discussion of the possible directions of movement of cations through the structure.[14]

Cations in spinel-type structures can have various combinations of formal charges, provided the necessary balance with the anionic charge is maintained. For compounds with the general formula XY_2Z_4, where Z is a chalcogenide, there are eight negative charges to be balanced and this can be achieved by the following combinations of cation charges: $(X^{2+}+2Y^{3+})$, $(X^{4+}+2Y^{2+})$ and $(X^{6+}+2Y^{1+})$. These are referred as 2,3, 4,2 and 6,1 spinels; typical examples being $Mg^{II}Al_2^{III}O_4$, $V^{IV}Mg_2^{II}O_4$ and $W^{VI}Na_2^{I}O_4$ respectively. When the anion is monovalent there are only four negative charges to be balanced, thereby limiting the combination of cation charges to $(X^{2+}+2Y^{1+})$. Typical examples are $NiLi_2F_4$ and $ZnK_2(CN)_4$.

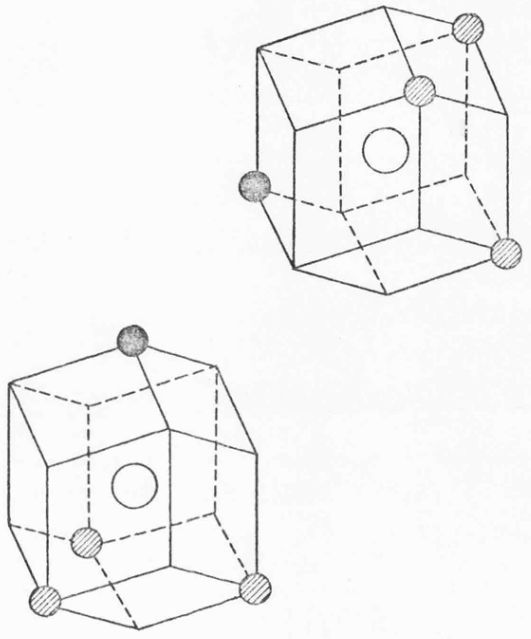

Fig. 1.3

Space filling block of the spinel structure. The central anion (open circle) is surrounded by one tetrahedral cation (black circle) and three octahedral cations (hatched circles). The structure is generated by joining the lower block to three of the identical upper blocks formed from the one shown by a rotation of 0°, 120°, and 240° about a vertical axis at the the tetrahedral cation

In addition to the above, binary spinels with the general formulae $X_{\frac{1}{2}}^{1+}Y_{5/2}^{3+}O_4$ and $X_{4/3}^{1+}Y_{5/3}^{4+}O_4$ have been found to occur, $Li_{\frac{1}{2}}Fe_{5/2}O_4$ and $Li_{4/3}Ti_{5/3}O_4$ being representative examples. Finally, some metal sesquioxides also crystallize with the spinel structure, leaving vacant some of the cationic sites. Two well known examples are the γ-forms of Fe_2O_3 and Al_2O_3 whose formulae can be written as $Me_{8/3}^{III}\square_{1/3}O_4$ (Me≡ metal ion, □≡ vacant cation lattice site).

1.2.1 The parameter u

The parameter u, known as the oxygen parameter in oxidic spinels, is defined by setting ua equal to the distance from a (001) cation plane of the tetrahedral sublattice to the next-nearest-neighbour (001) plane of the anion sublattice, as shown in fig. 1.4a. For an ideal face-centred-cubic oxide lattice this parameter takes the value u = 0.375 (i.e. 3/8) corresponding to a perfect close-packed array. In most spinels, however, the statement that the oxygen ions form an f.c.c. structure is true only to a first approximation. In reality slight deviations are found owing to a deformation caused by the metal ions. The tetrahedral sites, which are smaller than the octahedral ones, are in many oxidic spinels too small to contain a metal ion; as a consequence they are expanded by an equal displacement of the four oxygen ions

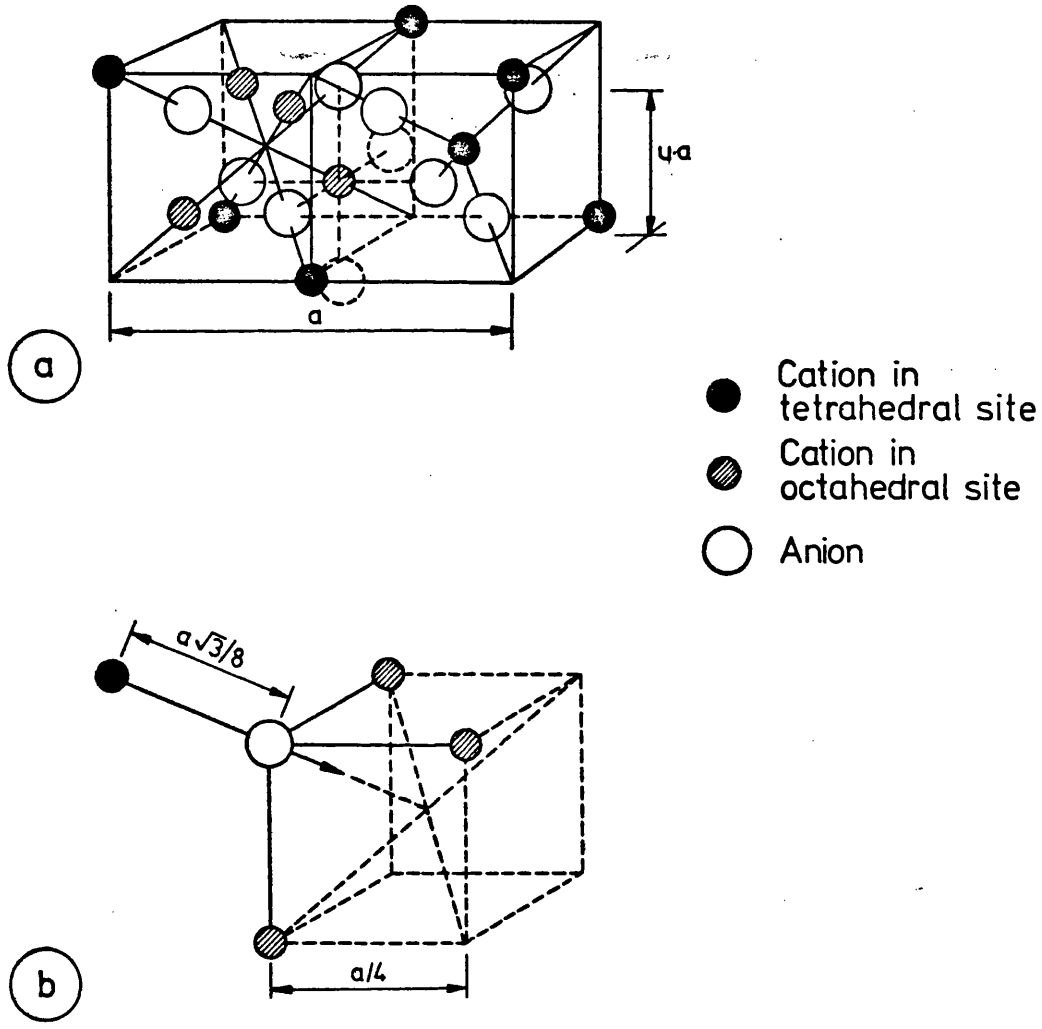

Fig. 1.4

a) The parameter u

b) The nearest neighbours of an oxygen ion in the spinel structure. The arrow indicates the direction in which the oxygen ion moves in the case where $u > 3/8$

outwards along the body diagonals of the cube. These four oxygen ions thus still occupy the corners of an enlarged tetrahedron, so that the arrangement around each tetrahedral cation retains cubic symmetry. The four oxygen ions in the octants with octahedral cations are shifted in such a way that this oxygen tetrahedron shrinks by the same amount as the first expands. Because of the regularity of this distortion within the eight segments of the unit cell the overall symmetry remains cubic. Fig. 1.4b shows the nearest neighbours of an oxygen ion indicating the direction in which this moves in the case of $u>3/8$. For small displacements the radii of the spheres which produce contact in the tetrahedral and octahedral sites are respectively given by:

$$r_{tet.} = (u-\tfrac{1}{4})a\sqrt{3} - R_{ox}$$

$$r_{oct.} = (\tfrac{5}{8}-u)a - R_{ox}$$

where R_{ox} is the radius of the oxygen ion.

1.3. Cation Distribution in Spinels

In 1915 Bragg[7] wrote the formula of magnesium aluminate as $Mg^{2+}\{Al_2^{3+}\}O_4$, where the magnesium ions occupy tetrahedral sites and the aluminium ions octahedral sites. The cations at octahedral sites are written between brackets in the above formula. In 1931 Barth and Posnjak[15] made a detailed study of the intensities of X-ray diffractions from the spinels

$MgFe_2O_4$ and $MgGa_2O_4$ and found that the experimental values of these intensities could not be reconciled with a structure in which all the iron (or gallium) ions are in octahedral positions. Instead, to account for the observed intensities, they found it necessary to assume that eight iron (or gallium) ions in the unit cell must occupy tetrahedral positions. Further research on other spinels, by the same authors,[9] led them to the conclusion that two fundamentally different arrangements of cations are possible in 2,3 spinels, namely, (i) an arrangement where all the divalent cations are located in tetrahedral sites and all the trivalent in octahedral sites, and (ii) an arrangement in which the divalent metal ions occupy octahedral sites and the trivalent ions are equally distributed among the tetrahedral and octahedral sites. Spinels with these arrangements were called "normal" and "inverse" respectively. Later research, carried out by many independent workers, has established that spinels with structures intermediate between normal and inverse occur frequently.

The general formula of a 2,3 spinel can, therefore, be written as $X_{1-x}Y_x\{X_xY_{2-x}\}Z_4$ where the brackets enclose the octahedrally sited ions and the parameter x represents the fraction of divalent cations with octahedral anion coordination, i.e., the degree of inversion. This parameter can, in general, take any

value in the range $0 \leqslant x \leqslant 1$. Normal spinels have $x = 0$, whilst completely inverse spinels have $x = 1$. For spinels with a totally random or "statistical" distribution of cations $x = 2/3$. Using the same nomenclature a normal 4,2 spinel is one in which the eight tetravalent cations in the unit cell occupy tetrahedral sites and the sixteen divalent cations occupy octahedral sites. A normal 6,1 spinel has all the hexavalent cations located at tetrahedral sites.

1.4. Factors affecting Cation Distribution in Spinels

The distribution of two different cations among tetrahedral and octahedral sites in compounds with the spinel structure is determined by the differential stability of the possible ionic configurations. The configuration with the greatest lattice energy is the most stable. Estimation of the lattice energy for any given configuration is a complex problem since there are several factors to take into account and the final result is very often determined by a fine balance among them. However, an analysis of the individual factors which contribute to the lattice energy allows some general conclusions to be derived and, in many cases, the most likely ionic configuration to be predicted. The main points to consider are:

(i) Ionic size.

(ii) Madelung potential

(iii) Crystal field stabilization energy

(iv) Covalency

(v) Anion polarization

(vi) Molecular orbital formation

(vii) Temperature

In what follows the discussion will be centred on 2,3 oxidic spinels. However, the same line of reasoning will, in general, be valid for any other spinel type. The effect of temperature will be considered in the thermodynamic treatment of section 1.5.

1.4.1 Ionic size

Considering the crystal structure to be stabilised when there is cation-anion contact, and the ions to be spherical, geometrical considerations show[16] that octahedral coordination is preferred when $0.414 \leqslant \rho \leqslant 0.732$, whilst tetrahedral coordination would be the most favoured one when $0.225 \leqslant \rho \leqslant 0.414$ (ρ= cation radius/anion radius). As trivalent cations are frequently smaller than divalent cations, this factor will tend to favour the inverse configuration in most cases. Exceptions are the indates of magnesium and the first row transition metal ions, where the trivalent cation is large.

1.4.2 The Madelung potential

Considering the chemical bond in spinels as purely ionic, the total Coulombic energy of the crystal per formula unit, XY_2O_4, is given by:[17]

$$V_c = -Me^2/a_o$$

where M is the Madelung constant, e the electronic charge and a_o the length of the unit cell. According to this expression it is clear that, other things being equal, the configuration with the higher Madelung constant will have the greater lattice energy and will, therefore, be the most stable.

Detailed calculations of the Madelung constant of 2,3 spinels as a function of the oxygen parameter u, and the charge distribution among tetrahedral and octahedral sites, have been carried out by Verwey et al [17,18] and more recently by Sakamoto[19] and by Hermans et al.[20] The results, reproduced in table 1.1, show that the normal configuration has the greater Madelung energy for u>0.380. Since the measured values of u for most 2,3 spinels are greater than 0.380, the Madelung potential favours a normal distribution.

In addition to the Coulombic attractive forces two other terms contribute to the total electrostatic energy of the spinel structure. These are the Born repulsive forces and the energy due to ordering between different ions in the same sublattice. Born repulsion energy tends to stabilize preferentially the inverse configuration, but its value is only about one tenth of the Coulomb energy[13] and therefore plays a minor role. Calculation of the effect of cation ordering on the electrostatic energy of spinels has been performed by de Boer et al[21] and by Sakamoto[19] who found

Table 1.1

Madelung potentials (in e^2/a_o units) of normal and inverse 2,3 spinels as a function of the parameter u.

u	M (normal)	M (inverse)	Reference
0.375	128.6	130.7	18
	128.567	130.774	19
	128.558	130.766	20
0.380	131.4	131.0	18
	130.4	130.6	19
	130.35	130.56	20
0.387	135.0	131.3	18
	132.6	130.2	19
	132.637	130.187	20
0.390	136.5	131.4	18
	133.5	129.9	19
	133.50	129.95	20
0.395	134.8	129.4	19
	134.705	129.432	20

that ordering would stabilise the inverse structure. Thus, for the case of 1:1 order on the octahedral sublattice[42] (the most commonly found order in 2,3 spinels), recalculation of the Madelung potential showed that the limit of stability for normal structures is now shifted toward slightly higher values of the parameter u.

1.4.3 Crystal field stabilization energy

According to the basic idea of crystal field theory, as laid down by Bethe,[22] the degeneracy of atomic orbitals will be lifted when an ion is subjected to a non-spherical electric field originating from the ligands. The nature of the orbital splittings will depend upon the geometrical arrangement of the ligands, and the formal description of the crystal field splitting involves the application of group theory and quantum mechanics to electrostatic theory. However, an intuitive view of this splitting, as applicable to d-orbitals of transition metal ions, can be gained considering the shape of the electronic charge distribution for the different d-orbitals and their orientation in relation to the ligands. It can be shown[23] that the effect of a non-spherical electric field upon the five degenerate d-orbitals of an atom or ion is to split them about the baricentre, the centre of gravity of the energy levels. The way in which the five-fold degeneracy is removed, i.e.

the number of degenerate orbitals of one symmetry type produced, depends only on the field symmetry. In both octahedral and tetrahedral fields, the d_{xy}, d_{xz} and d_{yz} orbitals remain equivalent, as do $d_{x^2-y^2}$ and d_{z^2} orbitals, but the energy levels of each subgroup are different. In an octahedral field the manifold d_{xy}, d_{xz}, d_{yz} (named t_{2g}) has a lower energy than the d-orbitals of the ion in a spherical field, whilst the manifold $d_{x^2-y^2}$, d_{z^2} (named e_g) has greater energy. In a tetrahedral field the energy levels are inverted, and the two subgroups are now named t_2 and e (*). The difference in energy between the two subgroups, denoted by Δ_o and Δ_t for octahedral and tetrahedral fields respectively, increases with increasing ligand field strength. Oxygen ligands in spinels provide what is known as a "weak field" and therefore stabilization energies due to crystal field splitting must be computed assuming that Hund's rules are obeyed.[23] Each electron in a t_{2g} orbital stabilizes a transition metal ion in octahedral coordination by $(2/5)\Delta_o$ whereas every electron in an e_g orbital destabilizes it by $(3/5)\Delta_o$. For tetrahedral coordination there is a stabilization of $(3/5)\Delta_t$ for each electron in an e orbital and a destabilization of $(2/5)\Delta_t$ for every

---

(*) This notation arises from group theory and makes reference to the symmetry properties of the different subgroups of orbitals (see e.g. F.A. Cotton: Chemical Applications of Group Theory, Interscience, 1963).

electron in a t_2 orbital. The crystal field stabilization energy represents the algebraic sum of these factors.

The magnitude of Δ depends on:

(i) The oxidation state of the ion, values of Δ for M^{3+} ions being higher than for M^{2+} ions.

(ii) The nature and type of ligand coordinated to the ion.

(iii) The interatomic distance between metal and ligand. Small decreases in interatomic distance lead to large increases in Δ.

(iv) The symmetry of coordinated ligands. The relative values of Δ_t and Δ_o are: $\Delta_t = -(4/9)\Delta_o$. The negative sign reflects the reversal of the order of the energy levels.

Fig. 1.5 illustrates the crystal field splitting of d-orbitals for octahedral and tetrahedral ligand field symmetries. Also shown in this figure is the additional splitting, δ, due to Jahn-Teller distortion. This distortion is a consequence of the Jahn-Teller theorem which establishes[24,25] that when the number of electrons in a non-linear molecule is such that in its most symmetrical configuration the molecule is electronically degenerate, a distorted structure, in which the degeneracy is removed by distortion, is the

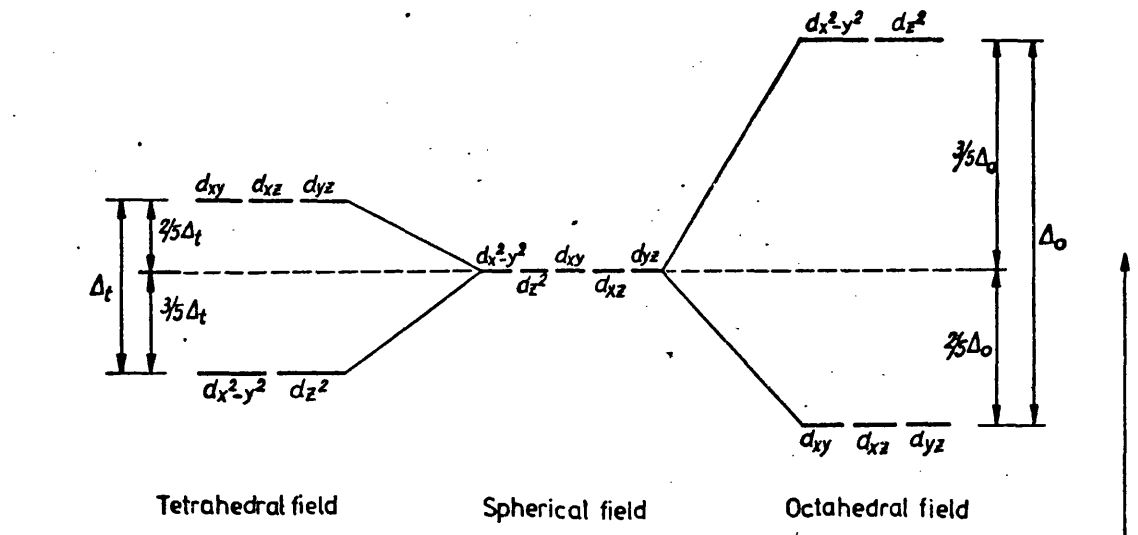

a

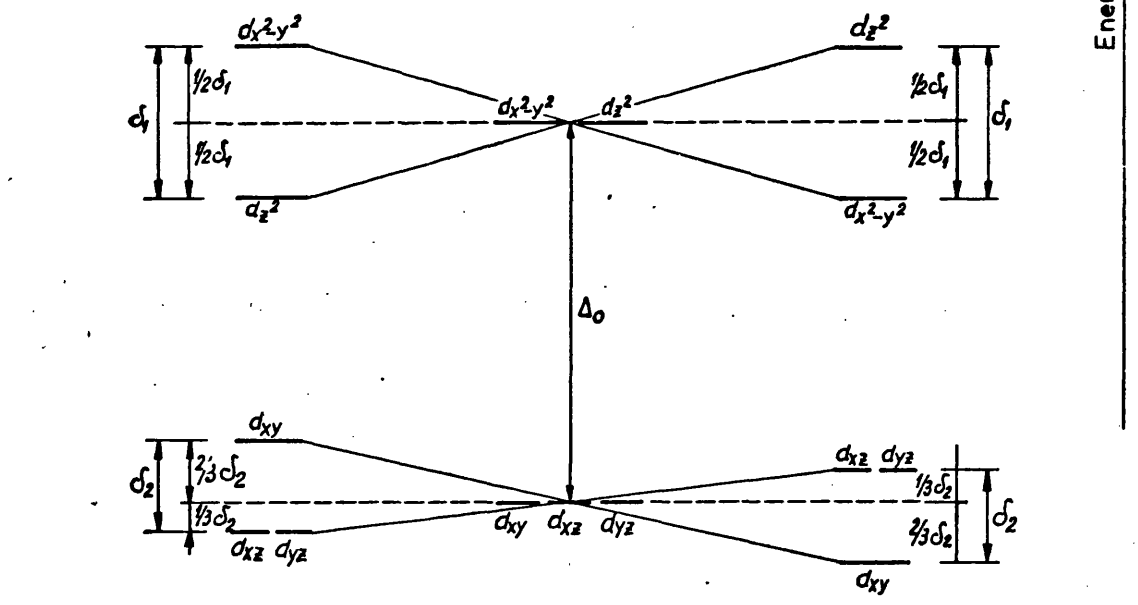

b

Fig. 1.5

a) Generalized splitting pattern for d-orbitals in tetrahedral and octahedral fields

b) Additional splitting due to Jahn-Teller effect (tetragonally distorted octahedral field)

more stable configuration. Thus, according to this theorem, an electronically degenerate complex is intrinsically unstable compared with distortions that remove the degeneracy.

In octahedral fields, for high-spin (weak field) ground state arrangements of the d-electrons other than d^3, d^5, d^8 and d^{10} the individual t_{2g} or e_g orbitals cannot be occupied equally. This means that the octahedral symmetry of the field cannot be matched exactly by the symmetry of the d-electron cloud. A more stable system can then be obtained by distorting the ligand octahedron so that in certain directions the d-electrons are less repelled than in others. The directional dependence of the repulsion will be greater for an unequal occupation by electrons of the e_g (which point at the ligands) than of the t_{2g} orbitals (which point between the ligands). For d^4 and d^9 cations, the simplest distortions to expect are the movement of two ligands along the z axis either away from or towards the cation. The resulting fields are both of tetragonal symmetry. Under the influence of a tetrahedral field Jahn-Teller distortions arise, as above, for all high-spin ions except d^2, d^5, d^7 and d^{10}. The presence in spinels of ions showing Jahn-Teller effects often gives rise to a tetragonal distortion of the cubic spinel structure.[26]

Using the rule $|\Delta_t| = (4/9)|\Delta_o|$ it can be shown that all high-spin d^n ions have an octahedral preference unless n=0, 5 or 10 for which configurations no crystal

field stabilization arises for either octahedral or tetrahedral symmetry. This is illustrated in fig. 1.6 which also shows that the octahedral field is preferred to the greatest extent by d^3 and d^8 ions. Strong preference for this symmetry is also displayed by ions with four and nine d-electrons due to Jahn-Teller effects, as discussed above. Thus, Mn^{3+} and Cu^{2+} are usually found in tetragonal, distorted octahedral, symmetry. When two different transition metal ions appear together in a compound with the spinel structure the important factor to be considered is, however, the differential octahedral preference energy. Estimation of crystal field stabilization energies for several ions has been carried out by Dunitz and Orgel[27], and by McClure,[28] whose results are given in table 1.2. Miller[29] has used several approximations to take into account electrostatic effects and his values, also shown in table 1.2, place more emphasis on tetrahedral preference.

1.4.4 Covalency

Pure electrostatic and crystal field effects proved to be inadequate to account for the stability of many spinels and it was appreciated that covalent bonding was likely to make a significant contribution to the stabilization of the spinel lattice. Covalent bonds in oxidic spinels can be formed as a result of the overlapping of

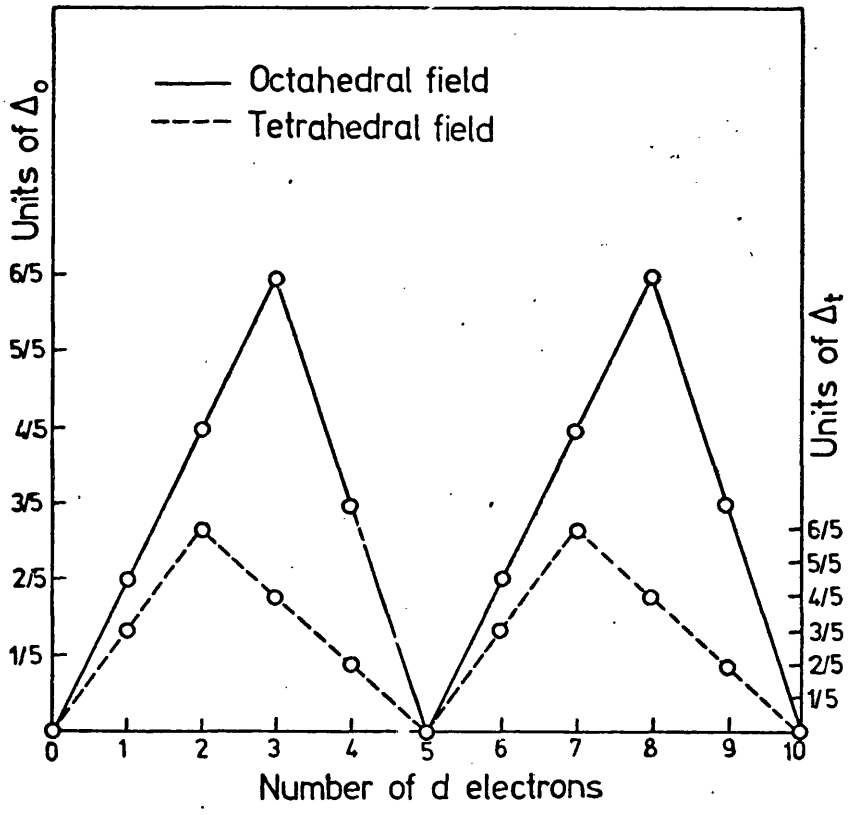

Fig. 1.6

Crystal-field stabilization energies for high-spin d^n ions in octahedral (left-hand scale), and tetrahedral (right-hand scale), fields)

Table 1.2

Site Preference Energies of Some Cations

Ion	No. of 3d electrons	Oct. stabilization Δ_o	Tet. stabilization Δ_t	Octahedral Preference (kJ)		
				Dunitz & Orgel	McClure	Miller
Mg^{2+}	0	-	-	-	-	-20.9
Al^{3+}	0	-	-	-	-	-10.5
Ti^{3+}	1	2/5	3/5	28.9	32.2	-91.7
V^{3+}	2	4/5	6/5	53.6	8.4	-48.6
Cr^{3+}	3	6/5	4/5	157.8	195.5	69.5
Mn^{3+}	4	3/5	2/5	95.5	105.9	13.0
Mn^{2+}	5	0	0	0	0	-61.5
Fe^{3+}	5	0	0	0	0	-55.7
Fe^{2+}	6	2/5	3/5	16.7	16.3	-41.4
Co^{3+}	6	2/5	3/5	-	79.5	-
Co^{2+}	7	4/5	6/5	31.0	8.8	-44.0
Ni^{2+}	8	6/5	4/5	86.2	95.5	37.7
Cu^{2+}	9	3/5	2/5	63.6	65.3	-0.4
Zn^{2+}	10	0	0	-	-	-132.3
Ga^{3+}	10	0	0	-	-	-64.5
In^{3+}	10	0	0	-	-	-168.3

the filled oxygen p-orbitals with empty cation orbitals. Such an overlap gives rise to a coordinate covalent bond (the bonding electrons coming from the oxygen ions) which reduces the polarity of the cation-anion bond, stabilizes the system, and reduces the effective anion radius. According to Goodenough and Loeb[30] the near neighbour oxygen ions perturb the cations to form stable, empty hybrid orbitals, which overlap with the p-orbitals from the oxygen. These hybrid orbitals are formed using the empty nd-, (n+1)s- and (n+1)p-orbitals of the cation and their presence is favoured under the following conditions:

(i) Small difference in energy between the inner d-orbitals and the s- and p-orbitals of the valence shell.

(ii) Not too great a difference in electronegativity between cation and anion.

(iii) Symmetry conditions that allow a large orbital overlap.

The oxygen ion has the configuration $1s^2 2s^2 2p^6$, the p-orbitals being three mutually perpendicular dumbbells. In the spinel lattice each oxygen ion has three near-neighbour octahedral cations located along three mutually perpendicular directions from the oxygen and one near-neighbour tetrahedral cation lying in the [111] direction away from the quadrant defined by the three octahedral ions. Due to this geometrical

arrangement strong covalent bonding is, in general, only possible with one type of cation. If the oxygen bonds covalently with any or all of the octahedral cations through its p-orbitals there are no anion orbitals directed toward the tetrahedral site, and the tetrahedral cation-oxygen bond is ionic. If, however, the tetrahedral cation-oxygen bond is strongly covalent, the oxygen p-orbitals do not point in the direction of the octahedral cations and this reduces the strength of these bonds. Thus, there may be competition between the tetrahedral and octahedral cations for orbital overlapping with the filled oxygen p-orbitals.

Three types of cation hybrid orbitals are of relevance when considered in relation to the steric restrictions imposed by the geometry of the spinel array. These are: (i) tetrahedral orbitals, (ii) octahedral orbitals and (iii) square orbitals, their relative strengths being 2.00, 2.236 and 2.694 respectively.[31]

(i) Tetrahedral orbitals

Tetrahedral orbitals, which point toward the four corners of a tetrahedron, result from the hybridization of sp^3 orbitals. They are predominantly formed in cations with a full d-shell, separated in energy by only a small interval from the next empty s- and p-shells, but will also tend to be formed for

ions with a half full, spherically symmetrical, d-shell. This accounts for the fact that d^5 Fe^{3+} ions prefer the tetrahedral positions in ferrites,[32-34] except for $ZnFe_2O_4$ and $CdFe_2O_4$[35,36] where Zn^{2+} and Cd^{2+} ions, with a d^{10} configuration, show a much stronger tetrahedral preference.

(ii) Octahedral orbitals

Octahedral orbitals are formed by the hybridization of d^2sp^3 orbitals, point toward the six corners of an octahedron, and are predicted to occur for ions with a d^3 or d^6 electron configuration.[31] In the case of d^3 ions no spin change is involved in passing from ionic to covalent bonding, and the bond can be partially covalent and partially ionic in nature. Thus, Cr^{3+}, a d^3 ion, can find an extra stabilization in octahedral sites by partial covalent-bond formation. However, for d^6 ions, such as Fe^{2+}, it is necessary to change the sign of two electron spins (pairing of two electrons) in order to leave two empty d-orbitals, in the valence shell, available for hybridization; this precludes the possibility of forming partially covalent bonds and the large electronegativity of the oxygen ion causes Fe^{2+} to form ionic bonds.

(iii) Square orbitals

Square, coplanar dsp^2 orbitals point toward the four corners of a square and can be accommodated in octahedral sites in the spinel structure. The formation of these orbitals implies the presence of one

empty d-orbital, as in the case of cations with four d-electrons. They are also predicted for ions with d^8 and d^9 configuration. In the case of d^8 the formation of the square dsp^2 hybrids implies pairing of electrons, whilst for a d^9 ion one nd-electron has to be promoted to the (n+1)p-orbital not used for hybridization, in order to provide the necessary empty d-orbital.

Cations with the outer electron configuration d^4, such as Mn^{3+}, can hybridize empty dsp^2 orbitals for coordinate covalence without altering their paramagnetic moment and can, therefore, be accommodated in octahedral sites with the formation of partially or completely covalent bonds. Ni^{2+}, with an outer electron configuration d^8, has two vacancies in the d-shell and can form dsp^2 hybrids provided there is previous reversal of one electron spin to reduce its paramagnetic moment to zero. It is known[31] that some complexes of nickel, such as $(Ni(CN)_4)^{2-}$, are both coplanar and diamagnetic. However, NiO has the sodium chloride structure with the Ni^{2+} electrovalently bonded and it may be assumed that Ni^{2+} forms electrovalent bonds in oxides with the spinel structure. With an outer configuration d^9, Cu^{2+} is known to form square bonds in complex ions,[37] cupric oxide,[38] and cupric salts.[38] Although the Cu^{2+} cation may, theoretically, form either tetrahedral sp^3 orbitals or square dsp^2 orbitals, the square-bond formation in CuO provides some indication that the latter bond type is the more stable in an oxide lattice.

1.4.5 Anion polarization

In the spinel structure each anion is surrounded by four cations, three octahedrally coordinated, along the cube edges, on one side and one tetrahedrally coordinated, along the body diagonal, on the other. Because of this asymmetrical arrangement of the metal ions about each anion the electrical field, E, at the centre of the anion is not zero and therefore gives rise to anion polarization. The corresponding polarization energy is $-\frac{1}{2}\alpha E^2$ (α=anion polarizability) and may contribute appreciably to the lattice energy. If the tetrahedral sites contain only divalent ions there will be a different polarization of the anion than if they contain both divalent and tervalent ions. Using a point charge model, Smit et al[39] have calculated the anion polarization energy and found it to be about 13 eV for normal and zero for inverse 2,3 spinels. Although the actual figure is probably much smaller than the calculated 13 eV, because of saturation,[40] the fact still remains that polarization will always favour a normal configuration.

Anion polarization arguments explain why Li^{1+} occupies tetrahedral sites in $Li_{0.5}Al_{2.5}S_4$[41] whilst in $Li_{0.5}Al_{2.5}O_4$ lithium is in octahedral sites.[42] The greater polarizability of the anion in the sulphospinel causes the polarization term to favour more strongly a normal distribution.

1.4.6 Molecular orbital formation

The molecular orbital theory of metal complexes, first introduced by Van Vleck,[43] combines the crystal field theory with covalency effects. The basic idea is the combination of the metal valence orbitals with ligand orbitals to form the so-called molecular orbitals in which the valence electrons are placed. The possible combinations of metal and ligand orbitals which can be used to form the molecular orbitals are determined by symmetry conditions. Thus, for an octahedral complex, the metal orbitals are designated as: s, a_{1g}; p_x, p_y and p_z, t_{1u}; $d_{x^2-y^2}$ and d_{z^2}, e_g; and d_{xy}, d_{xz} and d_{yz}, t_{2g}. The ligands have p, or s-p hybrid orbitals, available for σ-bonding, with symmetry e_g, a_{1g} and t_{1u} (*). Each of the six ligand orbitals plus a metal orbital of the same symmetry gives a σ molecular orbital. In this way six bonding and six antibonding molecular orbitals result (an antibonding molecular orbital involves reversal of the sign of a wavefunction). Since no ligand orbitals with t_{2g} symmetry are available the t_{2g} metal orbitals are nonbonding, albeit they may interact with a ligand combination orbital obtained from the p-orbitals of four ligands, perpendicular to the metal-ligand σ-bond, to form π molecular orbitals. However π-bonding is unlikely to be important in spinels since the p-orbitals involved in π-bonding with one metal ion would be simultaneously involved in σ-bonding with another metal ion.

(*) For an explanation of this terminology see e.g. F.A. Cotton: Chemical Application of Group Theory, Interscience (1963).

Fig. 1.7 shows the molecular orbital energy level diagrams for octahedral and tetrahedral complexes. The energy separation between the nonbonding and the antibonding orbitals, Δ, has a similar meaning as in crystal field theory. The σ-bonding orbitals are filled by the electrons from the ligands. The d-electrons of the metal ion occupy, in octahedral complexes, the nonbonding t_{2g} and, if necessary, the antibonding e_g^* level; for tetrahedral complexes the corresponding levels are the e and the t_2^* respectively.

A molecular orbital model, as outlined above, has been used by Blasse[42] to compute first the stabilization energy for transition metal ions in octahedral and tetrahedral sites and then the octahedral site preference energy. In carrying out such a computation he has neglected π-bonding and assumed that the stabilization energy due to the ligand electrons in σ-bonding orbitals is approximately equal for octahedral and tetrahedral complexes. Calculation of stabilization energies is done by subtracting from this stabilization energy the destabilization corresponding to metal electrons in antibonding orbitals, if any. Blasse's conclusions are that ions with configuration d^3 should prefer octahedral sites, ions with configuration d^5, d^6, d^7, d^9 or d^{10} should prefer tetrahedral sites, whereas ions with configuration d^0, d^1, d^2, d^4 and d^8 should not show a pronounced preference.

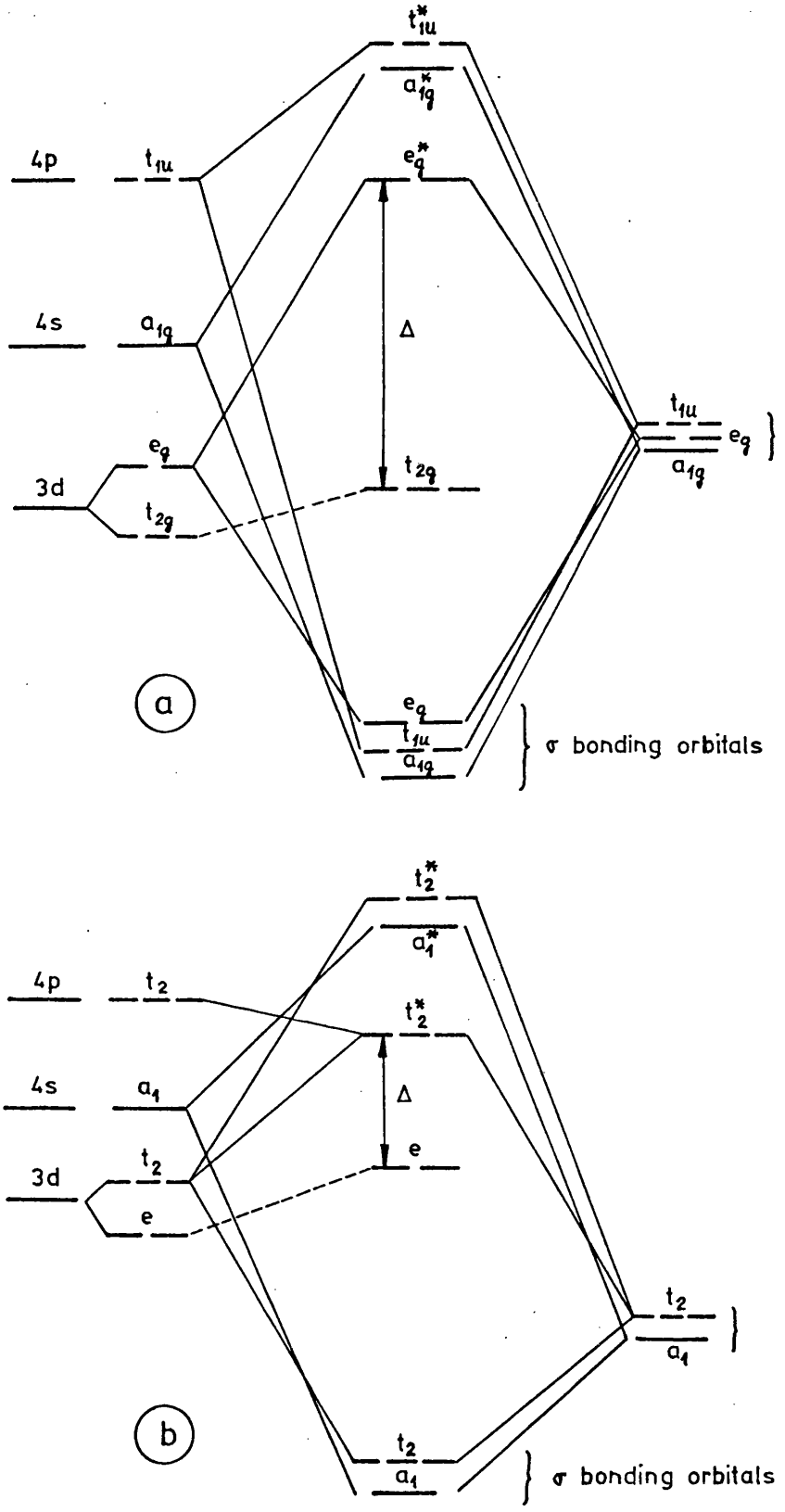

Fig 1.7

Molecular orbital energy level diagrams for transition metal ions in a) octahedral and b) tetrahedral coordination (Only σ interactions are considered)

1.5. Thermodynamic Treatment of Cation Distribution

A thermodynamic approach to the problem of cation distribution in spinels has been made by Schmalzried[44] and by Kröger,[45] among others. In essence, their arguments are as follows:

Let the interchange equation

$$X + \{Y\} = \{X\} + Y \qquad (1.1)$$

represent the inversion of an initially normal spinel $X\{Y_2\}O_4$. Let the free energy change be ΔG. Considering this equation as representing a quasi-chemical equilibrium and assuming that the ionic activity may be approximated by the corresponding ionic fraction, an equilibrium constant may be written as:

$$K = \frac{\{X\}\cdot Y}{X\cdot \{Y\}} = \frac{x^2}{(1-x)(2-x)} \qquad (1.2)$$

where $\underline{x}$ is the inversion parameter, as defined in pag. 10. Since

$$\ln K = -\frac{\Delta G^o}{RT} = \frac{\Delta S^o}{R} - \frac{\Delta H^o}{RT} \qquad (1.3)$$

it would be expected that the degree of inversion, x, would be dependent on temperature. This has actually been observed for a number of spinels, such as $MgFe_2O_4$,[46,48] $CuFe_2O_4$,[49] $NiFe_2O_4$[50] and $NiAl_2O_4$.[44] According to eq. (1.3), a plot of lnK versus 1/T will allow one to calculate the standard interchange enthalpy, ΔH^o, and entropy, ΔS^o. For some systems where data on

x are available over a range of temperature, plots of this type resulted in straight lines which intercept the ordinate axis near the origin, thus showing that, within the precision of experimental data, the non-configurational changes in entropy associated with the disordering process are negligible.

From equations (1.2) and (1.3) it follows that[51]

$$-\frac{\Delta H(\text{interchange})}{RT} = \ln \frac{x^2}{(1-x)(2-x)} \qquad (1.4)$$

In order to derive (1.4) the assumptions have been made that (i) the solid solution of the two ions on each sublattice is ideal and (ii) the entropy change associated with reaction (1.1) is configurational only. Equation (1.4) allows one to calculate interchange enthalpies for different pairs of ions when their distribution between tetrahedral and octahedral sites is known at a given temperature. In order to obtain a set of site preference energies for individual ions from the interchange enthalpies it is necessary to fix the site preference energy for one ion. From the calorimetrically determined enthalpy of transformation of γ-alumina to the α-modification (corundum), as well as from arguments relating the solid solubility of Al_2O_3 in aluminate spinels, Navrotsky and Kleppa[51] have adopted for the octahedral site preference of the Al^{3+} ion the value of -41.87 kJ/mole. Using this value, and following the above outlined treatment, these authors have calculated the site preference energies presented in fig. 1.8. For comparison this

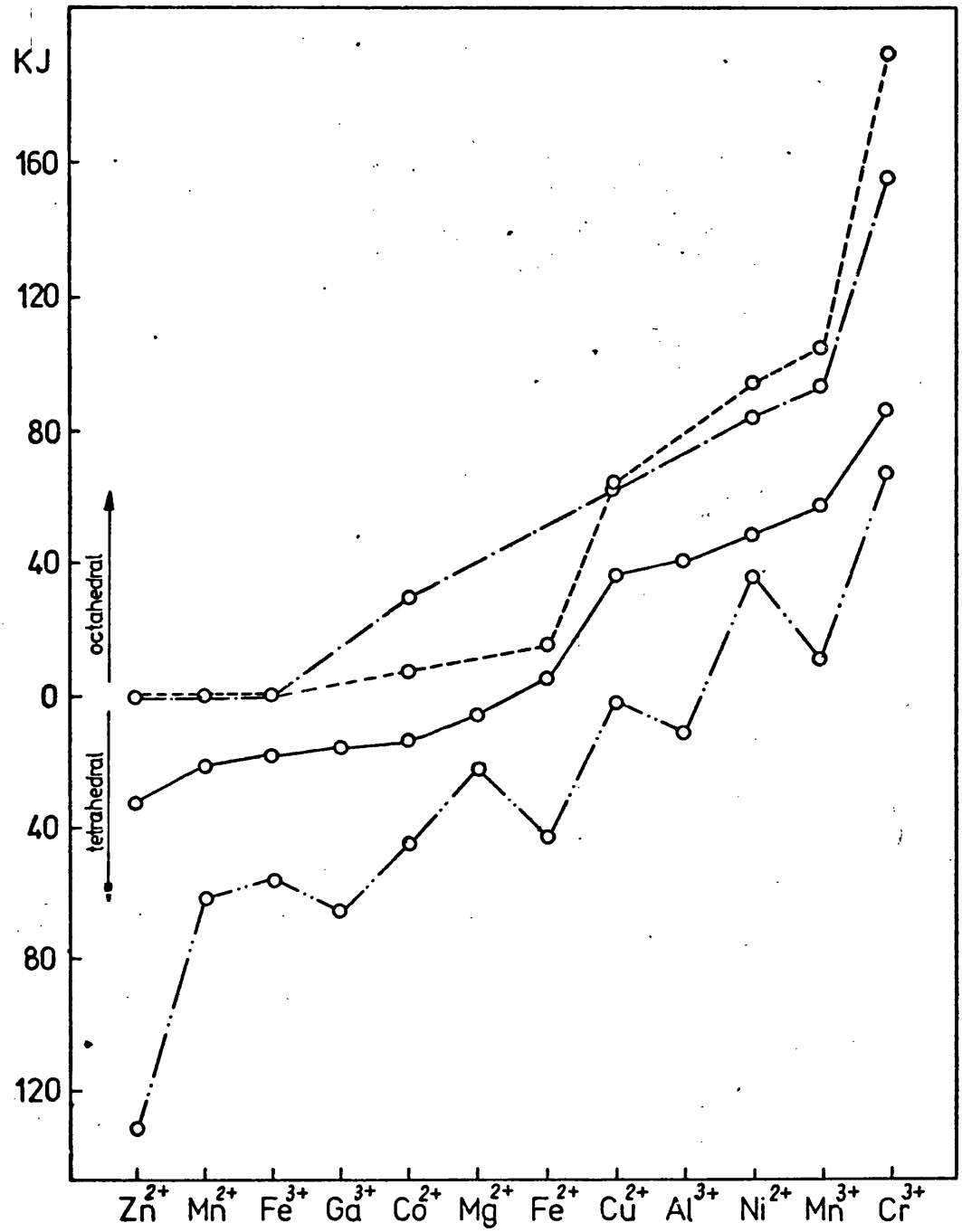

Fig. 1.8

Site preference energies according to different authors

—·— Dunitz and Orgel (27)

---- McClure (28)

—— Navrotsky and Kleppa (51)

—··— Miller (29)

figure also shows the values given by McClure, Dunitz and Orgel, and Miller previously reported in table 1.2. It may be pointed out that absolute values of site preference energy depend on the choice of zero and are not of much relevance. The relative values for different cations are more significant.

A somewhat more theoretical treatment based on statistical thermodynamics has been given by Men' [52-54] who writes for the free energy, G, as a function of the composition, C_i, temperature, T, and degree of inversion, x, a general expression of the form

$$G = g(x, C_i, T) - kT \ln \omega(x, C_i)$$

where the second term accounts for the configurational entropy. Or more explicitly[52]

$$G = -\sum_{i\mu} N_i^{\mu} \nu_i^{\mu} - kT \ln \prod_{\mu} \frac{M_{\mu}!}{\prod_{i} N_i^{\mu}!}$$

where the letters have the following meaning:

N_i^{μ} = number of atoms of kind $\underline{i}$ at lattice points of type $\underline{\mu}$.

ν_i^{μ} = absolute value of the energy of interaction of an atom of kind $\underline{i}$ at a lattice point $\underline{\mu}$ with the nearest oxygen atoms.

M_{μ} = number of lattice points in sublattice $\underline{\mu}$;

By minimizing the free energy in relation to the degree of inversion, i.e., setting $\delta G/\delta x = 0$, Men'

arrives at expressions for the degree of inversion as a function of temperature and composition. However, unless some oversimplifications are introduced, the estimation of either ν or the correct form of the function g, cannot be made without a knowledge of some physical parameters such as the dependence of specific heats on cation distribution or the variation of this distribution with temperature. In this sense Men's theoretical work does not differ substantially from the thermodynamic treatment outlined before.

1.6. Comments on Cation Distribution

Arguments based on crystal field theory alone fail to give a complete account of site preference energies for transition metal ions, due to neglecting of various other important factors. Moreover, from this approach, no conclusions can be drawn as to the site preference energy for cations with configuration d^0, d^5 or d^{10}. The molecular orbital approach developed by Blasse[42] seems to be more realistic, although it still has several obvious limitations. Blasse's conclusion that ions with configuration d^3 have a strong octahedral site preference is in good agreement with the reported experimental results (Cr^{3+} is always found in octahedral sites in spinels). So far as the tetrahedral site preference of ions d^5, d^6, d^7, d^9 and d^{10} is concerned, the concordance with experimentally determined cation distributions

is reasonably good, although Cu^{2+} (d^9) is frequently found in octahedral sites, presumably due to Jahn-Teller stabilization. It may be pointed out that the Blasse treatment affords the correct prediction of tetrahedral preference for cations with configuration d^{10} for which crystal field theory does not give any preferential stabilization energy. The experimental results indicate clearly that d^{10} ions, such as Zn^{2+}, Cd^{2+} and In^{3+}, do prefer tetrahedral sites. The main drawback of Blasse's treatment is its failure to give detailed information for ions with configuration d^0, d^1, d^2, d^4 and d^8, which are simply catalogued as ions without a pronounced tetrahedral or octahedral preference, but no relative values are given. It is important to notice that in this group is included Ni^{2+} (d^8) for which there is good experimental evidence for a fairly strong octahedral preference. In fact, most nickel(II) spinels are inverse, the main exception being the chromite where the strong octahedral preference of Cr^{3+} exceeds that of Ni^{2+}.

In the thermodynamic treatment described in section 1.5 no assumptions are made on the nature of the chemical bond, and it may be expected that thermodynamic analysis of experimental data can produce the most reliable set of values for the site preference energies of different cations. However, the determination of cation distributions at different temperatures is

often done by quenching the samples from high temperatures and subsequent X-ray analysis at room temperature. The efficiency of the quenching treatment is always questionable, i.e. there is always some remaining doubt as to whether the non-equilibrium cation distribution observed at room temperature is exactly the same as the equilibrium cation distribution at high temperature. It is desirable that more experimental data on the variation of cation distribution with temperature for many spinels be obtained, and, when possible, data should be gathered using high temperature diffraction methods.

From a critical analysis of the data of Miller,[29] Blasse,[42] and Navrotsky and Kleppa,[51] compared with reported data for cation distribution of several spinels, the following series of cations, arranged in order of increasing octahedral site preference, was obtained:

$$Zn^{2+} \leqslant In^{3+} \leqslant Cd^{2+} < Mn^{2+} \leqslant Ga^{3+} \leqslant Fe^{3+} < Co^{2+} \leqslant Fe^{2+} \leqslant Mg^{2+} < Al^{3+} \leqslant Cu^{2+} < Mn^{3+} < Ni^{2+} < Cr^{3+}$$

Spinels formed by two cations far from each other in this list are expected to be either normal or inverse, depending on whether the trivalent cation is high or low in the series, e.g. $ZnCr_2O_4$ (normal), $NiIn_2O_4$ (inverse). In the case of two cations close together in the above series the spinel should be partially inverse, with a degree of inversion very markedly dependent on temperature, e.g. $CuAl_2O_4$. As temperature is increased the spinel will tend to a random distribution (x=2/3) which is most favoured by the configurational entropic term.

1.7. Experimental Determination of Cation Distribution

The main methods for determining cation distributions in spinels are X-ray and neutron diffraction. However, other methods such as optical and infrared spectroscopy, magnetic susceptibility, electrical conductivity, etc., are often used either as main techniques or in order to complement the information obtainable by diffraction methods. An outline of the way in which some physical techniques can be used to gain knowledge about the ionic configuration of spinels will be given in this section.

1.7.1 Diffraction methods

In the spinel structure some lattice planes contain only octahedral sites, some only tetrahedral sites, and others a mixture. Therefore when X-rays, electrons, or neutrons are diffracted through the lattice the intensities of the various diffraction lines will be dependent upon the cation distribution, provided that the different cations present have different scattering power.

Diffraction studies of cation distribution imply, in essence, a theoretical calculation of the intensities of several diffractions over a whole range of possible ionic configurations, and an experimental determination of these intensities. Comparison between theoretical and experimental values allows one to decide which configuration provides a better agreement between calculated intensities and experimental results. Since the contribution of the anions to the intensities of diffraction depends upon the parameter u, there are two variables to

be adjusted: the parameter x, describing the degree of inversion, and the parameter u which describes the position of the anions within the lattice. In order to find the appropriate values of these two parameters two steps are usually followed. In the first step one of the parameters is fixed and the other is changed until the best agreement with the experimental results is reached. The value thus obtained is now used to adjust the parameter first left fixed.

The similarity between X-ray, electron and neutron diffraction lies in the fact that the geometric nature of the problem of structure determination permits the geometric theory of diffraction, originally developed for X-ray work, to be used in electron and neutron diffraction studies. The dissimilarities of the three methods are due to the differences in the interaction between the given radiation and the specimen. X-rays are scattered by the electron shells of the atoms, atomic nuclei being "invisible" to such radiation. Electrons are scattered by the electrostatic potential due to the atomic nuclei and their electron clouds. The distribution of electrostatic potential about an atom corresponds approximately to that of its electron density, but falls off less steeply as one goes away from the centre of the atom. Scattering of neutrons is due to their interaction with the nuclei and the scattering powers of different atoms do not follow a general trend as they do in the case of X-ray and electron diffraction.

The application of X-ray analysis to spinels, especially with respect to cation distribution, has been described by Bertaut,[55,56] Schmalzried,[44] and Huber,[57] among others. Recently Furuhashi et al.[58] have described an improved method that takes into consideration the effective temperature factor for the intensities of diffraction (a factor that takes into account the thermal vibrations of the ions in the crystal lattice). In Furuhashi's method the optimum values of the oxygen parameter u and the degree of inversion x are determined as those giving the best linearity of the relation between $\lg(I_{obs.}/I_{calc.})$ and $\sin^2\theta/\lambda^2$, according to the equation

$$\ln(I_{obs.}/I_{calc.}) = \ln k - 2 B_{eff}(\sin^2\theta/\lambda^2)$$

where $I_{obs.}$ and $I_{calc.}$ are the observed and calculated intensities of diffraction, k is a scale factor, B_{eff} is the effective temperature factor, θ the diffraction angle, and λ the wavelength of the radiation used.

The X-ray technique is adequate for the determination of cation distribution only in those cases where the scattering factors are sufficiently different, i.e. the X^{2+} and Y^{3+} cations do not have equal, or nearly equal number of electrons. When the scattering factors of the cations involved are very similar the technique loses resolution or even becomes completely unsuitable. In some cases this limitation can be circumvented by a careful selection of the incident wavelength so that diffraction occurs in the region of anomalous dispersion

for the ion of lower scattering factor.[17,56] This method, however, is not of general applicability.

Electron diffraction can be used for the determination of cation distribution in the same way as X-ray diffraction, but the problem of differentiating two ions of nearly the same atomic number still persists. In fact, electron diffraction does not show, in general, any substantial advantage over X-ray diffraction and the technique is only used in some rather special cases.

Neutron diffraction possesses several advantages over X-ray diffraction in the study of spinels. On the one hand the nuclear scattering factors for ions which have similar X-ray scattering factors may be significantly different.[59] On the other the nuclear scattering factor for oxygen is much greater and this enables the oxygen parameter to be determined with a much greater accuracy. A further advantage of neutron diffraction is the possibility of determining the magnetic structure of spinels with ferromagnetic or antiferromagnetic properties. In addition to the nuclear scattering there is a scattering of the incident neutron beam arising from the interaction of the neutron magnetic moment and the unbalanced spin moments of the ions.[60] For the case of a paramagnetic material, the ionic spin moments are uncoupled and are directed in a random orientation. The magnetic scattering is then incoherent. However, if the ionic spin moments are oriented in a parallel or antiparallel manner, the

magnetic scattering is coherent. The nuclear and magnetic contributions to the scattered intensity can, in general, be separated and this enables the magnetic spin distribution, and the orientations of the spin moments with respect to the crystallographic lattice, to be determined.

1.7.2 UV-vis spectroscopy

Ionic solids containing open-shell cations, such as spinels with 3d transition metals, exhibit spectra corresponding to optical transitions between the open-shell levels split by the electrostatic field of the nearest anionic neighbours. The d-d spectra of transition metal ions are characteristic not only of the electronic configuration of the ion, but also of its coordination symmetry. Therefore an analysis of d-d transitions, usually occurring in the range 25000 to 5000 cm^{-1}, gives information about the symmetry of the transition metal ion. This analysis is done by correlation of the electronic transitions displayed by the spectrum with the energy level diagrams[61] for the ion under consideration. In carrying out this correlation two important selection rules, derived from quantum mechanics,must be considered. These are (i) the spin-multiplicity selection rule and (ii) the Laporte selection rule.

(i) Spin-multiplicity selection rule

This rule specifies that electronic transitions may take place only between states which possess the same spin-multiplicity. However, spin-forbidden transitions can appear, albeit very weakly, due to spin-orbit coupling.

(ii) Laporte selection rule

The Laporte rule establishes that electronic transitions may occur only between states which differ in parity, this is, between states whose wave functions are not either both symmetric or both antisymmetric. According to this rule any transitions involving a redistribution of electrons within a single quantum shell are forbidden; thus d-d transitions are not allowed. There are some ways in which the Laporte rule may be relaxed for a transition metal ion in a compound. If the ion is in a non-centrosymmetric environment, such as is the case in tetrahedral coordination, mixing of the nd- and (n+1)p-orbitals may occur to some extent, thus relaxing the Laporte rule. In a site with octahedral coordination mixing of nd- and (n+1)p-orbitals does not occur when the cation lies at the centre of symmetry of the site, but lattice vibrations cause the cation to spend part of its time in non-centrosymmetric positions and thus some partial mixing of orbitals can occur. This mechanism is known as vibronic coupling.

Although all Laporte-forbidden transitions are expected to result in moderately weak absorption bands, those corresponding to ions in tetrahedral coordination are some 10 to 100 times more intense than the ones correspondin to ions in octahedral coordination. Spin-forbidden transitions, on the other hand, are about 100 times weaker than transitions in centrosymmetrically coordinated ions and they are not usually observed.

UV-vis spectroscopy is a powerful tool for the study of cation distribution in spinels with d^n-ions when $n \neq 0$ or 5 (every d-d transition being spin-forbidden in this case), as illustrated by Stone,[62] Stone et al.[63,64] and Schmitz-Dumont,[65] among others. The technique is more sensitive, and easier to apply, than the diffraction methods outlined before, but it has the disadvantage that only qualitative, or at the most semiquantitative, determinations can be made.

1.7.3. I.R. Spectroscopy

It seems likely that an analysis of the infrared spectrum of lattice vibrations in compounds with spinel-type structure would provide information about the distribution of cations between tetrahedral and octahedral sites. However, as will be seen, the assignment of the i.r. bands is not always unequivocal. Group theory considerations led Waldron[66] and White and DeAngelis[67] to conclude that there are four i.r. active modes in the lattice vibrations of a spinel. Waldron classifies these four modes into two groups. The two modes having the highest frequencies are assigned to the motion of oxygen ions with respect to the cations, whilst the two low-frequency modes are related to displacements of the metallic ions. Usually, however, only two main strong bands, appearing in the region 1000-400 cm^{-1}, are observed in the i.r. spectra of spinels.[66,68] These two bands have been assigned by Waldron[66] to the stretching vibrations of

the tetrahedral and octahedral groups, the band at highest energy corresponding to the tetrahedral group. Waldron's argument is as follows: In the spinel lattice every oxygen ion is bonded to three octahedral cations and one tetrahedral cation. The three octahedral bonds are mutually perpendicular, whilst the tetrahedral bond is directed along the diagonal of the quadrant defined by the octahedral bonds (Fig.1.4). To a first approximation there will be two vibrational modes of the oxygen ion, one in the direction of the tetrahedral cation (ν_1) and the other in a perpendicular direction (ν_2). The ν_1 mode, which is a stretching vibration of the tetrahedral group, corresponds to the highest restoring force and thus should be assigned to the high frequency band. The ν_2 mode (stretching vibration of the octahedral group) is then assigned to the low frequency band. This interpretation seems to be justified by the consideration that the three octahedral bonds provide an isotropic force field, whereas the tetrahedral bond introduces a supplementary restoring force in a preferential direction.

Preudhomme and Tarte[69] made the remark that the above interpretation will only be right if the tetrahedral cation-oxygen bond is stronger, or at least the same order of magnitude of strength, as the octahedral cation-oxygen bond. However, this is not always the case. Among cations whose masses and electronic structures are not too widely different the oxidation state is generally the most important factor determining the cation-oxygen bond strength

The higher the oxidation state the greater the bonding strength. With this in view, the above authors conclude that Waldron's assignment of the high frequency band to the tetrahedral stretching vibration is only correct when the tetrahedral cation is in a higher oxidation state than the octahedral one, the normal 2,4 spinel Ni_2GeO_4 being a typical example. In the case of 2,3 spinels the situation is less simple and it has been suggested[70] that, at least in some cases, the low frequency band corresponds to the stretching vibration of the tetrahedral group. The interpretation of the i.r. spectra of spinels appears to be further complicated by the fact that complex vibrations may take place, as a result of interactions between coordination polyhedra which may result in vibrations of the crystal lattice as a whole[71] or, at least, coupled vibrations of one sublattice.[72] Because of the geometry of the spinel structure it should be expected that the vibrational interactions would be stronger in the octahedral sublattice. The occurrence of such interactions in a specific case may be determined[72] by either isotopic or isomorphic replacement of the cations, but it should be clear that, so far, no general interpretation of the i.r. spectra of spinels can be given. Therefore infrared spectroscopy, which potentially may be very helpful in the problem of cation distribution, must be used with caution until further research allows more general conclusions to be drawn.

1.7.4. Other methods

Some other methods that can provide information about cation distribution in spinels are magnetic susceptibility measurements, magnetic resonance (NMR and ESR), measurements of electrical conductivity and Mössbauer spectroscopy. These methods however are of rather limited applicability and will not be discussed here.

1.8. Diffusion in the solid state

For a reaction in the solid state to proceed, and also for solid solutions to form from mixtures, it is necessary that there be transport of mass through the solid. A local non-convective flux of matter under the action of a chemical gradient is referred to as diffusion. In the present section a brief account will be given of the phenomenon of diffusion in solids and its possible mechanisms. A formal, detailed treatment, can be found in the monographs on this subject by Jost[73] and by Crank.[74]

1.8.1 Random movement and diffusion

Consider a crystalline bar that has a concentration gradient along the x axis, as shown in the figure, and

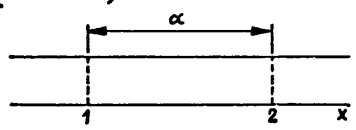

assume that diffusing atoms can only move along this axis, either to the left or to the right. Consider now two adjacent lattice planes, designated 1 and 2, a distance α

apart. Let there be n_1 diffusing atoms per unit area in plane 1 and n_2 in plane 2. If each atom jumps an average of Γ times per second, the number of atoms jumping out of plane 1 during a time δt is $n_1\Gamma\delta t$. Since half of these will go to the right, the number of atoms jumping from plane 1 to plane 2 in δt is $\frac{1}{2}(n_1\Gamma\delta t)$. Similarly the number of atoms jumping from plane 2 to plane 1 in δt is $\frac{1}{2}(n_2\Gamma\delta t)$. The net flux from plane 1 to 2 is thus:

$$J = \tfrac{1}{2}(n_1-n_2)\Gamma \qquad (1.5)$$

The quantity (n_1-n_2) can be related to the concentration by observing that $n_1/\alpha=c_1$ and $n_2/\alpha=c_2$. Thus

$$J = \tfrac{1}{2}(c_1-c_2)\alpha\Gamma$$

Considering that

$$c_1-c_2=-\alpha\frac{\delta c}{\delta x}$$

equation (1.5) can be written:

$$J = -\tfrac{1}{2}\alpha^2\Gamma\frac{\delta c}{\delta x} \qquad (1.6)$$

Fick's first law[73] establishes that if the x axis is taken parallel to the concentration gradient of a given component, i, the flux, J_i, of this component along the gradient can be given by the equation:

$$J_i = -D_i\left(\frac{\delta c_i}{\delta x}\right)_t \qquad (1.7)$$

where D is called the diffusion coefficient.

Comparison of equations (1.6) and (1.7) shows that the diffusion coefficient is given by

$$D_i = \tfrac{1}{2}(\alpha^2\Gamma_i)$$

The diffusion coefficient is therefore determined by the product of the square of the jump distance and the jump frequency. It has the dimension $cm^2 sec^{-1}$. The units of J_i can be arbitrarily chosen. However, the units of c_i must then correspond.

Fick's first law is valid at any instant even if the concentration and concentration gradient at the point being considered change with time, but a more useful expression for the case of concentration changing with time is[73]:

$$\frac{\delta c}{\delta t} = \frac{\delta}{\delta x} \left(D \frac{\delta c}{\delta x} \right) \qquad (1.8)$$

Equation (1.8) is referred to as Fick's second law. The essence of any formal treatment of diffusion phenomena is embodied in equations (1.7) and (1.8) and their solution under the limiting conditions imposed by every particular case.

1.8.2 Mechanisms of diffusion

Atoms, or ions, in a crystal oscillate about their equilibrium positions and occasionally these oscillations become violent enough to allow an atom (ion) to change sites. It is these jumps from one site to another which give rise to diffusion in solids. The presence, and nature, of defects in the structure is a major factor in determining the mechanism by which diffusion proceeds. The main mechanisms thought to give rise to diffusion in solids are:

(i) Vacancy mechanism

(ii) Interstitial mechanism

(iii) Interstitialcy and crowdion mechanisms

(iv) Ring mechanism

(i) Vacancy mechanism

In all crystals some of the lattice sites are unoccupied, thus leaving vacancies. If one particle (atom or ion) on an adjacent site moves into the vacancy, the particle is said to have diffused by a vacancy mechanism. As can be seen from fig. 1.9(a) the elementary step of a particle during vacancy diffusion is associated with an elementary step of a vacancy in the opposite direction. The distortional energy required to move particles by a vacancy mechanism is not too great and this mechanism of diffusion is well established to be the dominant one in the cases of fcc metals and alloys, as well as in a vast number of ionic compounds and oxides.[75]

(ii) Interstitial mechanism

A particle is said to diffuse by an interstitial mechanism when it passes from one interstitial site in the lattice to another in its nearest neighbourhood, as shown in fig. 1.9(b). It is clear that during this process there is an intermediate step where an appreciable local dilation of the lattice must occur. The energy required for such a lattice distortion prevents this mechanism from becoming dominant unless the interstitial atom is small compared with those at the normal lattice sites. Thus, the interstitial mechanism is thought to operate in metals and alloys for atoms which usually occupy interstitial positions

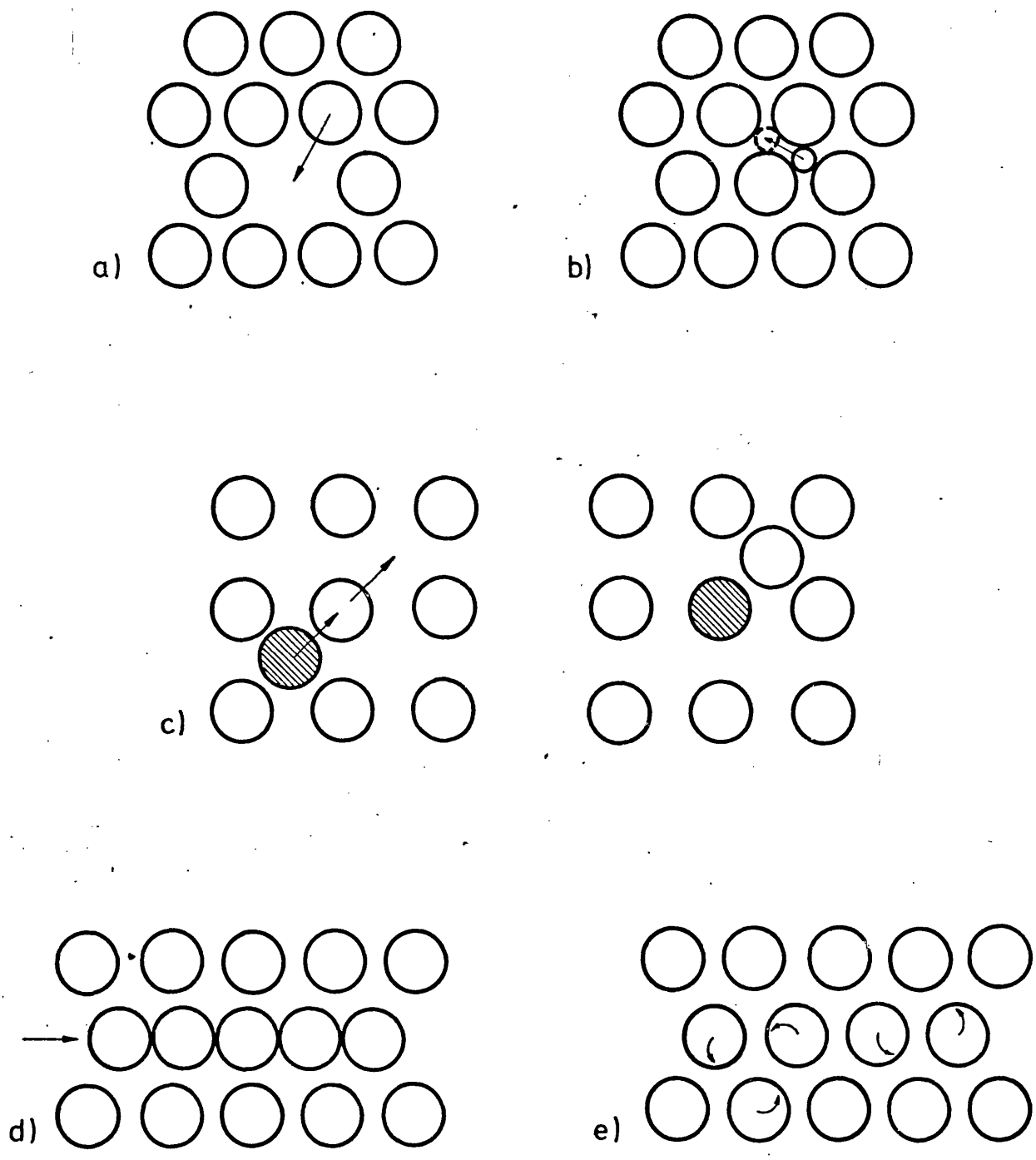

Fig. 1.9

Schematic diagrams of the elementary atomic steps for several diffusion mechanisms

a) Vacancy
b) Interstitial
c) Interstitialcy
d) Crowdion
e) Ring

such as C in α- and γ-iron. However, if the diffusing interstitial atom is as large as the atoms on the normal lattice sites, the distortion involved in this mechanism becomes too large and another diffusion mechanism becomes dominant.

(iii) Interstitialcy and crowdion mechanism

In the interstitialcy mechanism, schematically shown in fig. 1.9(c), an interstitial ion or atom moves onto a regular lattice site by displacing the particle which was originally there onto an interstitial site. When the interstitial atoms are not very small compared with the atoms of the matrix, this mechanism involves far less distortional energy than the interstitial one discussed above. Thus, the interstitialcy mechanism has been proved to be dominant for silver ions in AgBr.[76]

A variant of interstitialcy diffusion is the crowdion mechanism. Crowdion is the name given to an interstitial configuration which has the extra atom placed in a close-packed direction, thus displacing several atoms from their equilibrium position, as shown in fig. 1.9(d). This configuration can move in only one direction, but the energy to do so is quite small.

(iv) Ring mechanism

The simplest elementary diffusional step which could be envisioned in a crystal would be the direct exchange of two neighbouring atoms, but, for any reasonably dense packing, the activation energy for such a process would be very high, because it involves a large distortion of the lattice. However, as pointed out by Zener,[77]

the distortion of the simple exchange could be appreciably reduced if, instead of two atoms interchanging, three or more atoms rotate as a group. This can be realized by inspection of fig. 1.9(e). Up until now the existence of such a process has not been experimentally demonstrated, but the ring mechanism has been suggested as an explanation for some apparent anomalies in the diffusion coefficient of some bcc metals.

1.8.3. Temperature dependence of diffusion coefficients

It has been shown experimentally that for nearly all diffusion phenomena the coefficient of diffusion varies with temperature according to an exponential law of the form:

$$D = D_0 \exp.(-Q/RT) \qquad (1.9)$$

where D_0 is a constant, Q is the activation energy (per mole) for diffusion, R is the Boltzmann constant per mole, and T the absolute temperature. Equation (1.9) is an Arrhenius-type relation, characteristic of processes in which an energy barrier of magnitude Q must be overcome by thermal fluctuations. An interpretation of the form of eq. (1.9) in terms of lattice dynamics has been given by Rice.[78]

1.8.4. High-diffusivity paths

Besides vacancies and interstitials, in any real crystalline specimen, there are also free surfaces, dislocations, and often grain boundaries. It is well

established that regions of lattice imperfection are regions of increased mobility of structural elements, i.e. the mean jump frequency of an atom in these regions is much greater than that of an atom in a more perfect zone of the crystal. Depending upon the fraction of the total material which is included in the distorted regions, and depending upon the temperature, the diffusion in these regions can exceed the volume diffusion which has been briefly discussed so far.

Surface diffusion occurs when particles of the crystal, or adsorbed foreign particles, move along crystal surfaces. Since surfaces usually exist in contact with other phases, specific adsorption effects can occur. Because of these effects, and because of the complex structure of the surface, the diffusional processes here are very dependent upon experimental conditions, thus making it difficult to draw general conclusions from experimental results. However, it is clear that this diffusion path cannot be neglected, especially when dealing with powdered samples. Grain boundaries and phase boundaries are also regions of the crystal where high diffusivity should be expected. The loosening of the crystal lattice in, and near, these regions causes the average jump frequency of particles to be, in general, greater than in the bulk of the crystal. Finally, dislocations must also be taken into consideration as possible high mobility paths for diffusing particles.

In general, the activation energy for volume diffusion is higher than that for other diffusion mechanism.

Thus it is to be expected that, in fine-grained specimens, or in samples with high dislocation densities, diffusion will be structure-sensitive at lower temperatures, whilst near the melting point volume diffusion, which is independent of line and planar crystal imperfections, will prevail.

1.9. Solid Solutions

Solid solutions are single phase materials with a chemical composition which does not obey Dalton's law of subscripts consisting of small whole numbers in chemical formulae. They occur naturally in many minerals and are very widely used among man-made materials. Single phase alloys are a typical example.

From a structural point of view there are several ways in which solid solutions can form and, accordingly, they may be classified as follows:

(i) Substitutional solid solutions in which atoms (ions) of one element replace, at random, atoms (ions) of another element within the crystalline lattice. They can be considered as mixed crystals whose composition is gradually changing from one end member to another. A good example is provided by the olivine group minerals, $Mg_{2-x}Fe_xSiO_4$, where x can assume any value between 0 and 2, the two end members being försterite (Mg_2SiO_4) and fayaldite (Fe_2SiO_4) respectively.

Compounds in which the number of either anions or cations is slightly less than that required by stoichiometry can also be considered as substitutional solid solutions in which ions with a given oxidation state are replaced by ions of the same element but with different oxidation state, with the concomitant creation of vacancies in the lattice in order to preserve charge neutrality. These are sometimes referred to as 'omission solid solutions'.[10] Well known examples are the non-stoichiometric compounds wüstite and pyrrhotite whose chemical formulae can be written as $\square_x Fe_{1-x}O$ and $\square_x Fe_{1-x}S$ respectively ($\square \equiv$ cation vacancy). The stability of non-stoichiometric phases tends to increase with increasing temperature, because of the role played by the configurational entropy. Annealing under conditions which allow re-arrangement processes to occur often gives place to disproportionation and a succession of phases of fixed composition (homologous series) is formed.[79,80]

(ii) Interstitial solid solutions in which limited amounts of solute atoms occupy interstitial positions in the solvent crystal. This situation is very often found when the solvent presents a so-called "open structure" with large interstices which can accommodate the foreign species. A different example is provided by metal crystals which often contain

varying amounts of carbon, boron, hydrogen or nitrogen because these atoms are small enough to lodge in the unoccupied octahedral or tetrahedral interstices in a close-packed array of metal atoms.

Some authors define solid solutions as crystalline materials in which sites of a symmetry-equivalent set are occupied at random by atoms of two or more chemical species, in continuously variable proportions.[81] It is clear that in this definition interstitial solid solutions are not included as a particular case.

1.10 Substitutional Solid Solutions and Factors Governing their Formation

As stated in the preceding section substitutional solid solutions are formed when particles of one kind replace particles of a different kind in the crystalline matrix, this replacement being achieved without the formation of a new phase. The main factors affecting the formation of this type of solid solution will now be considered.

1.10.1 Energetic considerations

From an energetic point of view solid solutions are stable when the mixed crystal has a lower free energy than the alternatives of two crystals of different composition or the formation of a new compound. The free energy is given by the relation

$$G = U + pv - TS \qquad (1.10)$$

where U is the internal energy, p is the pressure, v is the volume, T the absolute temperature, and S the entropy. The pv product is small and can be neglected. U is determined mainly by the structural energy and, therefore, if an atom added at random greatly increases the structural energy, the solid solution is unstable and two crystal structures result. On the other hand, great decreases of structural energy on addition of foreign atoms are usually associated with the formation of a new phase. If the change in internal energy is small the entropy term plays the major role and, as the entropy is always increased by random additions due to the increase in disorder, the solid solution will have the lowest free energy and be the stable configuration.

The changes in configurational entropy and internal energy in the formation of a solid solution can be evaluated from a statistical model as follows: Suppose that two isostructural ionic substances, AX and BX, form a substitutional solid solution and consider an amount of this solid solution containing N_A atoms of A, N_B atoms of B, and $N_A + N_B$ atoms of X. It is clear that the first coordination shell of an A, or B ion will be occupied by X ions, but in the second coordination shell there will be A, B, or A and B ions. The occupational probabilities for two

sites, 1 and 2, in the second coordination shell will then be:

Probability of A on 1 and A on 2: $\frac{N_A^2}{(N_A+N_B)^2}$

Probability of A on 1 and B on 2: $\frac{N_A N_B}{(N_A+N_B)^2}$

Probability of B on 1 and A on 2: $\frac{N_A N_B}{(N_A+N_B)^2}$

Probability of B on 1 and B on 2: $\frac{N_B^2}{(N_A+N_B)^2}$

Since pairs A-B and B-A are indistinguishable, the occupational probabilities of a pair of sites by a pair of ions are:

A-A: $\frac{N_A^2}{(N_A+N_B)^2}$

A-B: $\frac{2N_A N_B}{(N_A+N_B)^2}$

B-B: $\frac{N_B^2}{(N_A+N_B)^2}$

If the coordination number of a site with respect to its second coordination shell is n, there will be a total

of $\frac{1}{2}n(N_A+N_B)$ pairs of sites such as 1 and 2, and the total number of adjacent pairs of A and B atoms will be:

$$\text{A-A:} \qquad \frac{nN_A^2}{2(N_A+N_B)}$$

$$\text{A-B:} \qquad \frac{nN_AN_B}{N_A+N_B}$$

$$\text{B-B:} \qquad \frac{nN_B^2}{2(N_A+N_B)}$$

If the substances AX and BX are to form a solid solution A and B must be chemically similar ions (both cations or both anions) and the interaction forces will, therefore, be repulsive. Let the increase in potential energy when a pair of atoms is brought from infinity to adjacent sites in the solid solution be W_{AA}, W_{BB} and W_{AB} for A-A, B-B and A-B pairs respectively. The contribution to the potential energy of the lattice due to the interaction energy of nearest neighbour A and B atoms will then be given by:

$$\frac{nW_{AA}}{2} \cdot \frac{N_A^2}{N_A+N_B} + \frac{nW_{BB}}{2} \cdot \frac{N_B^2}{N_A+N_B} + nW_{AB}\frac{N_A\,N_B}{N_A+N_B}$$

whereas the contribution of such nearest neighbour interaction to the potential energy for an equivalent amount of pure AX and BX components will be:

$$\frac{nW_{AA}}{2} \cdot N_A + \frac{nW_{BB}}{2} \cdot N_B$$

The increase in potential energy when N_A molecules of AX and N_B molecules of BX enter into solid solution is, therefore:

$$\frac{nN_AN_B}{N_A+N_B} \left(W_{AB} - \frac{W_{AA}+W_{BB}}{2} \right)$$

and the increase in energy per mole, i.e. the molar excess energy of mixing will be given by:

$$\Delta U^M = \frac{N\ nN_A\ N_B}{(N_A+N_B)^2} \left(W_{AB} - \frac{W_{AA}+W_{BB}}{2} \right) \qquad (1.11)$$

where N is Avogadro's number. Equation (1.11) shows that when the energy involved in the formation of pairs of unlike atoms is about equal to the mean energy for the formation of pairs of identical atoms the change in internal energy on mixing is small. Under these circumstances the entropic term in equation (1.10) becomes dominant.

Using the same statistical model, the entropy of a solid solution can be evaluated from the expression[82]

$$S = k \ln \Omega$$

where k is Boltzmann's constant and Ω is the number of ways in which the atoms can arrange themselves. In a

solid solution $A_xB_{1-x}X$ there are N_A+N_B sites that may be occupied by a number N_A of A atoms and a number N_B of B atoms. The number of possible arrangements of the A and B atoms on the N_A+N_B sites is then given by

$$\Omega = \frac{(N_A+N_B)!}{N_A!N_B!}$$

Therefore,

$$S = k \ln \frac{(N_A+N_B)!}{N_A!\ N_B!} \tag{1.12}$$

Since N_A and N_B are very large, Stirling's approximation $\ln n! = n \ln n$, can be used, and equation (1.12) re-written as

$$S = k\{(N_A+N_B)\ \ln(N_A+N_B) - N_A\ \ln N_A - N_B\ \ln N_B\} =$$

$$= -k(N_A+N_B)\ \{x \ln x + (1-x)\ \ln(1-x)\}$$

or, considering a mole of solid solution:

$$S = -R\{x \ln x + (1-x)\ \ln(1-x)\} \tag{1.13}$$

where R is Boltzmann's constant per mole. The entropy evaluated here is not the whole molar entropy of the solid solution at temperature T, but the configurational entropy due to random arrangement of different atoms on like structural sites. There will in addition be a contribution $\int_0^T Cp \cdot d\ln T$ to the total entropy due to thermal vibrational randomness of all the atoms in the

structure. Since there is no randomness in the arrangement of atoms in pure AX and pure BX the configurational entropy for each of these end members will be zero. If the approximation is made that

$$\int_0^T (Cp)_{ss} d \ln T = x \int_0^T (Cp)_{AX} d \ln T + (1-x) \int_0^T (Cp)_{BX} d \ln T$$

then the excess molar entropy of mixing for the solid solution is given by

$$\Delta S^M = -R\{x \ln x + (1-x) \ln (1-x)\} \qquad (1.14)$$

and since $0 < x < 1$, $\Delta S > 0$.

In terms of the statistical model, an ideal solid solution is defined[83] as that for which $W_{AB} = \frac{1}{2}(W_{AA}+W_{BB})$ and for which the excess molar volume of mixing, ΔV^M, equals zero. The restriction $W_{AB} = \frac{1}{2}(W_{AA}+W_{BB})$ implies that in an ideal solution there is no energetic discrimination between like and unlike pairs of atoms occupying adjacent structurally equivalent positions. From the first of these conditions, and equation (1.11), it follows that for an ideal solution $\Delta U^M = 0$, and since $\Delta V^M = 0$, combination of equations (1.10) and (1.14) gives for the free energy of mixing the value

$$\Delta G^M = RT\{x \ln x + (1-x) \ln (1-x)\} \qquad (1.15)$$

For $0 < x < 1$ this function is always negative and it passes through a minimum for $x = 0.5$. This minimum corresponds to maximum stability for an ideal solid solution $A_x B_{1-x} X$.

1.10.2 Ionic size

Ionic size is one of the most important factors in deciding whether two species can replace each other at random in the same symmetry-equivalent sites. In general, the greater the size difference the greater is the tendency to separate growth of two phases of different composition. However, it is not possible to lay down a rigorous rule as to the largest difference in radii beyond which two ions can not replace each other. From their studies on alloys, Hume-Rothery and associates [84] found that if the difference between the atomic radii of the elements forming an alloy exceeds about 14 or 15 percent, solid solubility is restricted. This is sometimes known as the 15 percent rule and, to a first approximation, it can also be applied to ionic solid solutions, although it must be borne in mind that other factors such as temperature and the type of crystalline structure have considerable effects.

Numerical values of ionic radii for the ions dealt with in this work are given in table 1.3, after Shannon and Prewitt[85,86]. The superscripts LS and HS denote "low-spin" and "high-spin" radii, respectively.

TABLE 1.3

Ion	Coordination number	Ionic radius (Å)
Ca^{2+}	VI	1.00
	VIII	1.12
Cd^{2+}	IV	0.84
	VI	0.95
	VIII	1.07
Co^{2+}	VI	0.65^{LS}
	VI	0.735^{HS}
Co^{3+}	VI	0.525^{LS}
	VI	0.61^{HS}
Cu^{+}	VI	0.96
Cu^{2+}	IV	0.62
	VI	0.73
In^{3+}	VI	0.800
Mg^{2+}	IV	0.49
	VI	0.720
	VIII	0.89

(continued)

Table 1.3 (cont.)

Mn^{2+}	VI	0.67^{LS}
	VI	0.830^{HS}
Mn^{3+}	VI	0.58^{LS}
		0.645^{HS}
Mn^{4+}	VI	0.540
Na^{+}	IV	0.99
	VI	1.02
	VIII	1.16

LS = Low-spin

HS = High-spin

Differences in ionic sizes of the ions which replace each other lead to local strains in the crystalline lattice which increase the crystal internal energy and have important effects on the properties of the solid solutions. In particular they lead to changes in the lattice parameters. Végard[87,88] has suggested that, in many cases, there is a linear relationship between change in lattice constants and composition when a continuous series of solid solutions is formed. According to this so-called Végard's law, the lattice constant a of a solid solution would be given by

$$a = xa_1 + (1-x)a_2 \qquad (1.16)$$

where a_1 and a_2 are the lattice constants of the pure components and x is the molar fraction of the first component. Although the above expression is widely used, one must expect solid solutions to show additivity of volumes (at least in first approximation) rather than lattice constants, i.e.:

$$v = xv_1 + (1-x)v_2 \qquad (1.17)$$

where v_1 and v_2 are the molar volumes of the pure components. For an isometric system, equation (1.17) becomes

$$a^3 = xa_1^3 + (1-x)a_2^3 \qquad (1.18)$$

It is clear, from comparison of equations (1.16) and (1.18), that the linear relationship between lattice parameter and composition is only an approximation. Zhdanov[89] and Zen,[90] among others, have discussed this point and suggested that a parabolic approximation might be more realistic. The fact that the different compressibilities of solvent and solute atoms must also be taken into account has been pointed out by Friedel[91] in a discussion on deviations from Végard's law in metallic solid solutions.

1.10.3 Valency

Although very often ions replacing each other have the same valency, or formal charge, this is not an indispensable requirement for interchangeability, provided that electrical neutrality be maintained by concomitant substitution elsewhere in the structure. This can be achieved either by a double set of substitutions or by leaving an occasional ionic site vacant. Examples of a double substitution are well known among silicate group minerals. Thus, in passing from albite ($NaAlSi_3O_8$) to anorthite ($CaAl_2Si_2O_8$) Ca^{2+} is a substitute for Na^+ and electrical neutrality is maintained by the coupled substitution of Al^{3+} for Si^{4+}. The system $MgAl_2O_4$ - Al_2O_3 provides a good example of the second way in which equal valency requirement can be circumvented. Extensive solid

solution is known to occur between both compounds,[92] corresponding to the substitution of Al^{3+} for some of the Mg^{2+} ions in the spinel. In order to maintain the charge balance each two Al^{3+} ions added must replace three Mg^{2+} ions, leaving one vacant site in the cationic sublattice of the magnesium aluminate spinel structure. The end member of this series is γ-Al_2O_3 which has a face-centered cubic packing of oxygen ions as in spinel[93] in a structure corresponding to $Al_{8/3}\square_{1/3}O_4$ with one-ninth of the total cation sites vacant.

Of special interest is the possibility of controlled valency[94] by the introduction of an altervalent ion into an ionic lattice. Thus, lithium may be introduced into the solid solution NiO-MgO when, for every Li^+ replacing a Ni^{2+} there is an additional positive charge on a neighbouring cationic site, i.e. a Ni^{3+} ion.[95,96] In this way a controlled number of Ni^{3+} ions is introduced.

1.10.4 Electronegativity

Any two chemical species capable of replacing one another at random in symmetry-equivalent sites must resemble each other in chemical behaviour; particularly, the electronegativities must be nearly equal in order to prevent the formation of a new compound as a result of the difference in affinity

for electrons. In an ionic crystal, therefore, the cationic and anionic species can only be replaced by a new cation or anion respectively.

More complex situations arise when the difference in electronegativity between the constituents of the host lattice is small or when the electro-negativity of the foreign species is approximately midway between that of the constituents of the lattice. In this case other factors, such as ionic size and crystal field effects, become important in deciding the choice of site, though the electronegativity factor cannot be totally neglected.[97-99] Thus silicon may occupy both gallium and arsenic sites in Ga As,[100-102] but only the Sb sites in In Sb[97-99] and Ga Sb,[99] and only the In sites in In As[103].

1.10.5 Crystal structure

Solid solutions of a particular series must be isostructural with one another over the whole range of composition possible to them. Consequently, if a continuous series of solutions is to be formed, both end members must necessarily have the same structure.

However, partial solubility is known to occur between compounds with different structure. For example copper(II) oxide, whose crystal structure is

monoclinic, dissolves in the NaCl structure type oxides of magnesium,nickel and cobalt.[104-107] The rock salt structure is maintained by solutions where the molar concentration of CuO is smaller than about 25%, and the monoclinic structure by those with CuO content over 95-98%. Intermediate compositions show, in general, the presence of more than one phase.

1.10.6 Temperature

Equation (1.10) shows that an increase in temperature will result in a decrease in free energy due to the contribution of the entropic term. Solid solution between a particular pair of end-members will, therefore, be favoured at high temperatures where the role played by the entropic term becomes more preponderant, and where the increased amplitude of lattice vibrations makes it possible for the structure to tolerate the local strains generated by random occupation of equivalent sites by ions of different size. Increased ionic substitution at higher temperatures is very common in many minerals and indeed this property provides a means of determining the temperature of mineral deposition (geological thermometry). If for a specific mineral the degree of atomic substitution has been determined for different temperatures, the composition of the

naturally occurring mineral may indicate the temperature of formation.

Random solid solutions formed at high temperatures can behave in various ways on cooling:

(i) conservation of the disordered structure

(ii) ordering of cations of different kinds on to distinct sets of equivalent sites (formation of a superstructure)

(iii) separation of two or more phases of different composition (exsolution).

Which of these processes is most likely to take place will depend on the rate of cooling and on those characteristics of each particular system which determine its thermodynamic stability. The final product, however, has not necessarily to be an equilibrium state at the final temperature. High temperature equilibrium states can often be frozen-in by rapid cooling.

1.11 The System CoO - MgO

CoO and MgO both have the sodium chloride structure with lattice parameters a_o = 4.260 Å and a_o = 4.211 Å respectively.[108-109] The variation of the lattice parameter with cobalt content in the CoO - MgO system has been measured over the complete range of composition by Robin[110] and at dilute cobalt concentrations by Cimino et al.[111] In both investigations a linear increase in lattice parameter with cobalt content was found.

1.11.1 The present work

Solid solution of transition metal ions in a diamagnetic matrix is a very convenient way to study the properties of individual transition metal ions, and the effects of increasing interactions between them. Since the radius difference between Co^{2+} and Mg^{2+} is only 2.08%, and since CoO and MgO both possess the same crystal structure, the formation of a whole series of solid solutions is highly predictable in the case of well sintered specimens. However, the prediction is not so straightforward in the case of very finely divided materials. The increased role played by free surfaces and grain boundaries in powders with very small crystallite size may, in principle, affect the stability of solid solutions in an appreciable way. Finely divided solids, on the

other hand, are very suitable for studies of heterogeneous catalysis and, in a wider sense, for studies of surface chemistry and reactivity of solids. In particular, they offer a way to learn more about surface coordination.

With the above premises in mind, it seemed desirable that more knowledge be gained on the properties of finely divided solid solutions. The CoO - MgO system was selected as a model for the comparative study of the solid state and surface chemistry of specimens with different degrees of subdivision. The work includes the preparation, characterization, and studies of surface reactivity of large and small crystallite size samples of CoO - MgO dilute in cobalt.

1.12 The System MnO - CaO

Both end-members have the sodium chloride structure, the values of the lattice parameters being a_o = 4.445 Å and a_o = 4.8105 Å for MnO and CaO respectively.[112,113] The difference in ionic radius between Mn^{2+} and Ca^{2+} is 21.95% which is far larger than the amount allowed by the Hume-Rothery rules for solid solution formation (see section 1.10.2). Solid solubility between MnO and CaO has been studied by several authors[114-118] with conflicting results. Natta and Passerini,[114] who prepared

the solutions by thermal treatment of coprecipitated hydroxides, report limited solid solubility, with an immiscibility gap between 25% and 65% of molar concentration in MnO. However, later work by Jay and Andrews,[115,116] Glasser[117] and Schenk et al[118] shows the formation of a complete series of solid solutions over the whole range of composition. The discrepancy in the results could, in principle, be due to a difference in the temperature of the preparation of the samples. Natta and Passerini carried out most of their experiments at 873 K, whilst the latter authors[115-118] have used temperatures in the range 1423-1573 K. However, there remains the fact that Natta and Passerini did prepare some specimens at 1173 K and report no increase in solubility, as compared with the specimens prepared at 873 K.

1.12.1 The present work

The system MnO - CaO is of interest because it affords the means to study the properties of Mn^{2+} ions at different stages of dispersion in a diamagnetic matrix of different ionicity from MgO. In view of this, and also because of the interesting anomaly with the Hume-Rothery rules, a detailed reinvestigation of this system has been undertaken. Also, with surface properties in mind, attention has

been given to preparing samples at lower temperatures than 1400 K. The temperature at which the specimens are prepared has a very pronounced influence on their degree of sintering, and therefore on the ratio of surface to bulk in the materials obtained. It is desirable, for studies of surface chemistry, that this ratio be as large as possible.

Manganese ions can easily take oxidation states higher than 2+; thus, the system MnO - CaO provides a good starting point for the study of controlled valency (section 1.10.3). This has been attempted by the introduction of Na^+ ions which are about the same size as Ca^{2+} (Table 1.3).

1.13 The System $CuIn_2O_4$ - $CdIn_2O_4$

Cupric oxide reacts with aluminium and gallium sesquioxides to form the spinels $CuAl_2O_4$ and $CuGa_2O_4$ respectively.[125,120] However, attempts to prepare the corresponding indium compound $CuIn_2O_4$ have so far been unsuccesful.[119] Solid state reaction between CuO and In_2O_3, carried out in air at 1173 K, produces the compound $Cu_2In_2O_5$ as the only new phase.[120,121] The apparent impossibility of the formation of the compound $CuIn_2O_4$ may, in principle, be thought of as due to the difference of ~10% in ionic radius between Cu^{2+} (0.73 Å) and In^{3+} (0.80 Å). It is conceivable that this difference could impose

destabilizing strains in the spinel structure. However, such an explanation meets with the difficulty that the difference is far larger in the case of $CuAl_2O_4$ (ionic radius of Al^{3+} = 0.53 Å[85]), the only difference being that Cu^{2+} is in that case the larger ion.

1.13.1 The present work

In order to gain further knowledge on this subject, a study of indium spinels in which the divalent ion is progressively replaced by Cu^{2+} has been made. In the present work the known spinel $CdIn_2O_4$ has been chosen as the starting compound in which to replace Cd^{2+} by Cu^{2+}. There are two reasons for this choice. First $CdIn_2O_4$ is the only indate which is known to form readily at a temperature lower than that of the decomposition of cupric oxide in air (about 1300 K[126]). Secondly this choice gives an opportunity of studying the crystal structure of $CdIn_2O_4$. The formation of $CdIn_2O_4$ by direct reaction between CdO and In_2O_3 has been reported by several authors.[122-124] However, although there is general agreement as to the formation and stoichiometry of cadmium indate ($CdIn_2O_4$), its crystal structure is not settled. Thus, Passerini[122] (1930) reports the compound to have a tetragonal structure with a_o = 8.65 Å and c_o = 9.87 Å, whilst Skribljak

et al[123] (1959) report a cubic, spinel-type, structure with a_o = 9.115 Å. A later report by Cruickshank et al[124] suggests an orthorhombic symmetry, although no actual data are given.

CHAPTER II

EXPERIMENTAL TECHNIQUES

2.1 X-ray Diffraction and the Determination of Accurate Lattice Parameters

X-ray diffraction is the most commonly used method for the determination of lattice parameters and crystal structures. The physical basis of X-ray methods in crystallography is adequately described in standard texts[127] and will not be considered here in detail. However, when accurate lattice parameters are sought, careful consideration has to be given to the possible sources of error, their relative importance, and the way in which the errors can be corrected or minimized. This subject will be discussed in sections 2.1.3 to 2.1.6, after an introduction to the powder diffraction method.[128]

It may be shown that, as a general rule, high accuracy for lattice parameter determination can only be attained by using high angle diffraction lines, i.e. lines occurring at angles near $\theta = 90^{o}$. At these angles the values of the d-spacings (the spacings between lattice planes), and therefore those of the calculated lattice parameters, are not very strongly influenced by small errors in the measured diffraction angles. This can be realised by considering the Bragg equation

$$\lambda = 2d \sin\theta \qquad (2.1)$$

where λ is the X-ray wavelength, d is the spacing between lattice planes and θ the angle of diffraction. Differentiation of eq. 2.1 gives:

$$\Delta\lambda = 2\,\Delta d \sin\theta + 2d \cos\theta\,\Delta\theta \qquad (2.2)$$

From eq. 2.1 and 2.2:

$$\frac{\Delta d}{d} = \frac{\Delta\lambda}{\lambda} - \cot\theta\,\Delta\theta$$

As θ approaches 90^{o}, $\cot\theta$ approaches zero; thus any errors in θ produce vanishingly small errors in d if the error in λ is assumed to be zero.

2.1.1 The Debye-Scherrer method

Soon after the discovery, made by Laue and his associates,[129] that individual crystals can act as diffraction gratings to X-rays, Debye and Scherrer,[130,131] and Hull,[132,133] devised a method that could be used with polycrystalline materials instead of single crystals. This technique is usually known as the Debye-Scherrer, or powder method. The latter name makes reference to the fact that the method usually requires the individual crystals of the aggregate to be about the size of grains of a fine dust.

In an ideal powder camera a monochromatic X-ray beam would strike a sample composed of a very

large number of small crystals in random orientation, and the rays diffracted by the crystals would be received by a suitably placed photographic film. Consider the set of planes in the crystals having the spacing d. If the crystals are suitably orientated these planes will diffract the X-rays through the angle 2θ, where θ is given by the Bragg equation

$$\theta_{hkl} = \sin^{-1} (\lambda n/2d_{hkl}) \qquad 2.3$$

In this equation h, k and l are the Miller indices of the diffracting planes, n is an integer (*) and λ is the X-ray wavelength. Since the orientation of the crystals is postulated to be random, most of the crystals will not be in the correct position to diffract the X-rays, but many will. The correct placing is to have the normal to the planes making an angle $\frac{\pi}{2} + \theta$ with the direction of the incident X-rays. Crystals satisfying this condition will diffract the rays along a direction making an angle 2θ with the direct beam. The orientation condition is not unique; a correctly placed crystal could be rotated through any angle about the beam direction without ceasing to diffract X-rays. The locus of all the diffracted rays will then be a conic surface of semi-angle 2θ, having its apex at the specimen and its axis in the direction of the incident beam.

(*) In X-ray crystallography the value of n is often set equal to unity; if so, the indices h, k, l may contain a common factor.

In any crystal there will be many sets of planes with different spacings d_1, d_2, ... Each of these sets will give rise to a cone of diffracted rays, the semi-angles of the cones $2\theta_1$, $2\theta_2$, ... being determined by inserting the succesive values of d in eq. 2.3. The powder pattern, characteristic of the substance and wavelength, consists of the intersection of the set of cones with the photographic film. This is usually disposed in the form of a cylindrical surface surrounding the specimen. In this way, the diffraction pattern consists of arcs of circumference symmetrically arranged around a central point which coincides with the direction of the incident beam. Measurement of the diameters of these arcs enables one to calculate the angles of diffraction and therefore the lattice spacings, according to eq. 2.3.

2.1.2 Relation of d-spacings to cell edges

Once the d-spacings are known the "reflections" can, in general, be indexed and the lattice parameters computed. For any crystal system there exists a relationship between the d-spacings, the unit cell edges a, b and c, and the angles between these edges α, β and γ. For a cubic system, in which $a = b = c$ and $\alpha = \beta = \gamma = 90^{o}$, the following relationship holds:

$$a = d_{hkl} \, (h^2 + k^2 + l^2)^{\frac{1}{2}}$$

2.1.3 The nature of the possible errors

The possible errors which can arise in the determination of lattice parameters may be classified in two different categories: (i) subjective errors, or errors of observation, and (ii) experimental errors. These two categories are sometimes referred to as random errors and systematic errors respectively.

2.1.4 Subjective errors

Subjective, or observational errors, arise as a consequence of the measurement of the position of the lines on the film. This measurement is usually done by setting a cross-wire on the centre of each line and reading its position on a vernier scale. The main sources of error are the location of the centre of the line and the inaccuracy in the readings on the scale. To reduce this error several measurements must be made on each line, if possible on two or more independent films, and the results averaged. The use of photometric methods has been suggested as an alternative in order to make the process of reading more objective. However, the usefulness of this alternative seems to be questionable because, although it is more objective, it is less precise.[134] This is due to the fact that the lines are not as sharp as they appear to the eye, and the position of their apex is very often rather imprecise on the microphotometer trace.

2.1.5 Experimental errors

There are several situations which cause a shift in the centre of an X-ray diffraction line from the position it ideally should occupy. These give rise to errors which are systematic functions of the position of the reflection. The main sources of experimental error are:

a) Eccentricity of the specimen with respect to the axis of the film cylinder.

b) Absorption of X-rays by the specimen.

c) Refraction of X-rays by the specimen.

d) Uneven distribution in the intensity of the background.

a) Eccentricity error

Fig. 2.1 illustrates the effect of displacing the specimen from the centre of the camera, C, to a position C'. Such a displacement may occur in any direction, but it is convenient to resolve it into its components parallel and perpendicular to the direction of the X-ray beam (Fig. 2.1(a) and 2.1(b) respectively). The effect of the component parallel to the beam direction is to shift both lines corresponding to a reflection towards (or away) from one another, thus introducing a total error $2 \cdot \Delta S$ in the arc length between the lines on the film. Bradley and Jay[135] showed that the error in d caused by this

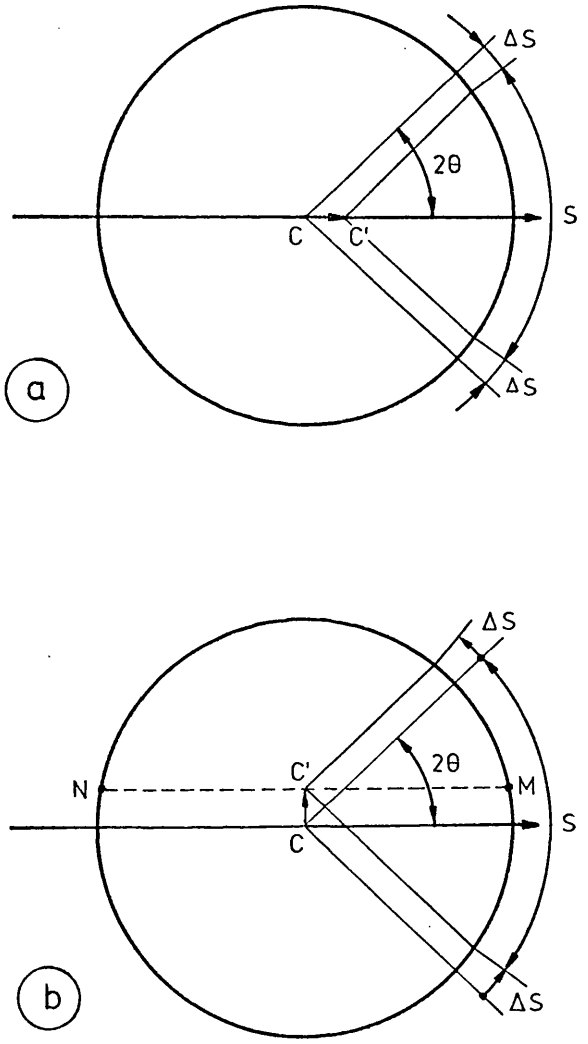

Fig 2.1

Illustration of the eccentricity error
a) Displacement parallel to the X-ray beam
b) Displacement perpendicular to the X-ray beam

displacement is proportional to $\cos^2\theta$. The effect of the component of the displacement perpendicular to the X-ray beam is to displace the diffraction line toward lower angles on one side of the film and toward higher angles on the other side. Although the distance, S, between the lines remains unchanged by this displacement, there will be a significant error when the Straumanis-Ievins arrangement[136] is used. This is due to the fact that the distance between M and N will now be smaller (or larger) than 180°. It can be shown[137] that, for high angle lines, the error in d caused by this displacement is proportional to $\left(\frac{\pi}{2} - \theta\right)\cot\theta$.

Eccentricity errors can be minimized by careful centering of the specimen in an accurately constructed camera. Another precaution to be taken is to press the film properly against the camera body. Any remaining eccentricity error would, in general, be negligible if high-angle lines are used to compute d-spacings and lattice constants.

b) Absorption of X-rays by the specimen

The effect of absorption of the X-ray beam by a cylindrical specimen is shown in fig. 2.2. It can be seen that absorption causes a displacement of the centre of gravity of the diffraction lines towards an angle 2θ larger than the theoretical

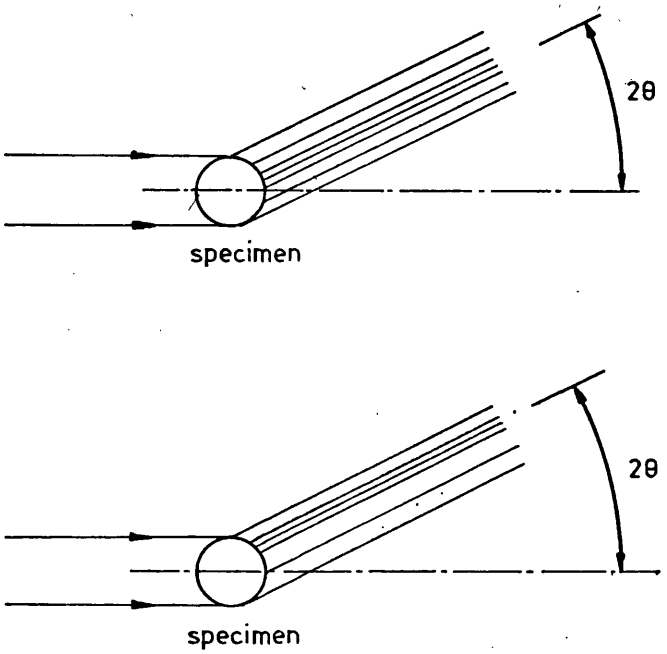

Fig. 2.2

Illustration of the absorption error
a) nonabsorbing, and b) absorbing specimen

value. Therefore the calculated d-spacing will be smaller than the true value. The magnitude of this error decreases as the angle of diffraction, 2θ, increases, and it would be zero for a theoretical reflection occurring at $2\theta = 180^{o}$. The error due to absorption could therefore be eliminated by finding a suitable function of the lattice parameter, or d-spacing, versus the Bragg angle, and extrapolating to $\theta = 90^{o}$. However, the theoretical analysis of the angular dependence of the absorption error appears complicated by the fact that, in practice, the X-ray beam is never strictly parallel, and the exact analytical form of the error has not yet been found. Bradley and Jay[135] showed that it is approximately proportional to $\cos^{2}\theta/\theta$, but later work by Taylor and Sinclair[138] has shown that an extrapolation against $\frac{1}{2}\cos^{2}\theta(\csc\theta + \theta^{-1})$ is a better approximation. Nelson and Riley[139] found that this function gives a good linear extrapolation for the specimens they have tested.

Absorption errors can be experimentally reduced by dilution of the specimen with a powder highly transparent to X-rays, and (or) by the use of very thin specimens. It is clear, however, that this experimental approach presents some limitations. Dilution is very often undesirable, and the preparation of very thin specimens meets with technical

difficulties. Nevertheless, the use of specimens as thin as possible is highly recommendable because not only can the absorption error be diminished, but also the width of the diffraction lines is reduced and therefore their position can be more accurately determined.

In the standard use of the Debye-Scherrer technique absorption is probably the most important source of error. It can produce as much as 10^{-2} Å error, mainly when dealing with highly absorbent specimens. The combined use of thin specimens, high angle reflections, and an extrapolation to $\theta = 90^{o}$ can minimize absorption errors to vanishing point. A suitable analytical treatment of the data[140-146] is an alternative to graphical extrapolation.

c) Refraction of X-rays by the specimen

X-rays, as all electromagnetic radiation, are refracted on passing from one medium to another having a different index of refraction. On the one hand, refraction will cause the X-rays to have a different wavelength within the crystal and, on the other, will cause the diffraction angles measured to deviate from their theoretical value. Since Bragg's law is correct only inside the crystal,[147-150] it is clear that refraction introduces two errors in the use of eq. 2.1. The first one is an error in

the wavelength: the wavelength, λ, inside the crystal should be taken as λ_v/n, where λ_v is the X-ray wavelength in vacuo and n the index of refraction of the crystal. The second one comes from the fact that the diffraction angles, θ, actually measured deviate from their theoretical value whenever $n \neq 1$, as a consequence of the refraction phenomenon.

An exact treatment of the effect of refraction on the d-spacings calculated according to the Bragg equation is difficult to make, except for the case of a flat single crystal specimen. However, from the work of Wilson[151] and Straumanis,[152] it follows that an approximate correction can be made by adding to the calculated lattice spacing a fraction 1/(1-n), that is:

$$d_{corr.} = d_{obs.}\left(1 + \frac{1}{1-n}\right)$$

For most materials the error due to refraction is usually of the order of 10^{-5} Å. It is not eliminated by the process of extrapolation to $\theta = 90^{o}$. It is worth noticing that the extent to which refraction occurs depends upon the wavelength; thus different radiations will produce different amounts of error.

d) Uneven distribution in the intensity of the background

Nonuniformities in the background have

the effect of shifting the position of the centre of the line in the direction of increasing background intensity. There are several factors which can contribute to uneven background on an X-ray film[128] and they are sometimes difficult to control. However, substantial improvements can often be obtained by adequate choice of the X-ray radiation or (and) by the use of a monochromator. The amount of shift in line position due to uneven background will depend on the particular case, but it very rarely exceeds the inaccuracy in the measurement of line positions.

2.1.6 The ultimate limits of accuracy

Since X-ray wavelengths are known to about 1 part in 10^5 it would appear possible to determine the value of a cell edge to this limit of accuracy. In practice, it has not been possible to obtain this mainly because of the subjective errors introduced in estimating the position of the centre of blackening of a line. The magnitude of the error introduced will depend upon the individual and upon the nature of the line. With a good film the position of a reflection can be estimated with a possible error of about $\pm$ 0.03 mm. Assuming that the systematic errors have been reduced to the vanishing point, and that only high-angle reflections are used, this reading error causes an error in the lattice parameter of about 3 to 5 parts in 10^5. It is possible to

reduce the effect of random errors by measuring several films and determining average values. In this way the above error can be reduced to about one third of its value. However, additional inaccuracies come from the fact that the lines may not be symmetrical (usually they are not). It seems therefore unlikely that the overall accuracy obtainable can, in any case, be better than about 3 parts in 10^5, at the present state of the technique. It should be noticed that the limits of error quoted in the literature are very often those of probable error. They are roughly one third as wide as the limits of possible error.

2.2 Electron Diffraction and the Determination of Accurate Lattice Parameters

Although X-ray diffraction is the standard technique for the determination of lattice parameters, there are some cases in which this technique is rendered of little use. One such case arises when the materials under investigation present a very high degree of subdivision. When the crystallite size of the sample under study is smaller than some 300 to 200 Å, there is a considerable broadening of the X-ray diffraction lines due to the small dimensions of the coherently scattering domains. Under these circumstances the diffraction lines (peaks) become too broad and their position can no longer

be determined with a reasonable degree of accuracy. For such highly divided crystalline materials, electron diffraction becomes a useful substitute for X-ray diffraction. This is due to the fact that the wavelength associated with a beam of electrons is, in general, far shorter than X-ray wavelengths; this shorter wavelength reduces considerably the broadening of diffraction lines due to small crystallite size.

The diffraction of electrons is possible because of their wave-mechanical behaviour and their conformity to the relationship[153-155]

$$\lambda = \frac{h}{mv} \qquad 2.4$$

where λ is the wavelength of the electrons, h Planck's constant ($h = 6.63 \cdot 10^{-34}$ J·s) and mv the momentum of the particle. Electrons accelerated by a potential difference of V volts have a kinetic energy of

$$\tfrac{1}{2} mv^2 = Ve$$

where e is the electronic charge. Eliminating v by using eq. 2.4 gives

$$\lambda = \frac{h}{(2meV)^{\frac{1}{2}}} = \frac{12.236}{V^{\frac{1}{2}}} \text{ Å} \quad (*) \qquad 2.5$$

For an accelerating potential of 100 kV, very often used in electron diffraction, the corresponding value

---

(*) When high accelerating voltages are used, a relativistic correction is needed; the wavelength is then given by

$$\lambda = \frac{12.236}{\{V(1+0.9788 \cdot 10^{-6}V)\}^{\frac{1}{2}}} \text{ Å}$$

of λ will be 0.0370 Å. It may be seen that this is a very short wavelength when compared with the value of 0.8 to 2.5 Å in which falls most X-ray radiation used in crystallographic work.

Electron diffraction is, nowadays, performed almost exclusively in an electron microscope. Generally speaking there are five diffraction modes of operation of the electron microscope; these are:

(i) selected area diffraction (SAD)
(ii) low angle diffraction
(iii) high resolution diffraction
(iv) reflection diffraction
(v) scanning electron diffraction

The particular mode of operation will be determined by the type of specimen from which diffraction information is required. As a general rule, the above techniques are used with the following materials (given in the same order):

(i) Finely divided metals, minerals, and in general materials with lattice spacing smaller than 25-40 Å.
(ii) Polymers and organic crystals with lattice spacing greater than 25-40 Å.
(iii) Materials, generally in an impure state, giving diffraction spots, or rings, so close together in the diffraction pattern that they cannot be resolved in (i).

(iv) Thick specimens, or specimens coated with a thin surface layer from which information is required.

(v) Specimens undergoing dynamic transitions, due to heating, cooling, or thin film growth; or when accurate quantitative measurements of the intensities of the diffraction spots (rings) are required.

In what follows attention will be focused on selected area diffraction.

2.2.1 Single crystal and polycrystalline diffraction patterns

The diffraction pattern from a crystalline specimen is a record of the periodic structure of that specimen. If the specimen is a single crystal, that is a single repeating array of atoms, the diffraction pattern will consist of a simple array of bright spots. This is known as the single crystal diffraction pattern. The arrangement of spots in the single crystal diffraction pattern depends on the orientation of the array of atoms in the sample with respect to the incident electron beam. Thus the diffraction pattern may be considerably altered by viewing that array at different orientations.

If the specimen consists of a large number of small discrete areas, each with exactly the same

atomic array, but at different orientations to each other, the specimen is referred to as being polycrystalline, and its diffraction pattern will then consist of a series of concentric rings. This pattern is, in principle, equivalent to a large number of single crystal diffraction patterns, each rotated by a small amount with respect to each other. Additional rings appear for all the other diffraction patterns which would occur by viewing the atomic array in different orientations.

There are also numerous intermediate diffraction patterns between these two extremes. In particular, if the specimen consists of two crystals, one being the mirror image of the other, the diffraction pattern will contain two superimposed patterns, rotated with respect to each other. This is the case of "twin crystals" which occurs quite often in metals and minerals.

2.2.2 The formation of the diffraction pattern in the electron microscope

Consider a crystalline specimen with one set of planes lying at a Bragg angle with the electron beam, as illustrated in fig. 2.3. It is an optical condition that whenever an image is formed in the image plane of the objective lens, a diffraction pattern occurs in the back focal plane. Fig. 2.3

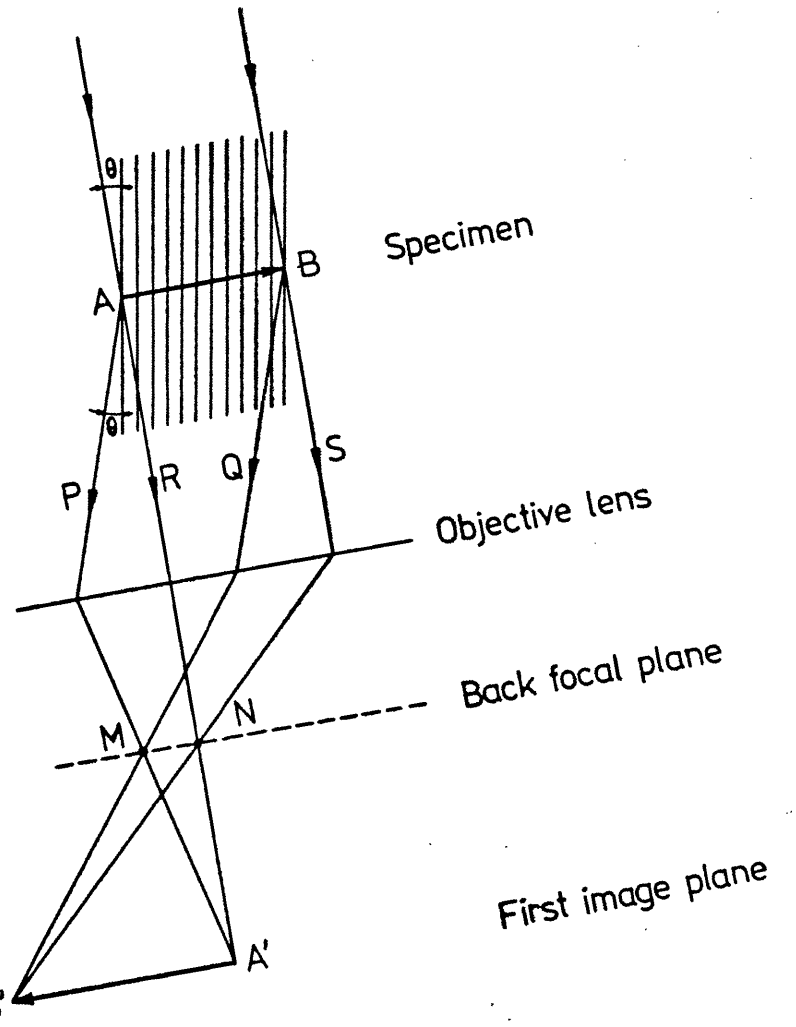

Fig. 2.3 Ray diagram showing the paths of the diffracted and transmitted beams of electrons through the objective lens to the back focal plane and the first image

shows the formation of such a diffraction pattern. Rays leaving the same point of the specimen are brought to focus in the first image plane. Thus rays leaving point A in the specimen are brought to focus at A' in the first magnified image, and rays leaving from B are focused at B'. In addition it can be seen that rays scattered in the same direction by the specimen are brought to a focus in the back focal plane of the objective lens. Thus rays P and Q are brought to focus at point M in the back focal plane, and rays R and S, which are not scattered, are brought to focus at point N. In general, rays that are scattered from the same point in the specimen are brought to a point focus in the first image plane, whereas rays that are scattered in the same direction from the specimen are brought to a point focus in the back focal plane. It is in the back focal plane of the objective lens where the diffraction pattern is formed.

In a standard electron microscope there are two (sometimes three) projector lenses following the objective lens. In the normal imaging, or magnification, mode of operation of the microscope the first projector lens (P_1 in fig. 2.4(a)) is focused on the first image and forms a second image in the object plane of the second projector lens, P_2. This lens then forms the final image on the

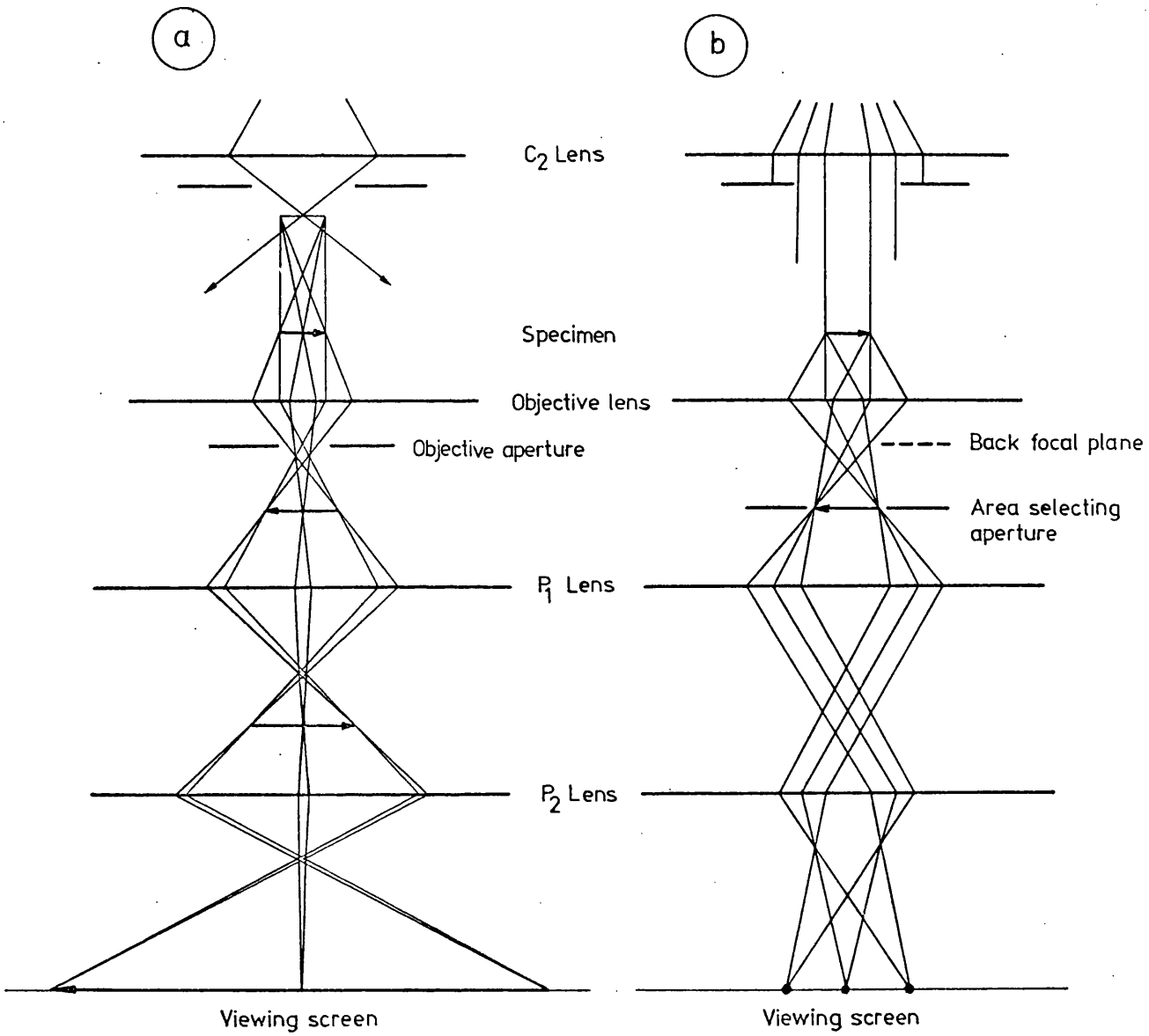

Fig. 2.4

Ray diagram showing, (a) the imaging and (b) the diffraction, mode of operation in an electron microscope

P_1, P_2: First, and second, projector lens

C_2: Second condenser lens

viewing screen. In the diffraction mode, the P_1 lens is weakened, i.e. it is operated with a lower current flowing through the lens coil. In this way the focal length is increased so that P_1 is focused on the back focal plane of the objective lens, instead of on the first image plane. The diffraction pattern is then first focused in the object plane of P_2 (second projector lens) and finally on the viewing screen. This is shown in fig. 2.4(b). The diffraction pattern can be recorded on a photographic plate, or film conveniently placed, instead of the viewing screen.

2.2.3 Operation of the electron microscope in the SAD mode

Most high resolution electron microscopes have a mechanism for inserting area selecting apertures of different sizes in the image plane (fig. 2.4(b)), and controls for centering the aperture around the area of interest while viewing the image. The correct procedure for obtaining a selected area diffraction pattern has been outlined by Agar;[156] it involves the following steps:

a) The first projector lens, P_1, (sometimes referred to as the intermediate or diffraction lens) is set to focus on the plane of the area-selecting aperture, by first inserting

the aperture and then adjusting the lens current until the image of the aperture is in focus on the viewing screen.

b) With P_1 focused on the plane of the area-selecting aperture, the objective lens is adjusted to focus the specimen image on the viewing screen. The specimen image is then co-planar with the selector aperture.

c) The microscope is now switched to the diffraction mode, either by depressing the relevant button or by reducing the strength of P_1 until the diffraction pattern comes into focus on the viewing screen. In the first case (direct switching from an imaging to a diffraction mode is available in some microscopes), a final fine adjustment of the lens is often required.

d) Adjust (defocus) the second condenser lens, C_2, to illuminate the specimen with a near-parallel beam of electrons. This sharpens the diffraction pattern.

Stages c) and d) of the procedure may be reversed.[157] The objective aperture which will normally be in place during operation in the imaging mode, surrounding the

central diffraction spot, must be removed in order to observe the full diffraction pattern.

2.2.4 Calculation of d-spacings from the diffraction pattern

Electrons are diffracted by a crystal in the same manner as X-rays. Electrons falling at a glancing angle θ to planes of atoms with interplanar spacing d are diffracted if the Bragg equation $2d \sin\theta = \lambda$ is satisfied. If a beam of electrons is incident on a polycrystalline specimen, the diffracted beams will form a cone of semi-angle 2θ, and therefore will fall on a photographic plate in a circumference of radius R, as shown in fig. 2.5. It can be seen from this figure that

$$\tan 2\theta = R/L \qquad 2.6$$

where L is the distance between the specimen and the photographic plate.

Since the angles θ, through which electrons are diffracted, are very small (usually less than 2^{o}) the approximation

$$\tan 2\theta = 2 \sin\theta$$

can be made with very little error. Then, combination of Bragg's equation and equation 2.6 gives:

$$R/L = \lambda/d$$

or

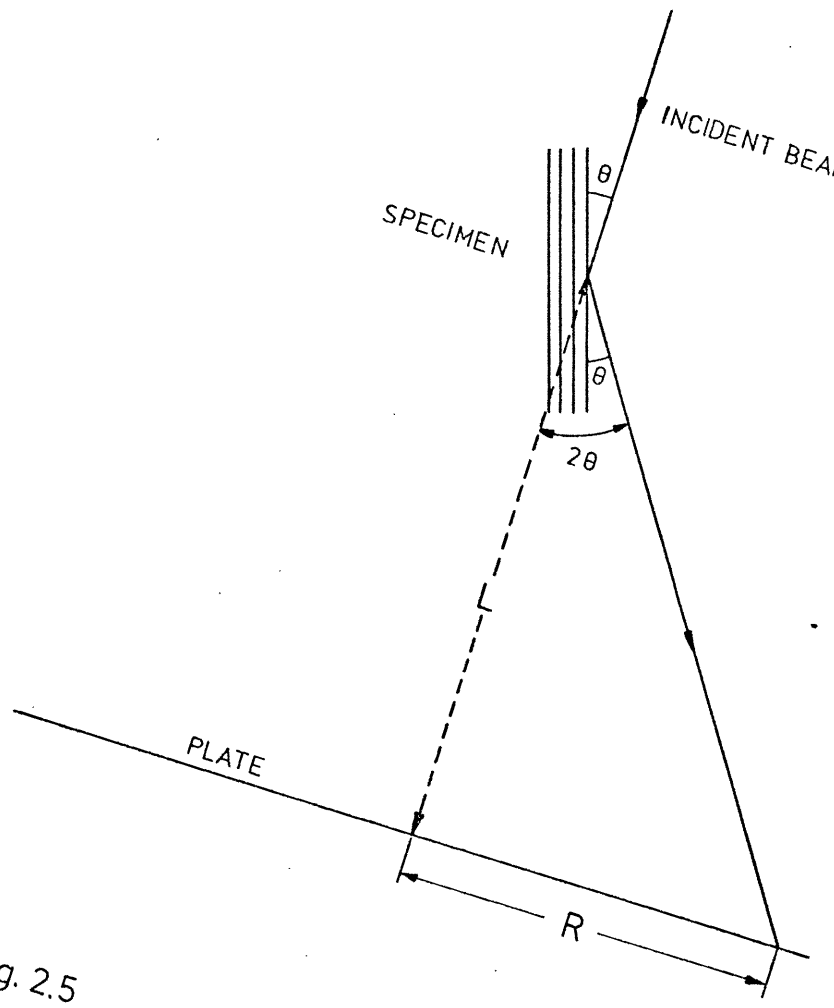

Fig. 2.5 The geometry of diffraction

$$Rd = \lambda L \qquad 2.7$$

So, if the values of R, L and λ for a particular diffraction ring (or spot) can be measured, then the d-spacing of the corresponding set of lattice planes can be determined. This procedure can be repeated for all the rings in the diffraction pattern, and a list of d-spacings can be compiled. From this list, the lattice parameters of the specimen can be computed in the usual way. In practice R (or 2R) is measured on the recorded diffraction pattern, but λ and L are not usually determined independently; most frequently only their product is evaluated. This λL product is known as the "camera constant".

2.2.5 Calibration of the camera constant

In order to analyse the diffraction pattern, as described in the preceding section, it is necessary to know the value of the camera constant, λL. When a good degree of accuracy is required, it is often insufficient to take predetermined values of λ and L, as both these values may alter. This may be due either to adjustments to the high voltage supply or the lens currents, or to instabilities in the electronic circuitry. Thus, from one experiment to another the value of λL may vary as[158]

$$\frac{\delta\lambda L}{\lambda L} = \frac{\delta\lambda}{\lambda} + \frac{\delta f_o}{f_o} + \frac{\delta M_1}{M_1} + \frac{\delta M_2}{M_2} \qquad 2.8$$

where f_o is the focal length of the objective lens and M_1 and M_2 are the magnification of P_1 and P_2 lenses respectively. The first term, $\delta\lambda/\lambda$ is usually less than 10^{-5} for a good instrument, but the other terms in eq. 2.8 may be considerably larger, depending upon hysteresis effects when the lens currents are adjusted. The variations of λL to be expected from these effects are of the order of 1%. Moreover, if the specimen height is altered λL will change, since a new value of f_o would be required to focus the image of the specimen. It follows that for accurate determination of d-spacings (and hence lattice parameters) the camera constant has to be calibrated for each diffraction pattern recorded. This is usually achieved by depositing on the specimen grid a thin layer of a material with known lattice parameters. Thallous chloride, aluminium, or gold are often chosen as materials for calibration. The recorded diffraction pattern will now show, besides the rings (spots) from the specimen, those from the calibrating material. These allow the camera constant to be computed.

2.3 X-ray Line Broadening

Under the ideal conditions of diffraction of a strictly parallel and monochromatic beam of X-rays, the Bragg equation $\lambda=2d \sin\theta$ predicts diffraction of a given wavelength λ by crystal planes of spacing d only at a discrete angle θ. However, in practice, these ideal conditions never exist. Departures from ideality cause a varying degree of diffraction to occur over a range of angles near θ, resulting in a broadening of the diffraction lines recorded on the X-ray film or diffractometer chart. Since the amount of broadening caused by a given instrumental setup remains the same, any additional broadening of the diffraction lines can be related to the degree of perfection of the crystals being analysed. Thus X-ray line broadening analysis can provide information about this degree of perfection. In particular it can be used as a very valuable method for the determination of the size of crystalline particles whose linear dimensions are less than about 2000 Å.

2.3.1 Factors causing line broadening

The main factors which can contribute to line broadening are:

a) Instrumental broadening

b) Small crystallite size

c) Strain

d) Structural faults

a) Instrumental broadening

Any X-ray diffraction line will have a minimum breadth determined mainly by the geometry of the apparatus used and the experimental conditions. In line broadening analysis the use of powder diffractometers is usually preferred, instead of the photographic methods. This is due to the fact that diffractometer traces are easier to obtain than the combination of the Debye-Scherrer (photographic) method plus microphotometry of the diffraction lines. They are also more reliable than microphotometer traces, unless special care is taken with the exposure and development of the film.

The geometry of a powder diffractometer is shown in fig. 2.6. When the apparatus is properly adjusted, the instrumental factors causing appreciable broadening of the diffraction peaks are (i) width of the X-ray source, (ii) flat rather than curved sample surface, (iii) vertical divergence, (iv) width of the receiving slit and (v) penetration of the sample by the beam. This last factor, although usually studied together with pure instrumental factors, is clearly dependent upon the nature of

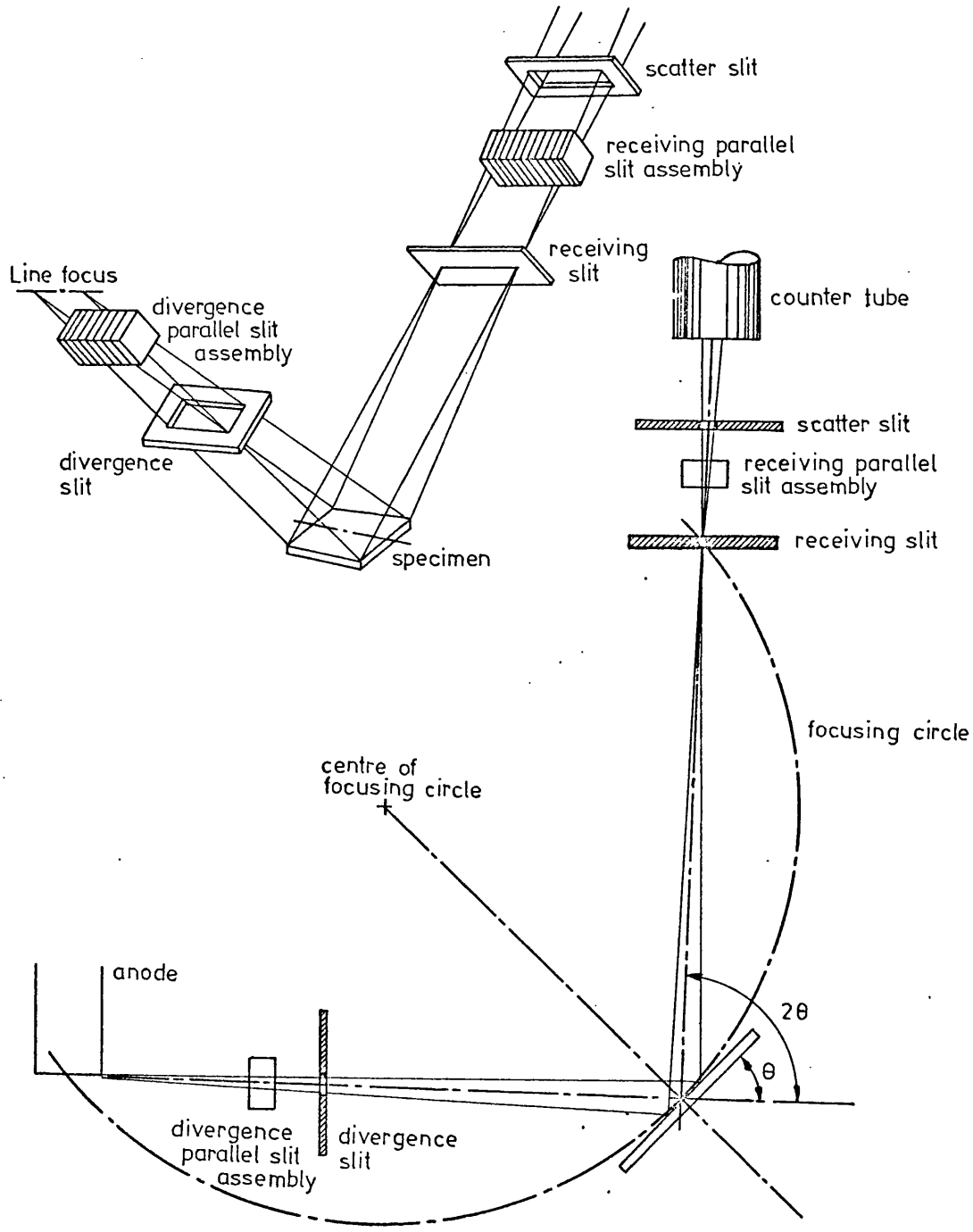

Fig 2.6

The geometry of the diffractometer

the specimen. Thus, when absorption in the sample is low, diffraction takes place not only in the surface layer, but also in the "interior" of the sample, giving rise to line broadening.[159] A detailed theoretical treatment of the above factors has been given by Alexander.[160] Since in practical work an overall correction for instrumental broadening is usually applied, no further discussion will be given here.

b) Small crystallite size

In the derivation of Bragg's law it is assumed that the diffracting crystal has an infinite dimension (compared with the X-ray wavelength), i.e that there are an infinite number of repeating structure units in the crystal. Under this condition, and for a crystal showing ideal perfection, the diffraction of a strictly monochromatic and parallel X-ray beam will only occur at discrete θ angles. However, if the linear dimensions of the crystal are finite, there will be a relaxation of Bragg's condition in the sense that diffraction will occur, although with decreasing amplitude, over an angular interval $\pm \Delta\theta$ on both sides of the Bragg angle. This will have the effect of broadening the diffraction lines. Such a broadening, which becomes very noticeable when the individual crystals are smaller than about 0.1 μm (1000 Å), can be related to the crystal

size by the Scherrer equation[161,162]

$$\beta = \frac{K\lambda}{D\cos\theta} \qquad 2.9$$

where β is the line breadth (in radians), K is a constant termed the shape factor, λ is the wavelength of the incident radiation, and D is the relevant crystallite dimension (thickness of the crystal in a direction normal to the diffracting planes).

The shape factor, or Scherrer constant, K, has a constant value 1.0747 for spherical crystallites, but for other crystal shapes K takes different values according to the index of the reflecting planes. Computation of K values has been performed by several authors.[163-166] Table 2.1 shows the results for some usual crystal shapes.

c) Strain

If the crystal is larger than 1 μm, diffraction may still take place over a considerable range if the crystal is otherwise imperfect. Thus, in a distorted crystal the interplanar spacing will not be constant throughout, and different parts of the crystal will diffract at different angles. If the maximum strain in the crystal is ε, the spacing will vary from $d(1+\varepsilon)$ to $d(1-\varepsilon)$, and θ will vary over a range equal to $2\varepsilon d(\delta\theta/\delta d)$, or $2\varepsilon \tan\theta$ (This result

Table 2.1

The ratio of the true to the apparent particle size (K factor) for various reflections from crystals having the form of a tetrahedron, a cube or an octahedron. For a sphere the ratio is constant at 1.0747.

Reflection	Tetrahedron	Cube	Octahedron
100	1.3867	1.0000	1.1006
110	0.9806	1.0607	1.0376
111	1.2009	1.1547	1.1438
200	1.3867	1.0000	1.1006
210	1.2403	1.0733	1.1075
211	1.1323	1.1527	1.1061
220	0.9806	1.0607	1.0376
221	1.1556	1.1429	1.1185
310	1.3156	1.0672	1.1138
311	1.2543	1.1359	1.1211
320	1.1538	1.0698	1.0902
321	1.1119	1.1394	1.0955
400	1.3867	1.0000	1.1006
410	1.3453	1.0583	1.1123
331	1.1135	1.1262	1.0963
420	1.2403	1.0733	1.1075
421	1.2104	1.1324	1.1133
332	1.1826	1.1513	1.1334
430	1.1094	1.0667	1.0786
431	1.0878	1.1240	1.0835
510	1.3597	1.0506	1.1101

can be attained by differentiating Bragg's equation). Since the deviation of the rays is 2θ, the angular range over which reflection is appreciable will be twice, that is

$$\beta = 4\varepsilon \cdot \tan\theta$$

In cases of broadening from this cause it is usual to define the "apparent strain", η, by[167]

$$\eta = \beta \cdot \cot\theta \qquad 2.10$$

Thus, the apparent strain is four times the maximum strain.

d) Structural faults

In certain crystals the atomic arrangement is such that the unit cells are all of the same size and shape, but differ in the disposition of atoms within them. Common cases are superlattices and stacking irregularities. If there were no relation between the different arrangements of atoms, a crystal consisting of domains in which the arrangements were different would behave simply as if each domain were a separate crystallite. Usually, however, the atomic arrangements, though different, are related, and all domains will scatter in phase for certain reflections, but out of phase or with a random phase relationship for other reflections. The crystals are thus "large" for reflections in which the domains cooperate, but "small" for reflections in which they do not. The

consequence is that whilst some diffraction lines are sharp others display considerable broadening.

2.3.2 Definitions of line breadth

Two different definitions of line breadth are in usual practice in X-ray line broadening analysis: half-peak breadth and integral breadth. The half-peak breadth is the distance between the two points on the line profile at which the intensity is half the maximum. Thus, if I_o is the maximum value of $I(\theta)$, and θ', θ'' are the values of θ for which $I(\theta) = \frac{1}{2} I_o$, the half-peak breadth, $\beta_{\frac{1}{2}}$, is defined as

$$\beta_{\frac{1}{2}} = 2(\theta''-\theta')$$

the factor 2 appearing because diffraction angles are usually measured as 2θ. The integral breadth, β, is defined as the breadth of a rectangle that has the same height, and the same area, as the diffraction peak. That is

$$\beta = \frac{\int I(\theta)\, d\theta}{I_o}$$

In practice the half-peak breadth is easier to measure, and more amenable to practical work. However, the integral breadth is a more precise parameter, and it is also easier to handle in theoretical analyses.

2.3.3 Determination of the pure diffraction broadening

As the broadening of a diffraction line will always have a contribution due to instrumental effects, it is necessary to separate instrumental broadening and broadening due to the specimen. The latter is often known as intrinsic broadening, or pure diffraction broadening. The effect of any X-ray diffraction apparatus in modifying a pure diffraction maximum can be analysed using the superposition theorem.[168] According to this theorem, the profile of the observed maximum, h(s), is the convolution of the instrumental aberration, g(s"), and the true intensity function, f(s'), that is

$$h(s) = \int_{-\infty}^{+\infty} f(s') \cdot g(s-s') \cdot ds' \qquad 2.11$$

where the function g expresses the sum total of the apparatus effects upon the pure function being measured, and the variable s measures the angular deviation of any point from the theoretical diffraction angle. In order to find the true diffraction broadening, f(s'), it is necessary to solve the convolution equation (2.11). This can be done by assuming certain approximate mathematical expressions for f(s') and g(s") or by means of either Fourier or iterative methods. The use of approximate functions is often sufficient, especially when only

relative values are sought, and will be the only method described here. Fourier methods have been firstly described by Stokes[169] and, in a computerized form, by De Angelis.[170] The application of iterative methods can be found in the work by Paterson[171] and by Ergun.[172]

The two most commonly assumed line shapes are the Gaussian

$$I(s) = I_p(s) \exp(-k^2 s^2)$$

and the Cauchy

$$I(s) = I_p(s)/(1+k^2 s^2)$$

where I_p is the intensity at maximum height and k is a numerical constant. If B, β, and b are respectively the total, intrinsic, and instrumental linebreadths, application of the convolution integral shows that for h, g and f all Gaussian

$$B^2 = b^2 + \beta^2 \qquad 2.12$$

whilst for all Cauchy profiles

$$B = b + \beta \qquad 2.13$$

Which of the two above equations will be better to use will depend, of course, on whether a Gaussian or a Cauchy function is a better approximation to the line shapes. Shoening[173] points out that broadening produced by small particle size tends to produce a Cauchy profile and that by strain broadening a Gaussian. However, very often the actual

profiles do not fit very well either of the functions and, moreover, the profile of the pure instrumental broadening may not have the same shape as that due to intrinsic broadening. These difficulties were overcome by Jones[174] who devised a method based on the direct comparison of broadened and sharp lines produced under the same experimental conditions.

For the case of broadening due to small crystallite size, Jones could determine, from his experimental work, the form of the functions h(s) and g(s) in equation (2.11). The form of h(s) was determined from lines with particle size broadening and that of g(s) from lines with only instrumental broadening, which can be obtained from a well sintered material. By numerical integration of eq. 2.11 Jones then found the most suitable function f(s) which would fit this relation when h(s) and g(s) had the forms that had been determined experimentally. He expressed his results in the form of a relation between b/B and β/B, as shown in fig. 2.7. The plot in this figure can be used to derive the pure line-breadth, β, after the total breadth, B, and that due to instrumental conditions, b, have been obtained. If possible b should be obtained from a well sintered specimen of the same material under investigation. It must be added

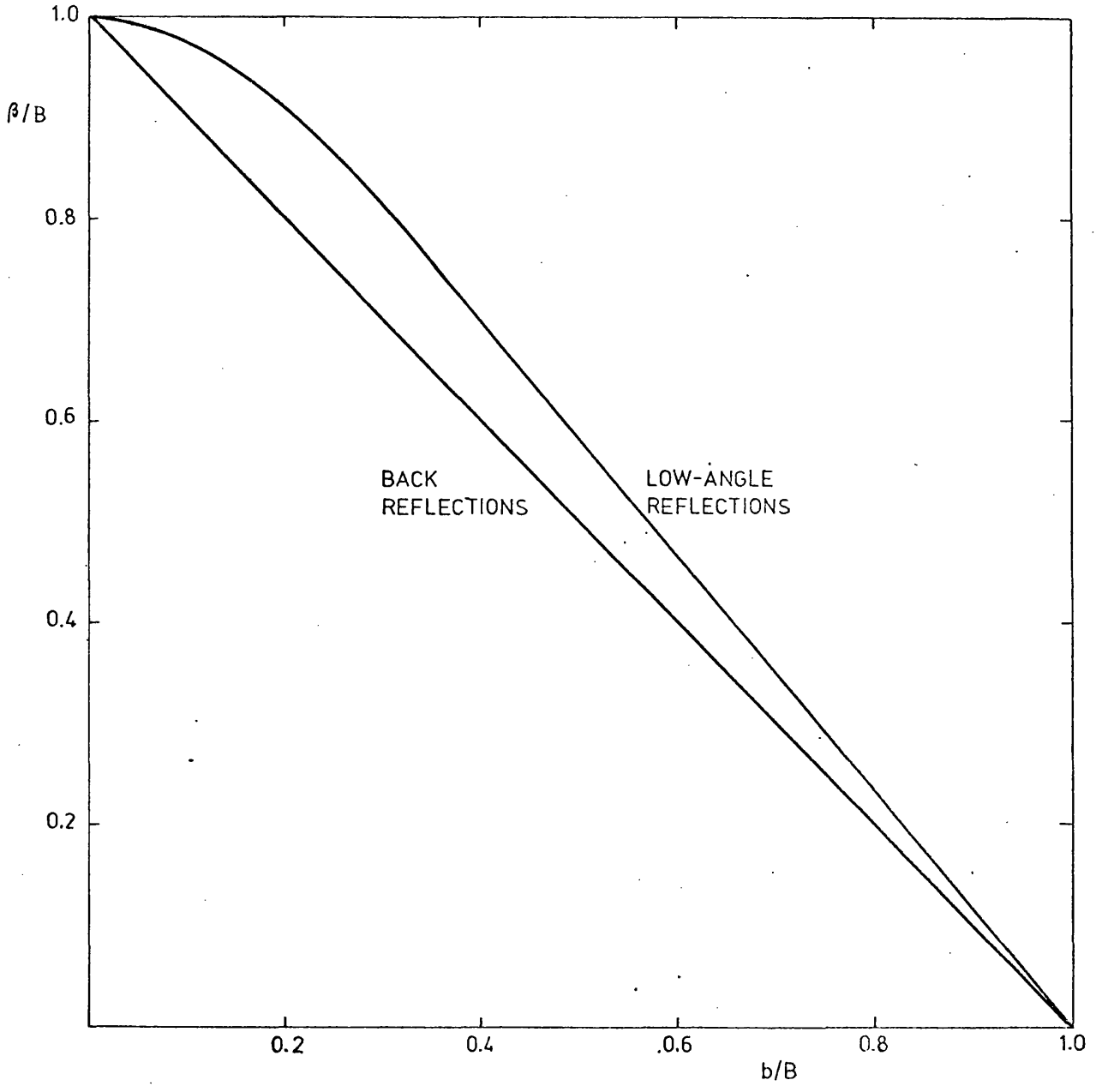

Fig. 2.7

Curves for correcting instrumental broadening

that the broadening due to the α_1 - α_2 doublet has to be allowed for before use of the plot in fig. 2.7. Simple methods for the deconvolution of the α_1 - α_2 doublet have been described by DuMond et al[175] and by Rachinger.[176-177]

2.4 Electron Spin Resonance

2.4.1 The resonance condition

The electron has a non-classical intrinsic angular momentum known as spin, and represented by the vector $\vec{s}$. The spin is characterized by the quantum number $s = \frac{1}{2}$ and the component of the spin vector along any direction specified by an experiment (usually designated as the z-axis) can only take the values $\pm\frac{1}{2}h/2\pi$, where h is Planck's constant. These values are characterized by the quantum number $m_s = \pm\frac{1}{2}$. The electron thus has two spin states differing in m_s, which are described by convention as follows:

$m_s = +\frac{1}{2}$: spin up ($\uparrow$) or α

$m_s = -\frac{1}{2}$: spin down ($\downarrow$) or β

The spin of the electron gives rise to a magnetic moment μ_e, whose z-component μ_e^z can assume only two values corresponding to the spin

quantum numbers $m_s = \pm\frac{1}{2}$. m_s and μ_e^z are related by the equation

$$\mu_e^z = - m_s g_e \beta = \begin{cases} - \frac{1}{2} g_e \beta & \text{for } m_s = +\frac{1}{2} \\ + \frac{1}{2} g_e \beta & \text{for } m_s = -\frac{1}{2} \end{cases}$$

where β is the Bohr magneton, a constant having the value of $9.2732 \cdot 10^{-28}$ J·gauss^{-1}, and g_e is a dimensionless number whose value for free electrons is 2.00232, but it may be different for electrons in atoms or molecules. Owing to the negative charge of the electron, μ_e^z and m_s differ in sign.

Since the z-axis can be chosen at will, it is convenient to identify it with some specific direction such as that of the applied magnetic field in the case of ESR. The component μ_e^z of the magnetic moment is then responsible for the behaviour of the electron in the magnetic field. In the absence of an external magnetic field, the two spin states with $m_s = +\frac{1}{2}$ and $m_s = -\frac{1}{2}$ are degenerate, i.e., they have the same energy. When a magnetic field H_o is applied along the z-axis, it interacts with the magnetic moment of the electron and lifts the degeneracy of the spin states (Zeeman effect). The energy of interaction, E, is given by the expression:

$$E = - \mu_e^z H_o = m_s g_e \beta H_o$$

The energy levels corresponding to the two spin states are then:

$$E_1 = - \tfrac{1}{2} g_e \beta H_o$$

$$E_2 = + \tfrac{1}{2} g_e \beta H_o$$

and the energy difference:

$$\Delta E = E_2 - E_1 = g_e \beta H_o$$

Transitions from one Zeeman level to the other (i.e between E_1 and E_2) can be induced by an electromagnetic radiation with a frequency, ν_o, given by the resonance condition:

$$h\nu_o = \Delta E = g_e \beta H_o \qquad (2.14)$$

The interaction which causes the transitions is between the magnetic dipole of the electron and the oscillating magnetic field accompanying the electromagnetic radiation. The resonance condition can be achieved by varying ν or H (or both). For technical reasons the frequency ν is kept constant and the field strength H is varied to bring it to the value at which the resonance condition is fulfilled. In principle it should be possible to use any combination of ν_o and H_o, satisfying the condition:

$$\nu_o/H_o = g_e\beta/h \quad (\simeq 2.8\cdot10^6 \text{ sec}^{-1} \text{ gauss}^{-1}),$$

to observe electron spin resonance absorption. In practice most ESR spectrometers work in the frequency region of 9000 to 10000 MHz, corresponding to a wavelength of about 3 cm, i.e. in the microwave region, X-band. Some work has also been carried out using wavelengths of about 1.25 cm ($\nu \simeq 2300$ MHz) and 0.8 cm ($\nu \simeq 3400$ MHz). These are known as K-band and Q-band respectively.

A schematic representation of the splitting of the spin levels of an electron under an applied magnetic field is given in Fig. 2.8. Also shown in this figure is the ESR signal, which is normally recorded as the derivative of the intensity A of the absorption with respect to the field strength H, and as a function of H, i.e. it is dA/dH vs. H. The line-width, ΔH, is generally taken as the abcissa distance between the maximum and the minimum of the dA/dH curve.

2.4.2 Multielectron systems

So far only the interaction of an isolated spin $\frac{1}{2}$ particle with an applied magnetic field has been considered. However, it is well known that, besides the spin magnetic moment, electrons in atoms or ions possess also a magnetic moment arising from the orbital motion. The orbital quantum number

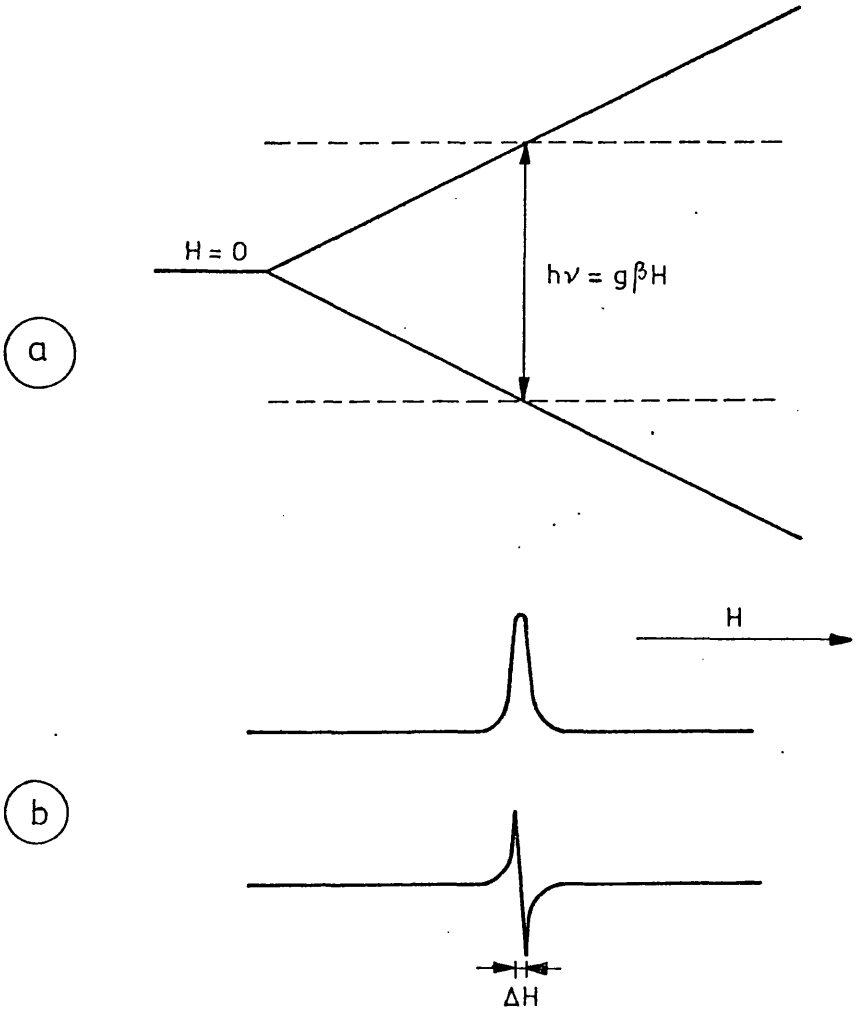

Fig. 2.8

a) Splitting of the spin levels of an electron in an applied magnetic field
b) ESR signal and its derivative

is designated by $\underline{l}$ and can take any integral value from 0 to (n-1), where n is the principal quantum number. A particular value of $\underline{l}$ is associated with an orbital angular momentum vector $\vec{\underline{l}}$, where $|\vec{\underline{l}}| = (\underline{l}(\underline{l}+1))^{\frac{1}{2}}$ in units $h/2\pi$. This vector may take up $2\underline{l}+1$ different orientations in space. If a particular direction in space is defined, by the application of an external magnetic field, the projections of $\vec{\underline{l}}$ in this direction range from $+\underline{l}$ to $-\underline{l}$ and are known as the magnetic quantum numbers $m_{\underline{l}}$.

The spin and orbital angular momentum vectors of electrons are able to couple in a variety of ways which correspond to the different possible interactions. These interactions may be exchange, electrostatic, or magnetic in origin and the effect of quantization is that in each case a number of discrete arrangements result, corresponding to different energies. For each particular energy the individual angular momentum vectors assume a particular inclination to each other and precess about the direction of their resultant.

In multielectron systems the types of coupling which can occur may be represented as:

$$\vec{s}_i\vec{s}_k,\ \vec{\underline{l}}_i\vec{\underline{l}}_k,\ \vec{s}_i\vec{\underline{l}}_i \text{ and } \vec{s}_i\vec{\underline{l}}_k$$

where $\underline{i}$ and $\underline{k}$ signify different electrons. The first three are known as spin coupling, orbital

coupling and spin-orbit coupling respectively. The fourth one, $\vec{s}_i\vec{l}_k$, is also a form of spin-orbit coupling, occurring between the spin and orbital angular momenta of different electrons. It is, however, too small to be of any real consequence.

The resultant angular momentum for the whole atom or ion will depend on the relative magnitudes of the above interactions. If any of the interactions are of comparable magnitude the situation is very complex, but two extreme cases may arise:

1. $\vec{s}_i\vec{s}_k > \vec{l}_i\vec{l}_k > \vec{s}_i\vec{l}_i$

2. $\vec{s}_i\vec{l}_i > \vec{s}_i\vec{s}_k > \vec{l}_i\vec{l}_k$

These are known as LS and JJ coupling respectively. LS coupling is the more appropriate description for transition metal ions of the first series and will now be considered in some detail.

LS or Russell-Saunders Coupling

In the first step to be considered the individual $\vec{s}$ vectors couple to give a resultant vector $\vec{S}$ of magnitude $|\vec{S}| = (S(S+1))^{\frac{1}{2}}\ h/2\pi$, where S is the resultant spin quantum number given by $S = \Sigma m_s$. The next step is the coupling of $\vec{l}$

vectors to give a resultant orbital angular momentum vector $\vec{L}$, the numerical magnitude of which is $(L(L+1))^{\frac{1}{2}}h/2\pi$, with $L = \Sigma m_l$. For each value of S there will, in general, be a number of possible values of L, each corresponding to a different energy. A particular pair of L and S values is known as a "term". Spin orbit coupling occurs, finally, between the $\vec{S}$ and $\vec{L}$ vectors for each term giving a resultant $\vec{J}$. The corresponding quantum number, J, can take the values L+S, L+S-1, ..., L-S (if L>S) or S-L (if S>L). The number of possible J values is 2S+1 and this is called the multiplicity of the term. This is only valid for L>S; whenever L<S the multiplicity is given by 2L+1. Terms are conventionally represented by the capital letters S, P, D, F, G, H, ... according to the value of L being 0, 1, 2, 3, 4, 5, ... The value of S is shown by the addition of a superscript known as the multiplicity of the term, which is 2S+1. The collection of possible values of J for a given term is known as a multiplet and each J value is a component of that multiplet. Alternatively the term is said to split into states. A particular state, or component, is represented by adding the value of J as a subscript to the symbol of the term.

2.4.3 Fine structure

Many of the ions of the transition elements have more than one unpaired electron and in their ground state have a total spin $S>\frac{1}{2}$. In such cases application of a magnetic field will split this energy level into 2S+1 magnetic levels. Transitions between adjacent levels according to the selection rule $\Delta M_s = \pm 1$ are induced by an oscillating field perpendicular to the static field. In a hypothetical simple system, as illustrated in Fig. 2.9a, all these transitions will occur at the same frequency and a single line will be observed. In general, however, paramagnetic ions are examined in crystals in which powerful electrostatic fields are present. These crystal fields may be sufficient to remove the degeneracy, i.e., to split the spin levels even in the absence of an external field. This phenomenon is referred to as zero field splitting. Such a situation is illustrated in Fig. 2.9b for an ion with total spin $S = {}^{3}/_{2}$. It is apparent that transitions for which $\Delta M_s = \pm 1$ will occur at different fields if observed at constant frequency, or vice versa. Such multiple transitions are called fine structure.

An important theorem due to Kramers[178,179] states that no electrostatic interactions can lift completely the degeneracy of a system containing

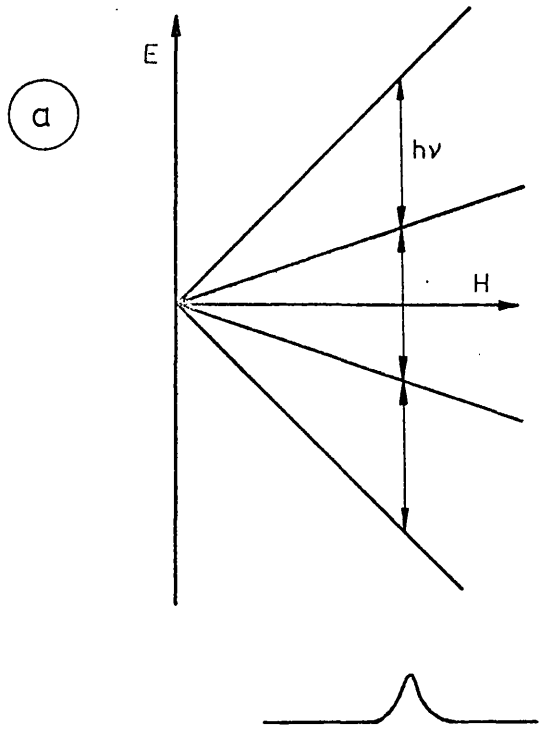

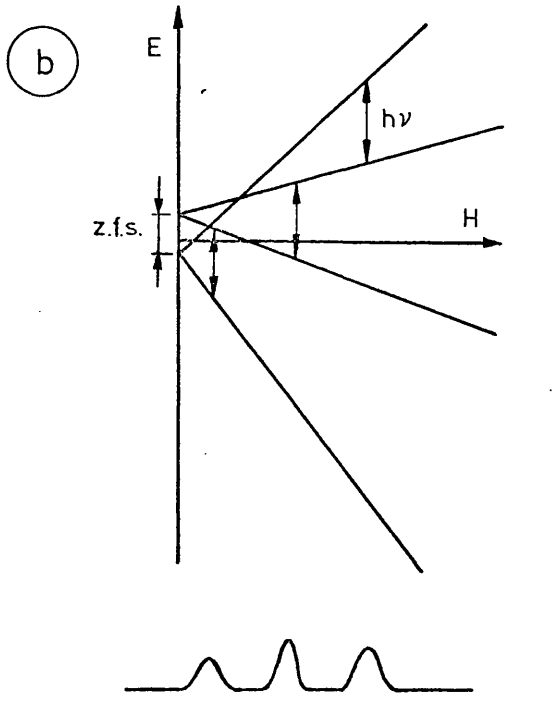

Fig. 2.9

Energy levels for a system with spin $S = 3/2$
a) With no zero-field splitting
b) With zero-field splitting $< h\nu$

an odd number of unpaired electrons. Systems with $S = \frac{1}{2}, {}^{3}/_{2}$, etc. are always at least doubly degenerate in the absence of a magnetic field. These zero field doublets are known as Kramers' doublets. It follows that in systems whose total spin is half-integral it is always possible in principle to observe at least one ESR transition. However, if the number of unpaired electrons is even ($S = 1, 2, \ldots$), the degeneracy may be completely lifted in zero magnetic field. If the ensuing separation of state energies is larger than the energy of the microwave quantum, it may be impossible to observe an ESR spectrum.

2.4.4 Nuclear hyperfine structure

If the nucleus of the paramagnetic atom or ion possesses a resultant angular momentum and thus a magnetic moment, this will interact with the electronic magnetic moment. Such interaction may be treated as arising from the interaction of the nuclear magnetic moment with the magnetic field at the nucleus set up by the electron cloud, or as arising from the interaction of the electron magnetic moment with the magnetic field set up by the nuclear magnetic moment.[180]

The spin of a nucleus is characterized by the quantum number I which can take one of the

values 0, $\frac{1}{2}$, 1, $^3/_2$, 2, ... In a magnetic field there are, for a nucleus of spin I, 2I+1 observable values of M_I, the component of $\vec{I}$ in the field direction. These have the values M_I = I, I-1, ..., -I, corresponding to the 2I+1 possible orientations of the nuclear magnetic moment with respect to the polarizing field. In a strong magnetic field the nuclear and electronic angular moments are decoupled, i.e., they are quantized separately along the direction of the applied field. The local magnetic field generated by the nuclear magnetic moment will add vectorially to the external magnetic field $\vec{H}_{ext}$ to give an effective field $\vec{H}_{eff}$; that is,

$$\vec{H}_{eff} = \vec{H}_{ext} + \vec{H}_{loc}$$

Since there are (2I+1) possible values of M_I, there will also be (2I+1) possible values of $\vec{H}_{loc}$. Thus resonance may be observed at (2I+1) values of the external magnetic field. The spectrum is thus split into a number of lines known as hyperfine splitting (usually abbreviated as hfs).

Fig. 2.10 illustrates the simplest case of hyperfine structure, an atom with S = $\frac{1}{2}$, I = $\frac{1}{2}$ and L = 0; each of the electronic levels (M_S = $\pm\frac{1}{2}$) is further split into two levels (M_I = $\pm\frac{1}{2}$). The two

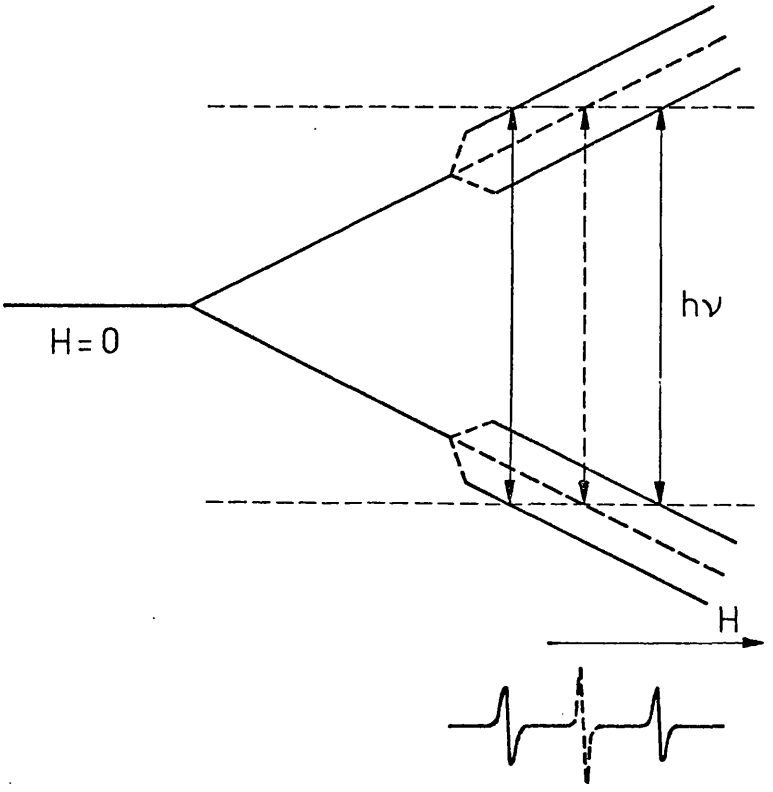

Fig. 2.10

Effect of the hyperfine splitting on the resonance absorption for a system with $S=1/2$, $I=1/2$, $L=0$. The dotted transition would be the only one observed in the absence of hyperfine interaction

values of the external magnetic field at which resonance will occur are given by

$$H_o = (H_o' \pm \frac{A}{2}) = (H_o' - AM_I)$$

where A/2 is the value of the local magnetic field, and H_o' is the resonant field when A = 0. A is measured by the splitting of the two hyperfine lines and is usually called hyperfine splitting constant.

Under the usual conditions of an ESR experiment the nuclear spin is unaffected by the oscillating field which causes the electronic transitions. Thus the selection rules for transitions are:

$$\Delta M_S = \pm 1, \ \Delta M_I = 0$$

The interaction between the unpaired electrons and the nucleus arises in two distinct ways. The first is essentially the classical interaction of two dipoles $\vec{\mu}_S$ and $\vec{\mu}_I$ separated by a distance $\vec{r}$. The only difference is that the dipole moment of the unpaired electron must be calculated quantum mechanically because an electron is, in fact, distributed over space. This interaction is directional in character and is usually referred to as the anisotropic or dipolar hyperfine interaction. The second form of interaction is non-classical and is known as the Fermi contact interaction. It arises when there is a non-zero probability of finding the unpaired electron at the position of the nucleus.

Because p-, d- and f-orbitals have nodal planes passing through the nucleus only electrons in s-orbitals need to be considered. This type of interaction is isotropic: it does not depend on the orientation of the paramagnetic species in the external magnetic field.

2.4.5 g-Factors and the g-tensor

The spectroscopic splitting factor, or g-factor, is defined by the resonance condition $h\nu_o = g\beta H_o$; therefore, in terms of the simple energy level diagram of Fig. 2.8, g expresses the proportionality between Zeeman levels. In section 2.4.1 the value of g was given as 2.00232. This is the value for a free electron. In general, however, the g-value of bound electrons is not the same as that of free electrons. The cause for the deviations of the g-values from 2.00232 is to be found in the magnetic interactions involving the orbial angular momentum of the unpaired electrons.

The value of g for an unpaired electron "gaseous atom" or ion, for which Russell-Saunders coupling is applicable, is given by the expression

$$g_J = 1 + \frac{J(J+1) + S(S+1) - L(L+1)}{2J(J+1)} \qquad (2.15)$$

where S, L and J are the same quantities defined before. For a free electron ($S = \frac{1}{2}$, $L = 0$, $J = \frac{1}{2}$), the value of $g = 2.0$ is easily calculated from eq. 2.15 (the contribution 0.00232 is due to a relativistic correction). However, when the unpaired electron is placed in a chemical environment (e.g. a crystal lattice), the orbital motion of the electron is strongly perturbed and the orbital degeneracy, if it existed before application of the chemical environment, is partly removed or "quenched". This affects the angular momentum and the spin-orbit coupling and therefore can cause g to deviate from the value given by eq. 2.15.

As a general rule, the larger the expectation value of the orbital angular momentum $\vec{L}$, the greater is the shift in the g-value away from $g_e = 2.00232$. The direction of the shift is strongly influenced by the sign of the spin-orbit coupling constant, ζ, in the Hamiltonian[181]

$$\mathcal{H}_{\text{spin-orbit}} = \zeta \hat{L}\hat{S}$$

$\hat{L}$ and $\hat{S}$ being the operators of the orbital angular momentum an electronic spin respectively. Ions which have an orbitally nondegenerate ground state such as Fe^{3+} ($^6S_{5/2}$) and Mn^{2+} ($^6S_{5/2}$) give g-values nearly equal to the free electron value, since there is practically no orbital angular momentum.

In general the magnitude of g depends upon the orientation of the crystal field with respect to the external magnetic field. This anisotropy of the g-factor is usually summarized in the form of a second-rank tensor. In a general Cartesian axis system, the g-tensor is written as

$$g = \begin{Vmatrix} g_{xx} & g_{xy} & g_{xz} \\ g_{yx} & g_{yy} & g_{yz} \\ g_{zx} & g_{zy} & g_{zz} \end{Vmatrix}$$

The g-tensor is almost always symmetric (i.e., $g_{xy} = g_{yx}$, etc.) and thus there exists a principal-axis system, X, Y, Z, in which it contains only diagonal elements; that is,

$$^{d}g = \begin{Vmatrix} g_{xx} & 0 & 0 \\ 0 & g_{yy} & 0 \\ 0 & 0 & g_{zz} \end{Vmatrix}$$

The elements of ^{d}g are called the principal values of the g-tensor. If X, Y and Z are equivalent, as in an octahedron, tetrahedron, or cube, then $g_{xx} = g_{yy} = g_{zz}$. In such a case the g-factor is isotropic and can be represented by a single value. This is also true if the paramagnetic entity is in a solution of low viscosity, such as in liquid water, where molecular tumbling causes all the g-factor anisotropy to be averaged out.

In a crystal containing a single threefold or higher axis of symmetry (Z), X and Y are equivalent. This is called axial symmetry and $g_{xx} = g_{yy} \neq g_{zz}$. It is common in such cases to designate the g-factors as $g_{\parallel}$, the g-factor parallel to the symmetry axis (i.e., $g_{\parallel} = g_{zz}$), and $g_{\perp}$ for the g-factor perpendicular to this axis (i.e., $g_{\perp} = g_{xx} = g_{yy}$).

2.4.6 The spin Hamiltonian

The spin Hamiltonian is a mathematical expression of the different interactions that exist in paramagnetic ions. It can be thought of as a shorthand way of representing these interactions. The ESR spin Hamiltonian for an ion in an axially symmetric field is:[182]

$$\mathcal{H} = D[S_z^2 - (1/3)S(S+1)] + g_{\parallel} \cdot H_z S_z + g_{\perp}(H_x S_x + H_y S_y) + A_{\parallel} \cdot S_z I_z + A_{\perp}(S_x I_x + S_y I_y) + Q'[I_z^2 - (1/3)I(I+1)] - \gamma\beta_N HI \qquad (2.16)$$

The first term describes the zero-field splitting, the next two terms describe the effect of the magnetic field on the spin multiplicity remaining after zero-field splitting, the terms in $A_{\parallel}$ and $A_{\perp}$ account for nuclear hyperfine interaction parallel and perpendicular to the main axis, and Q' measures the small

changes in the spectrum produced by quadrupole interaction. The final term takes into account the fact that the nuclear magnetic moment can interact directly with the external field; γ is the nuclear magnetogyric ratio and β_N the nuclear Bohr magneton. The effect of this term is usually negligible in comparison with the other terms.

The importance of the spin Hamiltonian is that it provides a standard phenomenological way in which the ESR spectrum can be described in terms of a small number of constants. Once values for the constants have been determined from experiment, calculations relating these parameters back to the electronic configurations and the energy states of the ion are possible. It must be pointed out that in eq. 2.16 S represents the effective spin.

2.4.7 Relaxation phenomena and linewidth

The excess of population of the ground state ($M_S = -\frac{1}{2}$) over that in the upper state ($M_S = +\frac{1}{2}$), for a single spin system, is very small. At a temperature of 300K, for a species for which g = 2, the ratio $n_{+\frac{1}{2}}/n_{-\frac{1}{2}}$ is 0.9986 with a magnetic field of 3000 gauss.[183] Thus the excess population in the ground state is only about 0.07%, yet the whole

phenomenon of ESR absorption depends on this difference. The a priori probability of transitions upwards equals that for transitions downwards, therefore if the unpaired spins were isolated from their surroundings, the two levels would rapidly become equally populated and absorption cease. There must therefore be other mechanisms by which energy absorbed and stored in the upper state can be dissipated to permit return to the ground state. Such mechanisms, which involve interactions between the spin system and its environment, are called relaxation processes. They involve spin-lattice relaxation and spin-spin relaxation.

a) Spin-lattice relaxation

This implies interaction between the spin-system, i.e. the species with the unpaired electrons, and the surroundings, known as "lattice" regardless of whether the material is crystalline, amorphous or fluid. The two commonly discussed mechanisms for transferring energy from the spin system to the lattice are described as direct and Raman processes. In the direct process relaxation occurs through transfer of energy from a single spin to a single vibrational mode of the crystal lattice which has essentially the same frequency.(184)

In the indirect or Raman process a phonon is inelastically scattered in the process of reversing a spin. The difference in energy between the incident and the scattered phonon corresponds to that between the two spin states $M_S = +\frac{1}{2}$ and $M_S = -\frac{1}{2}$.[181] Spin-lattice relaxation is characterized by a relaxation time T_1 which is the time for the spin system to lose a fraction 1/e of its excess energy. This relaxation time is strongly dependent on the temperature. When relaxation occurs via the direct process $T_1 \propto 1/H^2T$, where H is the magnetic field and T the absolute temperature.[181] In the indirect process the dependence of the relaxation time on temperature is given by $T_1 \propto 1/T^7$ for $T < \theta$, and $T_1 \propto 1/T^2$ for $T > \theta$, where θ is the Debye temperature.[185] Actually, the direct process is only important at low temperatures, e.g., below 4K.

b) Spin-spin relaxation

Unpaired electrons can interact with other magnetic dipoles in the vicinity, thereby spreading local disturbances over the entire spin system. Such interactions are not energy dissipating and thus do not contribute directly in returning the spin system to equilibrium; however, the spin-lattice transitions may be enhanced if the spin-spin

process brings the excess energy to a position for a propitious transition to the lattice. Spin-spin interactions depend obviously on the dipole concentration as well as their homogeneity. Since the dipole field decreases with the cube of the separation, many of the spin-spin interactions can be eliminated by diluting the environment with diamagnetic atoms, e.g. MnO-CaO, instead of MnO. This is a way to lengthen the spin-spin relaxation time, usually designated as T_2. Dipole-dipole interactions are also characterized by a dependence on orientation with respect to the external magnetic field.

The ultimate minimum line width is set by the Heisenberg uncertainty principle. By virtue of a finite lifetime (Δt) of a spin state, the energy of that state will have a finite width (ΔE) given by

$$\Delta E \cdot \Delta t \geq h/2\pi$$

Substituting $h\Delta\nu$ for ΔE, the uncertainty in the resonance frequency corresponds to a half band width of

$$\Delta\nu \geq \tfrac{1}{2}\pi \cdot (\Delta t)^{-1}$$

or, in terms of magnetic field,

$$\Delta H \geq \frac{h}{2\pi g\beta} \frac{1}{\Delta t}$$

where $\frac{1}{\Delta t} \propto \frac{1}{T_1} + \frac{1}{T_2}$, T_1 and T_2 being the relaxation time discussed above.

Small coupling forces lead to long relaxation times and narrow lines; conversely, short relaxation times and wide lines result from strong interactions. Either T_1 or T_2 can be the controlling relaxation time, but usually the temperature can be lowered to lengthen T_1 until the linewidth is set by T_2. Very broad lines are sometimes the cause of failure to observe ESR absorption.

CHAPTER III

METHODS AND RESULTS

3.1 The System CoO-MgO

Solid solutions in this system were prepared by the method of impregnation, followed by thermal treatment. In this method magnesium hydroxide is impregnated with the appropriate amount of a solution of cobalt nitrate; the mixture is then dried and the solid solution is formed by solid state diffusion at high temperatures. Two different temperatures were used for the firing of the samples: 1273 and 1673K. In this way, and by firing the samples either in air or under vacuum, three different ranges of subdivision could be obtained. These were characterized in the first instance by ranges of specific surface area, namely 1-10, 15-45 and 100-300 $m^2 g^{-1}$.

3.1.1 Nomenclature

Samples are designated MCoX, where X is the nominal content in cobalt expressed as mol % Co. Specimens fired at 1673K in air are designated MCoX LSA (LSA = low surface area). Specimens fired at 1273K in air are termed MCoX MSA (MSA = medium

surface area). Specimens fired at 1273K in vacuum are designated MCoX HSA (HSA = high surface area).

3.1.2 Preparation of solid solution mixtures

Magnesium hydroxide was prepared by dissolving about 50g of 'specpure' magnesium crystals in 2 litres of very dilute 'Aristar' nitric acid. The resulting solution was filtered, an equivalent volume of distilled water added, and excess dilute 'Aristar' ammonia solution added 100 ml at a time with vigorous stirring until precipitation was complete. The hydroxide was filtered off and washed until all traces of nitrate ion and ammonia were removed. After drying at 393K overnight, the hydroxide was sieved to 60-mesh.

The solid solution mixtures were prepared by impregnating the hydroxide with an approximately equal volume of 'specpure' cobalt nitrate solution of suitable concentration. The impregnation was performed in a round-bottomed flask which could be attached to a rotary evaporator. After swirling the mixture for 3 hours, it was transferred into a large evaporating dish, covered with a watchglass, and dried at 323K overnight. The low drying temperature was necessary to avoide decomposition of the cobalt nitrate to the oxide, which occurs at 328K.

The mixture was then ground, reslurried and the above procedure repeated twice more. This gave complete mixing throughout the hydroxide bed. Table 3.1 lists the source and nominal purity of the starting materials used.

3.1.3 Preparation of solid solutions

The LSA materials were prepared by firing the corresponding mixtures, contained in a platinum boat, at 673K overnight in a Griffin electric furnace. Samples were then transferred to a PCA 10 furnace (Metals Research Ltd.) and fired at 1673K for 3 hours. These thermal treatments were carried out in air. MSA samples were prepared in the same way, with a final ignition temperature of 1273K which was maintained for 12 hours. In this case the final thermal treatment was given in the Griffin furnace. The resulting solid solutions were pale-pink in the case of LSA materials and sand-brown in the case of MSA samples.

For the preparation of HSA samples each solid solution mixture was placed in a platinum boat and loaded into a specially designed furnace assembly (Fig. 3.1). The furnace tube was made of impervious mullite and was capable of holding a dynamic vacuum of 10^{-6} torr whilst at 1273K. The furnace had four high

TABLE 3.1

Material	Source	Stated impurities (ppm)	
Magnesium crystals	Johnson & Matthey	Silicon	3
		Iron	2
		Copper	1
		Manganese	1
Cobalt nitrate	Johnson & Matthey	Iron	3
		Silicon	2
		Silver	2
Nitric acid	BDH Chemicals	Calcium	0.5
		Mangesium	0.5
		Strontium	0.5
		Sodium	0.5
		Iron	0.2
Ammonia	BDH Chemicals	Calcium	0.5
		Magnesium	0.5
		Strontium	0.5
		Sodium	0.5
		Iron	0.01
		Cobalt	0.005
		Nickey	0.001
Acetone	BDH Chemicals	Iron	0.1

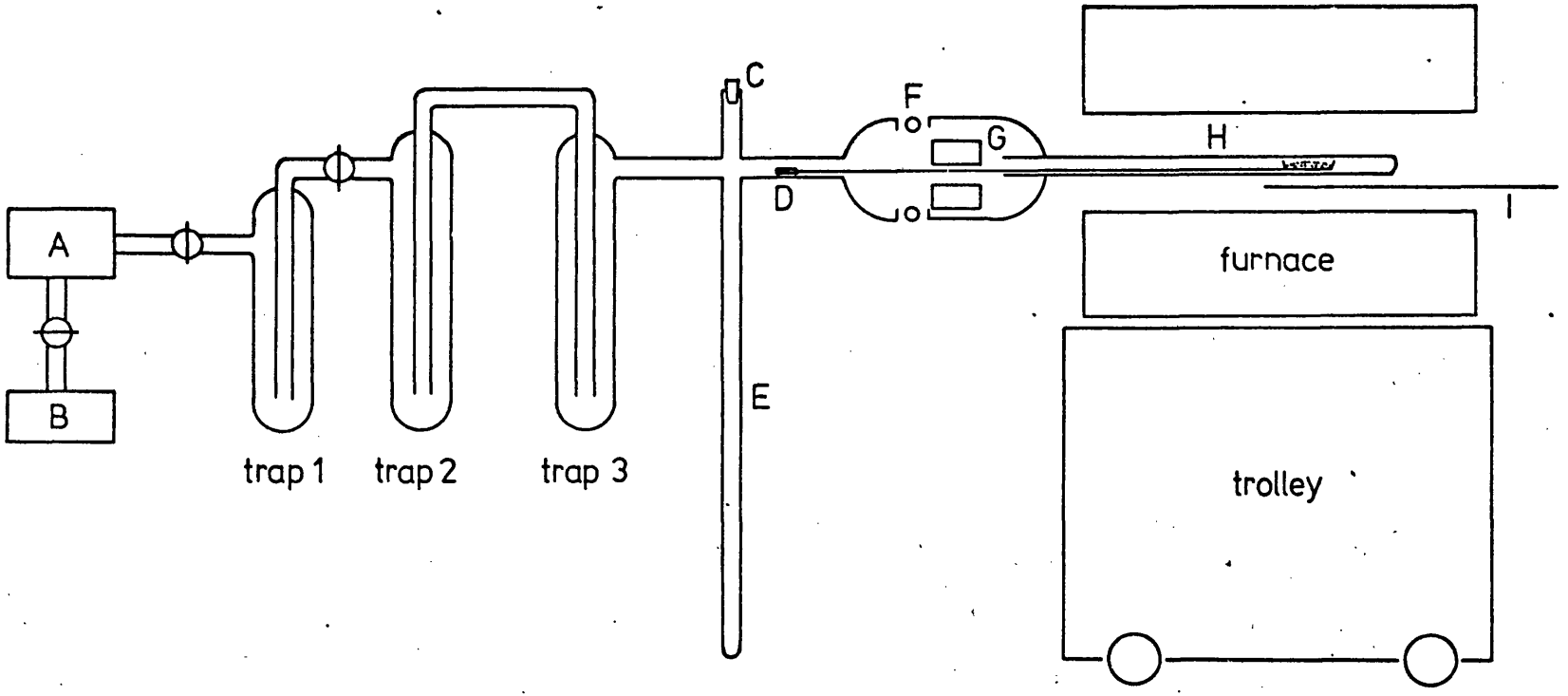

Fig. 3.1

High temperature-high vacuum system

A) diffusion pump, B) high speed rotary pump, C) ion gauge, D) iron bar, E) withdrawal tube, F) 'O' ring, G) copper cooling block, H) mullite tube, I) thermocouple

temperature elements made of crusilite and was capable of reaching 1473K. Power was supplied from a variable transformer. The furnace was mounted on a trolley which ran on a pair of rails, thus enabling it to be rolled away for easy access to the high temperature attachment. A small bar of iron, tied to the platinum boat by a thin platinum chain, allowed the sample to be magnetically withdrawn from the furnace and placed on a copper block for cooling whilst under vacuum.

The procedure for the heat treatment of the mixture was as follows:

1. With the boat in position, the sample was evacuated carefully using the rotary pump only.
2. The diffusion pump was switched on and liquid nitrogen put around trap 1. The temperature was raised slowly to 623K and kept overnight.
3. The furnace was switched off and the sample isolated from the pumping unit. Trap 1 (see fig. 3.1) was then allowed to warm up and the water vapour produced during the decomposition of the sample removed.

4. The system was brought back to high vacuum and, with liquid nitrogen round trap 1, the sample tube was again opened to the vacuum line and the temperature raised to 773K and maintained for a few minutes.
5. The temperature was then raised to 973K and liquid nitrogen was placed around trap 2.
6. The temperature was finally raised to 1273K and with liquid nitrogen around all three traps left overnight (12 hours).
7. With the temperature still at 1273K the sample was magnetically withdrawn into the copper block and left under high vacuum to cool.
8. The furnace assembly was then vented and the resulting oxide stored in sample bottles.

Throughout 2 - 8 the pressure was carefully monitored with an ion gauge to avoid the possibility of fluffing.

Approximately 1 - 2 g of solid solution could be prepared at a time. The resulting specimens were initially slate-blue, but exposure to air

immediately resulted in a coloration similar to that of MSA samples. HSA magnesium oxide was prepared from magnesium hydroxide using the same heat treatment.

3.1.4 Chemical analysis

LSA, MSA and HSA samples were prepared from the same starting mixtures. Chemical analysis was carried out on the HSA solid solutions obtained after the thermal treatment described above. To remove any traces of adsorbed water (and possibly carbon dioxide) suitable amounts of samples were dehydrated at 1073K on a stanton thermobalance. The dehydrated samples were dissolved in a minimum volume of 50:50 conc. nitric acid: distilled water and the resulting solution diluted to 100 ml. The cobalt content was determined from these solutions by two different methods, (i) measurement of the optical absorbance of the cobalt-nitroso R complex, and (ii) EDTA titration.

Optical absorbance of the cobalt-nitroso R complex was measured on a spectrometer at 412 nm against suitable standards of the complex.[186] The average of three measurements was taken, using fresh test and standard solutions each time. EDTA titration was carried out according to the method

described by West.[187] The cobalt content was determined from the average of three titrations, using a standardized 0.01M solution of EDTA. Blank titrations revealed that the magnesium ions of the MgO matrix did not interfere.

Results of the chemical analysis are shown in Table 3.2. The two techniques give results in satisfactory agreement, though correlation with the corresponding theoretical amount of cobalt initially impregnated into the magnesium hydroxide is not very good. The discrepancy is presumably due to unequal losses of cobalt and magnesium during the impregnation procedure.

TABLE 3.2

Sample	Weight % of cobalt (nitroso R method)	Weight % of cobalt (EDTA method)	Average weight % of cobalt	Average atomic % of cobalt
MCo 1	1.37	1.38	1.38	0.94
MCo 3	4.42	4.50	4.46	3.14
MCo 5	6.61	6.27	6.34	4.50
MCo 7.5	10.44	10.45	10.45	7.63
MCo 10	12.71	13.04	12.88	9.54

3.1.5 Surface areas(*)

Specific surface areas of MSA and HSA samples were measured by nitrogen adsorption at 77 K, using the BET method.[188-190] Each sample was first carefully outgassed at room temperature, then the temperature was raised to 773K over a period of several hours and this temperature maintained overnight before the adsorption isotherm was recorded. Results are shown in Table 3.3.

Table 3.3

Sample	BET surface area (m^2 g^{-1})	
	MSA samples	HSA samples
MgO	43	285
MCo 1	39	-
MCo 3	-	230
MCo 5	29	160
MCo 7.5	14	122
MCo 10	16	98

(*) Surface areas (sections 3.1.5 and 3.1.6) were measured by Dr. A.P. Hagan of Bath University, to whom the author is indebted.

3.1.6 Development of surface area on thermal treatment of the solid solution mixtures

The development of the surface area of MCo 3 solid solution mixture was followed from room temperature to 1273K in situ. After outgassing in vacuo overnight at the desired temperature, an adsorption isotherm was recorded; two further isotherms were recorded after outgassing the sample at the same temperature for 2 hours and an average surface area computed. The development of surface area with outgassing temperature is shown in fig. 3.2. The initial low surface area obtained after outgassing at room temperature and 473K is characteristic of the value obtained for magnesium hydroxide (38 $m^2\ g^{-1}$). Upon decomposition of the hydroxide at 473 to 573K, the surface area rises to a maximum value. As the outgassing temperature is increased, the material starts to sinter slowly until, after the final outgassing at 1273K, the value of the surface area is similar to that obtained for a HSA material prepared on the apparatus described in section 3.1.3.

3.1.7 Crystallite size

a) MSA samples

The crystallite size of MSA CoO - MgO solid solutions was measured using the X-ray line

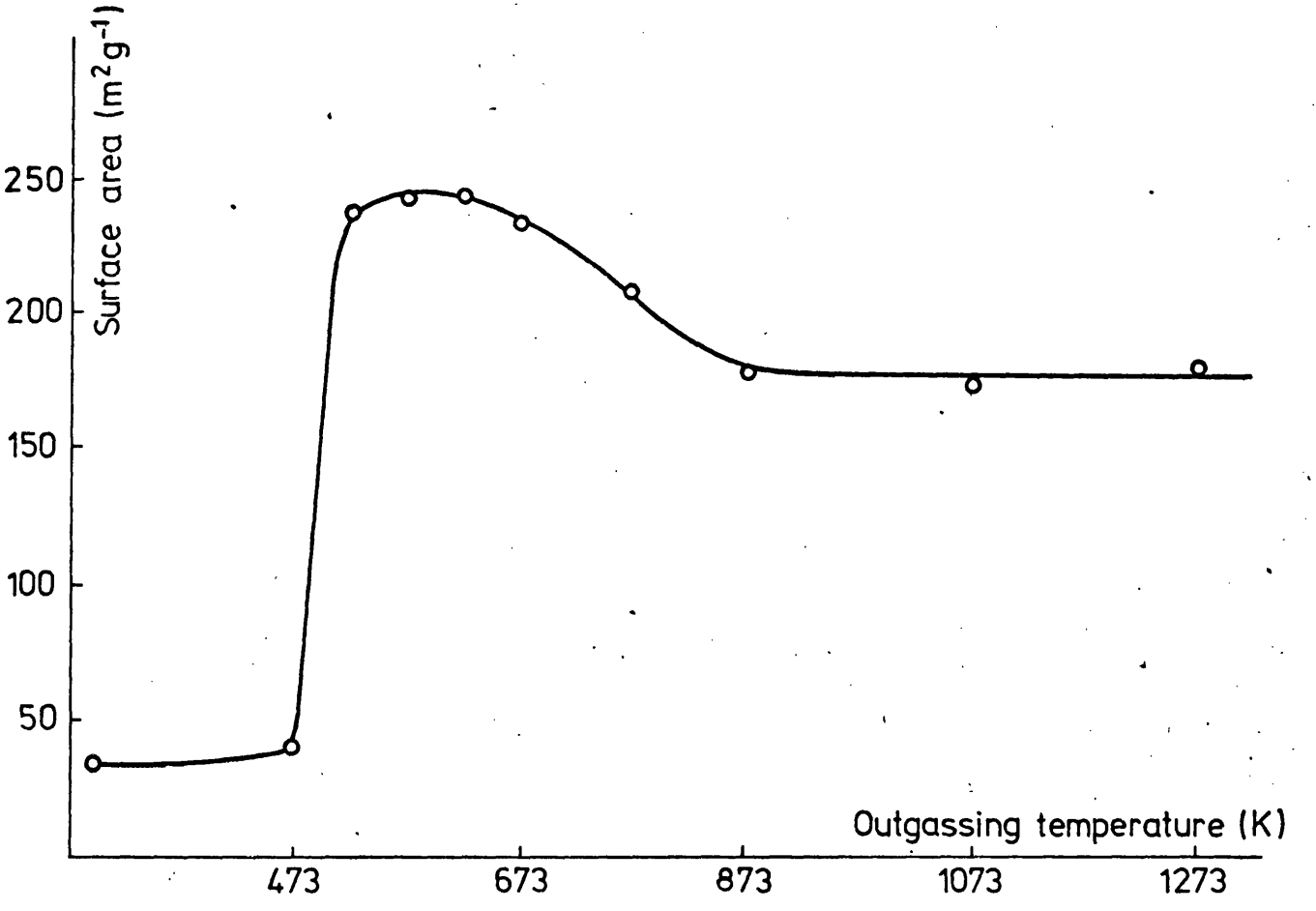

Fig. 3.2
Development of surface area with outgassing temperature for MCo 3 HSA

broadening technique described in section 2.3. The (200) and (422) reflections from each sample were slowly scanned in a Philips PW 1050/25 diffractometer under the following experimental conditions:

Radiation:	Nickel filtered CuKα
Divergent slit:	1^{o}
Receiving slit:	0.2 mm
Diffraction slit:	1^{o}
Scanning speed:	0.25^{o} min^{-1} (2θ)
Chart speed:	25 mm min^{-1}
Time constant:	10 sec.

For each diffraction peak the α_1-α_2 doublet was resolved using the method proposed by DuMond and Kirkpatrick.[175] This method, which was found to give better results than the method of Rachinger,[176] can be understood by referring to fig. 3.3. Let F(x) be the function representing the observed line profile. Let f(x) be the function representing the contribution to F(x) made by the α_1 line. If the relative maximum intensities of the α_1 and α_2 lines are assumed to be in the ratio 2:1,[176] then the contribution to F(x) made by the α_2 line will be $(\frac{1}{2})f(x-\delta)$, where δ is the angular separation between the α_1 and α_2 maxima. It follows that, for any value of x,

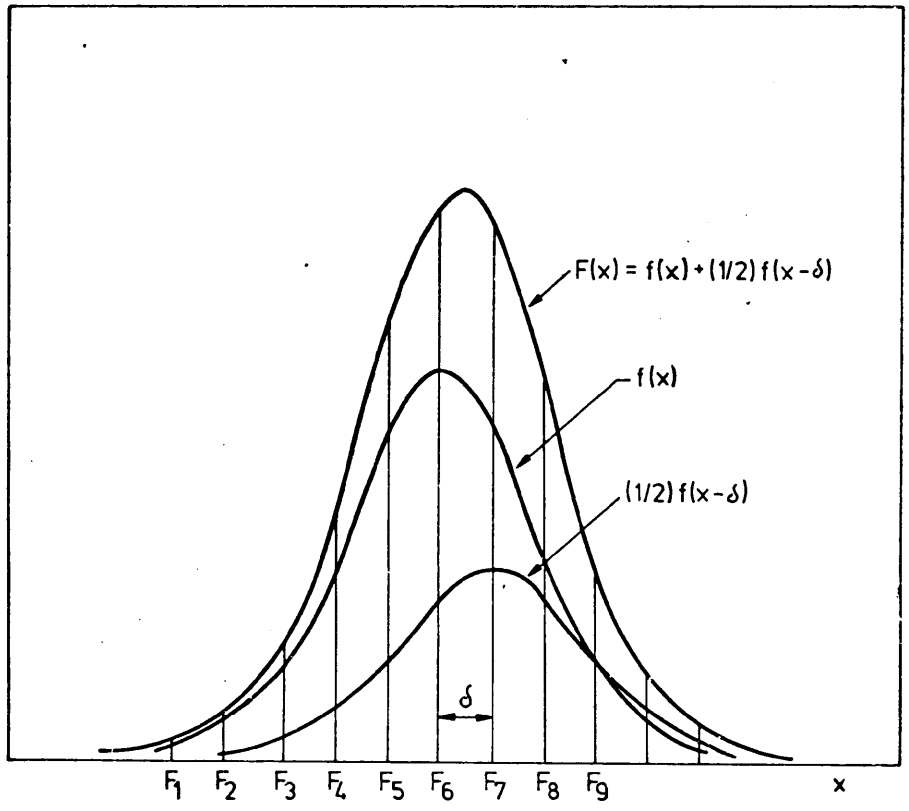

Fig. 3.3

Illustrating the method of resolution of the $\alpha_1 - \alpha_2$ doublet

$$F(x) = f(x) + (\tfrac{1}{2})f(x-\delta)$$

where F(x) is experimentally given and f(x) is to be found. To compute f(x) DuMond and Kirkpatrick proceed as follows: From the experimentally known function F(x) subtract the known function $(\frac{1}{2})F(x-\delta)$

$$F(x) - (\tfrac{1}{2})F(x-\delta) = f(x) + (\tfrac{1}{2})f(x-\delta) - (\tfrac{1}{2})f(x-\delta) - (\tfrac{1}{4})f(x-2\delta)$$

To this in turn add the known function $(\frac{1}{4})F(x-2\delta)$

$$F(x) - (\tfrac{1}{2})F(x-\delta) + (\tfrac{1}{4})F(x-2\delta) = f(x) - (\tfrac{1}{4})f(x-2\delta) + (\tfrac{1}{4})f(x-2\delta) + (\tfrac{1}{8})f(x-3\delta)$$

If this process is continued indefinitely the result will be

$$F(x) - (\tfrac{1}{2})F(x-\delta) + (\tfrac{1}{4})F(x-2\delta) - (\tfrac{1}{8})F(x-3\delta) + \ldots = f(x)$$

The error due to neglecting last terms will soon vanish due to the rapidly decreasing coefficients and to the diminution in $f(x-n\delta)$ as n becomes large. In practice the decomposition can be very rapidly effected graphically by the following procedure. Construct the curve F(x) representing the observed line profile and erect equally spaced vertical ordinates with the spacing δ (Fig. 3.3). The value of the ordinate F_4 (say) is corrected by subtracting from it half the value of F_3, then adding a quarter

of F_2, subtracting an eighth of F_1, etc., until the amounts to be added or subtracted from F_4 become negligible. All the ordinates are treated in the same way. Typical results of α_1-α_2 separation using this method are shown in figs. 3.4 and 3.5.

After resolution of the α_1-α_2 doublet the half-height widths of the α_1 peaks were measured and the true line broadening obtained after correction for instrumental broadening using Jones' plot as indicated in section 2.3.3. The instrumental broadening was obtained from the corresponding diffraction peaks of a magnesium oxide sample which had been sintered at 1673K during 4 hours under a flow of oxygen saturated with water vapour at 373K. The same instrumental broadening was obtained from a ground piece of a magnesium oxide single crystal supplied by W & C Spicer Ltd. The intrinsic broadening (i.e. the broadening corrected for instrumental effects) was assumed to be due only to small crystallite size. This assumption was substantiated by an analysis of the line profiles which showed them to depart markedly from a Gaussian shape.[173,191] An example of this analysis, for the (200) reflection of MCo 5 MSA is given in fig. 3.6.

From the line broadening the average crystallite size was computed using the Scherrer equation

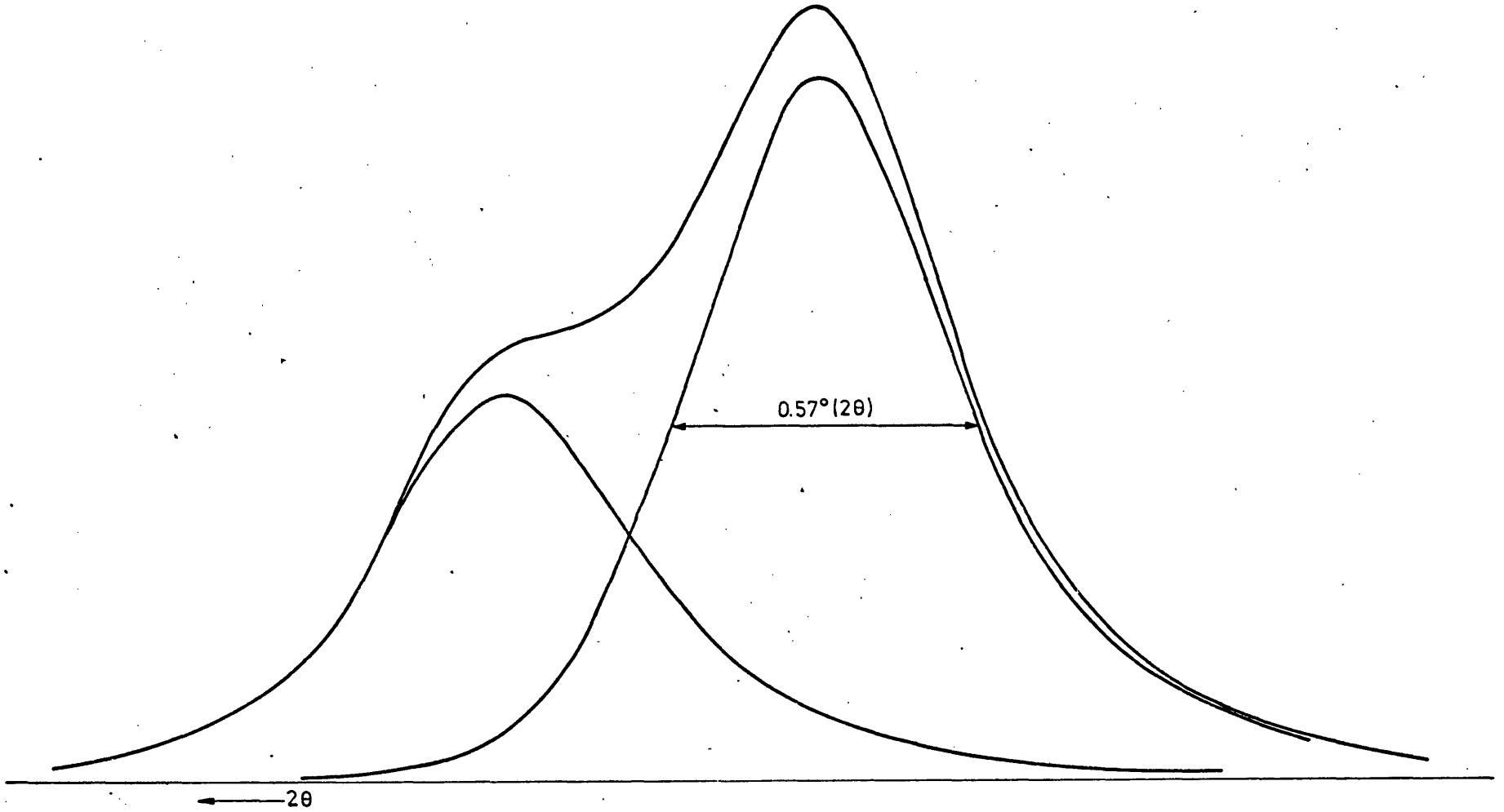

Fig 3.4

Resolution of the $\alpha_1 - \alpha_2$ doublet for the (422) reflection of MCo1 MSA

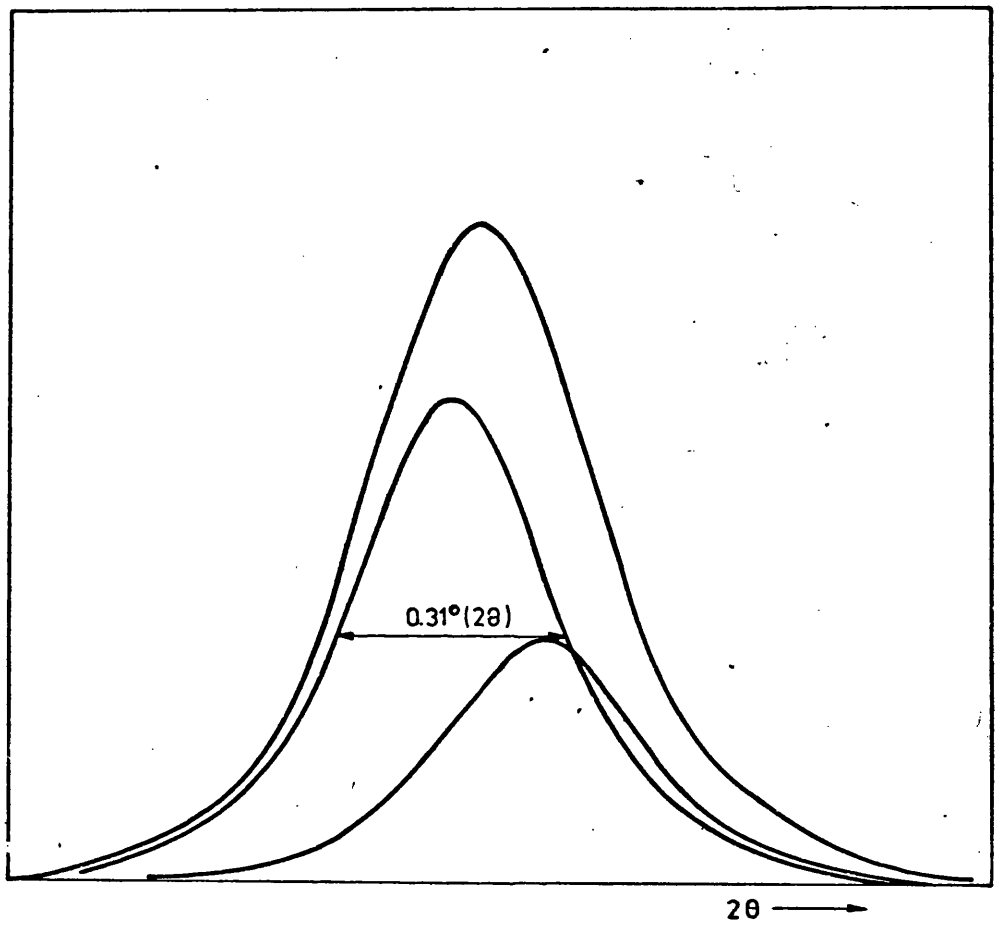

Fig. 3.5

Resolution of the $\alpha_1 - \alpha_2$ doublet for the (200) reflection of MCo 10 HSA

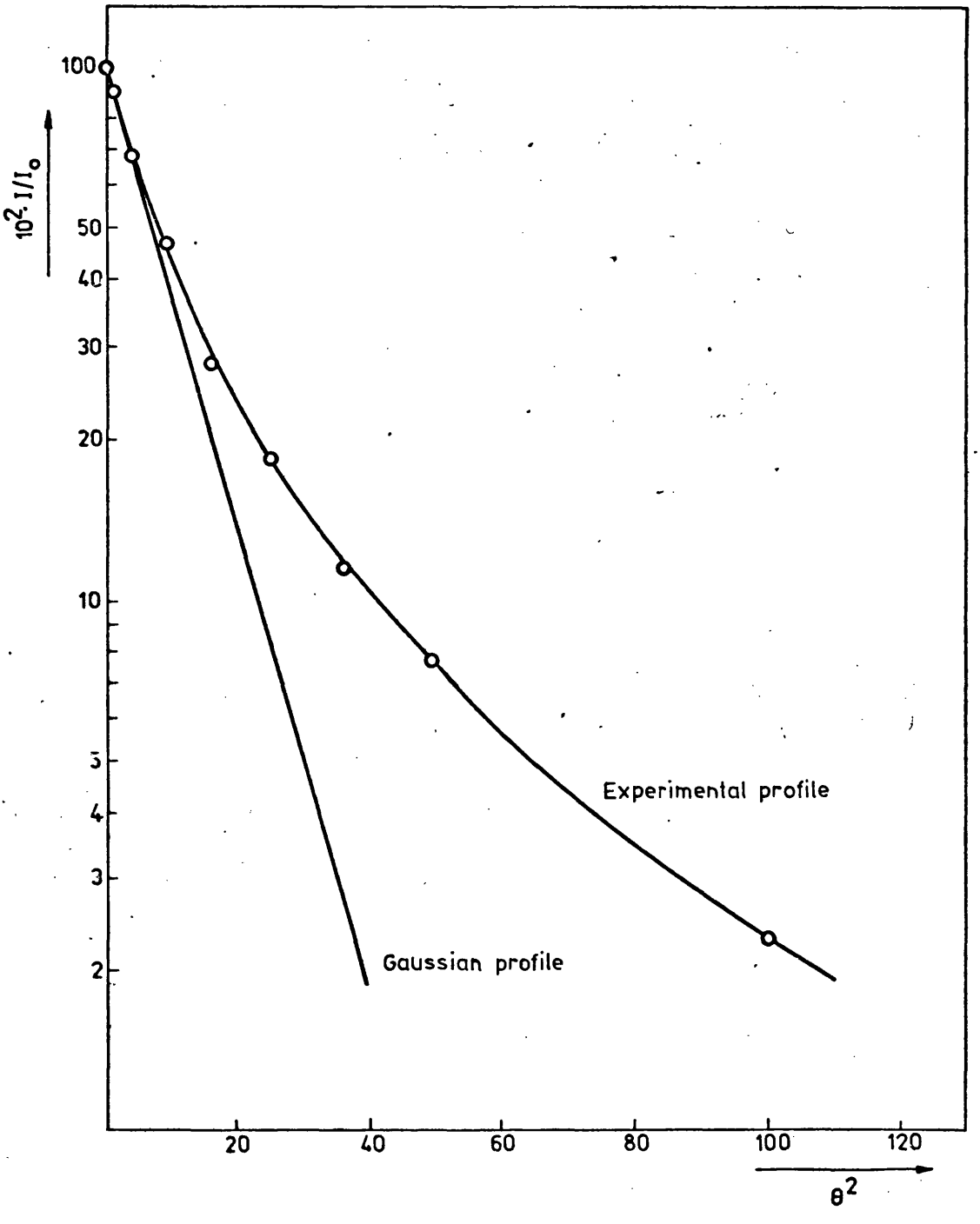

Fig 3.6

Departure of line profiles from a Gaussian shape [MCo 5 MSA, reflection (200)]

$$D = \frac{K\lambda}{\beta\cos\theta}$$

(Section 2.3.1). The appopriate values of the constant K were taken from Table. 2.1. The results are shown in Table 3.4, which also gives the values of the surface area, Σ_{XRD}, determined from the relation

$$\Sigma_{XRD} = \frac{6}{\rho\bar{D}}$$

where $\bar{D}$ is the average crystallite size and ρ is the density of the sample. This relationship is based on the assumption that the sample is composed of uniform cubic crystallites of side $\bar{D}$.

Table 3.4

Crystallite size and surface area of MSA CoO-MgO solid solutions

Sample	$D_{(200)}$ (Å)	$D_{(422)}$ (Å)	$\bar{D}$ (Å)	Σ_{XRD} (m^2g^{-1})
MgO	439	458	448	38
MCo 1	564	559	561	30
MCo 3	708	675	691	24
MCo 5	958	829	893	19
MCo 7.5	1078	980	1029	16
MCo 10	2112	2020	2066	-

b) HSA samples

Due to the possibility of strong contamination of the samples by water vapour adsorption during exposure to air in the diffractomter, X-ray line broadening measurements were made on Debye-Scherrer films. The samples were outgassed and sealed off under vacuum in X-ray capillary tubes using a cell which will be described in section 3.2.3. Debye-Scherrer diffraction films were then taken using nickel filtered CuKα radiation, with particular care to avoid overexposure, and the profile of the (200) reflection was recorded with a Joyce-Loebl MK III C microdensitometer. This is a double-beam microdensitometer in which two beams from a single light source are switched alternately to a single photomultiplier. If the two beams are of a different intensity, a signal is produced by the photomultiplier, which, after amplification, causes a servo motor to move an optical attenuator so as to reduce the intensity difference to zero. In this way a continuously null balancing system is obtained, in which the position of an optical attenuator is made to record the optical density at any part of a specimen. The optics of the microphotometer are illustrated in fig. 3.7. The experimental conditions at which it was operated were:

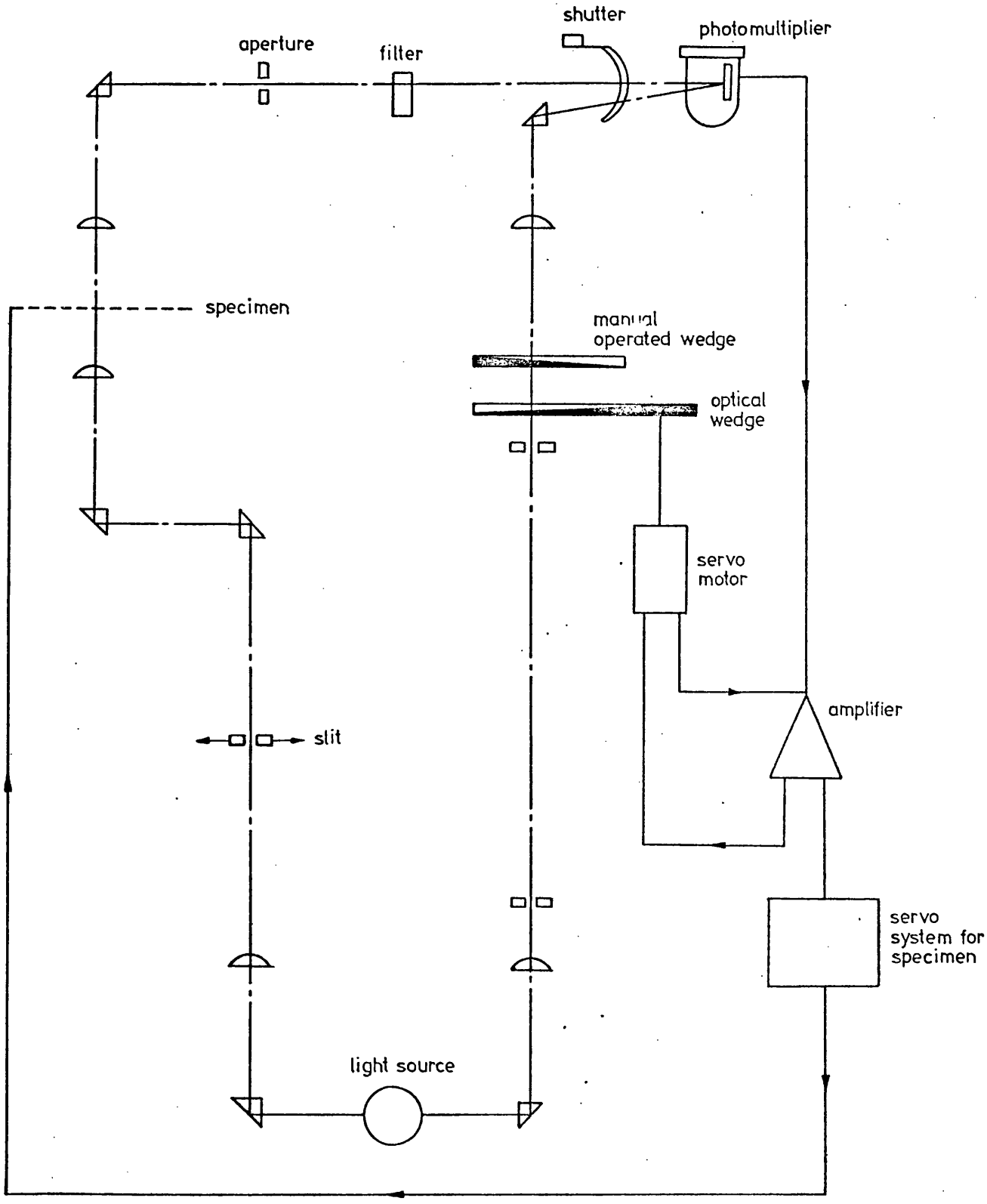

Fig. 3.7

Schematic diagram of the microphotometer

Slit width:	0.3 mm
Aperture:	15 mm
Ratio of record: sample travel:	50:1

The profile of the (200) line for each sample was recorded four times and an average line breadth computed following the same procedure as described for MSA samples. The results obtained for the crystallite size and X-ray surface area are shown in Table 3.5.

Table 3.5

Crystallite size and surface area of HSA CoO-MgO solid solutions

Sample	$D_{(200)}$ (Å)	Σ_{XRD} (m^2g^{-1})
MgO	137	122
MCo 3	208	78
MCo 5	262	61
MCo 7.5	355	44
MCo 10	482	32

3.1.8 Lattice parameters

a) LSA and MSA samples

Lattice parameters of LSA and MSA samples were obtained by X-ray diffraction using the Debye-Scherrer method. The specimens were placed into 0.3 mm diameter capillary tubes, made of Lindemann glass, and carefully centred in a 114.6 mm diameter camera. The film was mounted in the asymmetric (Straumanis and Ievins) position[136] and nickel filtered CuKα radiation was used in all cases. Variations in temperature during the exposures were measured by means of a maximum and minimum thermometer and they were never found to be larger than ±1 K. Care was taken to avoid non-uniform shrinkage during the development of the films. Typical films are shown in plate I.

In order to minimize reading errors all films were measured several times and the results averaged. Lattice parameters were computed from the α_1 component of the reflections (311), (420), (422) and (333) which occur at θ angles in the range of 50° to 75°. In order to attain best accuracy the values of the lattice parameters corresponding to a theoretical reflection at $\theta = 90^{\circ}$ were obtained using the Nelson-Riley extrapolation.[139] This extrapolation is made by plotting lattice parameter against a function of the diffraction angle,

PLATE I

1. MgO HSA
2. MgO LSA
3. MCo 3 HSA
4. MCo 3 MSA
5. MCo 1 LSA
6. MCo 5 LSA
7. MCo 10 LSA

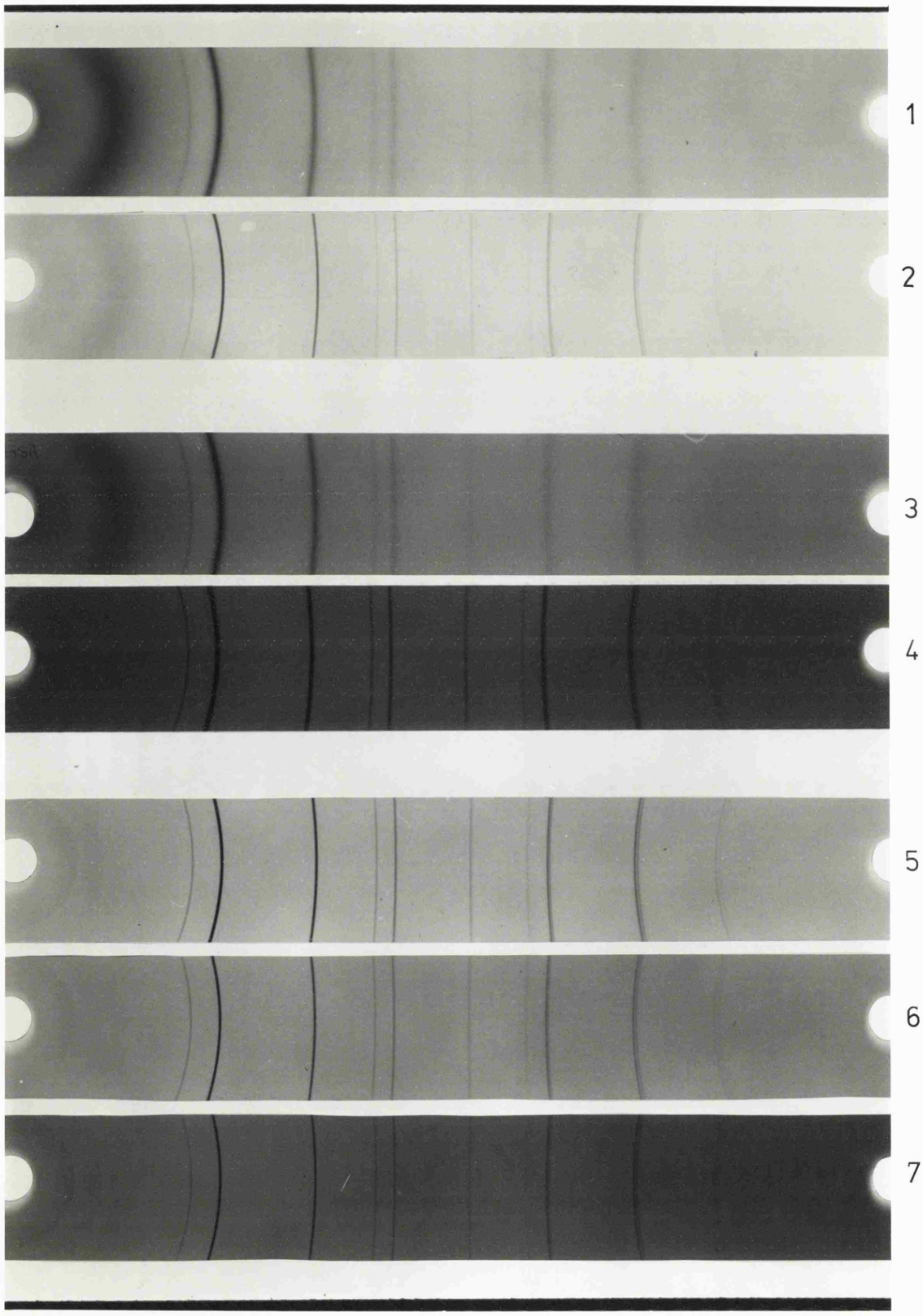
1
2
3
4
5
6
7

θ, given by

$$f(\theta) = \cos^2\theta(\csc\theta + \theta^{-1})$$

Typical Nelson-Riley plots are shown in fig. 3.8.

Finally, all experimentally determined lattice parameters were normalized to 294 K using the value of 1.3×10^{-5} Å per degree for the thermal expansion coefficient.[192] No correction was made for refraction. The overall accuracy is estimated to be about $\pm 1.5 \times 10^{-4}$ Å. The results are shown in tables 3.6 and 3.7. Plots of the lattice parameter, a_o, versus cobalt content are shown in fig. 3.9a and 3.9b. The expected increase of a_o with cobalt content can be observed.

Table 3.6
Lattice parameters of LSA CoO-MgO solid solutions

Sample	At. % Co	a_o (Å)
MgO	0.00	4.2112
MCo 1	0.94	4.2118
MCo 5	4.50	4.2140
MCo 10	9.54	4.2165

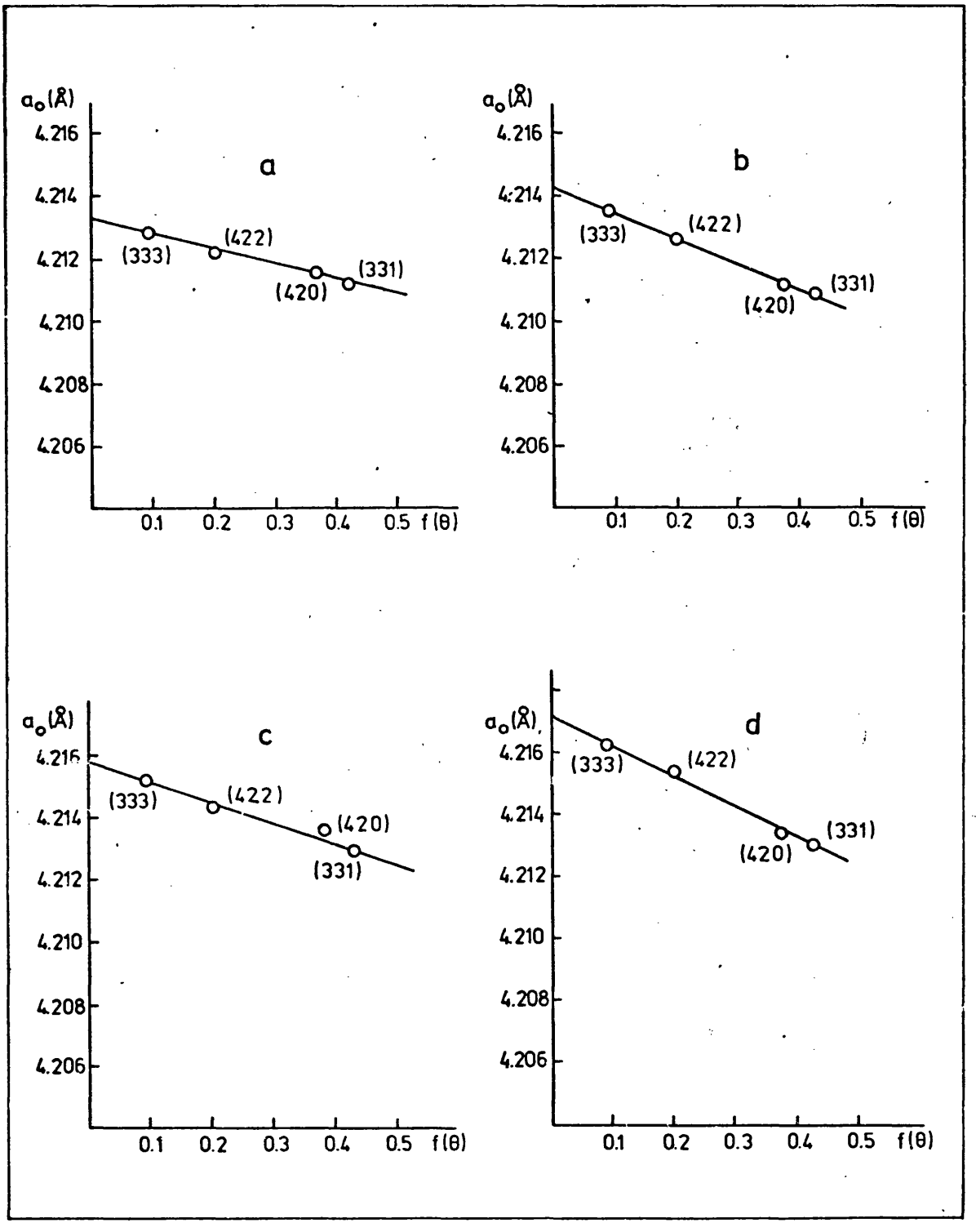

Fig. 3.8

Typical Nelson-Riley plots for MSA CoO-MgO specimens
a) MCo 3, b) MCo 5, c) MCo 7.5, d) MCo 10

Table 3.7

Lattice parameters of MSA CoO-MgO solid solutions

Sample	At. % Co	a_o (Å)
MCo 1	0.94	4.2121
MCo 3	3.14	4.2133
MCo 5	4.50	4.2142
MCo 7.5	7.63	4.2157
MCo 10	9.54	4.2170

b) HSA samples

Accurate lattice parameters could not be determined from X-ray diffraction films of HSA samples due to the severe broadening of the diffraction lines. This broadening, which can be appreciated in Plate I, makes the location of the centre of the reflections very imprecise, if not impossible. Line broadening due to small crystallite size diminishes with decreasing wavelength of the incident radiation; it was therefore considered that the use of high energy electron diffraction should be investigated as an alternative technique for the determination of lattice parameters.

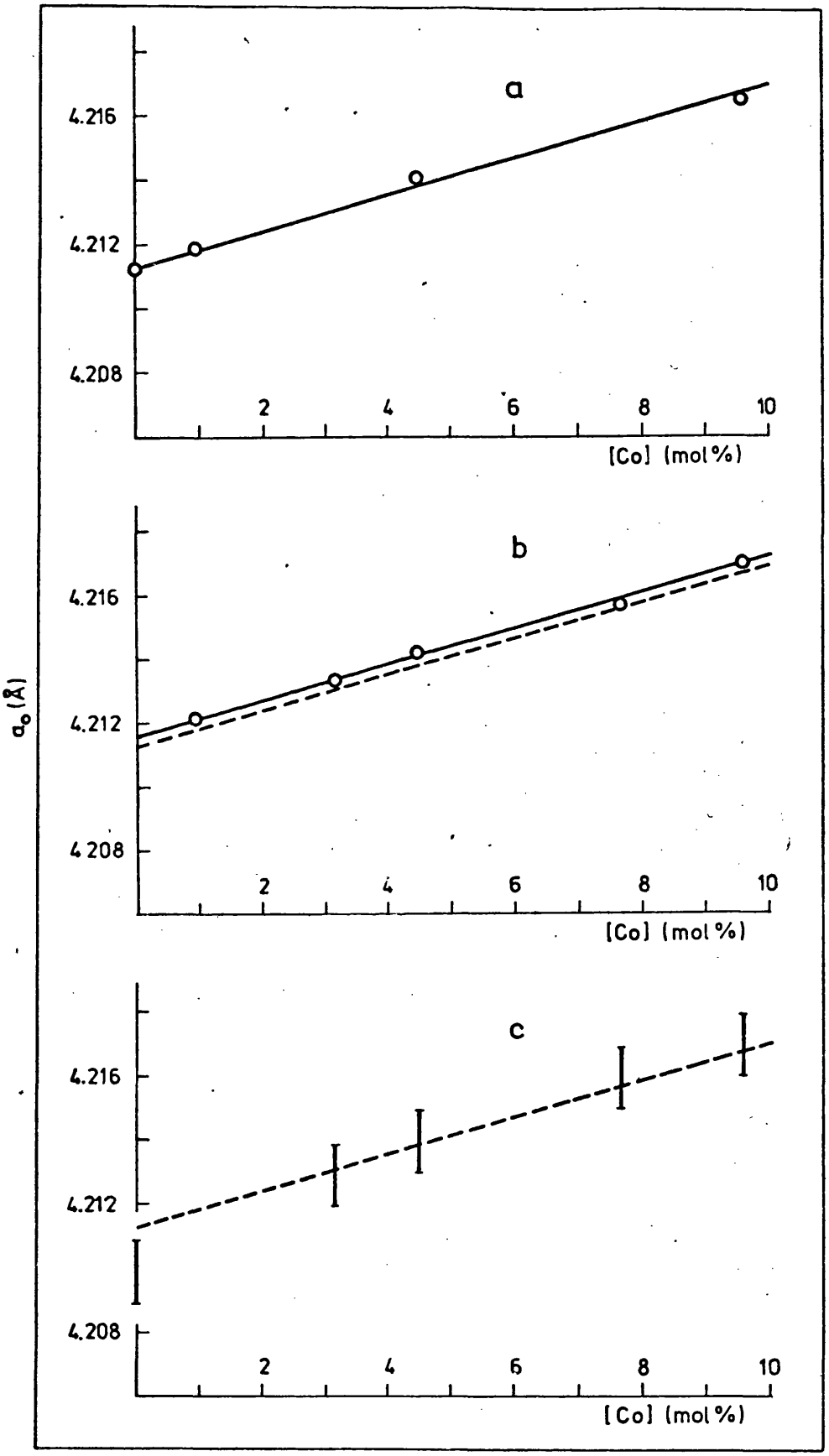

Fig 3.9

Lattice parameter versus cobalt content. a) LSA, b) MSA, and c) HSA MgO-CoO oxides
The dashed line in b and c shows the position of the corresponding line for LSA oxides

Procedures for accurate determination of lattice parameters by electron diffraction have been described by Andrews et al[193] and by Lodder and Berg,[194] among others. However, the application of the technique to the present problem is not straightforward. On the one hand there is the need for accurate calibration of the camera constant, and on the other hand, there is the additional difficulty posed by the high reactivity of finely-divided magnesium oxide, which is likely to adsorb water vapour and carbon dioxide from the atmosphere during the process of the preparation of the samples for examination. Severe adsorption of water vapour would cause dilation of the crystal lattice[192] and would therefore be an important source of error in the determination of lattice parameters. For reasons to be discussed below, gold was chosen as internal standard for the calibration of the camera constant. Inaccuracy due to surface contamination of the samples by water vapour and carbon dioxide was avoided by heating the specimens in situ under the operational vacuum of the electron microscope.

Electron diffraction was carried out in a high resolution AEI EM802 electron microscope operated at an accelerating potential of 100 KV (λ =

0.0370 Å) in the SAD mode (Section 2.2). As discussed in section 2.2.5, the camera constant is likely to change from exposure to exposure by an amount of a few parts in a hundred, and therefore no permanent calibration was attempted; instead, the internal standard method was used. The choice of standard was made by considering the following requirements: (i) it must be a polycrystalline material, of known lattice parameter, capable of giving sharp diffraction rings (broad rings or spot patterns cannot be measured with the same accuracy as sharp rings). (ii) The diffraction rings from the standard and the unknown must not coincide, but it is desirable that they appear fairly close together in the diffraction pattern. In this way no correction will be needed for the change in camera constant with diffraction angle.[193] (iii) The standard should be chemically inert towards the unknown, even at temperatures above 873 K (see later). The substance which best met these requirements without adding many technical difficulties to the preparation of the samples was found to be a thin film of gold.

Samples were prepared by first dispersing a small amount of specimen in n-hexane, using an ultrasonic bath. A drop of the dispersion was then deposited on a thin film of carbon covering

the specimen grid and the hexane was allowed to vaporize. After this operation was carried out for all the samples they were taken together to the vacuum evaporating unit where a thin film of gold (50 - 80 Å) was deposited on them. This ensured that the conditions for deposition of the standard were the same for all the samples. The specimen grids were then mounted on a heating stage (AEI EM802) which allowed the samples to be heated in situ at 973 K in order to remove the surface contamination. This temperature was maintained for 10 - 15 seconds under the operational vacuum of the microscope and the samples were then allowed to cool before the diffraction pattern was recorded. Several diffraction plates were taken from each sample.

For the calculation of lattice parameters all the diffraction patterns were measured several times in two mutually perpendicular directions and the results averaged. Finally the values of the camera constant and lattice parameter were computed from the (220) and (422) reflections of the standard and the unknown using the expression

$$Dd = C$$

where D is the diameter of the diffraction ring, d the corresponding interplanar spacing and C the

camera constant.(*) The value of a_o for gold was taken as 4.0784 Å.(195) The results are presented in Table 3.8, and a plot of lattice parameter versus cobalt content is shown in fig. 3.9c. Typical electron diffraction patterns are shown in Plate II.

Table 3.8

Lattice parameters of HSA CoO-MgO solid solutions

Sample	At. % Co	a_o(Å)
MgO	0.	4.210
MCo 3	3.14	4.213
MCo 5	4.50	4.214
MCo 7.5	7.63	4.216
MCo 10	9.54	4.217

3.1.9 Reflectance spectroscopy

Experiments described in this section have been carried out by Dr. A.P. Hagan(196) (University of Bath) to whom the author is indebted. They are described here because the results will be used in the discussion of surface coordination in HSA

(*) For convenience of calculation the camera constant is defined here as $C = 2\lambda L$ instead of $C = \lambda L$ (Section 2.2.4)

PLATE II

1 Au
2 MgO-Au
3 MCo 3-Au
4 MCo 5-Au

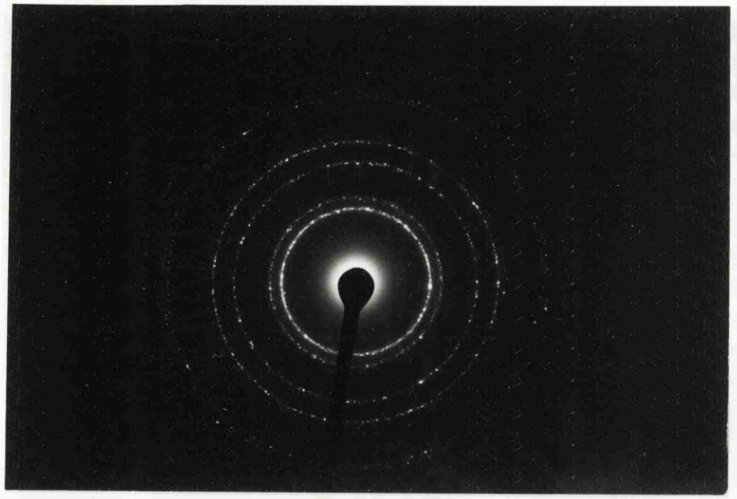

1

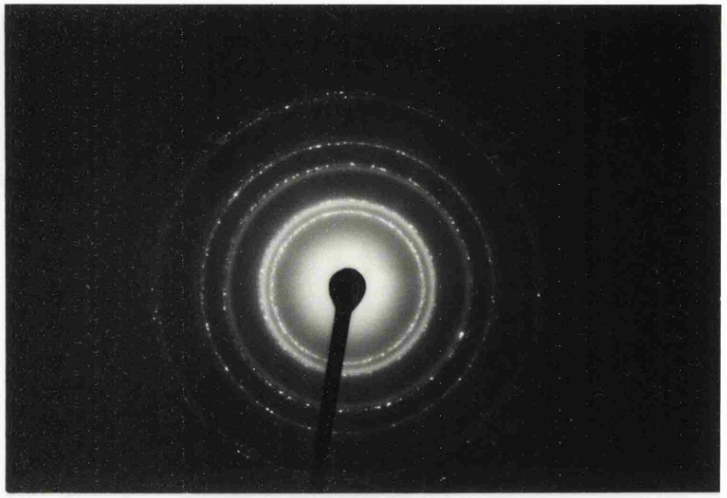

2

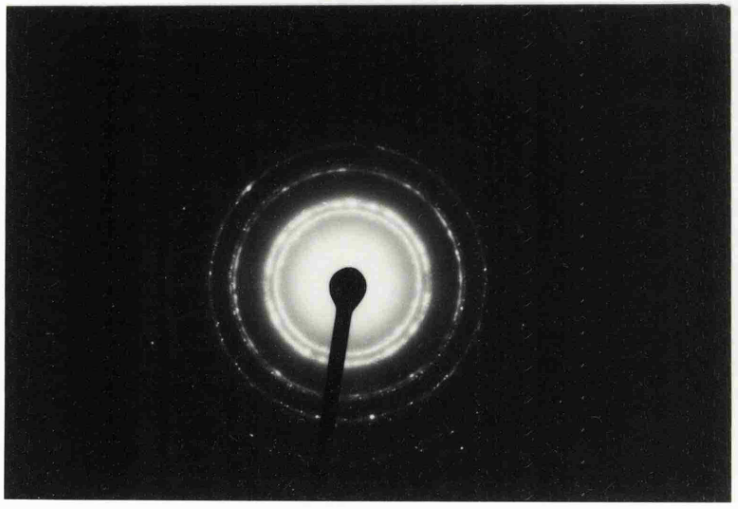

3

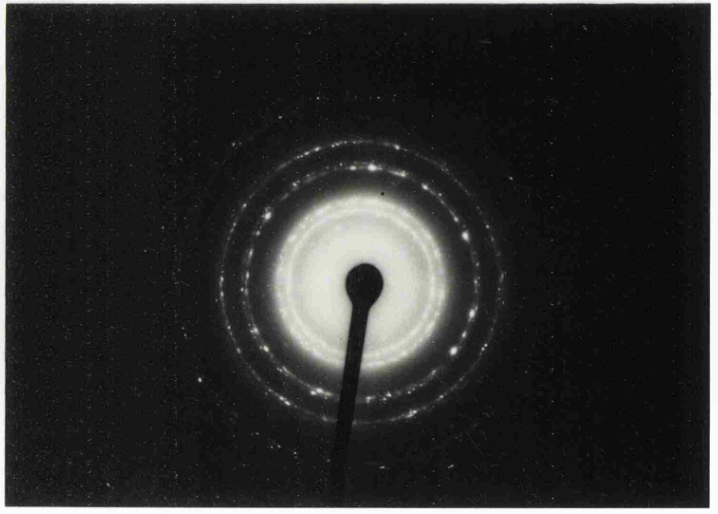

4

CoO-MgO solid solutions (Sections 4.1.5 - 4.1.8).

a) The spectrometer, vacuum system and reflectance cell

UV-vis spectra were taken on a Pye Unicam SP 700 spectrometer, using radiation from a tungsten filament (4,000-30,000 cm^{-1}) or deuterium arc lamp (30,000-50,000 cm^{-1}). Low surface area silica (Spectrosil) was used as reference.

A full description of the vacuum cell can be found in the work by Zecchina, Lofthouse and Stone.[197] The main features of this cell are portrayed in fig. 3.10. The cell was attached to a vacuum line (Fig. 3.11) and could be heated and evacuated or dosed with gas in situ.

b) Experimental measurement and presentation of the spectra

For solid materials available in the form of fine powders, the most suitable technique for measuring their visible and UV spectra is reflectance spectroscopy. The experimental technique and its application to the study of adsorbed species have been extensively reviewed by Klier.[198]

Two distinct processes are responsible for the reflection of radiant energy from powder surfaces. The first is the mirror-type specular reflection, and the second is diffuse reflection. The former is frequently referred to as 'regular' reflection;

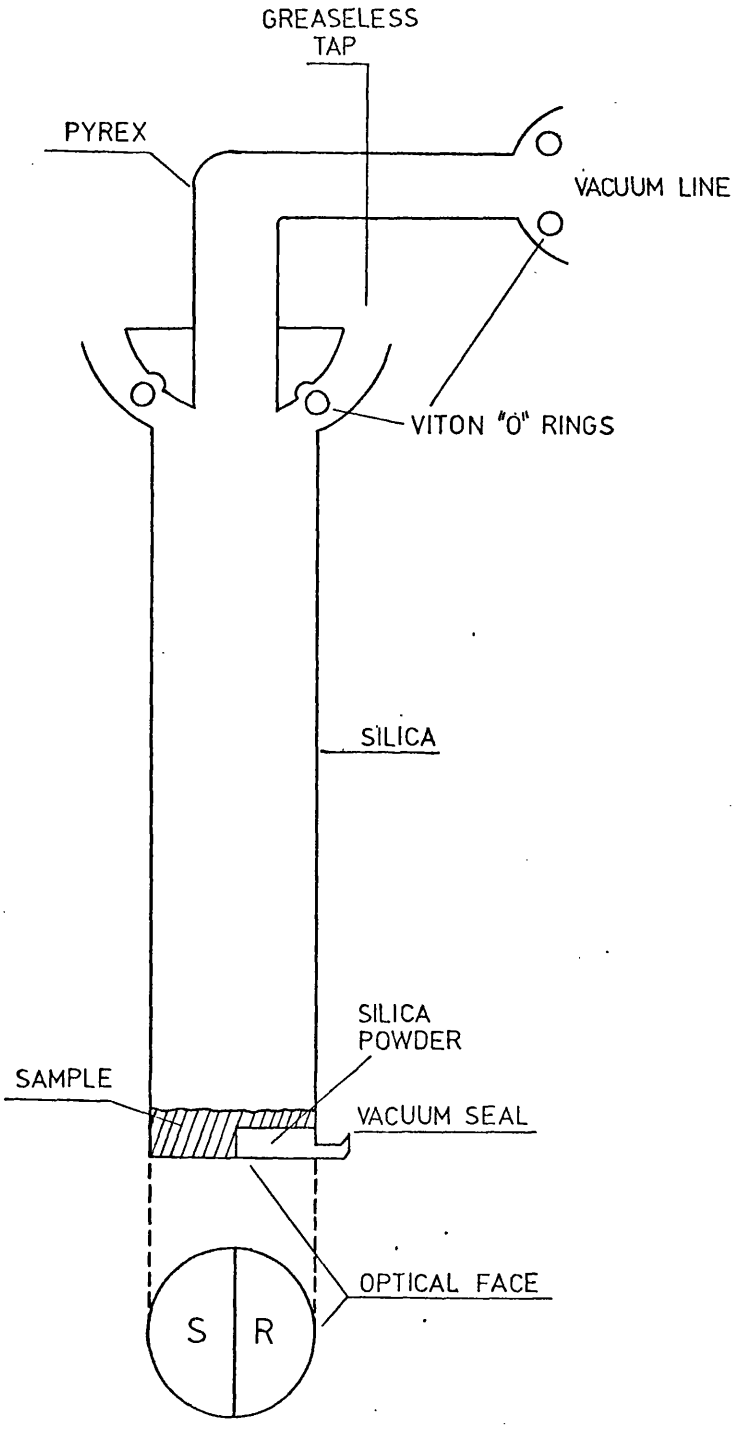

Fig. 3.10

The reflectance cell

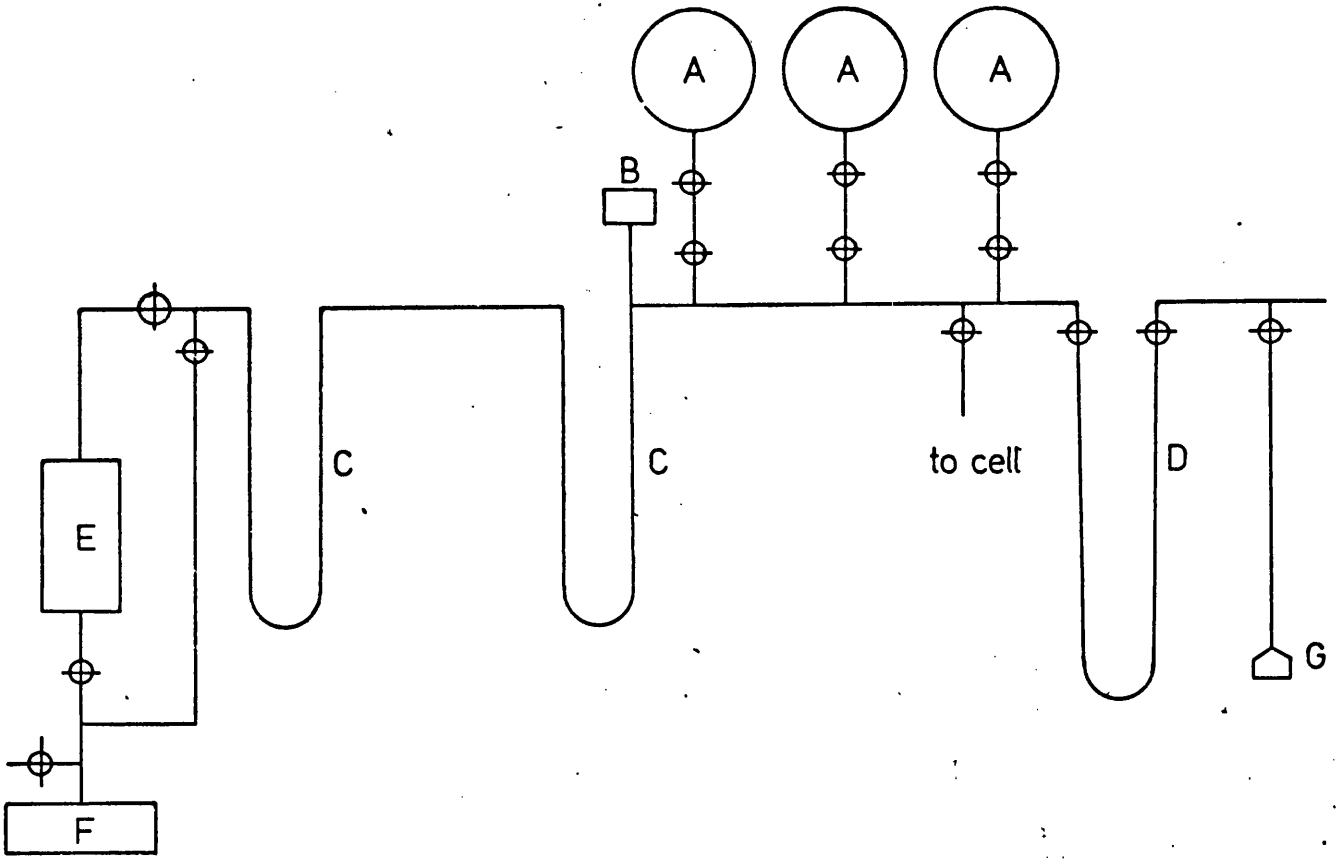

Fig. 3.11

Vacuum system for the reflectance cell
A) Gas storage bulbs, B) ion gauge, C) cold traps, D) mercury manometer, E) diffusion pump, F) rotary pump, G) gas inlet sinter

it is governed by Fresnel's equations which for the case of perpendicular incidence may be written[199]

$$\frac{I}{I_o} = \frac{(n-1)^2 + n^2\kappa^2}{(n+1)^2 + n^2\kappa^2} \qquad (3.1)$$

where I is the intensity of the reflected radiation, I_o is the intensity of the incident radiation, n is the refractive index and κ is the absorption index defined through Lambert's law[199]

$$I = I_o \exp(-4\pi n\kappa d/\lambda_o)$$

where λ_o is the wavelength of the incident radiation in vacuum and d is the layer thickness. The diffuse reflection arises as a result of the incident light penetrating into the interior of the sample. Some of this radiation is returned to the surface of the sample after partial absorption and multiple scattering at the boundaries of the individual particles which make up the powder.

Regular and diffuse reflection are usually present together, the relative proportion of each depending on the nature of the reflecting medium. For strongly absorbing materials, equation 3.1 indicates that the regular reflection approaches unity.

Under such conditions, the absorption maxima associated with these materials are interpreted assuming both regular and diffuse reflection. For weakly absorbing materials, the regular reflection is less significant and diffuse reflection prevails.

When only diffuse reflection is considered, the Kubelka-Munk equation may be derived:[199]

$$f(R_\infty) = (1 - R_\infty)^2/R_\infty \qquad (3.2)$$

This equation is valid for samples of infinite thickness; experimentally this condition is fulfilled for finely divided powdered samples in depths of 1 to 3 mm. The Kubelka-Munk function $f(R_\infty)$ is the ratio of the total light reflected from a material to the total intensity of light illuminating the material for infinite thickness. In practice, the absolute diffuse reflecting power is not measured; instead measurements are made relative to a suitable white standard such as MgO or SiO_2.

All the spectra shown in this section are presented as the Kubelka-Munk function vs. cm^{-1} on a linear scale. Table 3.9 shows the ligand field transitions and their respective energies for cobalt(II) in octahedral CoO-MgO and tetrahedral

Table 3.9

Sample	Coord.	Atom % Co.	Author	Transition (cm^{-1})				
				$^4T_{1g} \rightarrow {}^4T_{2g}$	$^2T_{1g}$ and/or $^2T_{2g}(G)$	$^4A_{2g}$	$^4T_{1g}(P)$	$^2T_{1g}(P)$
CoO-MgO	oct.	unspecified	Low (200)	8,500	17,200	18,700	19,600	20,500
CoO-MgO	oct.	3.0	Cimino et al (201)	8,500	-	-	20,000	-
CoO-MgO	oct.	unspecified	Pappalardo et al (202)	8,000	-	-	20,000	-
				$^4A_2 \rightarrow {}^4T_2$	$^4T_1(F)$	$^4T_1(P)$		
CoO-ZnO	tet.	0.2	Pappalardo et al (202)	4,100	6,100 6,800 7,500	15,500 16,300 17,650		

CoO-ZnO as determined by several workers. The two major, spin-allowed transitions, for octahedral cobalt(II) are $^4T_{1g}(F) \rightarrow {}^4T_{2g}(F)$ and $^4T_{1g}(F) \rightarrow {}^4T_{1g}(P)$; the transition $^4T_{1g}(F) \rightarrow {}^4A_{2g}$ is a two-electron transition and therefore is very weak in intensity. Major spin-allowed transitions for tetrahedral cobalt(II) are $^4A_2 \rightarrow {}^4T_2$, $^4A_2 \rightarrow {}^4T_1(F)$ and $^4A_2 \rightarrow {}^4T_1(P)$; the absorptions arising from these transitions may be split into triplets as a consequence of spin-orbit coupling. The origin of these transitions can be understood by reference to the energy level, Tanabe-Sugano, diagram[61] shown in fig. 3.12.

c) Spectra of magnesium oxide

Before reporting the spectra of CoO-MgO solid solutions it is relevant to present the reflectance spectra of the pure MgO matrix. Fig. 3.13 shows the spectra, at room temperature, of MSA and HSA MgO, as follows:

A. MgO MSA in vacuum (after outgassing at 1273 K for 15 hours).
B. MgO MSA as above exposed to the atmosphere for 14 days.
C. MgO HSA in vacuum prepared in situ.
D. MgO HSA as above exposed to the atmosphere for 5 hours.

d^7 Tanabe-Sugano Diagram

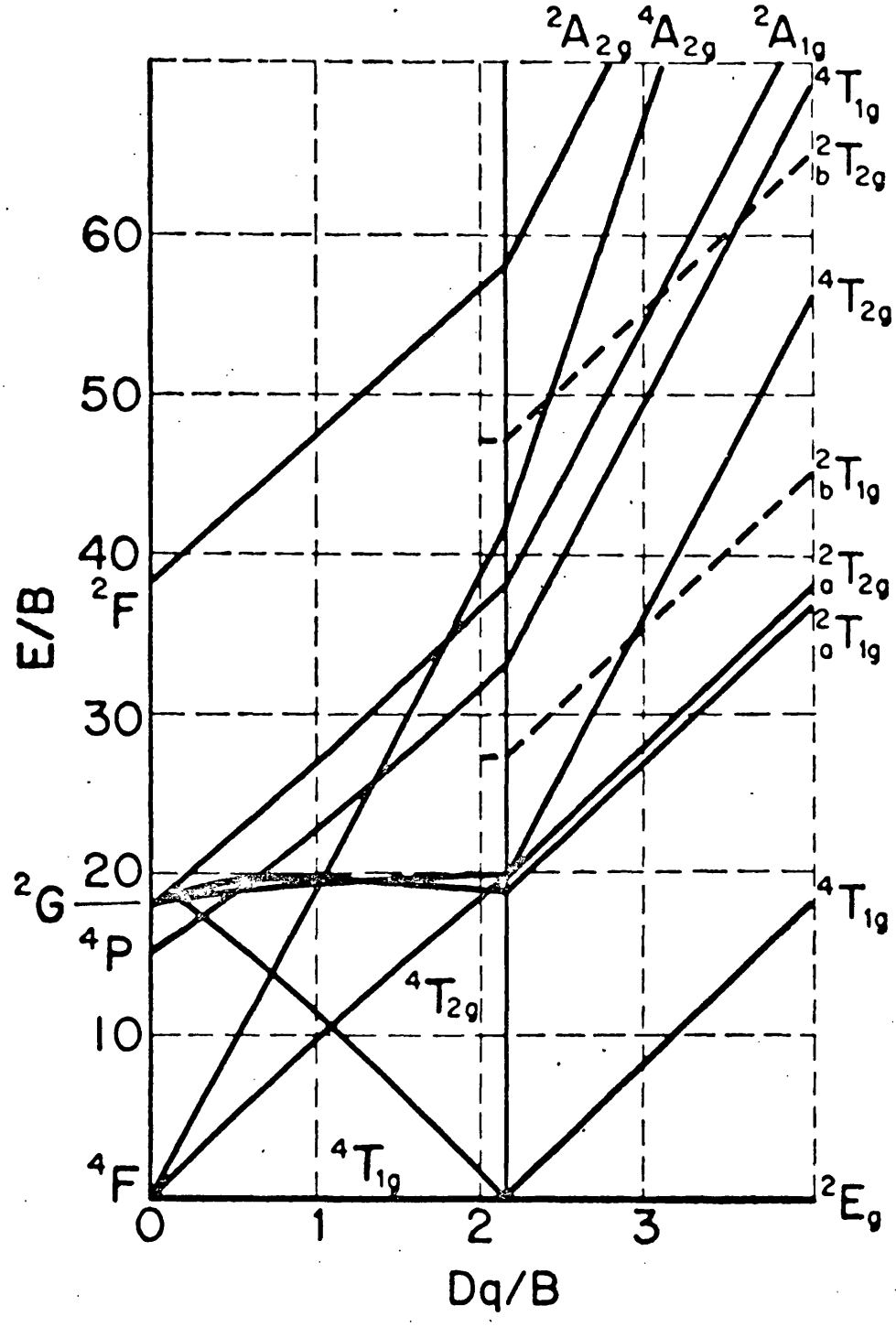

Fig.3.12

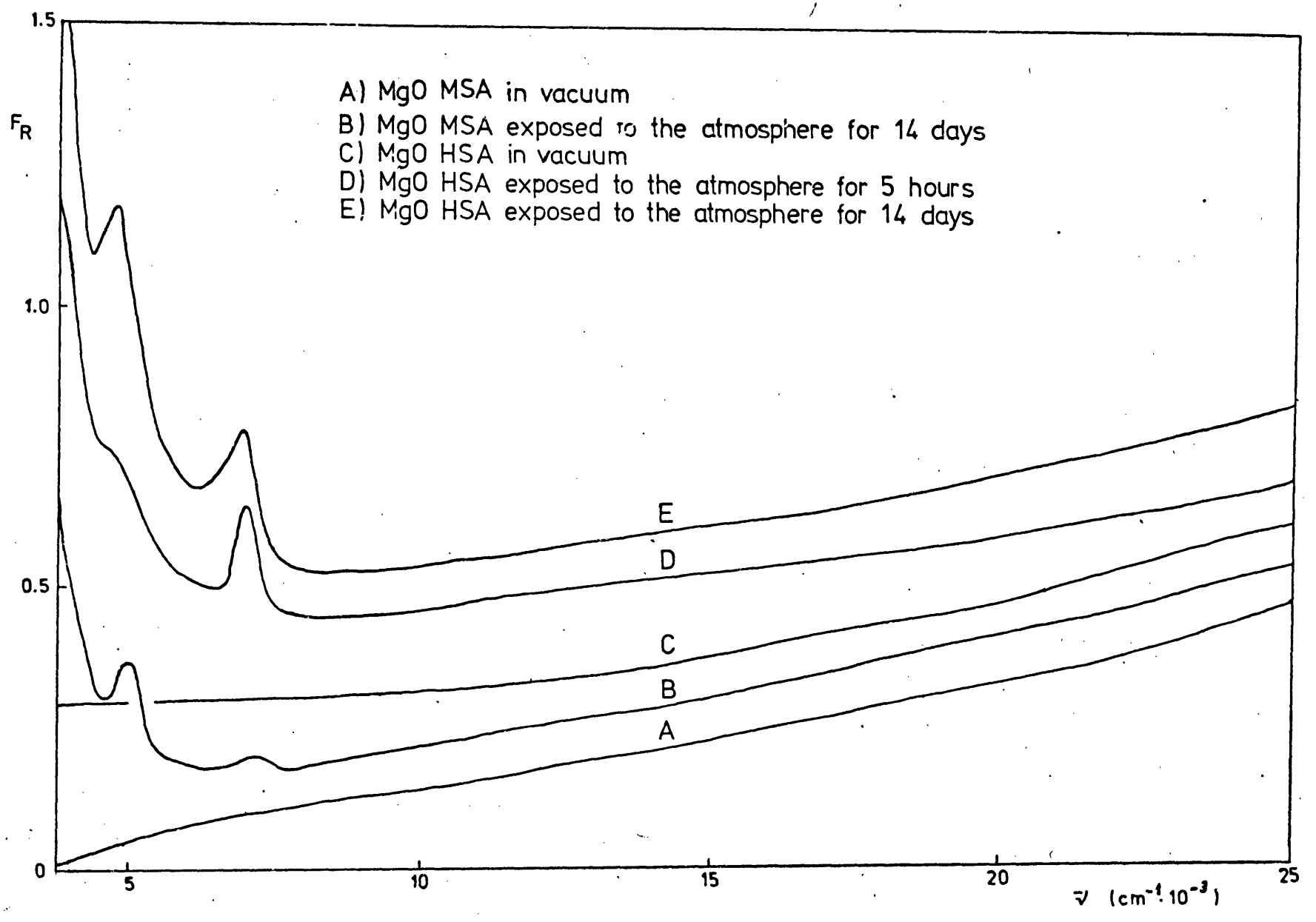

Fig. 3.13 Reflectance spectra of MgO

E. MgO HSA as above exposed to the atmosphere for 14 days.

As might be expected, the vacuum spectra of MSA and HSA MgO exhibit no bands in the range 25,000-4,000 cm^{-1}. Upon exposure of both samples to the atmosphere, however, two bands appear at the infrared end of the spectrum at 7,500 and 5,100 cm^{-1} together with a further intense band extending into the infrared. These bands have been assigned to water vapour.[196] The intensity of the bands in the MSA sample exposed to the atmosphere for 14 days (curve B) is much lower than in the HSA sample exposed to the atmosphere for five hours (curve D) despite the much longer exposure time; such an observation is further confirmation of the ability of the HSA materials to adsorb water vapour rapidly from the atmosphere.

d) Spectra of solid solutions

The UV-vis spectra of LSA, MSA and HSA MCo 3 recorded at room temperature are shown in Fig. 3.14. Conditions were as follows:

A. MCo 3 LSA in vacuum outgassed at 1273 K for 15 hours.

B. MCo 3 MSA in vacuum outgassed at 1273 K for 15 hours.

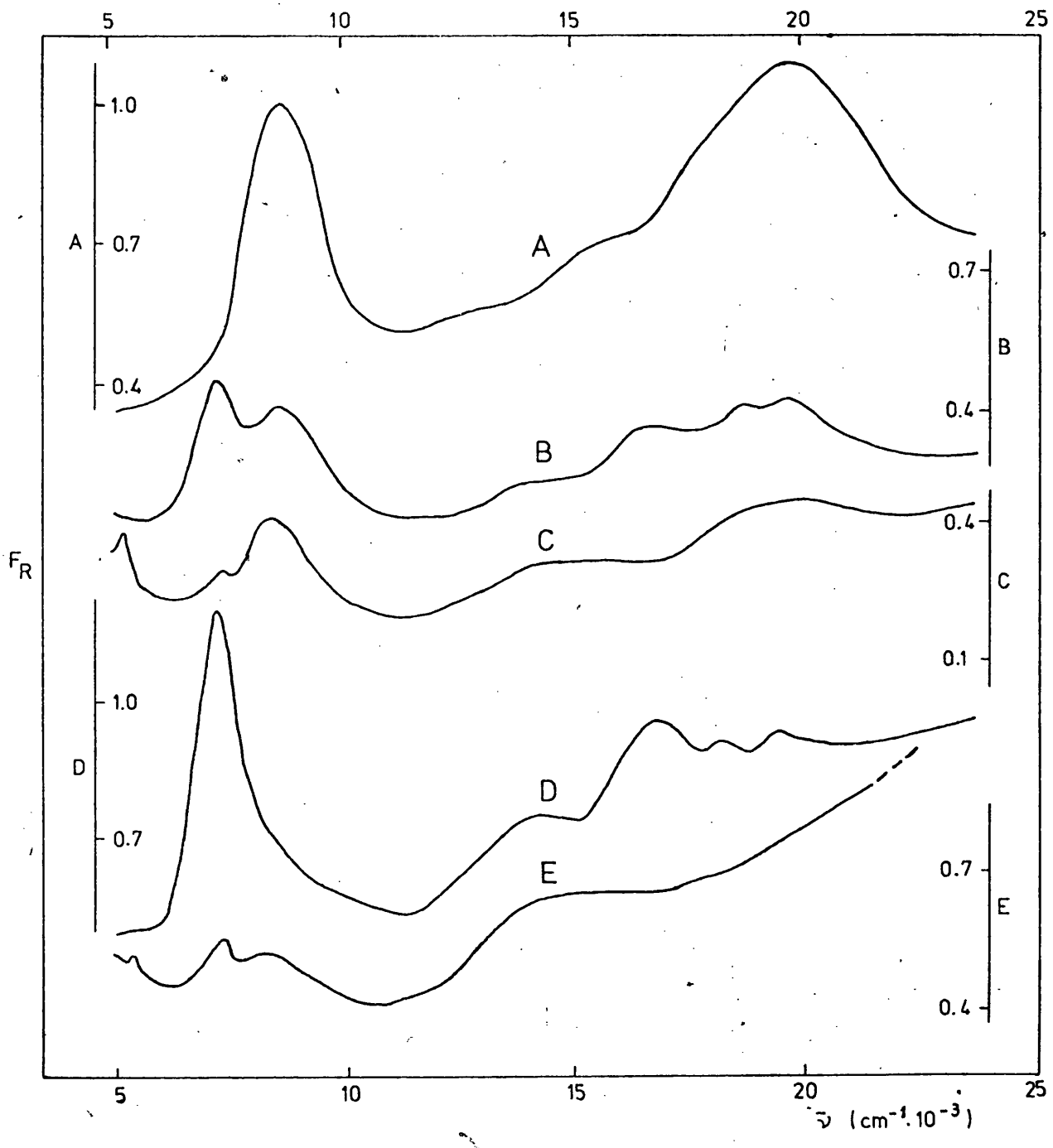

Fig. 3.14

Reflectance spectra of MCo 3
A) MCo 3 LSA in vacuum
B) MCo 3 MSA in vacuum
C) MCo 3 MSA exposed to air for 10 days
D) MCo 3 HSA in vacuum
E) MCo 3 HSA exposed to air for 10 days

C. MCo 3 MSA as above exposed to the atmosphere for 10 days.

D. MCo 3 HSA in vacuum prepared in situ.

E. MCo 3 HSA as above exposed to the atmosphere for 10 days.

The spectrum of LSA MCo 3 shows the two well known octahedral bands of cobalt(II) at 8,500 cm^{-1} ($^4T_{1g}(F) \rightarrow {}^4T_{2g}(F)$) and 19,600 cm^{-1} ($^4T_{1g}(F) \rightarrow {}^4T_{1g}(P)$). The spectra of MSA and HSA samples, however, show some remarkable features. The octahedral band of cobalt(II) at 8,500 cm^{-1}, displayed by the LSA oxide, is completely dominated in the HSA oxide by an intense band at 7,100 cm^{-1} which displays a high energy tail at about 8,500 cm^{-1} almost certainly corresponding with the maximum in the same position in curve A. MSA oxide shows both bands at comparable intensities. The non-octahedral band (at 7,100 cm^{-1}) is clearly a function of the surface area. Exposure of MSA and HSA oxide to the atmosphere reduces very markedly the non-octahedral 'surface band' and leaves the octahedral spectrum. Referring to curve D it can also be seen that in the visible region of the spectrum there are new bands at 13,900, 16,800 and 18,300 cm^{-1}, apart from the octahedral band at 19,400 cm^{-1} which, although slightly displaced, has probably the same origin as the band at 19,600 cm^{-1} in A, i.e., it

corresponds to the $^4T_{1g}(F) \rightarrow {}^4T_{1g}(P)$ transition. The three new bands are also present, although less clearly resolved, in the spectrum of MSA oxide under vacuum. Exposure to the atmosphere again quenches the 'surface bands' in this region. A tentative explanation of the nature of the chromophores giving rise to the non-octahedral ('surface') bands will be given in section 4.1.6.

e) Spectral study of the effect of adsorbed oxygen

The effects of adsorption and desorption of oxygen on the UV-vis spectrum of a HSA MCo 7.5 sample are shown in fig. 3.15 as follows:

A. MCo 7.5 HSA in vacuum prepared in situ.
B. MCo 7.5 HSA as above exposed to 260 torr of oxygen.
C. MCo 7.5 HSA exposed to 260 torr of oxygen and then outgassed at room temperature.
D. MCo 7.5 HSA as above outgassed at 1273 K.

It can be seen that the four surface bands decrease in intensity, although they are not completely destroyed, on oxygen adsorption and that the original spectrum is regained on outgassing at 1273 K. The specimen with adsorbed oxygen also shows a broad

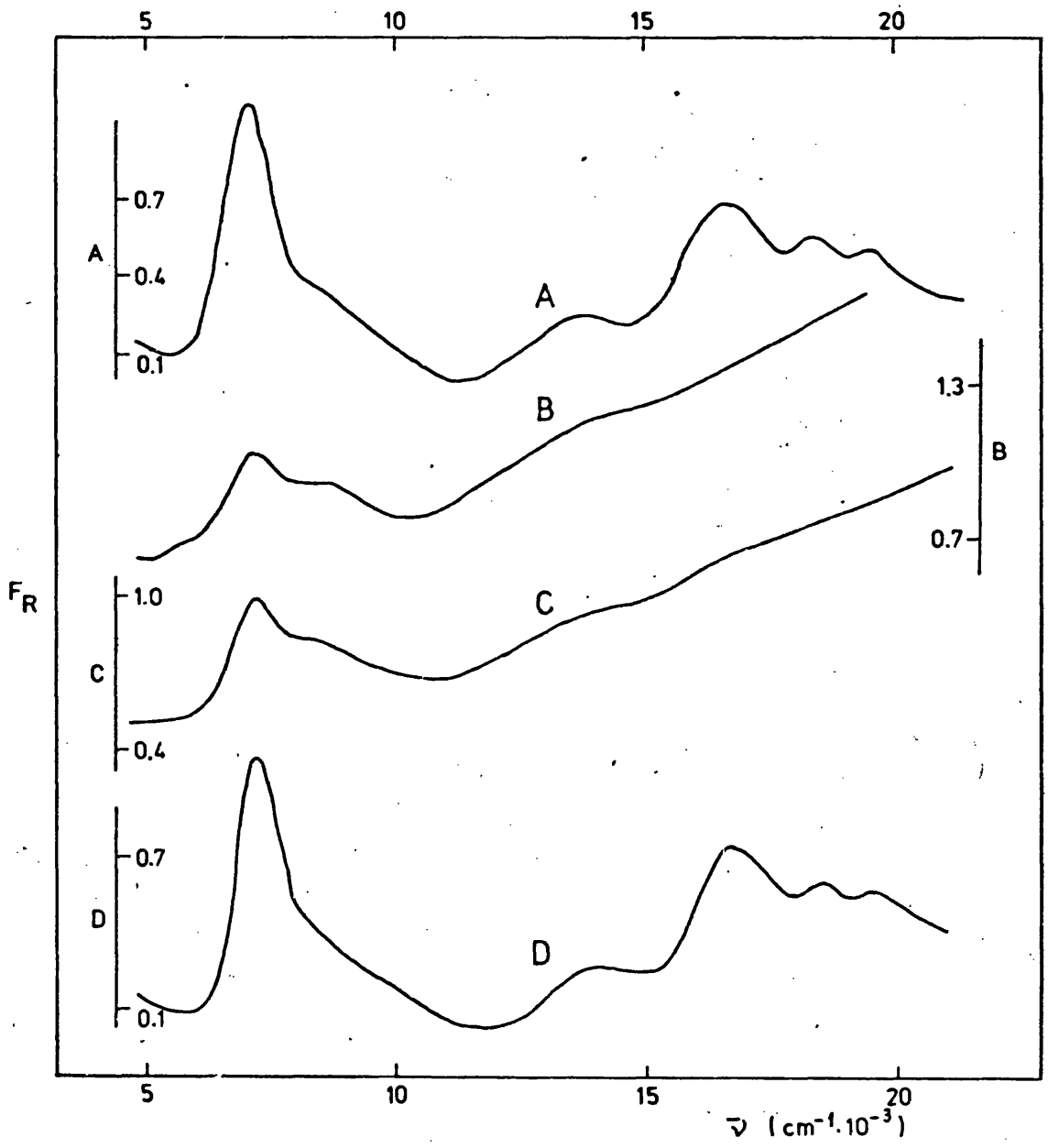

Fig 3.15 Reflectance spectra of MCo 7.5

A) MCo 7.5 in vacuum
B) MCo 7.5 after dosing 260 torr oxygen
C) As above after outgassing at room temperature
D) As above after outgassing at 1273 K

absorption band which develops above 10,000 cm^{-1} and extends into the UV. This band is most likely due to a charge transfer process (e.g. $O_2(g) + 2Co(II) \rightarrow 2O_{ads} + 2Co(III)$) probably accompanied by intervalence absorption.

3.2. The Systems MnO-CaO and MnO-CaO-Na_2O

Samples in the system MnO-CaO have been prepared by firing in vacuum coprecipitated carbonates of manganese and calcium. The reasons for choosing this method instead of an impregnation technique similar to that used for the CoO-MgO solid solutions were (i) Mn^{2+} is easily converted into higher oxidation states of manganese and therefore the presence of an oxidizing anion (NO_3^-) is not desirable. (ii) When Mn^{2+} and Ca^{2+} are coprecipitated as carbonates a solid solution between rhodochrosite and calcite forms,[203] thus providing a random dispersion of the metallic ions which should facilitate the formation of solid solution between the oxides.

Samples in the system MnO-CaO-Na_2O were prepared by firing in air mixtures of coprecipitated $MnCO_3$-$CaCO_3$ with 3 mol % of Mn and variable amounts of Na_2CO_3. One sample containing {Mn} = 0.1% and {Na} = 0.4% (initial concentration) was also prepared by the same procedure. Due to the high

volatility of Na_2O at high temperature the final amount of Na_2O in the fired samples was presumably far smaller than that corresponding to the initial amount of Na_2CO_3 in the mixture.

3.2.1 Nomenclature

Samples in the system MnO-CaO were designated CM X where X is the nominal content in manganese expressed as mol % Mn. Samples in the system MnO-CaO-Na_2O prepared by addition of variable amounts of Na_2O to a sample of MnO-CaO with 3 mol % of Mn were designated 3N X, where X is the nominal ratio Na/Mn. The sample with 0.1% Mn and 0.4% Na was termed 0.1N 4.

3.2.2 Preparation of the coprecipitated carbonates

'Specpure' manganese flake and 'Specpure' calcium carbonate were dissolved in dilute 'Aristar' nitric acid and distilled water was then added so as to prepare 0.2M solutions of $Mn(NO_3)_2$ and $Ca(NO_3)_2$ respectively. These nitrate solutions were then used for the preparation of all the samples.

Coprecipitated Mn-Ca carbonates were obtained from mixtures of the above nitrate solutions in the desired proportion. Each mixture was added, drop by drop, to a large volume of 0.5M solution of 'Analar' ammonium carbonate whilst stirring vigorously.

Before, and during the precipitation, a flow of nitrogen was bubbled through the solutions to purge any dissolved oxygen. The precipitated carbonate was filtered off and washed free of ammonium and nitrate ions whilst protected from the air by a layer of carbon dioxide (produced from a piece of 'dry ice' in the Buchner funnel containing the precipitate). The carbonate was then dried by evacuation in a desiccator overnight.

Pure manganese and calcium carbonates were prepared in a similar way. However, in the case of calcium carbonate there was no need to avoid exposure to the atmosphere.

Table 3.10 lists the source and purity of the materials used. Sodium carbonate is also included because it was used for the preparation of the MnO-CaO-Na_2O samples.

3.2.3 Preparation of solid solutions

a) System MnO-CaO

MnO-CaO solid solutions were prepared by thermal treatment in vacuum of the corresponding coprecipitated carbonates. Due to the high reactivity of finely divided calcium oxide it was desirable to avoid exposure of the samples to atmospheric air. Therefore a cell was designed(*) which allowed the

(*) The author is grateful to Mr. M.R. Lock for his help in the design of the vacuum cell and for sealing off the samples after each preparation.

Table 3.10

Material	Source	Stated impurities	(ppm)
Manganese flake	Johnson & Matthey	Magnesium	70
		Calcium	20
		Iron	1
		Silicon	1
		Tin	<1
		Aluminium	<1
		Copper	<1
Calcium carbonate	Johnson & Matthey	Strontium	3
		Magnesium	2
		Indium	1
		Iron	1
		Barium	<1
		Copper	<1
Nitric acid	BDH Chemicals	Calcium	0.5
		Magnesium	0.5
		Strontium	0.5
		Sodium	0.5
		Iron	0.2
Ammonium carbonate	BDH Chemicals	Calcium	20
		Magnesium	20
		Sodium	100
		Potassium	50
		Iron	1
		Heavy metals	1
Sodium carbonate	Johnson & Matthey	Calcium	3
		Iron	1
		Copper	1
		Aluminium	<1
		Lithium	<1
		Magnesium	<1
		Strontium	<1

carbonate to be decomposed under dynamic vacuum and the resulting oxide to be transferred into appropriate reservoirs which were sealed off whilst still under vacuum. These reservoirs were two X-ray capillary tubes, one ESR tube and one small bulb to retain the remainder of the sample. A photograph of this vacuum cell is shown in Plate III.

The procedure for the preparation of the solid solutions was as follows:

1. About 1g of carbonate was placed in a platinum boat which fitted into the silica tube of the vacuum cell.
2. The cell was attached to a vacuum line and the sample outgassed at room temperature for 3 hours.
3. A Gallenkamp electric furnace was placed round the silica tube of the cell. This furnace was connected to a Skil temperature controller actuated by a platinum-platinum 13% rhodium thermocouple placed between the silica tube and the internal wall of the furnace, at the level of the platinum boat.
4. The temperature was carefully raised to 573 K and maintained for 3 hours.

PLATE III

1 Silica sample tube
2 Greaseless joint
3 Greaseless tap
4 Sample grinder
5 X-ray tubes
6 Sample reservoir
7 ESR tube
8 Sliding vacuum seal
9 To vacuum line

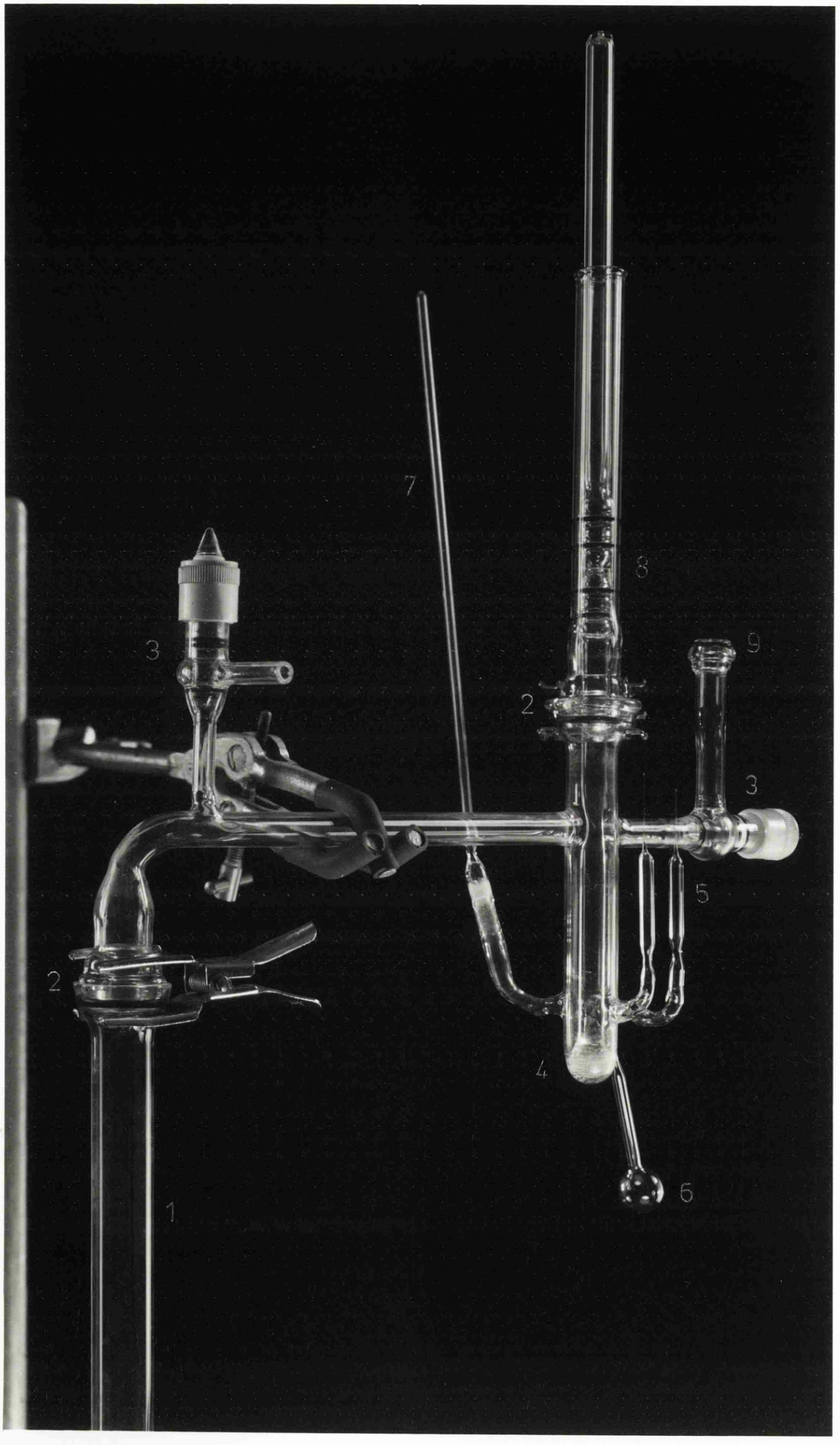
7
8
9
3
2
3
5
2
4
1
6

5. The temperature was carefully raised to 873 K and maintained for 12 hours. During this period the decomposition of the carbonate was accomplished.
6. The temperature was rapidly raised to 1273 K and maintained for 15 hours.
7. The part of the cell outside the furnace was flamed with a Bunsen burner flame.
8. The cell was isolated from the vacuum line and removed.
9. By careful manipulation the sample was transferred to the grinding tube, ground if necessary, and then tapped into the X-ray and ESR tubes. The remainder was collected into the round bulb.
10. All the sample tubes were sealed off whilst still under vacuum.

Throughout 2 - 10 a dynamic vacuum was maintained by a mercury diffusion pump backed by a rotary pump. Two liquid nitrogen traps were inserted between the diffusion pump and the vacuum cell. The trap nearer to the cell was not cooled until the end of step 5. The vacuum during step 6 (monitored with an ion gauge) was of the order of 10^{-6} torr.

Pure calcium and manganese(II) oxides were prepared by the same procedure, starting from $CaCO_3$ and $MnCO_3$ respectively. The oxides obtained showed a colour gradually changing from white to pale-pink, grey-green and dark-green, with increasing manganese content. Pure calcium oxide was white and pure manganese(II) oxide olive-green.

Under the final firing conditions, 1273 K and $\sim 10^{-6}$ torr, the most stable oxide of manganese is MnO, as shown in the phase diagram given in fig. 3.16. It is important, however, that the decomposition of the carbonates be complete before the temperature is raised above 873 K, because if carbon dioxide is present at 973 K part of the manganese ions are oxidized to Mn^{3+} with the formation of $CaMn_2O_4$. This was found to be the case in the preparation of one sample of CM 10 where the final stage of decomposition of the carbonates was carried out at 973 K. This sample showed a brown colour and exhibited in the X-ray diffraction pattern new lines corresponding to the crystalline phase $CaMn_2O_4$. Oxidation of Mn^{2+} was probably caused by the oxygen released in the decomposition of carbon dioxide into carbon monoxide and oxygen.

b) System $MnO-CaO-Na_2O$

One coprecipitated Mn-Ca carbonate with 0.1 mol % of $MnCO_3$ was mechanically mixed, in an

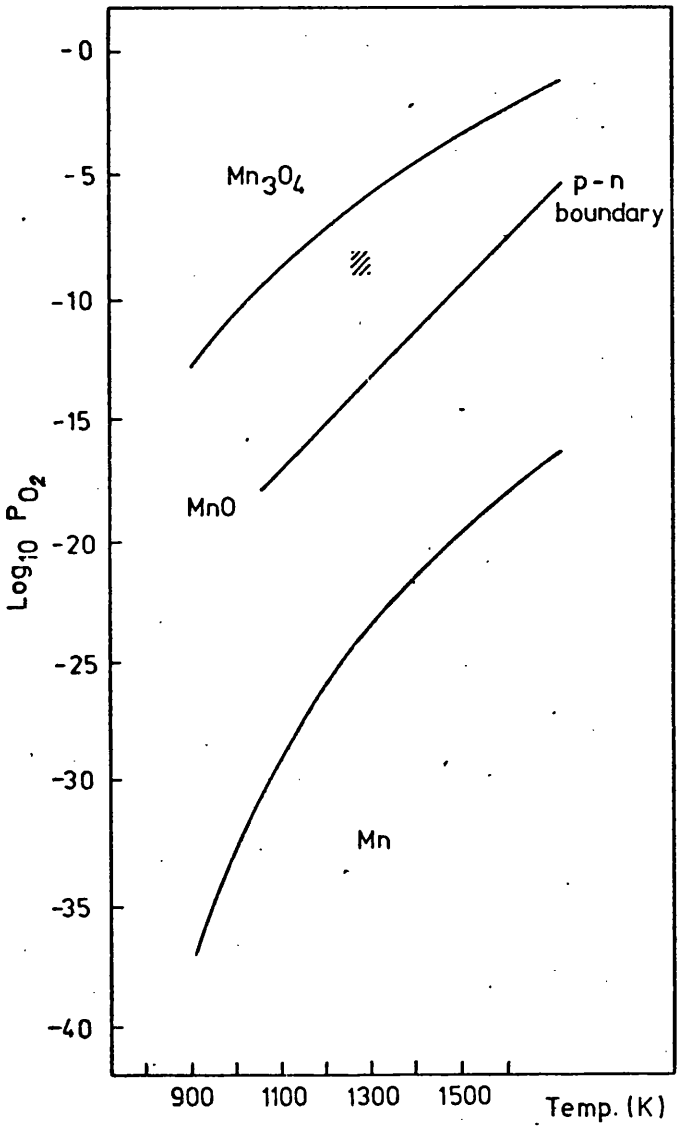

Fig. 3.16

Phase diagram of oxygen pressure vs temperature for the phase field of manganous oxide.[259]

(▨ Corresponding area of diagram at which MnO-CaO specimens were prepared)

agate mortar, with 'Specpure' sodium carbonate. The amount of Na_2CO_3 was such that there were 4 atoms of sodium per atom of manganese in the mixture. This mixture was then fired in air at 1273 K for 15 hours and the resulting sample termed 0.1N 4. It possessed a white colour.

Several portions of a coprecipitated Mn-Ca carbonate with 3 mol % of $MnCO_3$ were similarly mixed with the appropriate amounts of sodium carbonate so as to provide Na/Mn ratios of 1, 2, 4 and 8 respectively. These mixtures were fired in air at 1273 K for 15 hours and the resulting samples, which had a brown colour, were designated 3N 1, 3N 2, 3N 4 and 3N 8 respectively. A portion of the same Mn-Ca carbonate, without sodium, was also fired under the same conditions and the resulting sample termed 3N 0. The colour of this sample was also brown.

3.2.4 Lattice parameters

a) System MnO-CaO

Lattice parameters of the MnO-CaO specimens were determined by X-ray diffraction using the Debye-Scherrer method. As described in section 3.2.3 the samples were sealed off under vacuum in X-ray capillary tubes. These tubes were approximately 0.4 mm in diameter, drawn in pyrex and with thin

walls. Nickel filtered copper Kα radiation and a 114.6 mm camera, with the film mounted in the asymmetric position, were used in all cases. The Debye-Scherrer films showed always sharp lines (apart from the film corresponding to pure calcium oxide), as can be appreciated from Plate IV. All films showed only reflections corresponding to a NaCl-type structure.

Two diffraction films were taken for each sample; the postition of the lines were read several times and the results averaged. Finally the lattice parameter, a_o, was computed from the high angle reflections ($45^o < \theta < 80^o$) using the Nelson-Riley extrapolation (typical plots are shown in fig. 3.17). Table 3.11 shows the values of a_o along with the manganese content. With the exception of pure calcium oxide, the accuracy of the a_o values is estimated to be better than $\pm 2.10^{-4}$ Å. No accurate value of a_o could be calculated for CaO due to considerable broadening of the high angle reflections. No chemical analysis was made on the samples, but the precipitation of Mn^{2+} and Ca^{2+} as carbonates may be assumed to be quantitative on account of the very reduced solubility of these carbonates (0.015 and 0.065 $g \cdot l^{-1}$ for $CaCO_3$ and $MnCO_3$ respectively), and there is no

PLATE IV

1. CaO
2. CM 1
3. CM 5
4. CM 10
5. CM 25
6. CM 75
7. CM 85
8. MnO

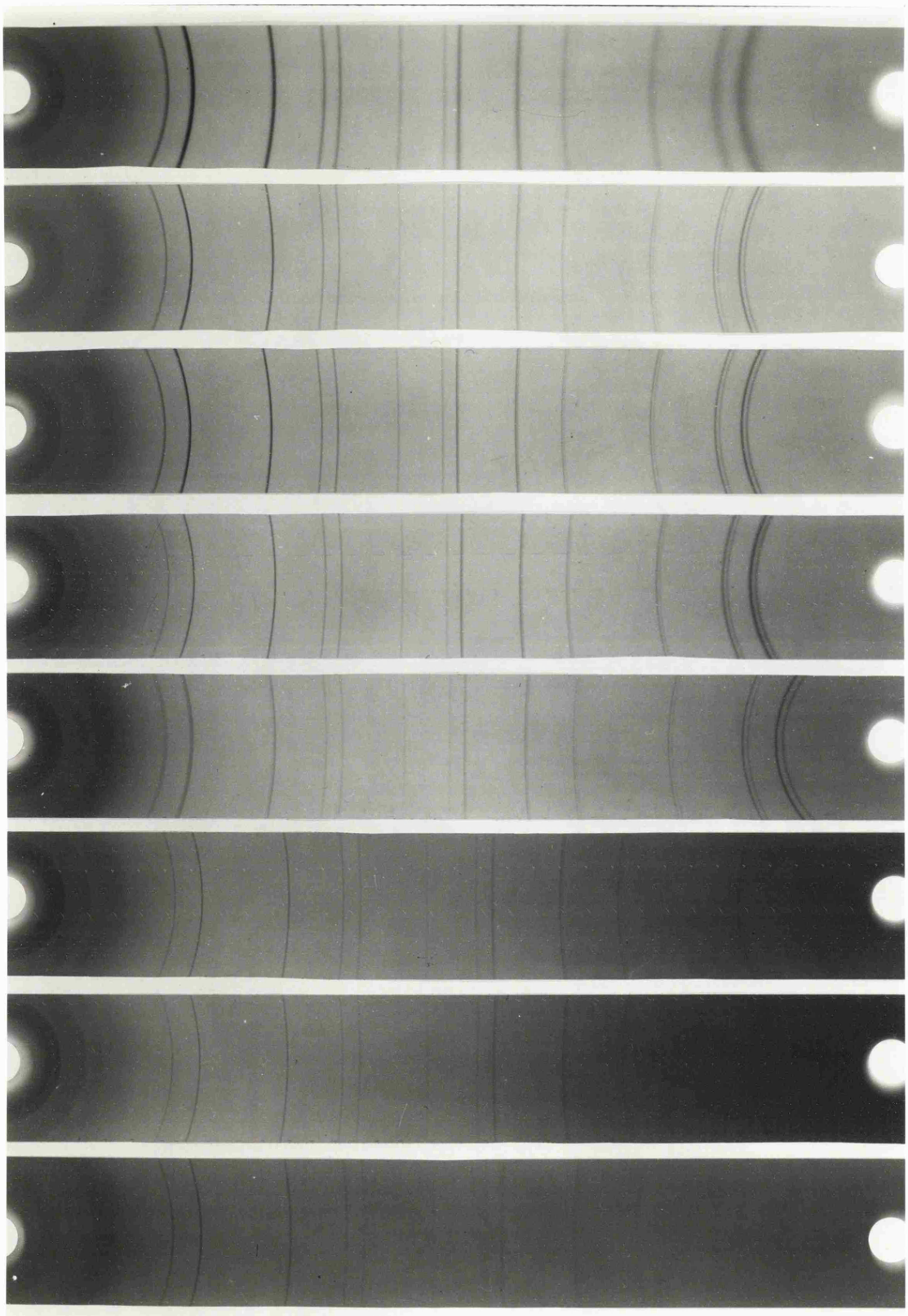
1
2
3
4
5
6
7
8

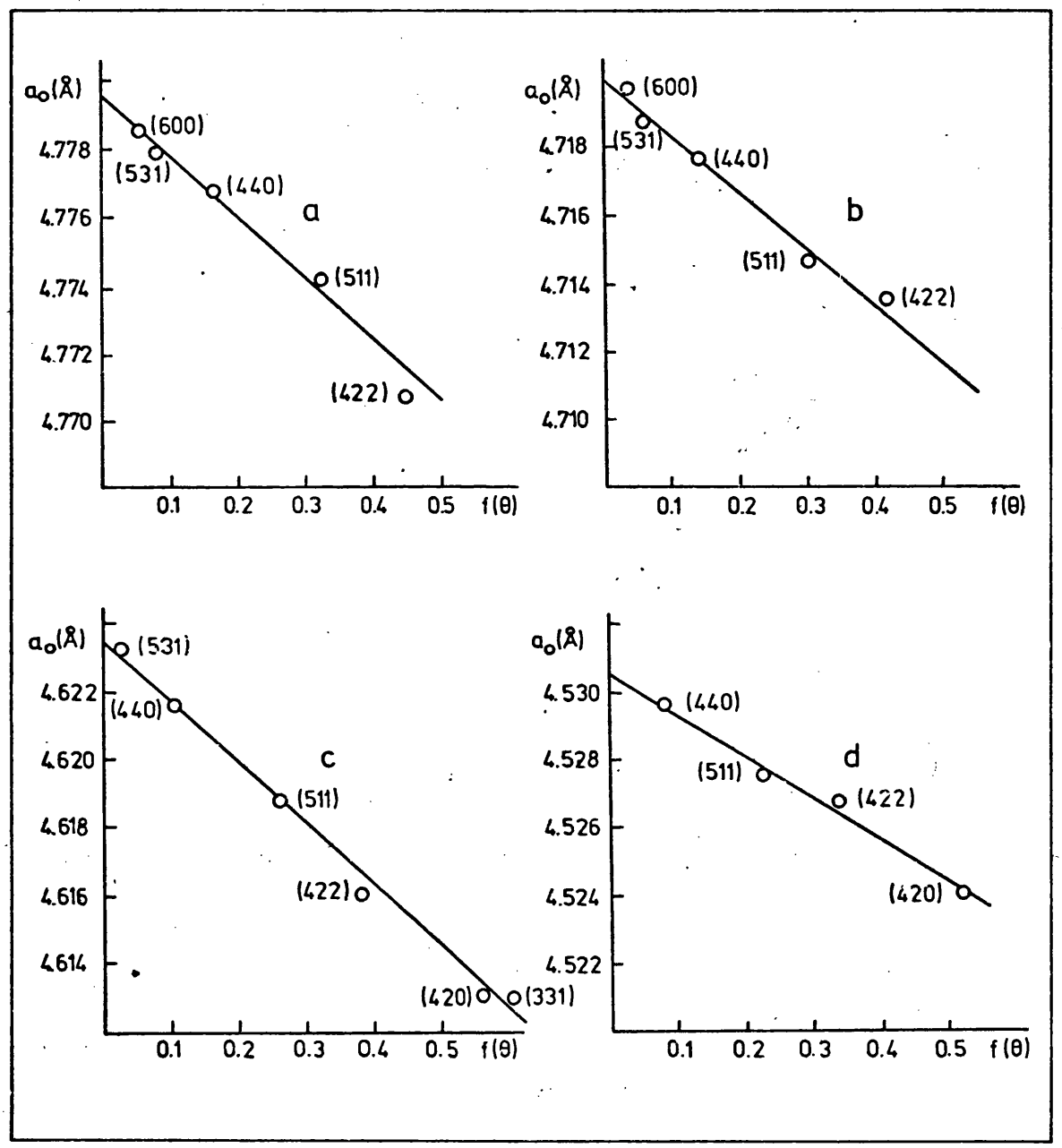

Fig. 3.17

Typical Nelson-Riley plots for MnO-CaO specimens
a) CM 10, b) CM 25, c) CM 50, d) CM 75

Table 3.11

Lattice parameters of MnO-CaO solid solutions

Sample	At. % Mn	a_o (Å)
CaO	0.00	4.810
CM 0.025	0.025	4.8097
CM 0.5	0.5	4.8086
CM 1	1.00	4.8062
CM 3	2.91	4.8007
CM 5	4.76	4.7949
CM 10	9.09	4.7795
CM 25	25.00	4.7200
CM 25 HT	25.00	4.7201
CM 50	50.00	4.6234
CM 65	65.00	4.5607
CM 65 HT	65.00	4.5606
CM 75	75.00	4.5301
CM 75 HT	75.00	4.5301
CM 85	85.00	4.4955
MnO	100.00	4.4449

reason to expect that significant amounts of either oxide could be lost during the heat treatment. Values of [Mn] given in table 3.11 are those corresponding to the initial mixture of nitrate solutions. A plot of lattice parameter versus manganese content is shown in fig. 3.18. This plot shows that the variation of a_o with manganese content is linear up to 50 mol % Mn. However, the experimental values of a_o depart markedly from the straight line for [Mn] > 50%. This is the behaviour which could be expected if not all the CaO entered into the MnO lattice. Although the X-ray patterns show no evidence for two different crystalline phases (even after 24 hours exposure time), it is to be expected that very small amounts of a CaO phase will not be detected by X-rays. To add new light to this point it was decided to prepare specimens of CM 25, CM 65 and CM 75 at higher temperature (1523 K) to see if the lattice parameter of the resulting oxide would show any temperature dependence. However these three "high temperature specimens", marked with the letters HT in Table 3.11, showed the same lattice parameter as the corresponding specimens prepared at 1273 K. It must be added that these specimens were quenched in ice-water; all other samples were quenched in air.

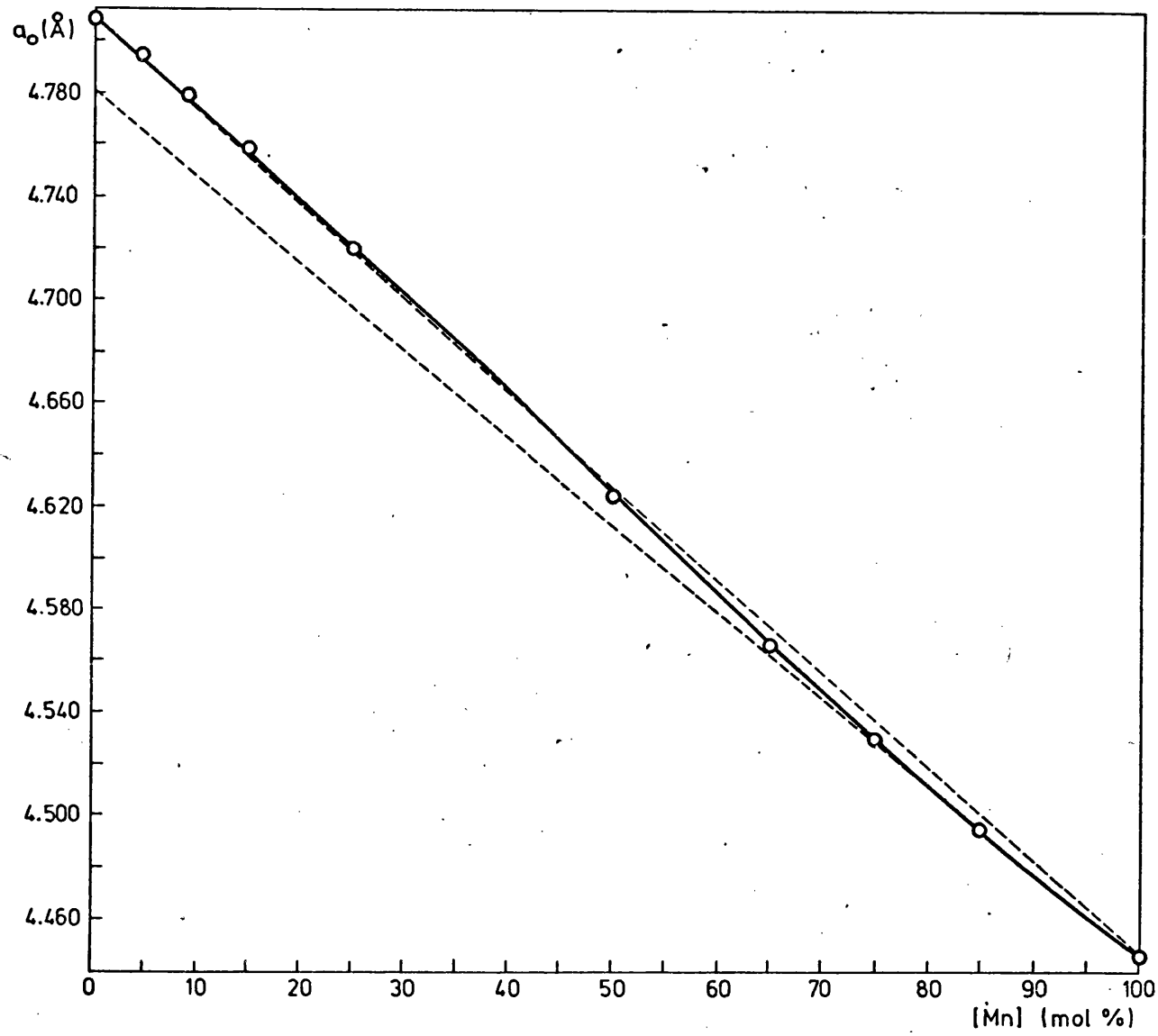

Fig 3.18

Lattice parameter vs [Mn] for MnO-CaO specimens

b) System $MnO-CaO-Na_2O$

Specimens were placed in 0.3 mm diameter Lindemann tubes and examined by X-ray diffraction in the same way as described for MnO-CaO samples. Values of a_o for the different specimens are given in Table 3.12 along with the initial Na/Mn ratio. The diffraction patterns of all the samples with 3 mol % Mn showed the presence of lines corresponding to the phase $CaMn_2O_4$ in addition to those of the calcium oxide phase. For comparison, pure $CaMn_2O_4$ was also prepared by solid state reaction between CaO and MnO (molar ratio 1:2) at 1273 K in air (12 hours). Values of d-spacings and relative intensities for this compound are given in Table 3.13 together with the values reported by Toussaint.[204] Calculated d-spacings for the phase $CaMn_2O_4$ present together with the CaO phase in the samples with 3 mol % Mn, were in very good agreement with those shown in Table 3.13. Fig. 3.19 shows a plot of lattice parameter versus initial Na/Mn ratio in the mixed carbonates for samples with [Mn] = 3%.

Table 3.12

Lattice parameters of $MnO-CaO-Na_2O$ samples

Sample	At. % Mn	Initial ratio Na/Mn	a_o (Å)
0.1N 4	0.1	4	4.8105
3N 0	3	0	4.8108
3N 1	3	1	4.8102
3N 2	3	2	4.8098
3N 4	3	4	4.8097
3N 8	3	8	4.8098

Table 3.13

d-spacings and relative intensities for the compound $CaMn_2O_4$

d(Å)		I/I_o		
Present work	Toussaint	Present work	Toussaint	hkl
4.817	4.82	30	30	101
3.448	3.45	30	30	102
3.002	3.00	50	60	112
2.861	2.86	70	70	200
2.686	2.69	100	100	103
2.578	2.58	60	60	120
2.491	2.49	60	60	121
2.292	2.29	70	70	004
2.214	2.22	100	100	122
2.1612	2.16	50	60	104
2.0563	2.05	100	100	220
1.6198	1.620	60	60	303
1.6032	1.604	60	60	230
1.5668	1.567	60	70	133
1.4909	1.491	85	100	232
1.4736	1.471	100	100	106

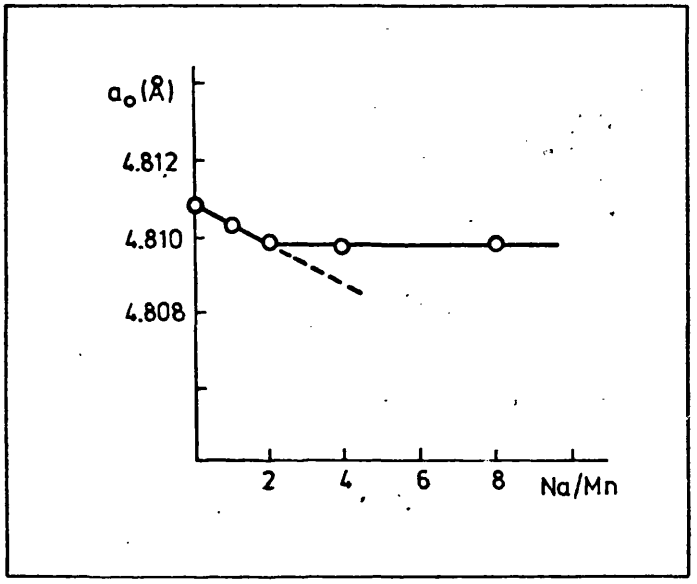

Fig. 3.19

a_o versus Na/Mn ratio for
$MnO-CaO-Na_2O$, [Mn] = 3 mol %

3.2.5 ESR spectroscopy

a) The ESR spectrum of Mn^{2+} ions

If the ground state of the Mn^{2+} ion were a pure $^6S_{5/2}$ state the ESR spectrum would be remarkably simple. The sextet would have no splitting other than that due to the Zeeman interaction, and a single line would be observed at the free spin value g = 2.00232. Although manganese has a nuclear spin I = 5/2, no hyperfine splitting would, in principle, be expected for the single resonance line because the d^5 configuration has spherical symmetry and the d-orbitals have nodal planes passing through the nucleus. In practice, however, the spectrum is rather complex, with both fine and hyperfine structure. Spin-orbit coupling produces a slight breakdown of LS-coupling,(205) introducing a small admixture of the excited state $^4P_{5/2}$ (which in turn has a contribution from $^2D_{5/2}$) into the ground state $^6S_{5/2}$. An octahedral field can split the ^2D level and this reacts back via spin-orbit coupling to split the $^6S_{5/2}$ state in zero magnetic field into three Kramers' doublets, as shown in fig. 3.20. This figure also shows hyperfine splitting of the fine structure lines. The origin of the hyperfine splitting can be assigned

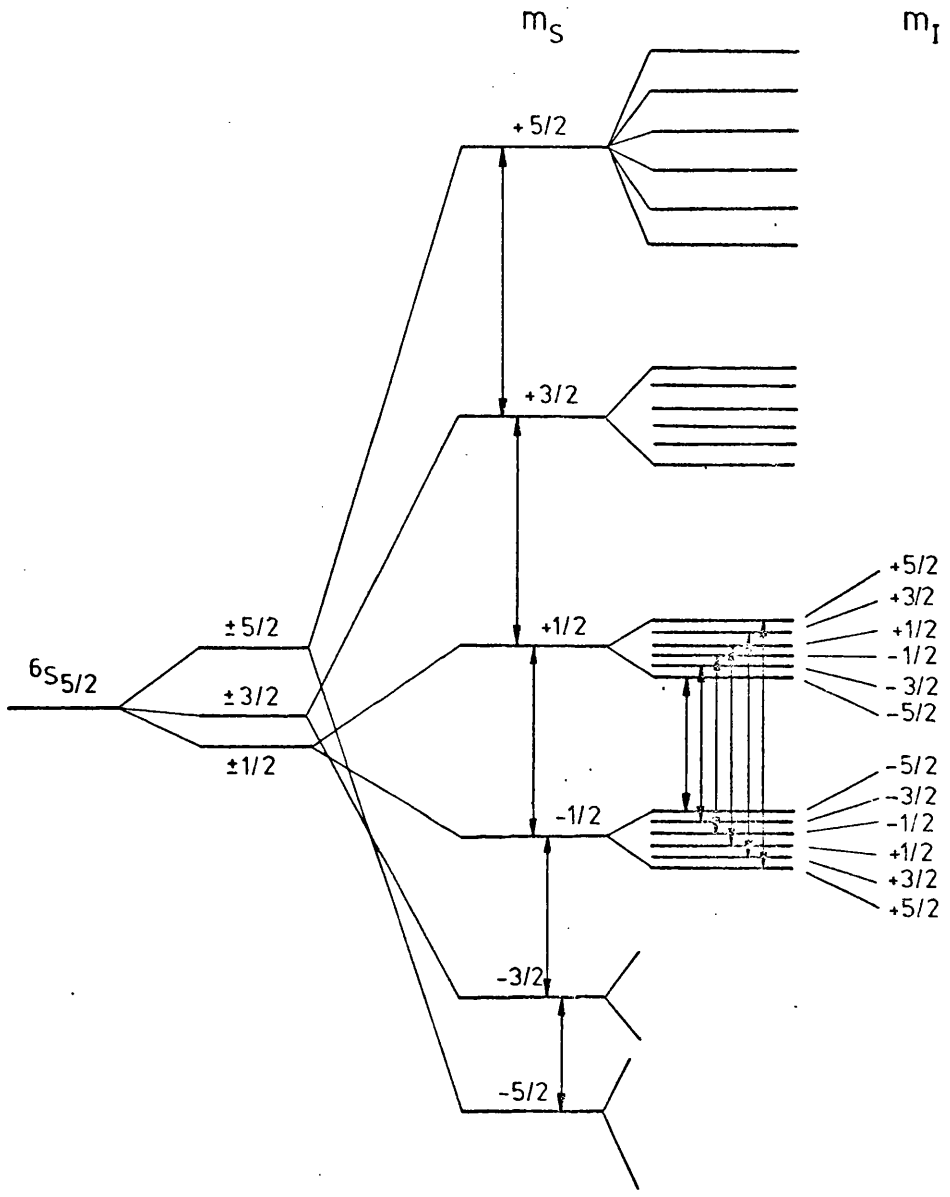

Fig. 3.20

Energy levels for the Mn^{2+} ion in an octahedral crystal field. The five $\Delta m_S = \pm 1$ transitions are shown, together with the nuclear hyperfine transitions $\Delta m_I = 0$ for the $+1/2 \leftrightarrow -1/2$ transition

either to exchange polarization,[206] or to an admixture to the $3s^2 3p^6 3d^5$ configuration of a small fraction of a configuration in which one 3s-electron has been promoted to a 4s-state.[207,208]

As shown in fig. 3.20, the overall degeneracy due to the electron spin S = 5/2 and the nuclear spin I = 5/2 produces a total of 36 energy levels. Application of the selection rules ($\Delta m_S = \pm 1$, $\Delta m_I = 0$) allows 30 transitions between the 36 energy levels, and the expression for the allowed energy differences is of the form[209]

$$\Delta E = g\beta H + aD(\cos^2\theta - \tfrac{1}{2}\sin^2\theta) + bA + \frac{cA^2}{g\beta H + dA} \qquad (3.3)$$

where a, b and c are parameters which can assume particular combinations of discrete values,[209] and θ is the angle between the z-axis of the crystal and the applied field. (The remaining letters have the same meaning as in section 2.4). The most interesting aspect of equation (3.3) is that for the six transitions $m_S = \frac{1}{2} \leftrightarrow m_S = -\frac{1}{2}$, a = 0. As a result the angular dependence vanishes for these transitions and the spectrum is essentially isotropic. This is an important requirement for an ESR spectrum to be observed in powdered samples with random orientations relative to the external magnetic field. The remaining 24 transitions are quite inhomogeneously

broadened due to the angular dependence of the D term and they cannot be recorded for powders.

b) The ESR spectrometer

Spectra were recorded with a Varian E-3 spectrometer using X-band (9.53 GHz) microwave radiation provided from a Klystron tube. The magnetic field was controlled by a Varian field dial unit connected to a Hall-effect magnetic sensor. A small 100 kHz modulating field provided the output signal from which resonance was observed as the absorption derivative.

All spectra were recorded at room temperature, with the samples contained in silica tubes ('Spectrosil') of 2 mm bore.

c) Experimental determination of g-values and line width

The g value for resonance was found by calibration against the free radical diphenyl-picryl-hydrazyl (DPPH). A capillary made from 'Spectrosil' silica was filled with a few grains of DPPH and sealed to the bottom of the ESR tube; thus, when the tube was positioned in the cavity, the resonance of the sample and DPPH were recorded simultaneously. From the known g value of DPPH,[210,211]

g_{ref} = 2.0036, the g value of the sample, g_{unk}, was calculated as follows:

$$h\nu = g\beta H$$

$$g_{ref} = \frac{h\nu}{\beta H_{ref}}$$

$$g_{unk} = \frac{h\nu}{\beta H_{unk}}$$

Let $h\nu$ = const.

then

$$g_{unk} = g_{ref} \frac{H_{ref}}{H_{unk}}$$

The line width was measured as the peak to peak difference of the resonance line in gauss.

d) ESR spectra of MnO-CaO solid solutions

Room temperature spectra of MnO-CaO solid solutions dilute in manganese are shown in figs. 3.21 to 3.29. Most spectra were recorded in vacuum. However, two samples were opened to the atmosphere after the vacuum spectrum had been recorded, and the spectrum taken again. As can be seen from figs. 3.21, 3.22, 3.24 and 3.25 (and Table 3.14), exposure to atmosphere causes a narrowing of the resonance lines. Similar narrowing was also observed in the vacuum spectrum of a sample fired at 1523 K (all other samples were fired at

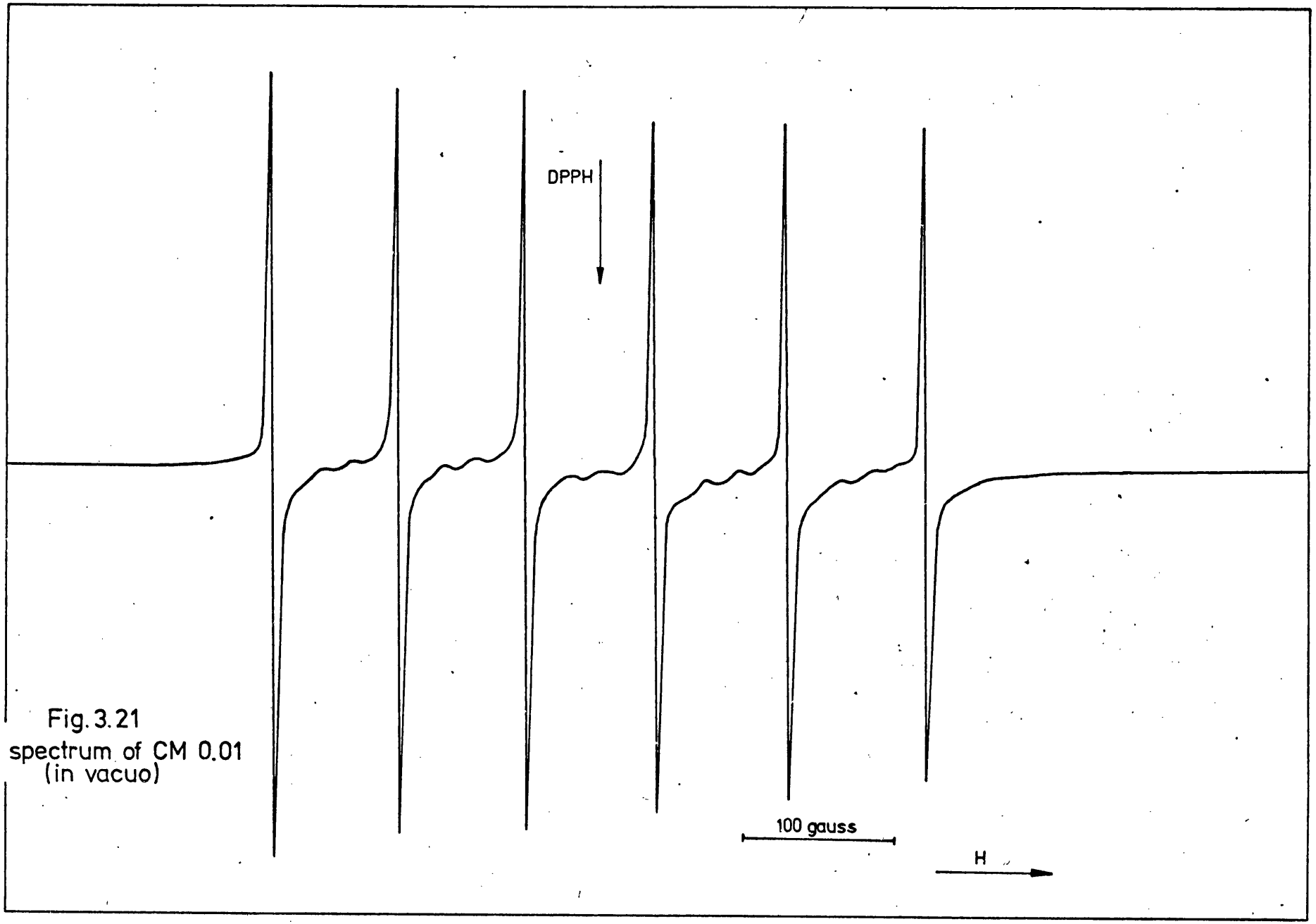

Fig. 3.21
ESR spectrum of CM 0.01
(in vacuo)

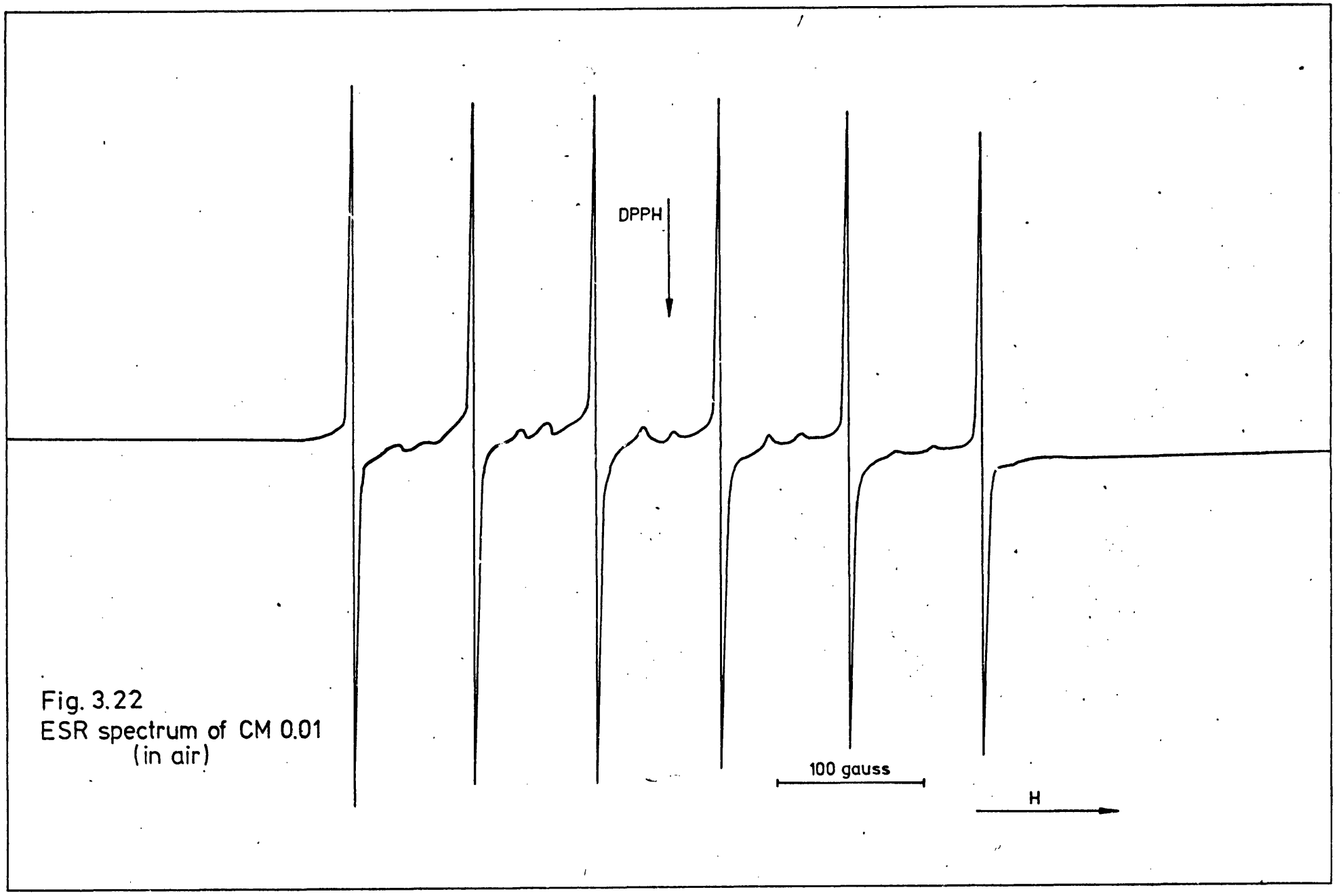

Fig. 3.22
ESR spectrum of CM 0.01
(in air)

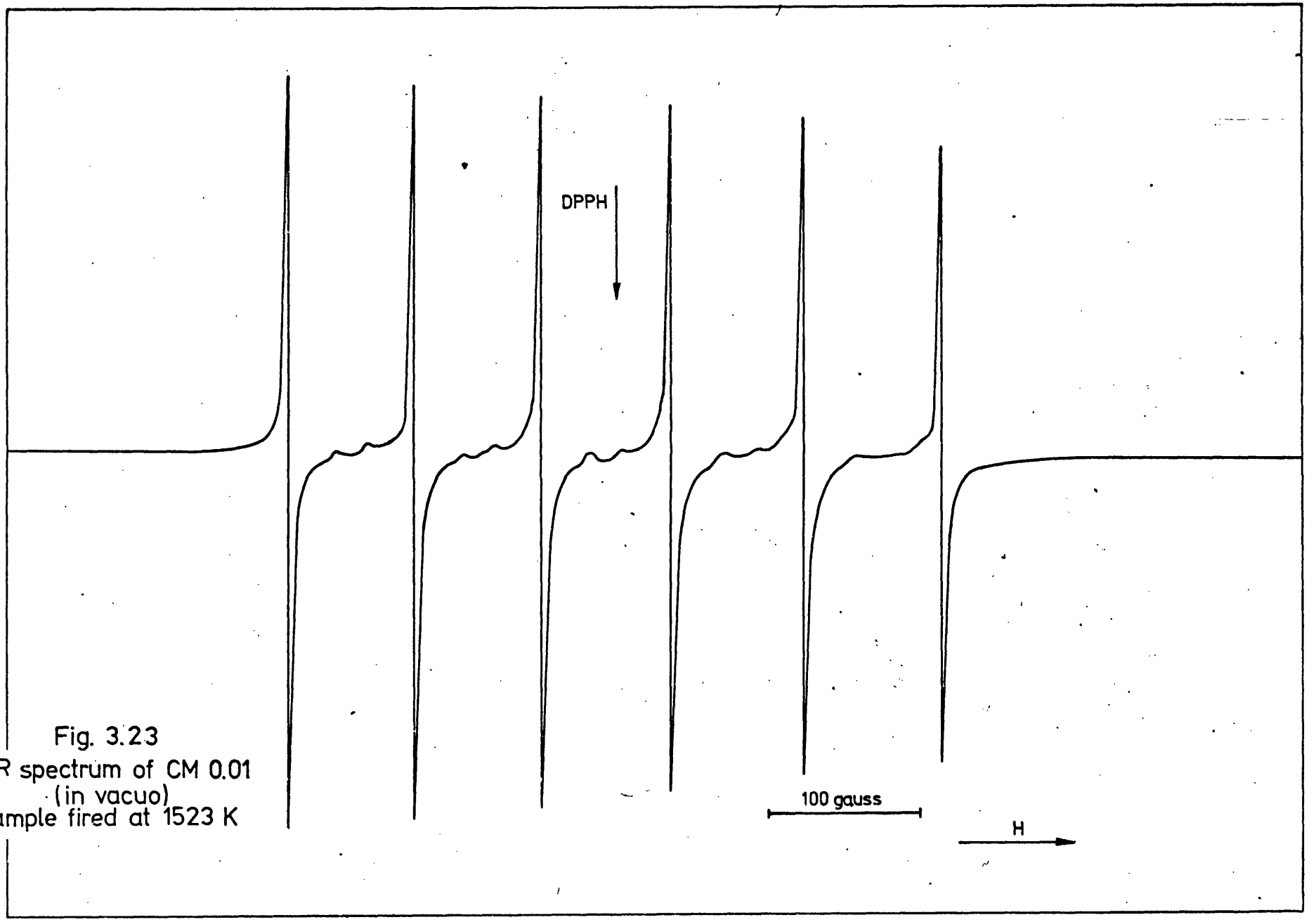

Fig. 3.23
ESR spectrum of CM 0.01
(in vacuo)
Sample fired at 1523 K

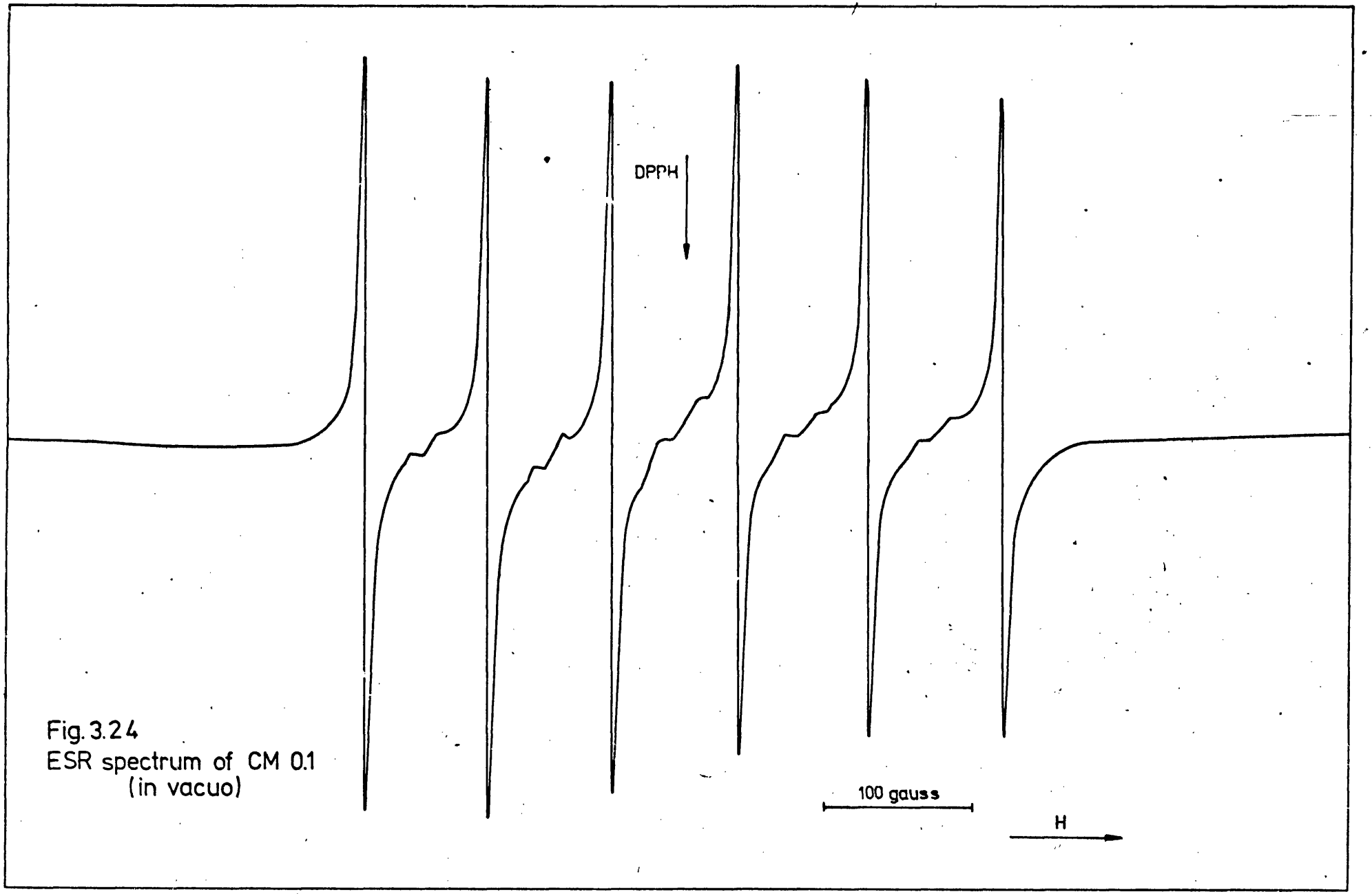

Fig. 3.2.4
ESR spectrum of CM 0.1
(in vacuo)

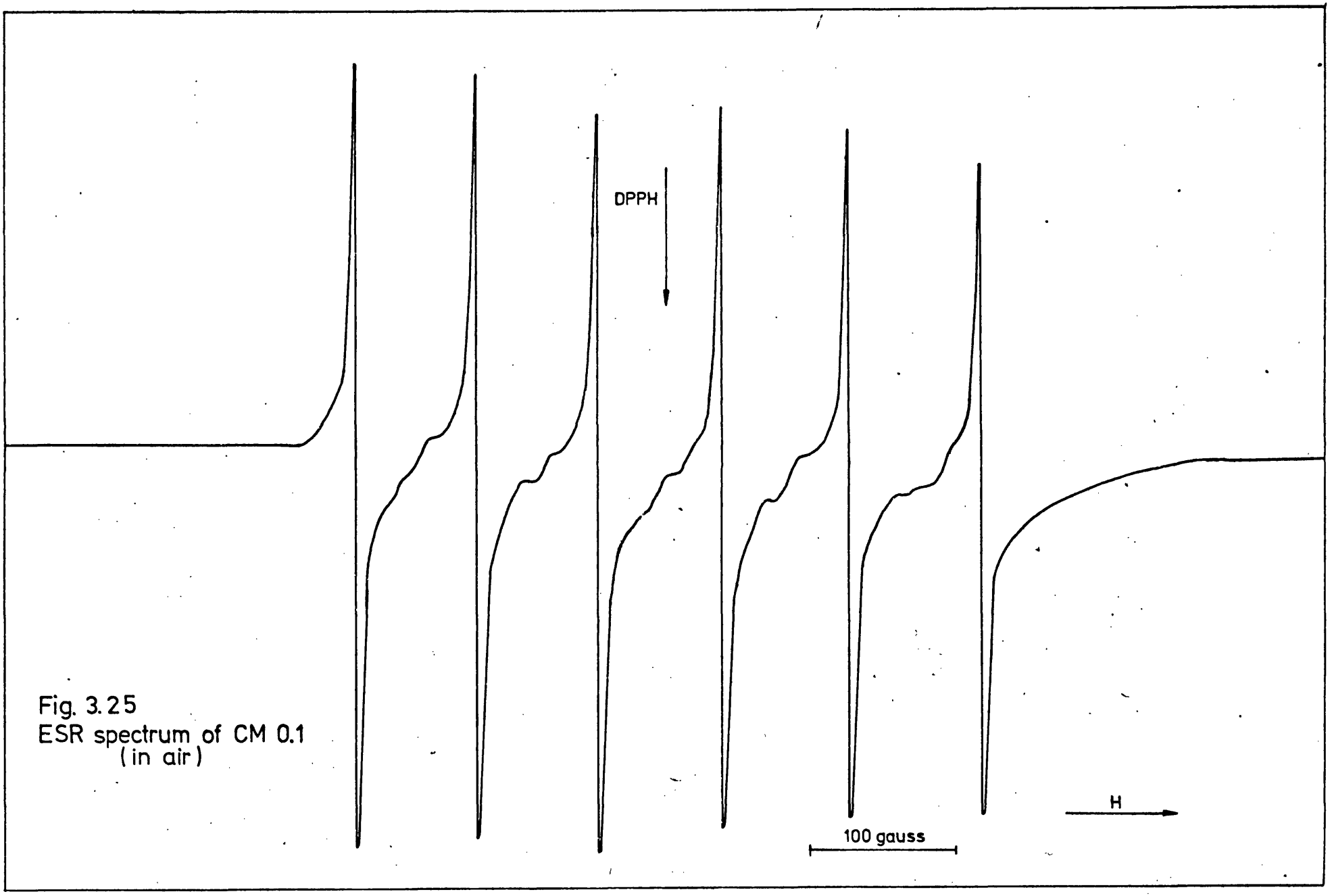

Fig. 3.25
ESR spectrum of CM 0.1
(in air)

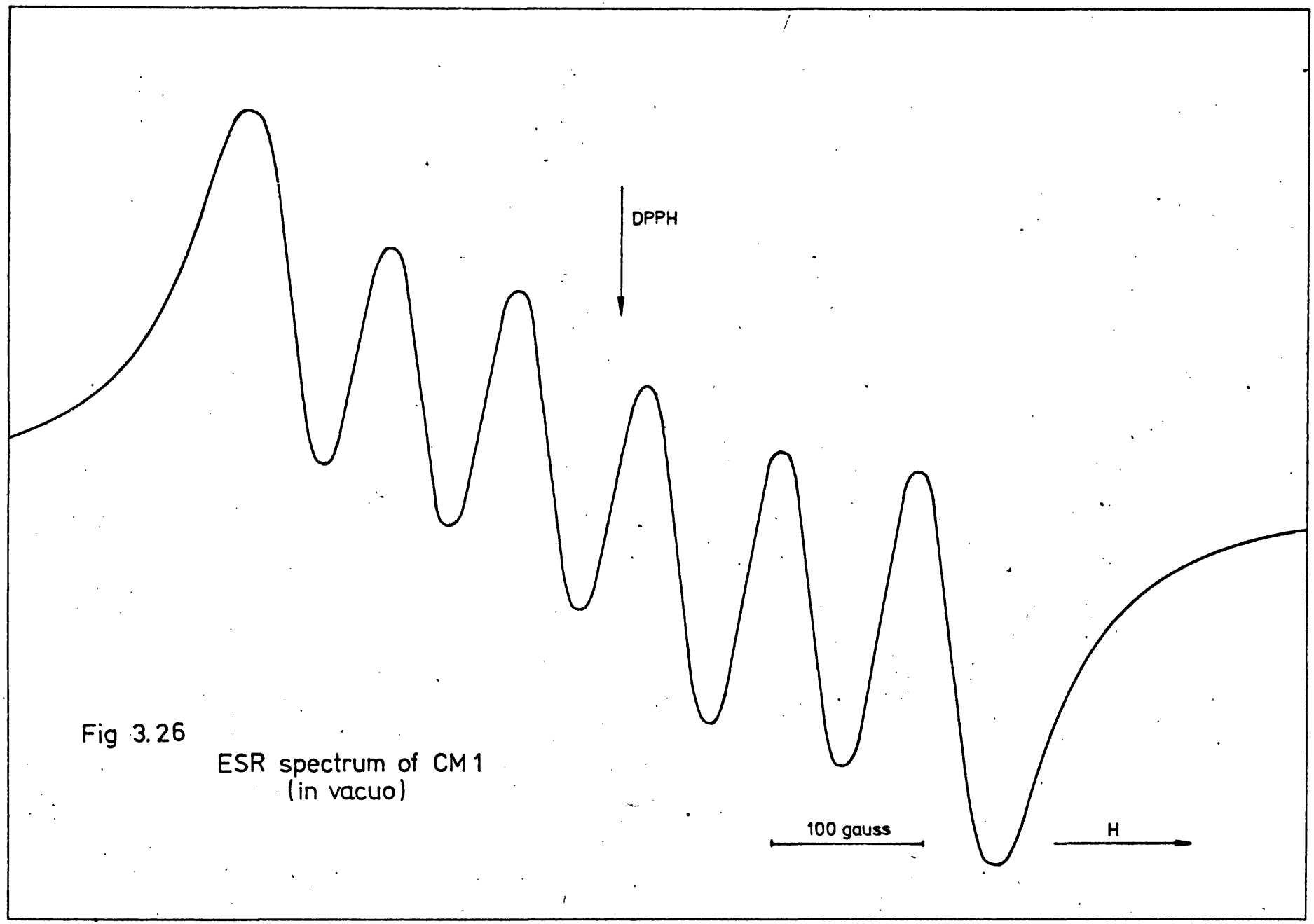

Fig 3.26

ESR spectrum of CM 1
(in vacuo)

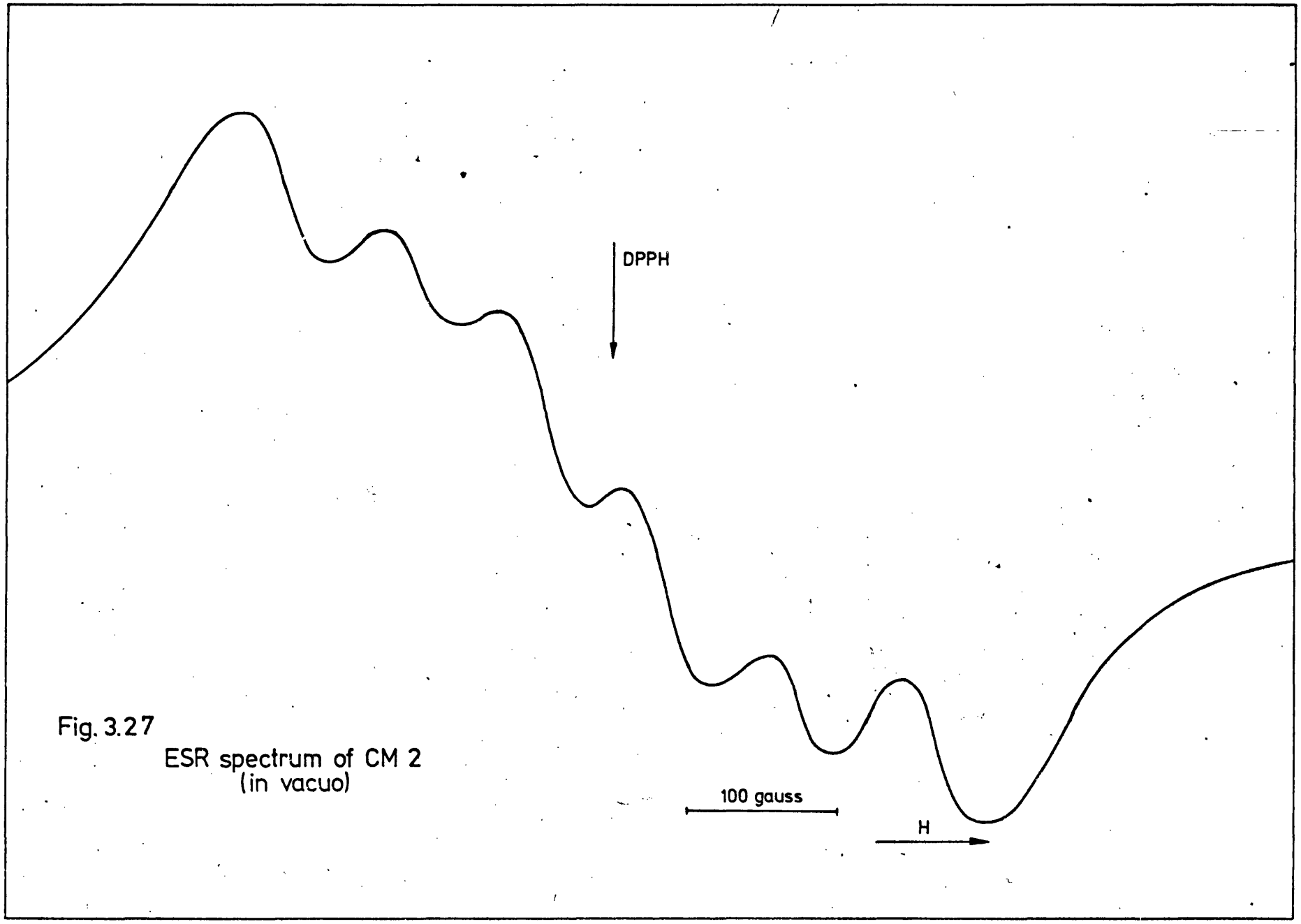

Fig. 3.27
ESR spectrum of CM 2
(in vacuo)

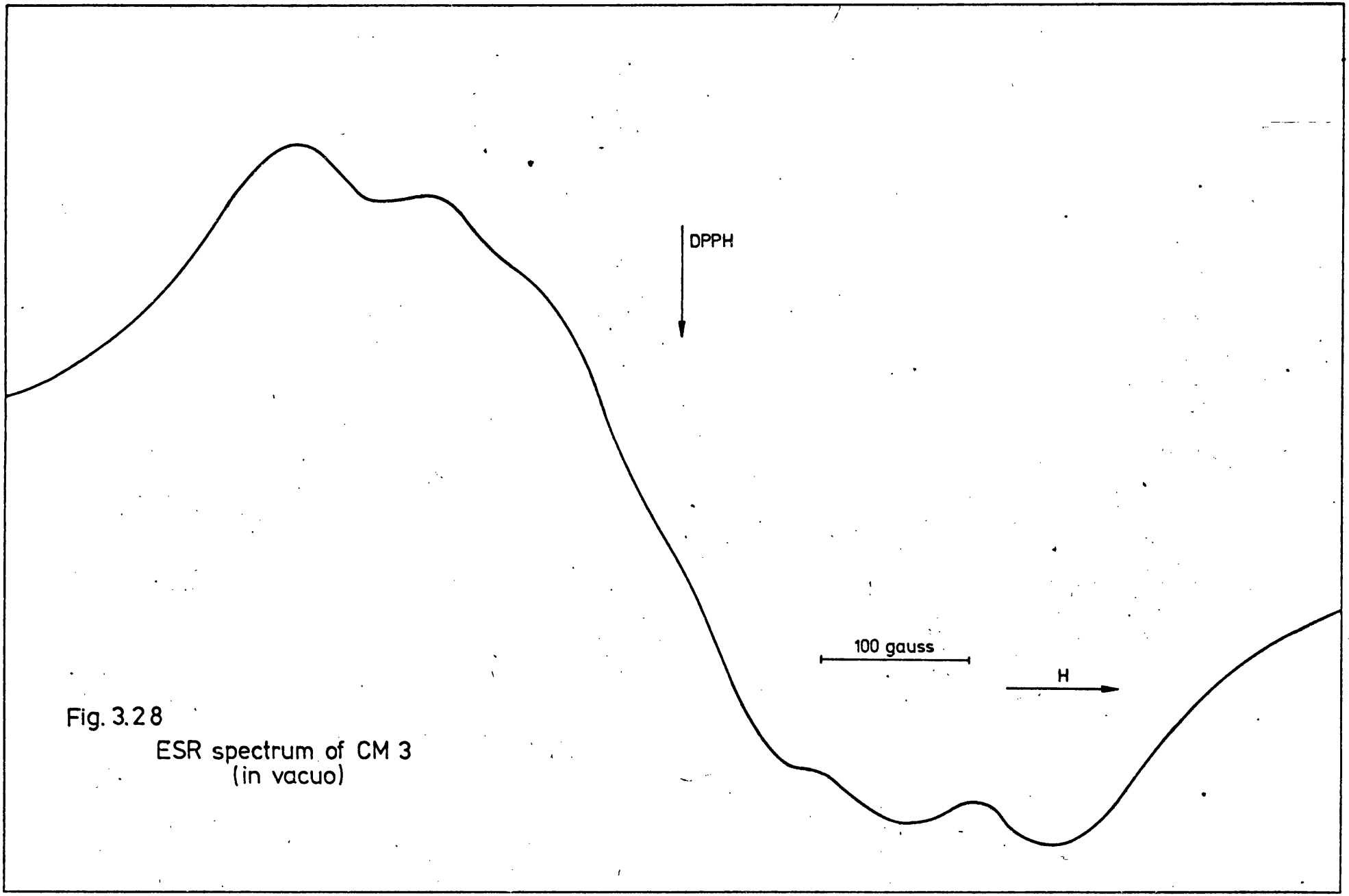

Fig. 3.28
ESR spectrum of CM 3
(in vacuo)

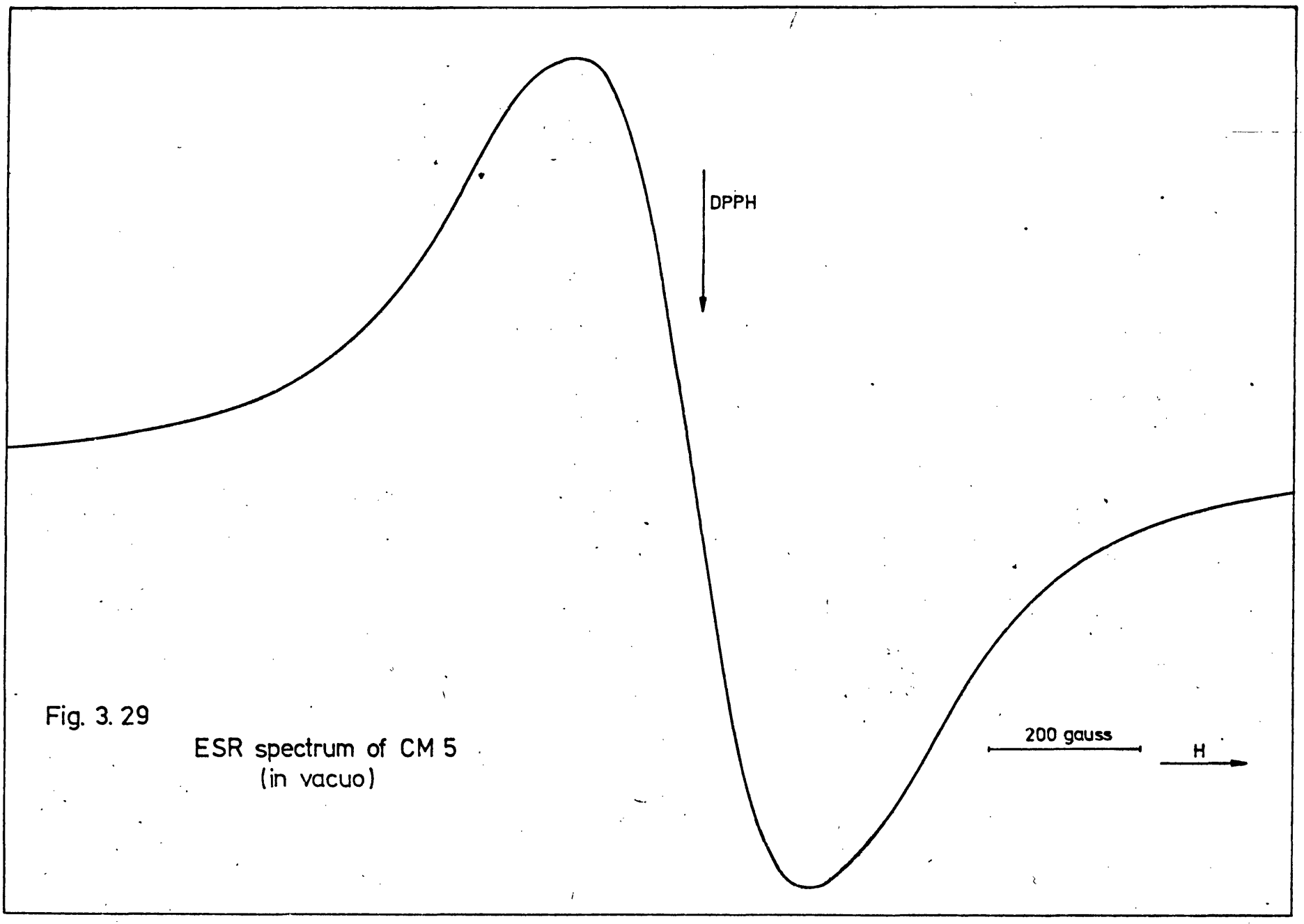

Fig. 3. 29

ESR spectrum of CM 5
(in vacuo)

1273 K). Comments on this effect will be given in section 4.2.3.

Table 3.14 shows the main parameters of the ESR spectrum for each sample. The g values were measured from the centre of symmetry of the two central lines of the spectrum. The hyperfine splitting constant, A, increases slightly with increasing magnetic field; values given in Table 3.14 correspond to the separation of the two central lines. Similarly, values of line width are an average of the peak to peak distance of these two lines.

Table 3.14

Main parameters of the ESR spectra of MnO-CaO solid solutions

Sample	g (±0.0005)	A (gauss)	Line width (gauss)
CM 0.01 (vac.)	2.0070	85	5
CM 0.01 (air)	2.0070	85	2.5
*CM 0.01 (vac.)	2.0070	85	0.5
CM 0.1 (vac.)	2.0068	85	5
CM 0.1 (air)	2.0067	85	2.5
CM 1 (vac.)	2.0067	85	42.5

(*) Sample fired at 1523 K, all other samples were fired at 1273 K.

e) ESR spectra of $MnO-CaO-Na_2O$ specimens

Room temperature ESR spectra of 0.1N 4 and 3N 1 samples (in air) are shown in figs. 3.30 and 3.31 respectively. The most remarkable feature of these spectra is the splitting of the hyperfine structure lines. A tentative explanation for this splitting will be given in section 4.2.5. The g value and hyperfine splitting constant (central lines) are g = 2.0067 and A = 85 gauss, for both samples. The ESR spectrum of $CaMn_2O_4$ is shown in fig. 3.32.

3.3 The System $CuIn_2O_4$-$CdIn_2O_4$

Specimens in this system were prepared by solid state reaction between the corresponding oxides. Three different series of samples were prepared, according to three different thermal treatments of the starting oxide mixture. These were (i) 1173 K in air, (ii) 1223 K in air and (iii) 1323 K in oxygen. Details will be given in the following sections.

3.3.1 Nomenclature

Samples in the system $CuIn_2O_4$-$CdIn_2O_4$ were designated CICu X, where X is the nominal content in copper expressed as the molar fraction. Specimens fired at 1173 K in air were termed CICu X(LT)

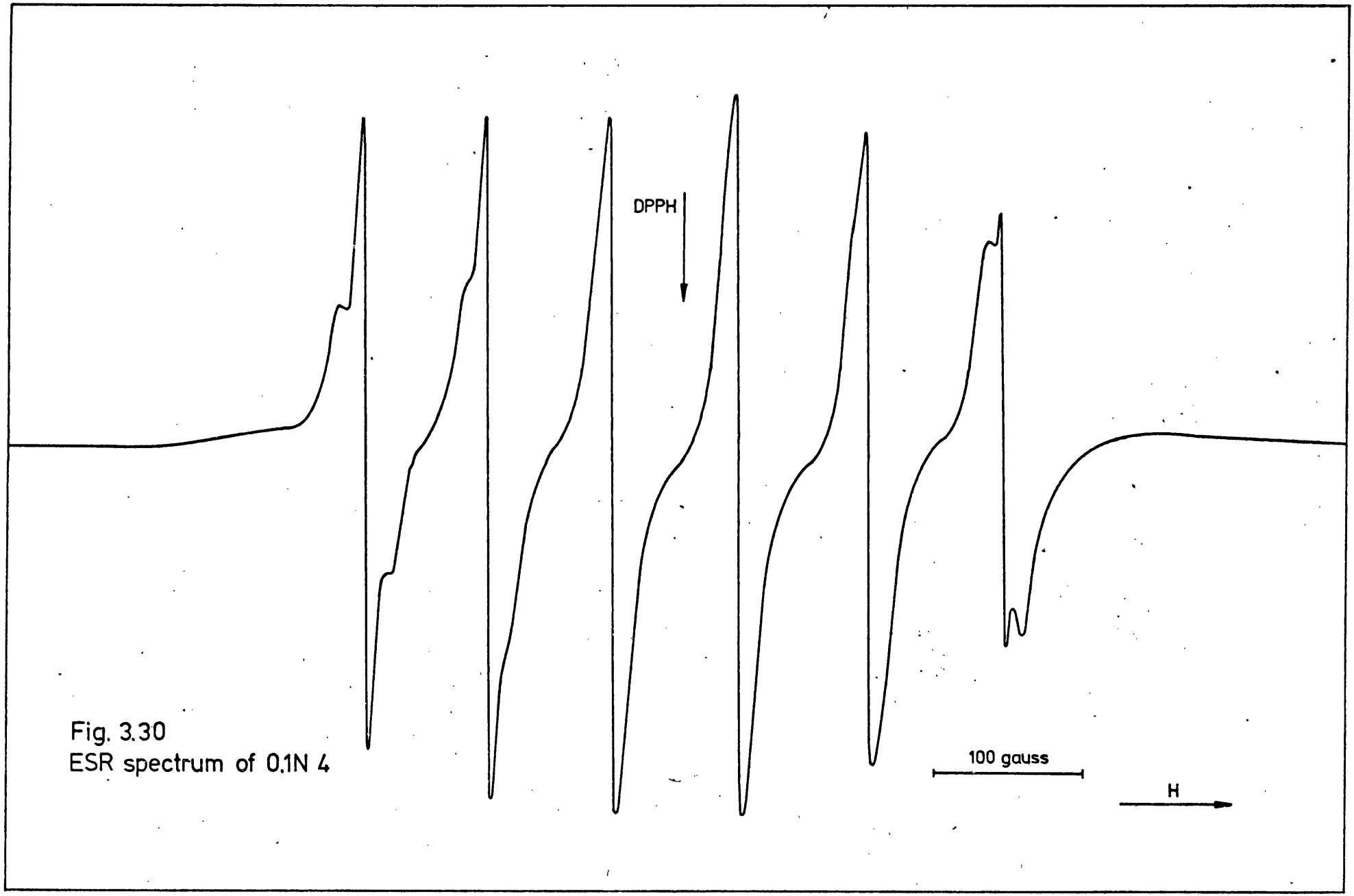

Fig. 3.30
ESR spectrum of 0.1N 4

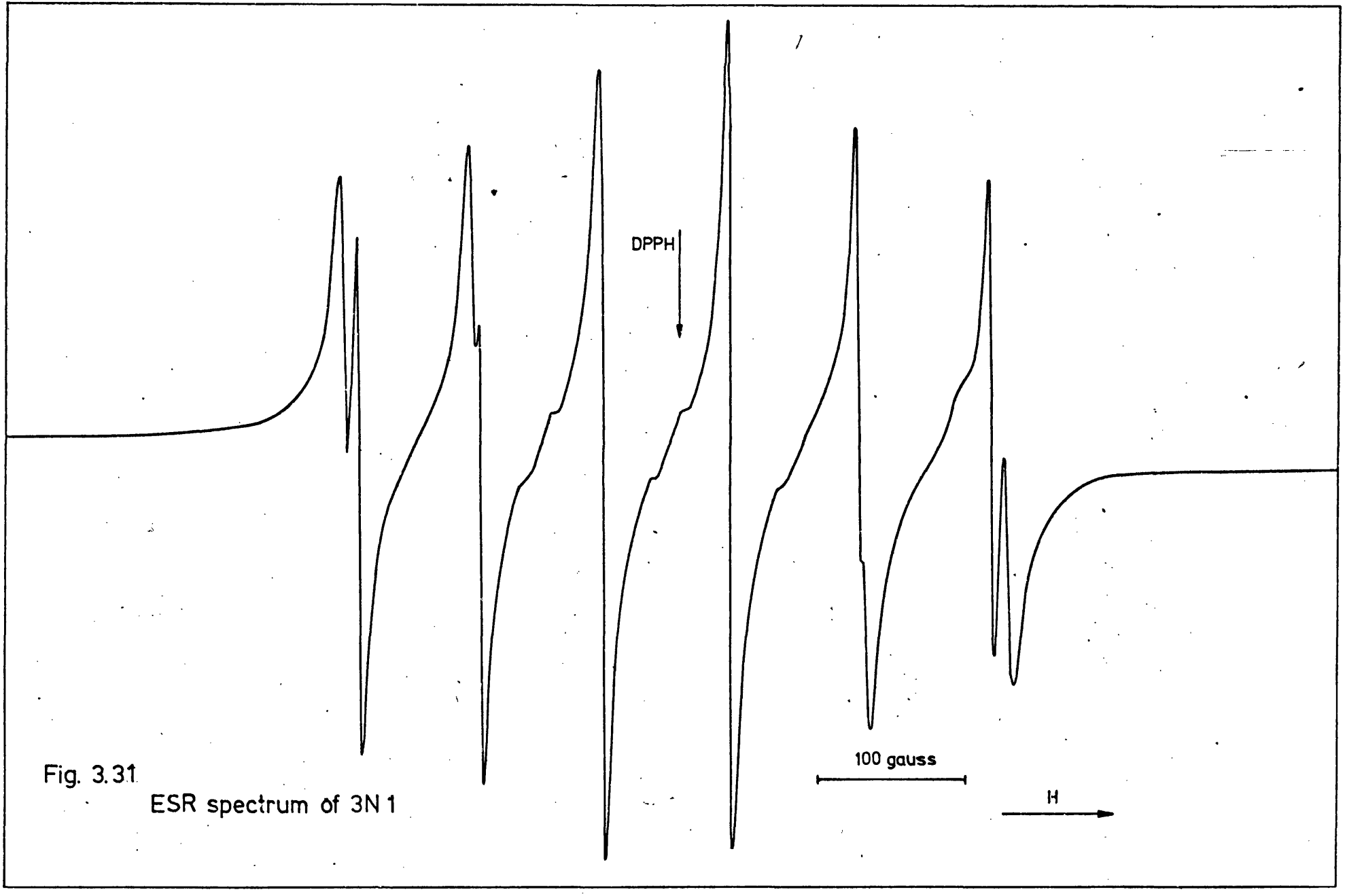

Fig. 3.31 ESR spectrum of 3N 1

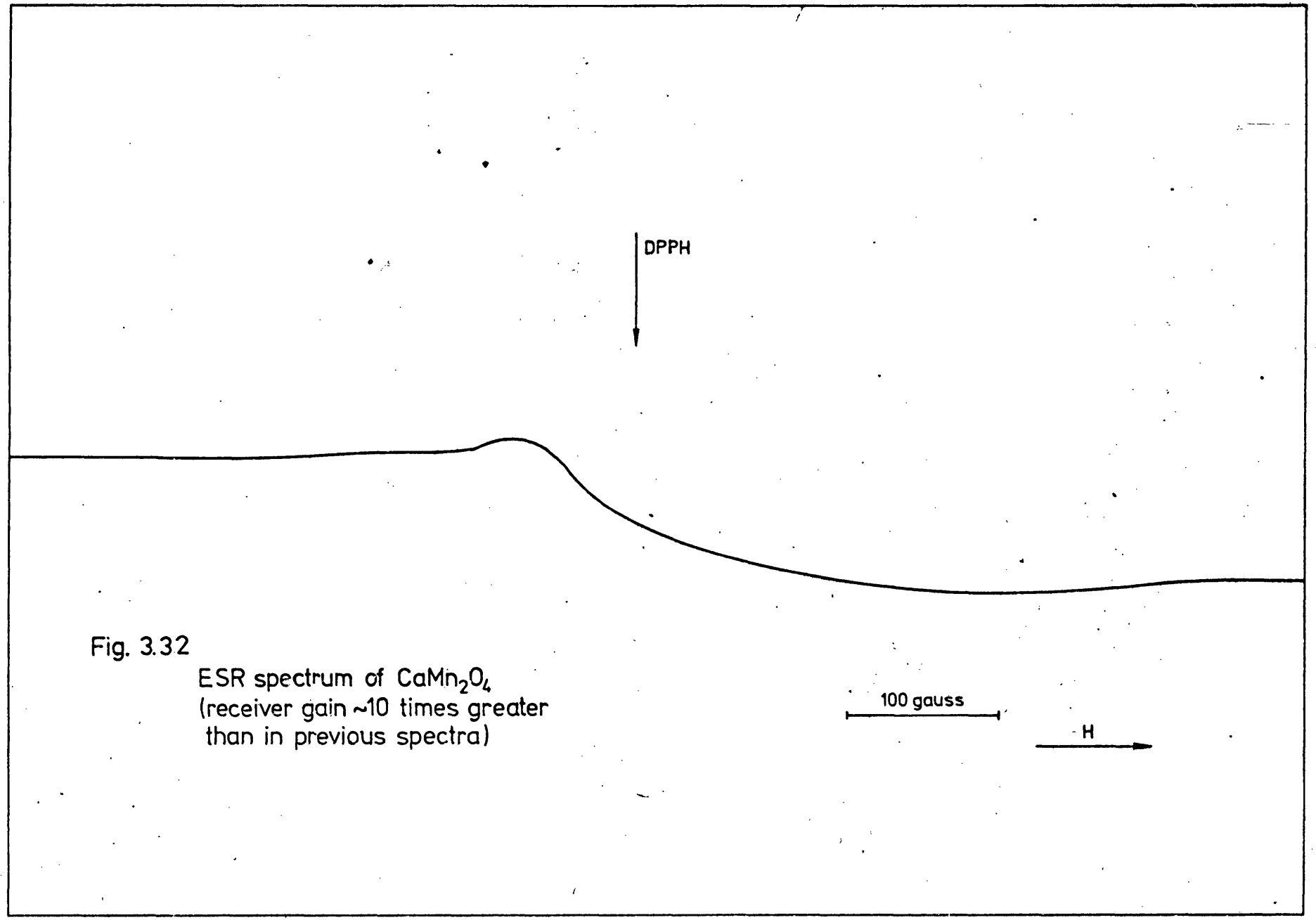

Fig. 3.32

ESR spectrum of $CaMn_2O_4$
(receiver gain ~10 times greater
than in previous spectra)

(LT = low temperature). Specimens fired at 1223 K in air were designated CICu X(MT) (MT = medium temperature. Specimens fired at 1323 K in oxygen were termed CICu X(HT) (HT = high temperature). Pure $CdIn_2O_4$ specimens prepared under the same conditions were termed CI (LT), CI (MT) and CI (HT) respectively.

3.3.2 Preparation of cadmium indate

Cadmium indate ($CdIn_2O_4$) was prepared by solid state reaction between CdO and In_2O_3. 'Specpure' cadmium oxide, with nominal content of impurities as listed in Table 3.15, was supplied by Johnson & Matthey; 99.999% pure indium oxide was supplied by Koch-Light. Equimolar amounts of CdO and In_2O_3 were intimately mixed in an agate mortar and the mixture was placed in a platinum boat and fired at 1173 K in a Gallenkamp electric furnace. The progress of the reaction was followed by taking the sample out of the furnace every five hours, grinding it and recording an X-ray diffractogram which was compared with a diffractogram of the starting oxide mixture.

Table 3.15

Material	Source	Stated impurities (ppm)	
Cadmium oxide	Johnson & Matthey	Aluminium	5
		Calcium	4
		Silicon	1
		Iron	<1
		Chromium	<1
		Copper	<1
		Magnesium	<1

After a total of 25 hours of heat treatment the cadmium oxide lines were no longer present in the diffractometer trace. However a vestige of the most intense line of indium oxide could still be observed, as shown in fig. 3.33. This residual line, which is symptomatic of the presence of a small excess of unreacted indium oxide, did not disappear after further firing of the sample for another 25 hours. Repeated attempts to prepare cadmium indate following the procedure described above have always led to the same results, i.e., the final product showed always an excess of indium oxide. This led to the assumption that small amounts of cadmium oxide were volatilized during the firing process, thus causing the final product to show a corresponding excess of indium oxide. Attempts to avoid losses of cadmium oxide by enclosing the sample in a sealed silica ampoule were not successful.

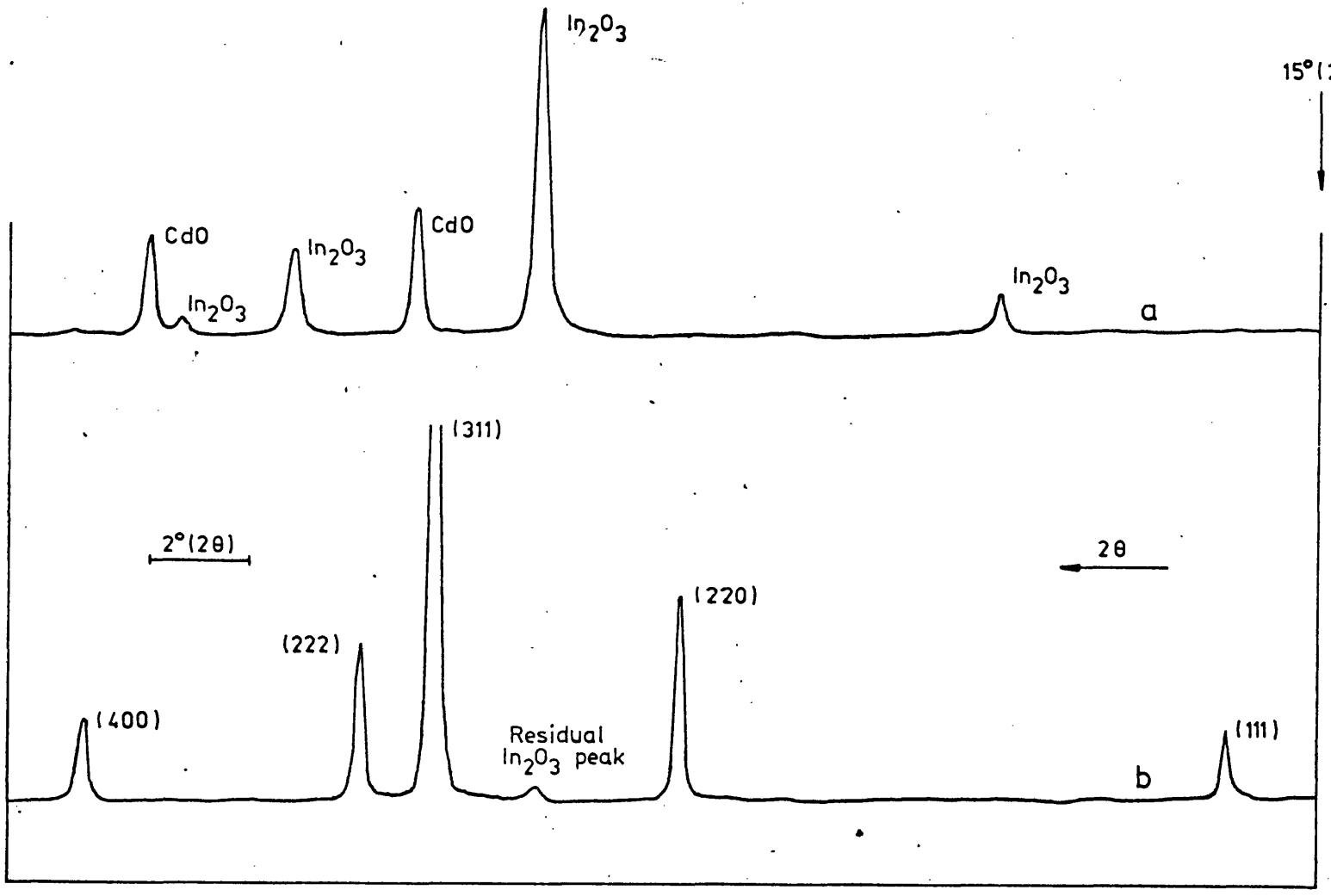

Fig. 3.33

Diffractograms (Cu K_α) of
a) CdO/In_2O_3 (starting oxide mixture), b) $CdIn_2O_4$

To avoid volatilization of cadmium oxide from the reaction mixture the following preparative method was devised:

A silica tube which fitted into the electric furnace was closed at one end and an indentation was made at 6 cm from this end; on this indentation rested the platinum boat which contained the reaction mixture (see fig. 3.34). Pure cadmium oxide was placed on the bottom of the tube and this was fitted into the furnace vertically so that, whilst the bottom of the tube (containing pure cadmium oxide) occupied the central part of the furnace, the boat containing the reaction mixture was closer to one end. Because of the temperature gradient along the furnace, this disposition provided a simple method by which the reacting mixture could be kept in an atmosphere saturated with cadmium oxide vapour. Fig. 3.35 shows a plot of the temperature gradient along the furnace, as measured with a platinum-platinum 13% rhodium thermocouple. It can be inferred from this plot that the temperature difference between the pure cadmium oxide and the reacting mixture was about 75 K.

Using this experimental arrangement, an equimolar mixture of CdO and In_2O_3 was heated at 1173 K and the progress of the reaction monitored

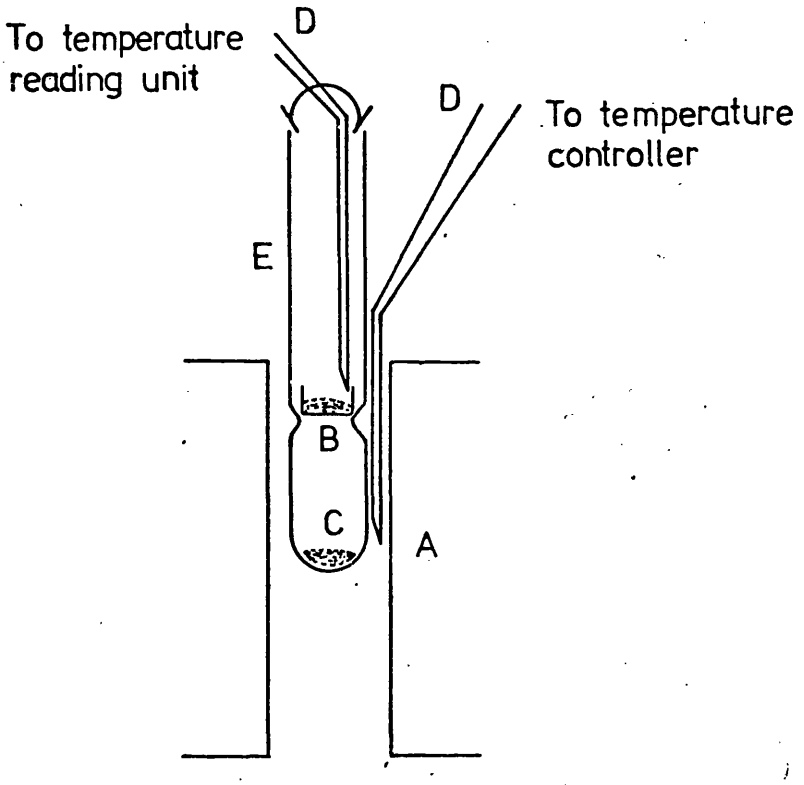

Fig. 3.34

Experimental setup for the preparation of $CdIn_2O_4$ and $Cu_xCd_{1-x}In_2O_4$ specimens in air
A) Electric furnace
B) Platinum boat with reacting mixture
C) Cadmium oxide powder
D) Thermocouples
E) Silica tube

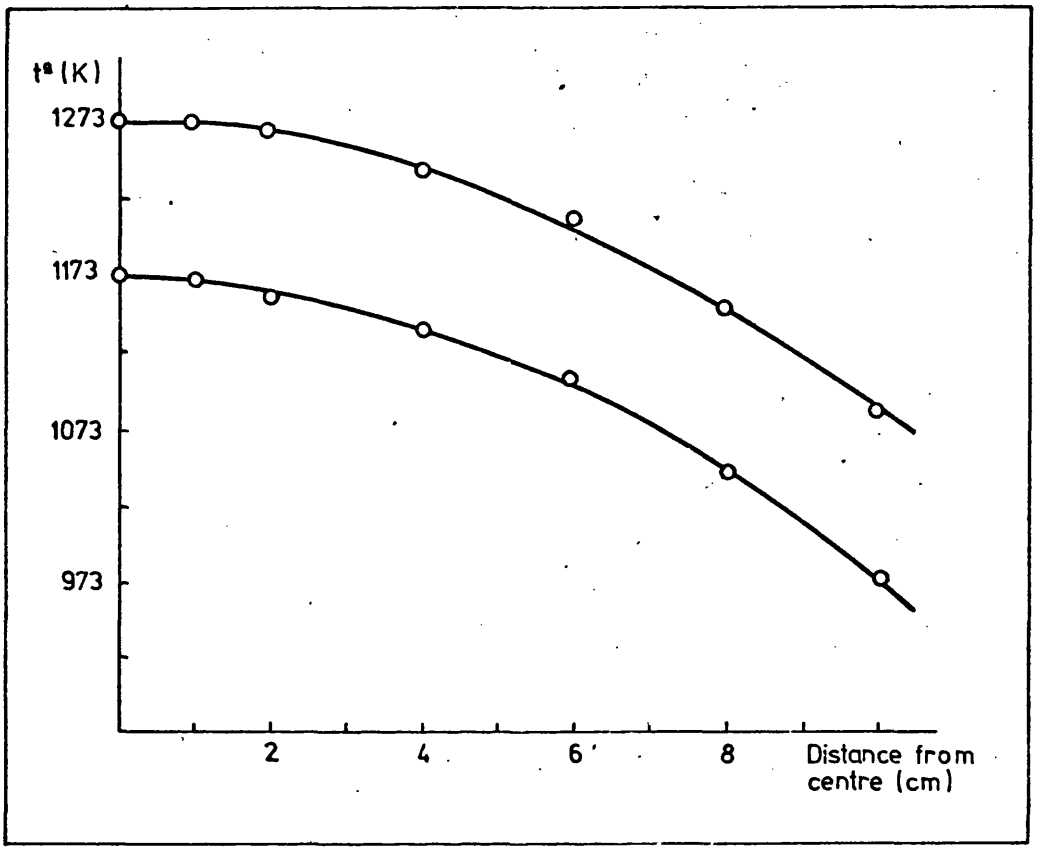

Fig. 3.35

Temperature gradient along the furnace tube

by X-ray diffraction in the same way as described before. After an overall heating time of 25 hours the reaction was found to be complete, and the diffractometer trace of the reaction product showed only lines corresponding to the new phase formed ($CdIn_2O_4$). This diffractometer trace is shown in fig. 3.36. During the reaction the temperature of the furnace was controlled with a Skil S9C/S125 temperature controller, and the temperature of the reacting oxides was monitored with a chromel-alumel thermocouple connected to a Cropico P6 reading potentiometer. The sample obtained showed a yellow colour and was termed CI (LT).

Using the same experimental arrangement as described above, three more samples of $CdIn_2O_4$ were prepared, at firing temperatures of 1073, 1223 and 1323 K and with firing times of 120, 15 and 6 hours respectively. The sample fired at 1223 K for 15 hours was termed CI (MT). All these samples showed the same yellow colour as CI (LT). To match the conditions used in the preparation of the high-temperature solid solutions one sample of $CdIn_2O_4$, termed CI (HT), was prepared in an atmosphere of oxygen at a firing temperature of 1323 K (6 hours). The atmosphere of oxygen was used to prevent decomposition of copper(II) oxide during the

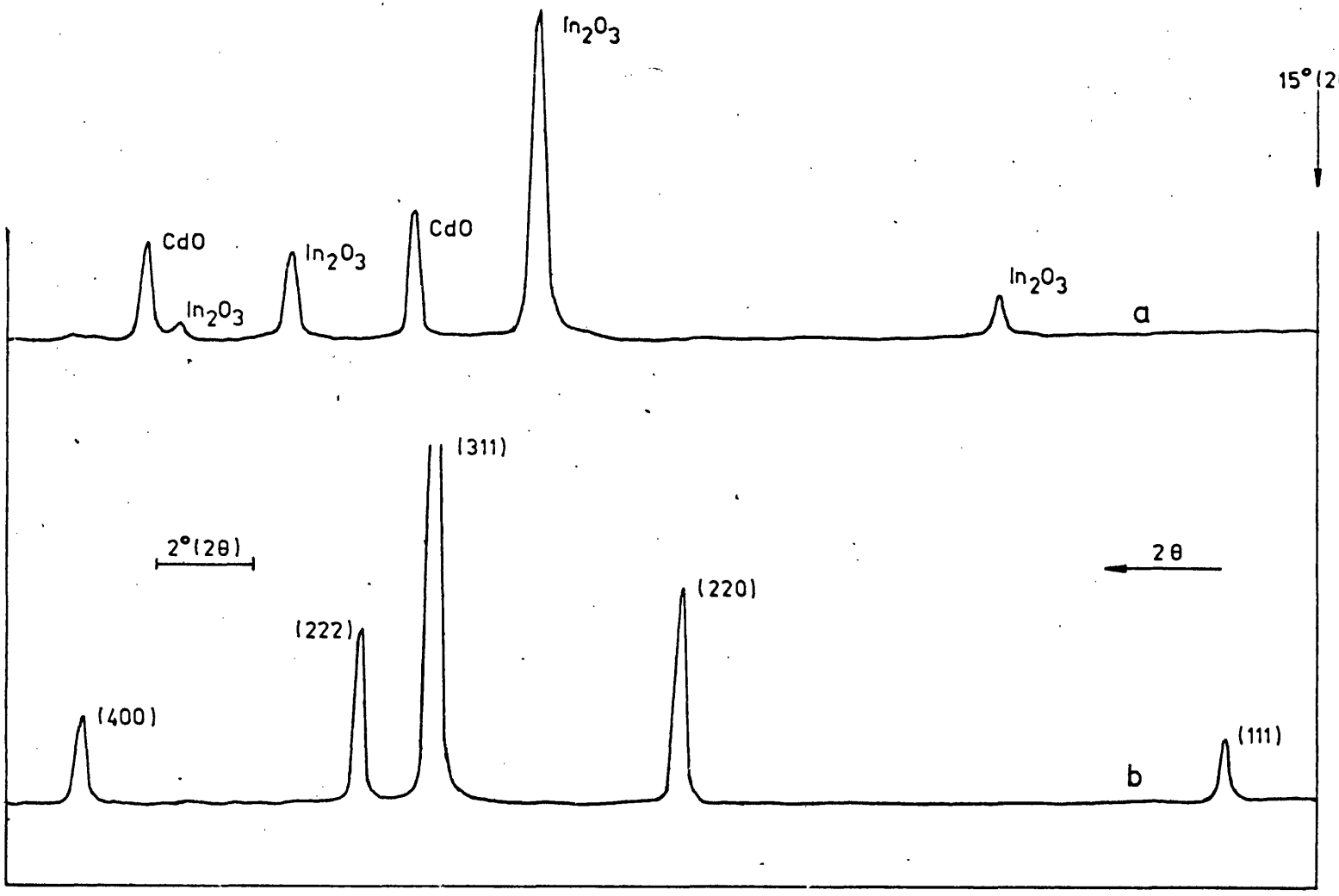

Fig 3.36

Diffractograms (Cu K_α) of
a) CdO/In_2O_3 (starting oxide mixture), b) $CdIn_2O_4$

formation of solid solutions (section 3.3.6). For this preparation the oxide mixture, contained in a platinum boat, was placed into an ampoule of silica which was sealed off whilst flowing oxygen inside it.(*) The ampoule (fig. 3.37) was designed so as to provide an end at which pure cadmium oxide could be placed and kept at a higher temperature than the reacting mixture. This higher temperature was achieved taking advantage of the temperature gradient inside the furnace as described before. A chromel-alumel thermocouple placed inside the ampoule allowed the temperature of the sample to be read out, whilst an external platinum-platinum 13% rhodium thermocouple was used to actuate a Skil temperature controller. At the end of the firing period (6 hours) the sample was quenched by immersion into a large container with ice-water. The ampoule was then carefully broken and the sample taken out. Cadmium indate prepared in this way showed a dark-yellow colour.

3.3.3 Chemical analysis

Samples CI (LT) and CI (HT) were analysed as follows:

A small known amount of sample was dissolved in 1:1 hydrochloric acid and the solution made up

(*) The author is grateful to Mr. M.R. Lock for preparing and sealing off the silica ampoules.

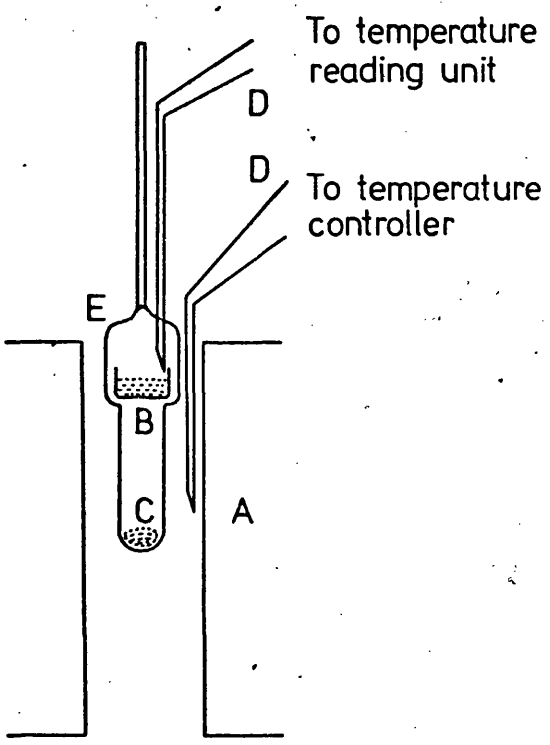

Fig. 3.37

Experimental setup for the preparation of $Cu_xCd_{1-x}In_2O_4$ specimens in oxygen
A) Electric furnace
B) Platinum boat with reacting mixture
C) Cadmium oxide powder
D) Thermocouples
E) Sealed ampoule with oxygen

to 250 ml with distilled water. 20 ml of this solution were titrated with 0.02M EDTA at pH 7 (ammonium acetate buffer) using 1-(2-pyridylazo)-2-naphthol (PAN) as indicator of the end point. In this way cadmium and indium are titrated together.[212,213] Another 20 ml of the solution were titrated in the same way after adding a large excess of potassium cyanide to mask cadmium, so only indium is titrated.[214] The results of the analysis are shown in Table 3.16.

Table 3.16

Chemical analysis of $CdIn_2O_4$

Sample	Cd $g \cdot mol^{-1}$		In $g \cdot mol^{-1}$		In/Cd	
	Found	Theoret.	Found	Theoret.	Found	Theoret.
CI (LT)	114.88	112.40	233.66	229.64	2.034	2.043
CI (HT)	113.21	112.40	231.27	229.64	2.043	2.043

3.3.4 Crystal structure and lattice parameter of $CdIn_2O_4$

Cadmium indate samples prepared as described before were examined by X-ray diffraction using the Debye-Scherrer technique. Samples were placed in Lindemann capillary tubes of 0.3 mm diameter and carefully centred in a 114.6 mm camera. Nickel

filtered CuKα radiation was used in all cases, and the temperature was measured with a maximum and minimum thermometer; variations in temperature during the exposure were never larger than ± 1 K.

All lines appearing in the diffraction pattern could be indexed in the cubic system, and the systematic absences were consistent with the space group Fd3m, i.e., the observed lines met the conditions:

hkl: h + k, k +1, 1 + h = 2n

hhl: 1 + h = 2n

Okl: (k, 1 = 2n); k + 1 = 4n

Table 3.17 lists d-spacings, indexing, and relative intensities for $CdIn_2O_4$ prepared at 1073 K in air. The data of Skribljak et al[123] are also given for comparison.

Lattice parameters were computed from the α_1 component (λ = 1.54051 Å) of the high angle reflections ($55^o < \theta < 85^o$). The Nelson-Riley extrapolation was used to derive the value of a_o corresponding to a diffraction angle of $\theta = 90^o$. A typical example of a Nelson-Riley plot for $CdIn_2O_4$ is shown in fig. 3.38. All the calculated lattice parameters were normalized to 294 K using the value of $7.3 \cdot 10^{-5}$ Å per degree for the thermal expansion coefficient (Section 3.3.5). The results are shown in Table 3.18. The probable accuracy was estimated at ± 0.0001 Å.

Table 3.17
Crystallographic data for $CdIn_2O_4$

d(Å) Present work (Cu Kα)	d(Å) Skribljak et al. (Mo Kα)	hkl	I/I_o Present work	I/I_o Skribljak et al.
-	5.31	111	-	14
3.215	3.23	220	30	40
2.745	2.757	311	100	100
2.630	2.620	222	25	30
2.280	2.287	400	20	25
-	1.973	331	-	4
1.864	1.863	422	20	25
1.759	1.755	511	60	50
1.616	1.609	440	70	50
1.547	1.536	531	10	4
1.448	1.438	620	15	6
1.394	1.381	533	40	45
1.379		622	40	
-	1.318	444	-	10
-	1.275	711	-	6
1.223	1.216	642	30	12
-	1.186	731	-	45
-	1.136	800	-	16
-	1.071	822	-	6
1.0575	1.050	751	40	35
1.0506	-	662	15	-
-	1.024	840	-	6
0.9604	0.953	931	15	18
0.9350	0.931	844	20	20
0.8985	-	1020	15	-
0.8857	-	951	40	-
0.8817	-	1022	20	-
0.8366	-	1042	15	-
0.8263	-	1111	30	-
0.8100	-	880	30	-
0.7858	-	1060	20	-
0.7774	-	1133	50	-
0.7746	-	1062	40	-

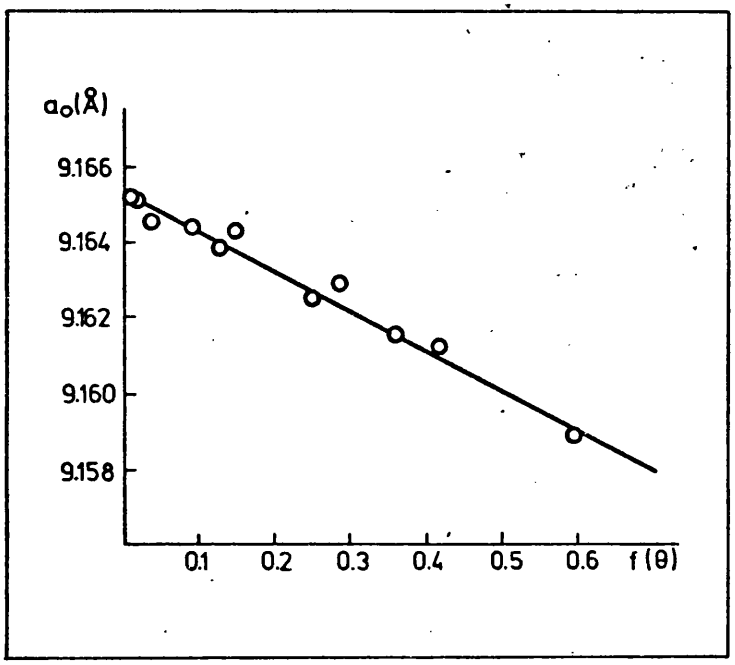

Fig. 3.38
Nelson-Riley plot for $CdIn_2O_4$

From the values of a_o presented in Table 3.18 it can be observed that a_o for cadmium indate prepared in oxygen is considerably smaller than the corresponding values for samples prepared in air. Comments on this discrepancy will be delayed until section 4.3.2.

Table 3.18

Lattice parameter, a_o, for $CdIn_2O_4$

Sample	Conditions of preparation	a_o (Å)
$CdIn_2O_4$	1073 K (air)	9.1653
$CdIn_2O_4$	1173 K (air)	9.1652
$CdIn_2O_4$	1223 K (air)	9.1653
$CdIn_2O_4$	1323 K (air)	9.1653
$CdIn_2O_4$	1323 K (oxygen)	9.1635

A mechanical mixture of CdO and In_2O_3 in the molar ratio 0.8:1 was heated at 1223 K in air for 25 hours. The resulting sample showed both the $CdIn_2O_4$ and the In_2O_3 phases. However, the lattice parameter of the $CdIn_2O_4$ phase proved to be a_o = 9.1653 Å. Similarly, heat treatment of a mixture of CdO and In_2O_3 in the molar ratio 1:0.8 led to a sample with $CdIn_2O_4$ and CdO in excess. Again the lattice parameter of the $CdIn_2O_4$ phase was 9.1653 Å. These experiments show that there is no appreciable solubility of either CdO or In_2O_3 in cadmium indate.

3.3.5 Thermal expansion of $CdIn_2O_4$

The thermal expansion coefficient of cadmium indate was measured by X-ray diffraction using a 190 mm high temperature Unicam S 150 camera, which was calibrated using α-Al_2O_3 as standard. A small amount of CI (MT) was placed inside a 0.5 mm diameter silica tube which was sealed off and carefully centred in the camera. Diffraction films were taken at different temperatures from room temperature up to 1390 K, using nickel filtered CuKα radiation. Lattice parameters were then computed from the α_1 component of the high angle reflections. Table 3.19 shows a_o values at different temperatures, and fig. 3.39, shows a plot of a_o versus temperature. From this plot the thermal expansion coefficient value of $7.3 \cdot 10^{-5}$ Å per degree was obtained. There are no data in the literature on the thermal expansion of $CdIn_2O_4$.

Table 3.19
Thermal expansion of $CdIn_2O_4$

Temperature (K) (± 5)	a_o (Å) (± 0.004)
294.5	9.165
519	9.184
678	9.195
1084	9.222
1245	9.235
1390	9.247(*)

(*) Due to severe line broadening arising from thermal scattering this value is probably not accurate to more than 0.01 Å.

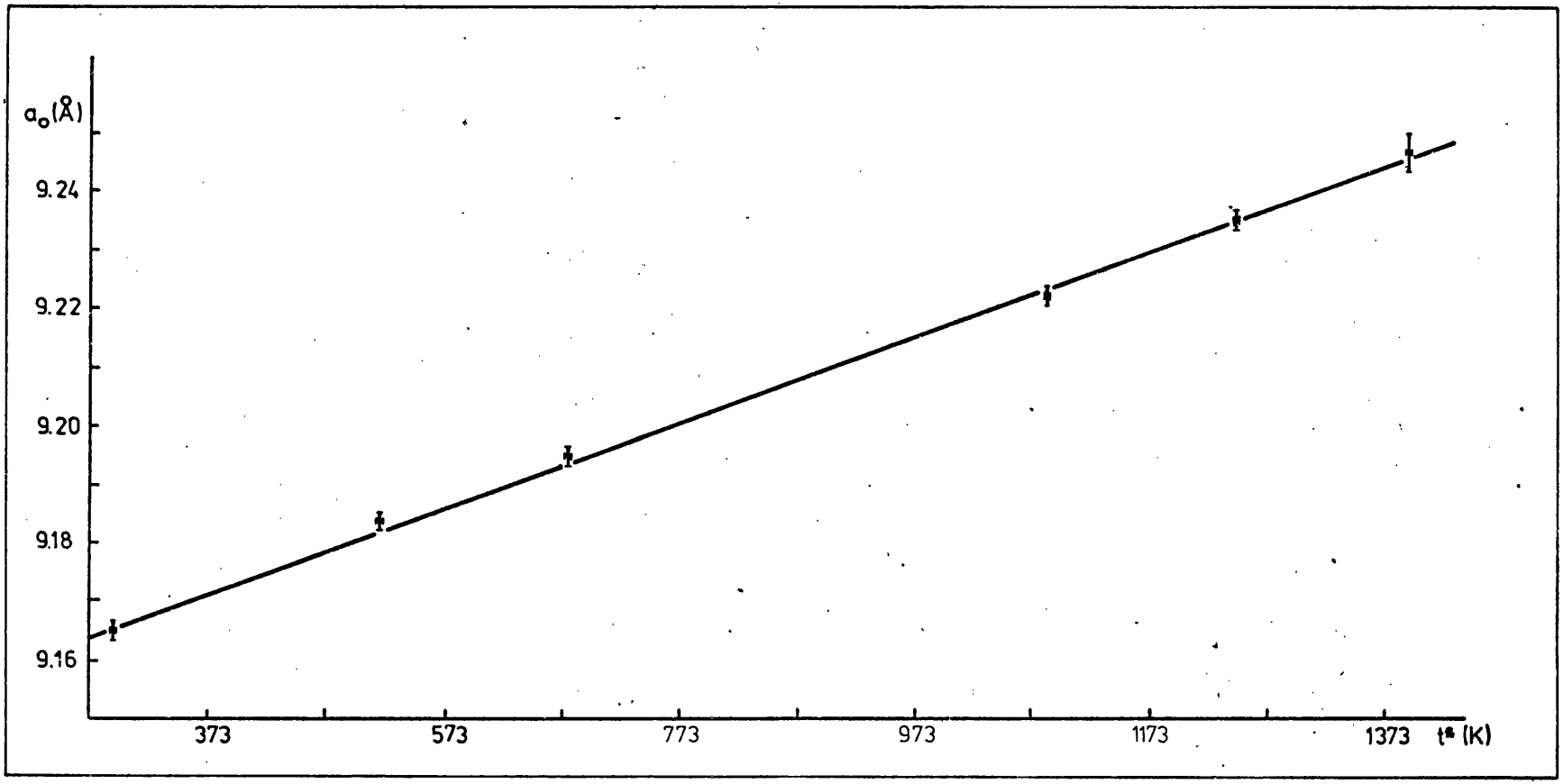

Fig. 3. 39

Thermal expansion of $CdIn_2O_4$

3.3.6 Preparation of solid solutions

Solid solutions $Cu_xCd_{1-x}In_2O_4$ were prepared starting from mechanical mixtures of CuO, CdO and In_2O_3 in the desired molar ratio. CdO and In_2O_3 were supplied by Johnson & Matthey and Koch-Light respectively; their purity was as stated in section 3.3.2; CuO was also supplied by Johnson & Matthey and the nominal purity was as indicated in Table 3.20. In all cases the oxides were thoroughly mixed in an agate mortar and the resulting mixture placed in a platinum boat for thermal treatment. Firing conditions and experimental setup were as indicated in section 3.3.2 for the preparation of cadmium indate. However, due to the technical difficulties involved in sealing the thermocouple leads through the walls of the silica ampoule, the internal thermocouple shown in fig. 3.37 was not used in the preparation of the high temperature solid solutions. The temperature of the reacting mixture was assumed to be the same as the temperature read by the external thermocouple. A calibration run with both thermocouples in place showed that this assumption does not involve an error greater than ± 10 K.

Table 3.20

Material	Source	Stated impurities (ppm)	
Cupric oxide	Johnson & Matthey	Silicon	3
		Iron	2
		Calcium	1
		Silver	1
		Magnesium	<1
		Manganese	<1
		Sodium	<1

Three different series of solid solutions were prepared at firing temperatures of 1173, 1223 and 1323 K; they were termed LT, MT and HT samples respectively (Section 3.3.1). The heating times were 25, 15 and 6 hours respectively (these heating times had been found previously to give complete reaction). In all cases the sample was taken out at the middle of the heating period, reground and taken back to the furnace. At the end of the heating process the samples were quenched in ice-water, as described in section 3.3.2 for HT cadmium indate.

Since CuO is known to become unstable towards Cu_2O when heated in air at about 1273-1323 K,[215] a test was carried out to check that CuO decomposition did not occur during heating of the samples at 1223 K. Pure cupric oxide was heated in air at 1223 K for 20 hours, and an X-ray diffractogram was recorded. Fig. 3.40 shows the diffractometer trace along with a trace from pure Cu_2O (BDH Chemicals). It can be seen that no decomposition of CuO is apparent.

Fig 3.40
Diffractograms (Cu K_α) of
a) CuO after 20 h. at 1223 K in air
b) Cu_2O

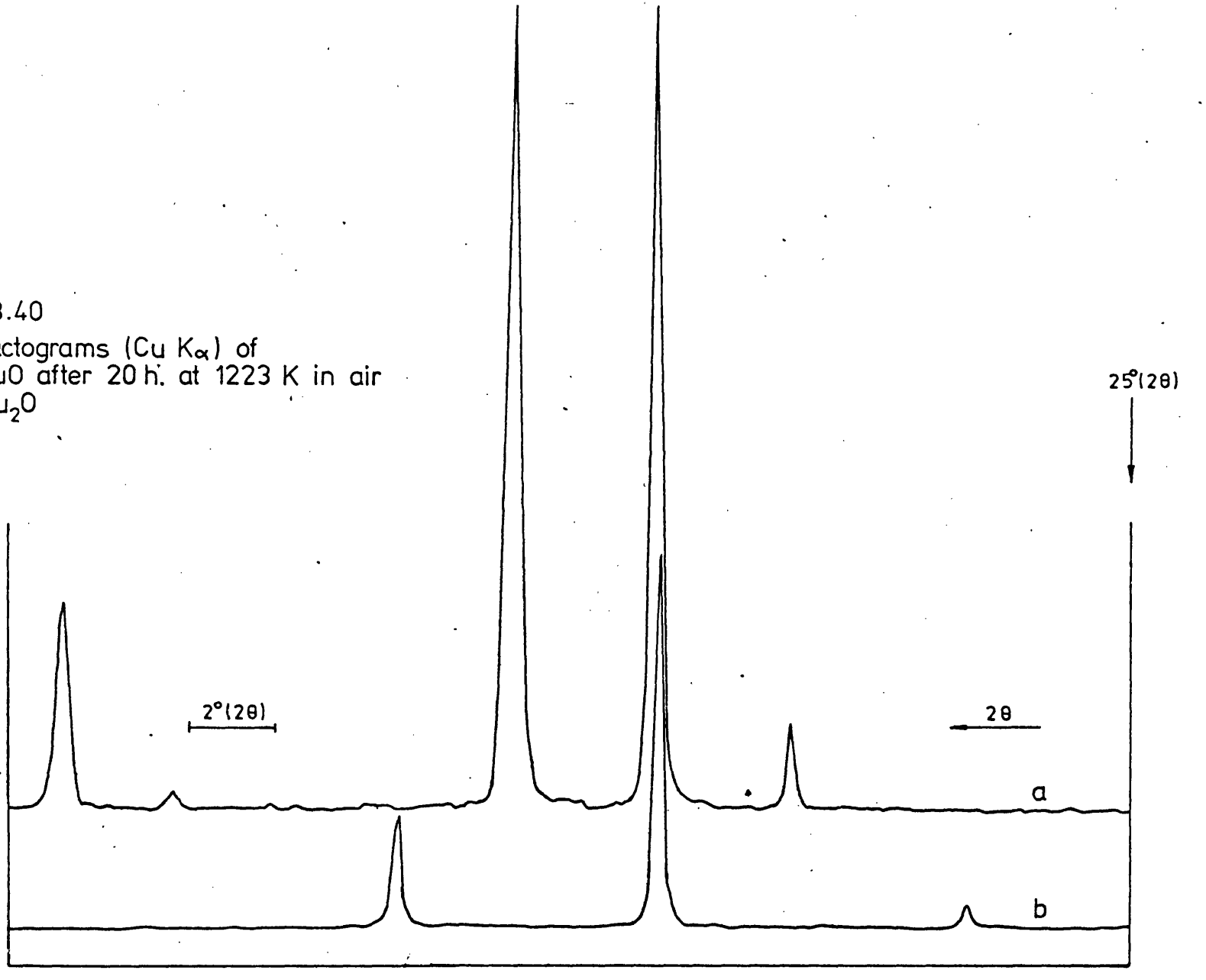

Samples prepared in 1323 K were heated in an ampoule sealed off in oxygen (Section 3.3.2). The pressure of oxygen created by the rise in temperature was estimated to be of the order of 3 atm. No decomposition of CuO is likely to occur under these conditions of temperature and oxygen pressure.[215]

3.3.7 Chemical analysis

After heat treatment, the copper content of all samples was analysed by atomic absorption. Suitable known amounts of each sample were dissolved in a minimum volume of conc. hydrochloric acid and the resulting solution diluted to 100 ml with distilled water. Solutions were then analysed in a Hilger Watts H 1170 spectrometer using the 3248 Å line of copper. A standard solution of cupric chloride was used to construct the calibration curve. The average results of three determinations are shown in Table 3.21. The colour of the samples is also given in this table.

3.3.8 Lattice parameters of $Cu_xCd_{1-x}In_2O_4$ samples

For the determination of lattice parameters all samples were analysed by X-ray diffraction using the Debye-Scherrer method. Small amounts of each sample were placed in a 0.3 mm diameter Lindemann

Table 3.21

Sample	Mol % CuO in the original mixture	Mol % CuO found in product	Colour
CICu 0.5(LT)	0.5	0.5	light-yellow
CICu 1(LT)	1.0	1.1	yellow
CICu 2(LT)	2.0	2.0	yellow
CICu 4(LT)	4.0	3.9	yellow
CICu 10(LT)	10.0	9.8	green-yellow
CICu 2.8(MT)	2.8	2.8	yellow
CICu 4(MT)	4.0	3.9	yellow
CICu 10(MT)	10.0	-	green-yellow
CICu 2(HT)	2.0	1.9	dark-yellow
CICu 4(HT)	4.0	3.9	dark-yellow
CICu 15(HT)	15.0	14.9	green-yellow

tube which was carefully centred in a 114.6 mm diameter powder camera. Nickel filtered CuKα radiation was used for all the specimens and the lattice parameters were computed from the α_1 components of the high angle reflections. All films were measured several times and the results averaged. The Nelson-Riley extrapolation was again used to derive values of a_o corresponding to a theoretical reflection at $\theta = 90^o$. The results obtained were normalized to 294 K using the value of $7.3 \cdot 10^{-5}$ Å per degree for the thermal expansion coefficient. This value, which corresponds to pure cadmium indate (section 3.3.5) was assumed to be a good approximation for the solid solutions, since only small amounts of copper were taken into solution.

Table 3.22 lists the a_o values for the different samples, and fig. 3.41 shows a plot of a_o versus copper content. From this plot it can be seen that the limits of solubility are at 2.4, 2.9 and 5.2 mol % Cu for temperatures of 1173, 1223 and 1323 K respectively. Typical Debye-Scherrer diffraction patterns are shown in Plate V.

3.3.9 UV-vis spectroscopy(*)

In an attempt to determine the distribution of

(*) These results were obtained in collaboration with Mr. M.A. Trevethan (University of Bath) to whom the author is indebted.

Table 3.22

Lattice parameters of $Cu_xCd_{1-x}In_2O_4$ specimens

Sample	[Cu] (mol %)	a_o (Å) (± 0.0001)
CI (LT)	0.0	9.1652
CICu 0.5(LT)	0.5	9.1639
CICu 1(LT)	1.1	9.1629
CICu 2(LT)	2.0	9.1613
CICu 4(LT)	3.9	9.1602
CICu 10(LT)	9.8	9.1603
CI (MT)	0.0	9.1653
CICu 2.8(MT)	2.8	9.1596
CICu 4(MT)	3.9	9.1593
CICu 10(MT)	-	9.1592
CI (HT)	0.0	9.1635
CICu 2(HT)	1.9	9.1595
CICu 4(HT)	3.9	9.1555
CICu 15(HT)	14.9	9.1532

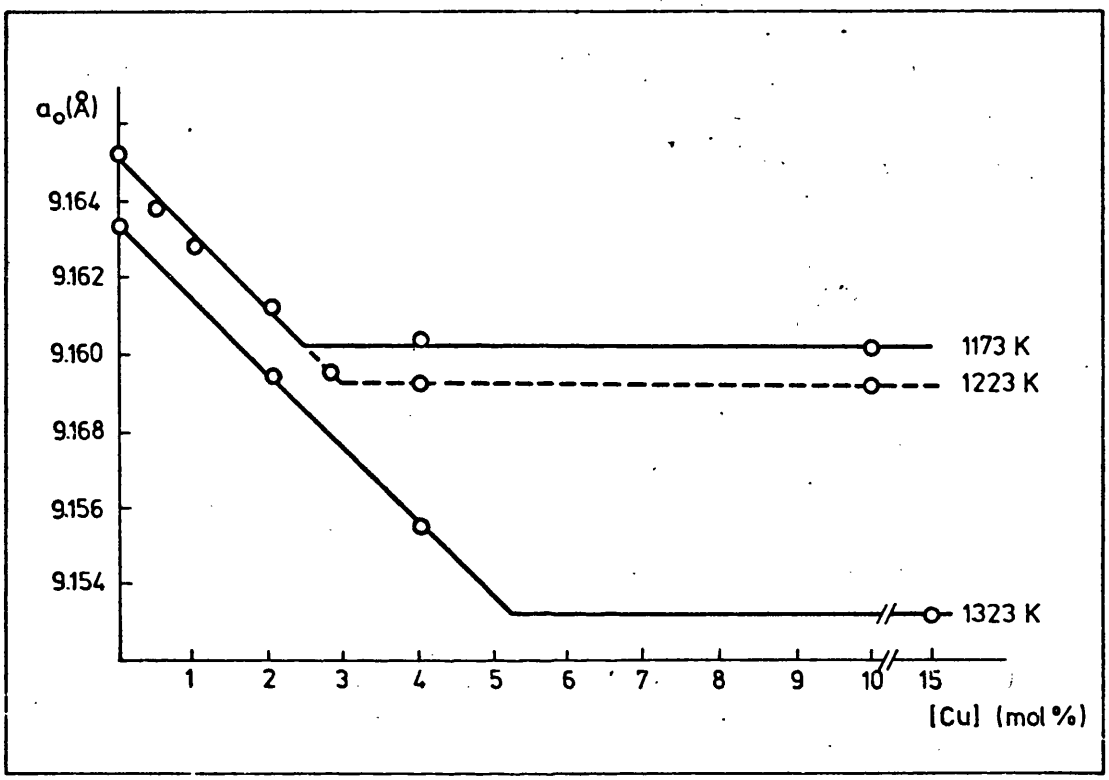

Fig. 3.41

Lattice parameter (a_o) vs. copper content for $Cu_xCd_{1-x}In_2O_4$

PLATE V

1. $CdIn_2O_4$ (LT)
2. $CdIn_2O_4$ (HT)
3. ClCu 1 (LT)
4. ClCu 2 (LT)
5. ClCu 4 (HT)

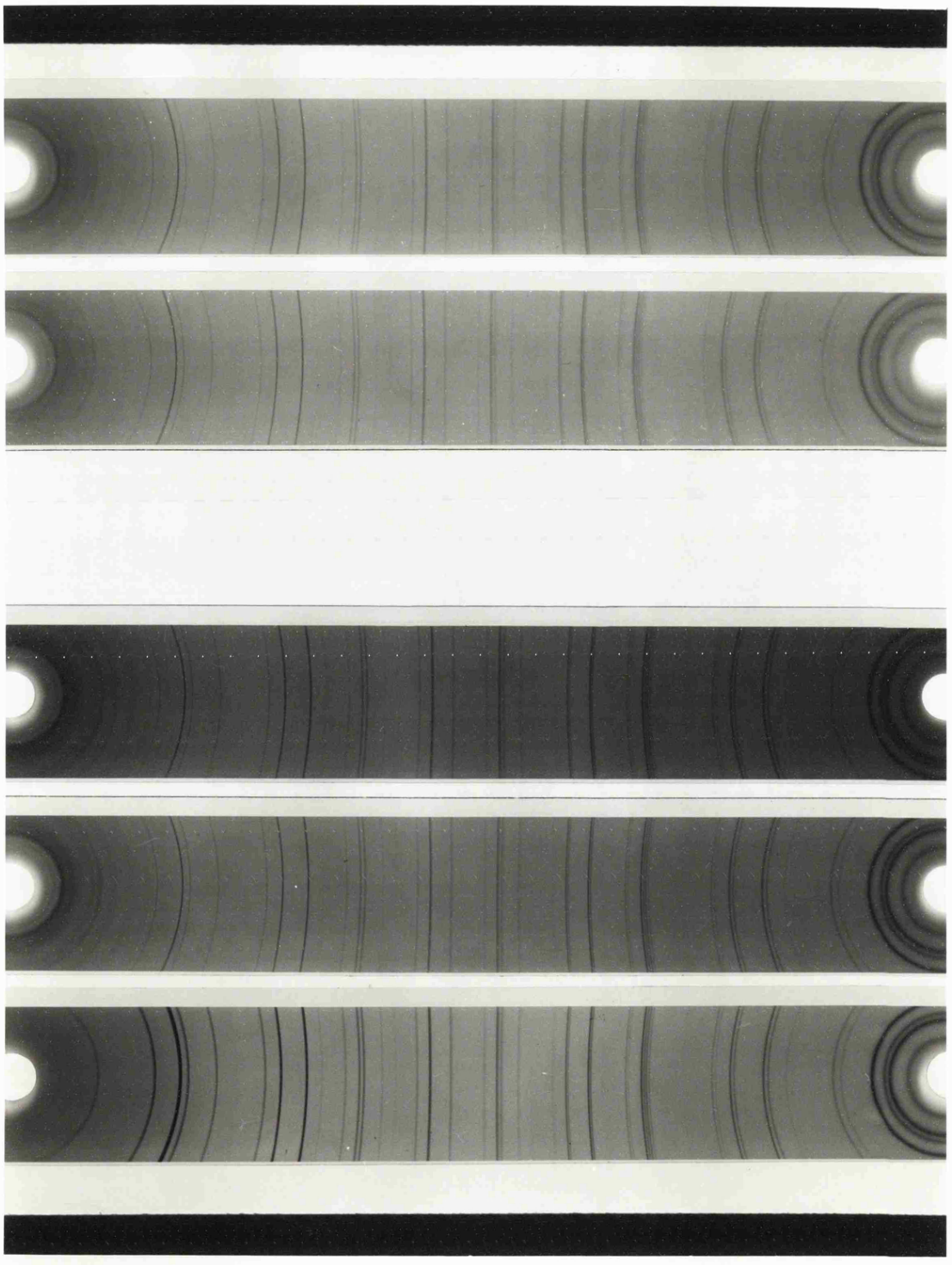
1
2
3
4
5

copper between tetrahedral and octahedral sites, UV-vis spectra were obtained from samples CICu 1(LT), CICu 2(LT) and CICu 4(HT). Spectra were recorded in a Pye Unicam SP 700 spectrometer using finely divided magnesium oxide in the reference side of the cell. Fig. 3.42 shows the spectra obtained, along with the spectra of pure cadmium indate and pure copper gallate (Copper gallate was prepared by solid state reaction between CuO and Ga_2O_3 at 1173 K in air). The two absorption bands appearing at 11,300 and 5,800 cm^{-1} in the spectrum of copper gallate have been assigned respectively to the $^2E_g \rightarrow {}^2T_{2g}$ and $^2T_2 \rightarrow {}^2E$ transitions of octahedrally and tetrahedrally coordinated copper.[119] Comments on these spectra will be delayed until section 4.3.4.

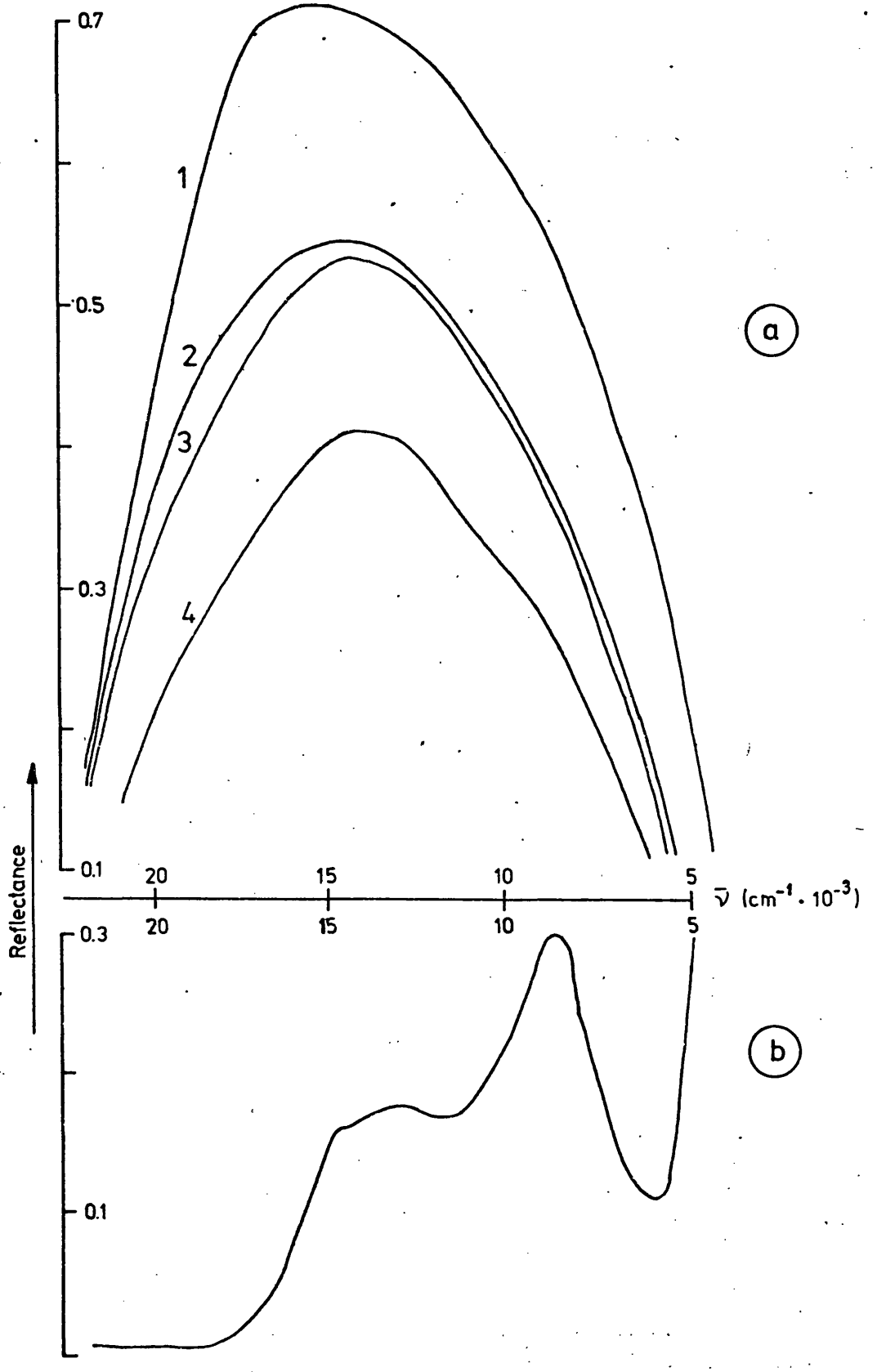

Fig. 3.42

Reflectance spectra of a) $Cu_xCd_{1-x}In_2O_4$ and b) $CuGa_2O_4$
1) $CdIn_2O_4$ (CI LT), 2) $Cu_{0.01}Cd_{0.99}In_2O_4$ (ClCu 1 LT),
3) $Cu_{0.02}Cd_{0.98}In_2O_4$ (ClCu 2 LT), 4) $Cu_{0.04}Cd_{0.96}In_2O_4$ (ClCu 4 HT)

CHAPTER IV

We must remember that what
we see is not Nature, but Nature
exposed to our method of questioning.

W. Heisenberg

DISCUSSION AND CONCLUSIONS

4.1 Studies on CoO-MgO

4.1.1 Surface area variations

Results in Table 3.3 show two main facts:
(i) For both, MSA and HSA oxides the specific surface area decreases with increasing cobalt content;
(ii) Surface areas of samples prepared in vacuum are about six times larger than those of the corresponding specimens prepared in air.

The decrease of specific surface area with increasing cobalt content is clearly a consequence of the enhanced sintering rate caused by the presence of cobalt ions in the magnesium oxide lattice. Diffusion of Co^{2+} in MgO is easier than self-diffusion of Mg^{2+}, the activation energies being 2.06 and 3.43 eV for Co^{2+} and Mg^{2+} respectively.[216,217] Migration of Co^{2+} through the solid will cause the corresponding anion transport so as to preserve local charge balance, and the overall process will result in an enhanced sintering rate. It is also very likely that the ionic arrangement in the surface layers is affected by the addition

of Co^{2+} ions, with the creation of local crystalline imperfactions which could facilitate surface diffusion.

Since the firing temperature, and time, were approximately the same for MSA and HSA specimens, the smaller surface area of the oxides prepared in air, as compared with those prepared in vacuo, indicates a higher sintering rate when the samples are fired in air. This higher sintering rate is most probably caused by the presence of water vapour formed during the thermal decomposition of magnesium hydroxide. In the case of oxides prepared in dynamic vacuum the water vapour is continuously removed and therefore will not have a pronounced role in the sintering phenomena.

Enhanced sintering of MgO in the presence of H_2O was reported by Dell and Weller[218] and by Anderson and Horlock.[219] This enhanced sintering has been further confirmed by the work of Anderson and Morgan[220] who carried out a detailed investigation of the effects of water vapour on sintering of fine particles (~ 100 Å) of magnesium oxide obtained by thermal decomposition of magnesium hydroxide. They found that sintering in vacuum ($P_{H_2O} < 10^{-5}$ torr) at 1173 K for 2 hours resulted in an oxide with surface area $\sim 210\ m^2 g^{-1}$, whilst sintering in 4.6 torr of H_2O for the same time

produced magnesium oxide with surface area ~36 m^2g^{-1}. It is relevant to point out that whilst MSA magnesium oxide prepared in air, as described in section 3.1.3, showed about the same specific surface area as that reported by Anderson and Morgan, HSA MgO, prepared in vacuum had a surface area of 285 m^2g^{-1}, therefore significantly larger than the corresponding value quoted by the above authors. The main merits of the procedure described in section 3.1.3 for the preparation of oxides with very high surface area are, (i) a dynamic high vacuum ($\sim10^{-6}$ torr) was maintained throughout the firing process; (ii) a long outgassing period (12 hours) at a relatively low temperature (623 K) allowed most of the water vapour to be pumped away before the temperature was high enough for sintering processes to take place; (iii) a thin, loosely packed, bed of magnesium hydroxide allowed removal of the remaining hydroxyl groups (stage 6, pag. 131) in the lower layers without prolonged exposure of the upper layers to water vapour.

The role of water vapour in the sintering of magnesium oxide has been assigned by Anderson and Morgan[220] to an effect on surface diffusion through an increased surface mobility brought about by H_2O adsorption. It is likely that the adsorption and desorption of the water molecule provides a mode of transport for the O^{2-} ion. The activation energy

for the diffusion of O^{2-} in magnesium oxide is about 1.4 times greater than that for the diffusion of Mg^{2+}, [221] so that anion migration is normally the rate limiting process in the sintering of MgO. However, it is possible that when interaction with water takes place cation migration becomes rate limiting.

Another effect of adsorption-desorption of water could be the formation of oxygen bridges between different crystallites.[220] H_2O chemisorption on magnesium oxide probably leads to splitting of the molecule[196,220] so that the OH^- group is located above a Mg^{2+} ion while the remaining H^+ lies above an adjacent O^{2-} ion, as follows:

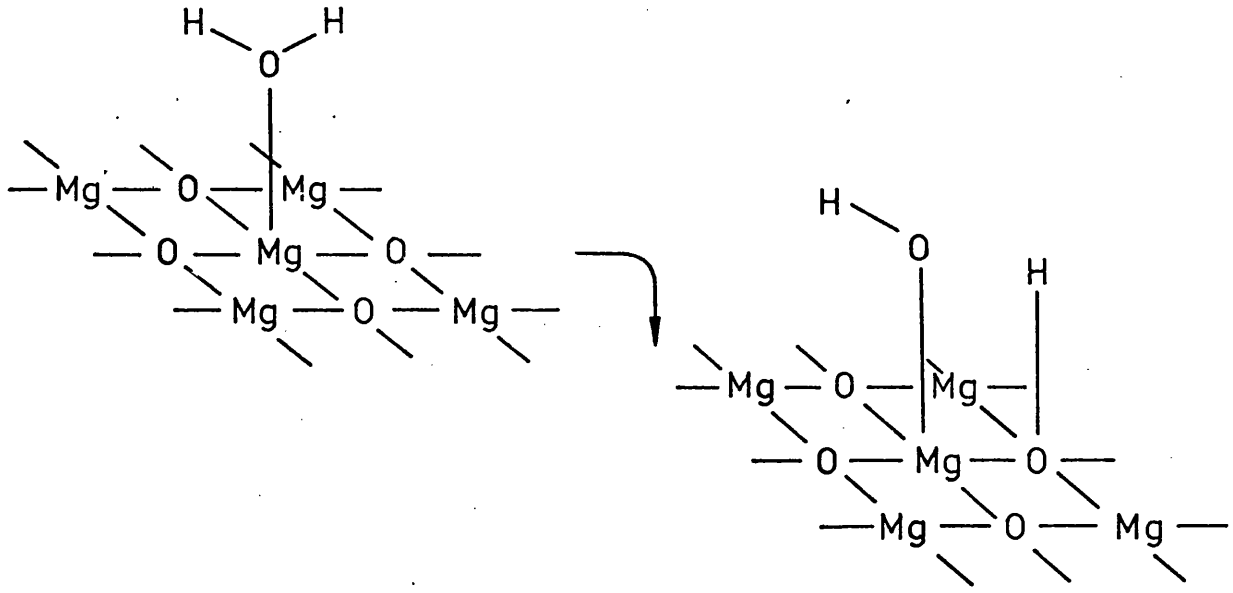

Desorption of H_2O would now occur by condensation between two adjacent surface hydroxyl groups. It is conceivable that, in some cases, these hydroxyl groups will be located on two juxtaposed crystallites, or on two diametrically opposed sides of a narrow pore and in such cases hydroxyl condensation and subsequent removal of a water molecule will produce a linking oxygen bridge.

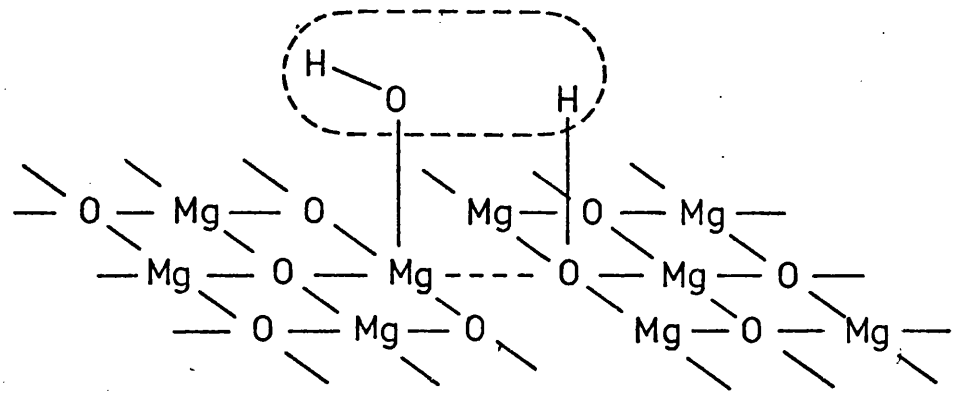

This process would be the analogue, at the atomic level, of neck formation between particles as observed in microscopic studies of sintering.

4.1.2 Crystallite size

The calculation of crystallite size from X-ray line broadening carried out as described in section 3.1.7 presupposes that small crystallite size is the sole source of intrinsic broadening. It was pointed out in section 2.3.1 that two other factors could give rise to intrinsic line broadening, viz. strain and stacking faults. However, the departure of the line profile from a Gaussian shape, as shown in figure 3.6, is a clear indication[171,191] that the oxides

under study do not possess significant lattice strain. This conclusion is further substantiated by the work of Pampuch and Librant[222] who found that there was no appreciable strain in magnesium oxide obtained by thermal decomposition of polycrystalline $Mg(OH)_2$ at 1023 K, and by that of Cutter and McPherson[223] who report that annealing at 1123 K removes strain from abraded MgO powder. The presence of stacking faults would cause selective broadening of some diffraction peaks, i.e. those corresponding to the lattice planes perpendicular to the direction of the defective stacking sequence. For the oxides under study, however, there was no indication of such selective broadening, and therefore this source of line broadening can also be ruled out.

It must be pointed out that solid solution can, by itself, produce diffraction broadening.[224] When foreign ions of different ionic radius replace regular ions in the host matrix all the ions in the crystal are moved slightly from the regular sites appropriate to the lattice type. These deviations from the regular lattice can in principle modify X-ray reflections in a similar way to thermal agitation. However, in the case of CoO-MgO solid solutions the difference in ionic radius between Co^{2+} and Mg^{2+} (2.08%) is far too small to produce

any appreciable broadening of the diffraction lines from this effect. Indeed it is questionable whether diffraction broadening caused by random solid solution could be experimentally detectable even in the case of far larger radius differences.

It is therefore concluded that the line broadening observed in MSA and HSA CoO-MgO oxides is due to small particle size only. However, the values of crystallite size given in tables 3.4 and 3.5 must be cautiously interpreted. First, it must be stressed that only a mean value is given, and it is very likely that the crystallite size distribution covers a wide range.[225] Secondly, crystallites whose size is smaller than ~ 40 Å will escape detection by X-rays, and it is also possible that even the broadening effect of slightly larger crystallites will appear only in the tails of the diffraction peaks and hence it would be neglected when measuring line breadth as half height width.

From the electron diffraction studies it can be concluded that the crystallite size, as determined by X-ray line broadening, does not correspond to the particle size, i.e. most particles consist of aggregates of crystallites. This conclusion is based on the fact that the observed electron diffraction pictures did not, as a rule, show the spot pattern corresponding to single crystals, even when individual particles were selected for diffraction.

4.1.3 Comparison between BET and X-ray surface areas

From tables 3.3, 3.4 and 3.5 it can be observed that values for BET surface areas are, in all cases, greater than the corresponding values for X-ray surface areas, the differences being more pronounced in the case of HSA oxides. Thus, whilst MSA oxides show BET values greater than X-ray values by a factor of ~ 1.4, this factor becomes ~ 2.7 for HSA specimens. Considering the entirely different physical bases of gas adsorption and X-ray methods and considering the inaccuracies inherent to both techniques (probably an error of $\sim 20\%$ should be allowed in either case), a small discrepancy in the results would be expected. However, in the present case, discrepancies are far too large to be accounted for on this basis.

The method used to compute X-ray surface areas presupposes that each particle is an individual cubic crystallite. It is clear that this assumption involves an error, since electron diffraction showed most particles to be aggregates. The model one particle-one crystallite is only a crude approximation. The effect of such a crude approximation, however, will be to yield values of X-ray surface area larger than those for BET surface area. In practice the contrary is observed. As discussed in the previous

section the smallest crystallites escape detection by X-rays, yet they contribute prominently in physical adsorption. This provides part of the explanation for the BET surface areas being larger than the X-ray surface areas.

The possibility that the crystallites may present rough surfaces is another important point to consider. Thus, in the hypothetical case of cubic crystallites with a cross section like that depicted in the figure, the areas available for physical adsorption would be twice the areas "seen" by X-rays. Clearly it cannot be expected that the crystals would have such "periodically irregular" surface, but the fact still remains that surface roughness will result in BET surface areas greater than X-ray surface areas.

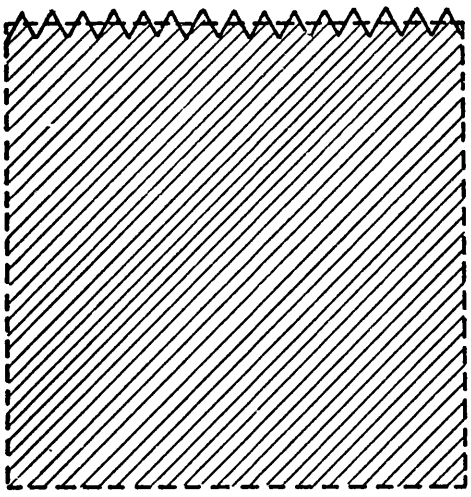

Finally, the existence of porosity in the crystallite aggregates could also cause a difference between BET and X-ray surface areas, in the sense that the former would most likely be greater. An adsorption-desorption isotherm for HSA MgO is shown in fig. 4.1. This isotherm shows a hysteresis loop, therefore revealing porosity in the sample.[226] It is likely that porosity (and the corresponding "internal" area) be located at the crystallite boundaries in the aggregates.

To summarize, the following factors can cause discrepancy between BET and X-ray surface areas:

(i) Crystallite aggregation

(ii) Very small crystallites not detectable by X-rays, but contributing to physical adsorption

(iii) Surface inhomogeneities

(iv) Porosity

Factor (i) will cause X-ray surface areas to be greater than BET surface areas, but the other factors will produce the opposite effect. MSA and HSA CoO-MgO studied in the present work will probably have a contribution from each factor, but the results show that factors (ii)-(iv) outweigh factor (i). It is significant that the discrepancies between BET and X-ray surface areas are larger for HSA specimens.

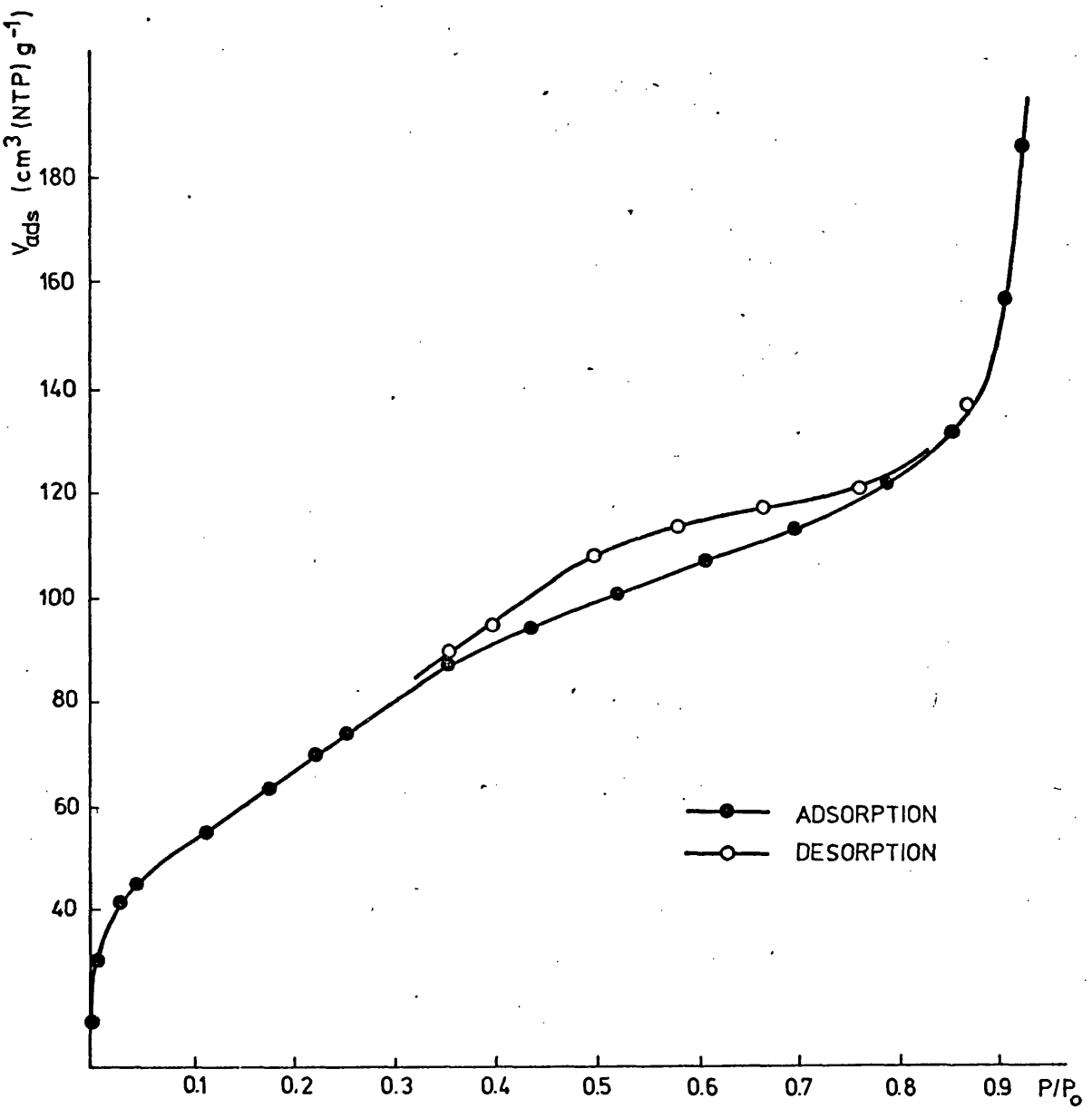

Fig. 4.1

N_2 adsorption-desorption isotherm (77 K) on MgO HSA (outgassed at 873 K)

[This isotherm was obtained by Dr. M. J. Torralvo (University of Madrid) to whom the author is grateful]

This is most likely to be due to a greater "internal" area in these samples, together with a larger proportion of very small crystallites.

4.1.4 Lattice parameters

Figure 3.9 shows that in all three cases, LSA, MSA and HSA specimens, there is a linear increase in lattice parameter with cobalt content. This, together with the fact that in the diffraction patterns of the samples no lines other than those of the (expanded) MgO lattice were observed, is a good indication of solid solution formation. New valuable evidence comes from the work of Hagan[196] who measured the magnetic susceptibility of the same samples between 78 and 373 K and found that, in all cases, the values of magnetic susceptibility and Weiss constant were those corresponding to Co^{2+} ions uniformly dispersed and with octahedral coordination.

The increase in lattice parameter, Δa_o, is $+5.8 \cdot 10^{-4}$ Å for one cobalt ion per 100 cobalt + magnesium ions. This is in good agrrement with the value of $\Delta a_o = +5 \cdot 10^{-4}$ Å per cobalt ion reported by Cimino et al[111] for CoO-MgO solid solutions dilute in cobalt (specimens in the MSA region). The theoretical value of Δa_o calculated assuming that Végard's law holds is $\Delta a_o = +4.9 \cdot 10^{-4}$ Å per cobalt ion (a_o MgO = 4.2112 Å, a_o CoO = 4.260 Å). Thus, the

system CoO-MgO shows a positive deviation from Végard's law over the concentration range studied.

The most important aspect of the present work is the finding that the increase in lattice parameter with cobalt concentration is the same for LSA, MSA and HSA oxides. This, together with the magnetic work quoted before provides the proof that the property of solid solutions can be maintained even when crystallite sizes are below 500 Å.

The a_o versus [Co] line for MSA oxides (fig. 3.9) lies slightly above the line for LSA oxides. Since the lattice parameters of MSA specimens were determined by X-ray diffraction in air, this slight shift can be ascribed to a thin surface layer of hydroxide which imposes a dilatant volume strain on the crystallite interior, measurable when the crystallite size is in the range of 500 to 2000 Å,[192] as in the present case.

As shown in fig. 3.9, the value of a_o for HSA MgO was found to be smaller than the value of a_o for LSA MgO, the difference being ~ 0.0015 Å. This difference in a_o values may be explained as the result of lattice contraction, due to very small crystallite size, in HSA MgO. Very small crystallites have an excess surface energy arising from surface distortion. This excess surface energy creates a surface tension which can modify the lattice

parameter.[227,228] In general, surface tensions in ionic crystals are calculated to be positive and therefore small crystals would be expected to have a smaller lattice parameter than large crystals.

Theoretical calculations of the decrease in lattice parameter with decreasing crystallite size have been performed, for some ionic compounds, by Anderson and Scholz.[229] Their results, for the case of MgO, are summarized in fig. 4.2 According to these theoretical calculations the decrease in lattice parameter for HSA MgO with a crystallite size of 137 Å (N ≈ 53 in fig. 4.2) should be 0.006 Å. The experimentally found value of ~0.0015 Å is of this order of magnitude. Taking into account the approximate character of Anderson and Scholz's computations and making allowances for experimental errors, the agreement is satisfactory.

4.1.5 Reflectance spectra of pure MgO

Fig. 3.13 shows that, as might be expected, the vacuum spectra of MSA and HSA MgO exhibit no bands in the range 25,000-4,000 cm^{-1}. Upon exposure to the atmosphere two bands appear at the near infrared end of the spectrum (7,200 and 5,100 cm^{-1} respectively), together with a further intense band extending into the infrared. According to Hagan[196] these three bands are due to adsorbed water vapour.

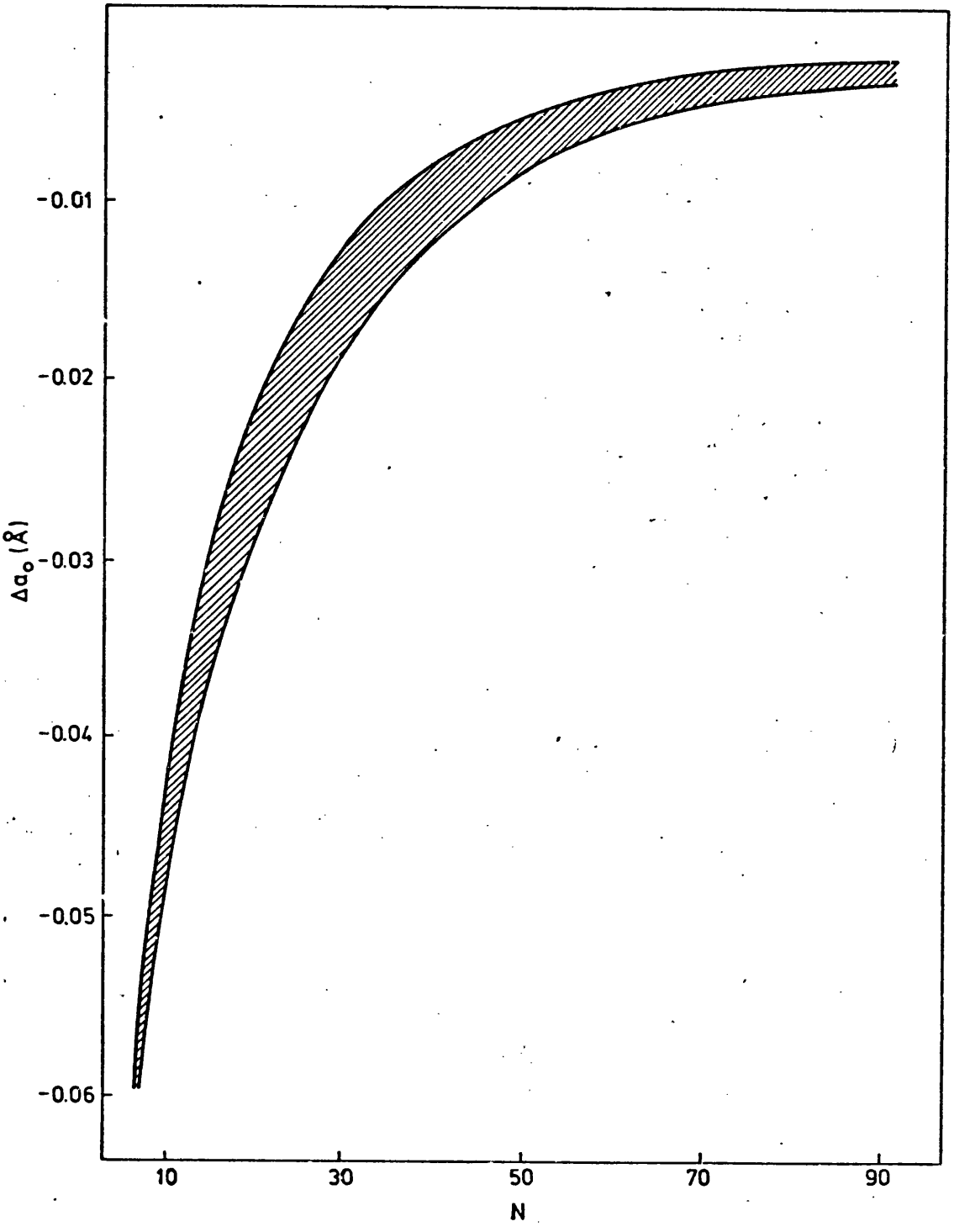

Fig. 4.2

Change in lattice parameter with crystal size for perfect cubes of N^3 ions

(They also develop when water vapour is dosed at a pressure of a few torr to the outgassed samples). The UV-vis spectra show the much more pronounced reactivity of HSA MgO, as compared with MSA MgO. Thus, after exposure of HSA oxide to the atmosphere for only 5 hours, the intensity of the adsorbed water vapour bands is much greater than in MSA oxide exposed to the atmosphere for 14 days.

4.1.6 Reflectance spectra of MCo 3 solid solutions

The vacuum spectrum of LSA MCo 3 (fig. 3.14A) displays two broad absorption bands at 8,500 and 19,800 cm^{-1}, together with a shoulder at 16,500 cm^{-1}. The position of these absorption maxima is in very good agreement with the data reported by Low [200] and by Pappalardo et al [202] for the UV-vis spectrum of single crystal CoO-MgO, as can be appreciated by inspection of Table 4.1. It is therefore concluded that the spectrum in fig. 3.14A corresponds to octahedrally coordinated Co^{2+} in MgO.

The vacuum spectra of MSA and HSA MCo 3 show additional absorption bands at about 7,100, 13,900, 16,800 and 18,000 cm^{-1}. These absorption bands, which are not present in the spectrum of LSA oxide, are well developed in MSA oxide, and they become dominant in HSA oxide. It is therefore concluded that they arise from a chromophore species which is

Table 4.1

Absorption maxima (cm^{-1}) Low's study	Crystal field transition	Absorption maxima (cm^{-1}) Present work
8,470	$^4T_{1g} \rightarrow {}^4T_{2g}$	8,500
9,080	$^4T_{1g} \rightarrow {}^2E_g(G)$	-
17,200	$^4T_{1g} \rightarrow {}^2T_{2g}$ and/or $^2T_{1g}(G)$	16,500
18,700	$^4T_{1g} \rightarrow {}^4A_{2g}$	19,800
19,600	$^4T_{1g} \rightarrow {}^4T_{1g}(P)$	
20,500	$^4T_{1g} \rightarrow {}^2T_{1g}(P)$	
24,600	$^4T_{1g} \rightarrow {}^2A_{1g}(G)$	-
28,500	$^4T_{1g} \rightarrow {}^2T_{1g}(H)$	-

found only in the surface layer, or layers near to the surface. The interpretation of this "surface spectrum" (which is probably a composite spectrum) is not as straightforward as that of the "bulk spectrum" exhibited by LSA MCo 3. It is clear, however, that the surface spectrum must be due to cobalt species, since HSA MgO does not exhibit any absorption bands in the region 25,000-5,000 cm^{-1}.

It is reasonable to expect that, in the surface region, cobalt ions would be in a five- or four-fold anion coordination. The latter is very likely, since Co^{2+} is known to form many tetrahedral complexes; in fact it forms more tetrahedral complexes than any other transition metal ion,[230] and it also occurs very often at tetrahedral sites in spinel-type oxides (section 1.6, and reference 42). Five-coordinate compounds of cobalt(II) have also been reported in the literature[231-234] and, in principle, a fivefold coordination could be expected for cations at {100} faces of MgO crystals.[235]

The spectra of cobalt(II) in tetrahedral[236] and square pyramidal[237] coordination are shown in fig. 4.3, and the corresponding energy level diagrams[238] in fig. 4.4. Tetrahedral cobalt(II) gives absorption maxima at about 7,000, 15,300, 16,300 and 17,700 cm^{-1} (Fig. 4.3 and Table 3.9). The presence of cobalt(II) in tetrahedral coordination

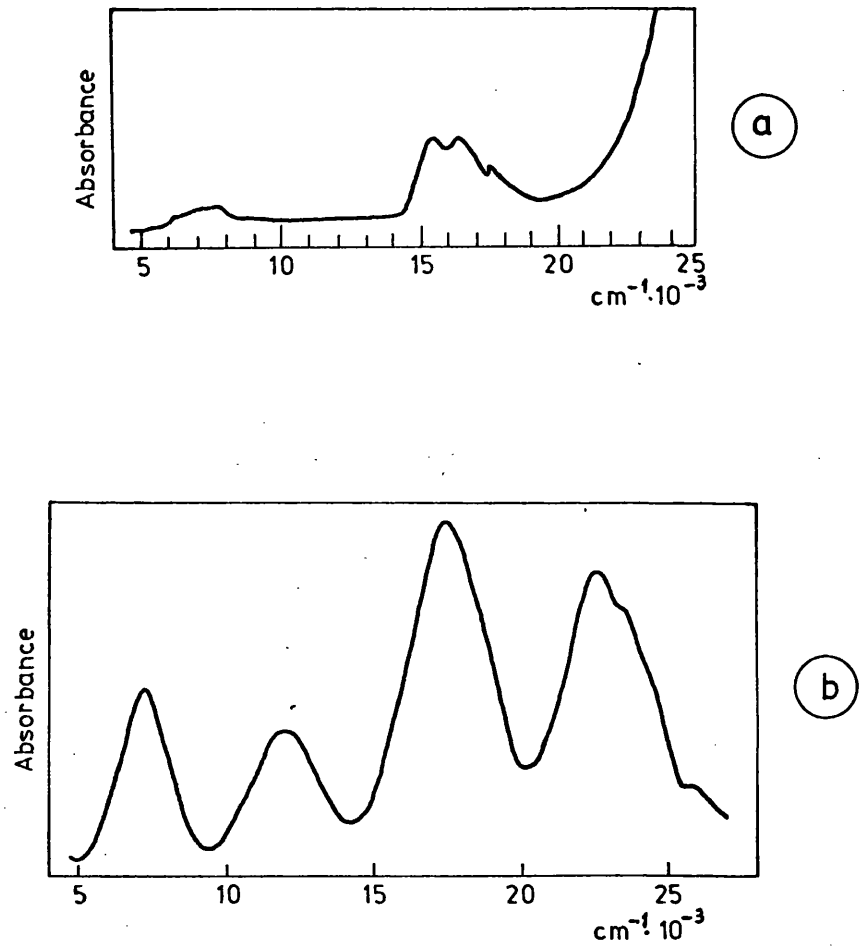

Fig 4.3

Optical spectra of Co^{2+} in a) tetrahedral and b) square pyramidal coordination

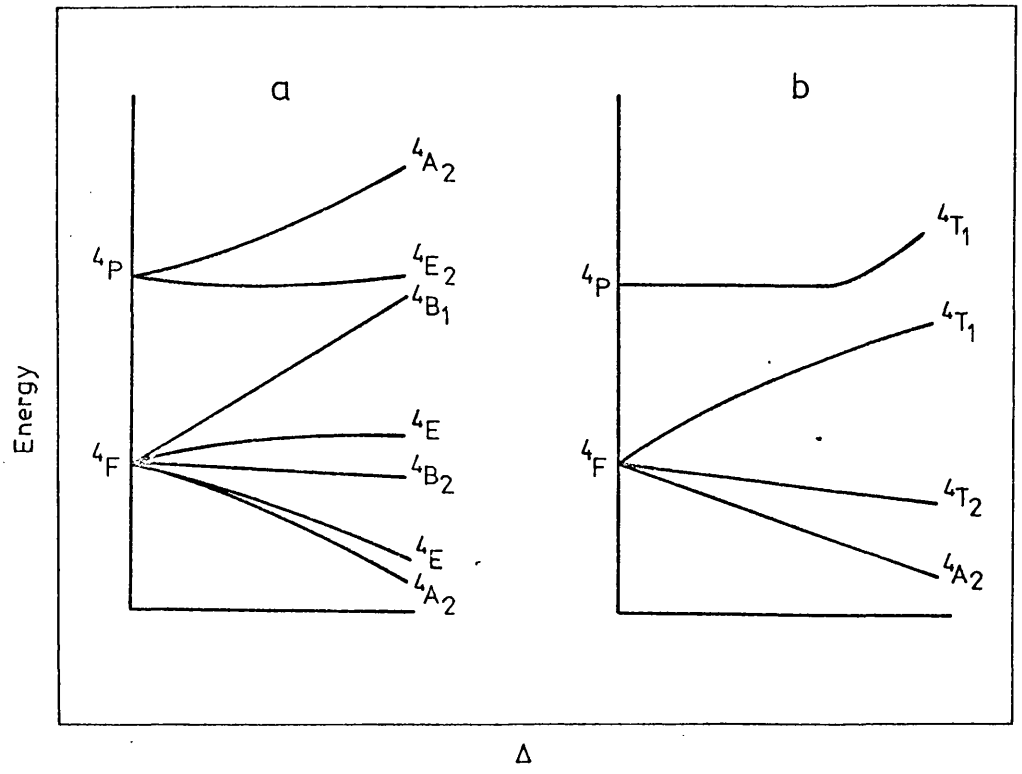

Fig. 4.4

Energy level diagrams for cobalt(II) in a) square pyramidal, and b) tetrahedral coordination

could therefore explain the observed absorption maxima at 7,100, 16,800 and 18,000 cm^{-1} in MSA and HSA CoO-MgO solid solutions. However, the band at 13,900 cm^{-1} has still to be accounted for. An absorption band in this region appears in the spectrum of cobalt(II) in square pyramidal coordination, as shown in fig. 4.3, but any attempt to assign the 13,900 band to a fivefold (square pyramidal) coordinated Co^{2+} surface species meets with the difficulty that the absorption band at about 22,000 cm^{-1} in fig. 4.3(b) is not observed in the spectrum of CoO-MgO specimens. However, the presence of small amounts of fivefold coordinated Co^{2+} on the {100} crystal surfaces cannot be completely ruled out. It is likely that the cation and the surface anions in the base of the square pyramid relax their relative positions so causing a distortion of the cation coordination symmetry. This would give rise to changes in the intensity (and position) of the absorption maxima in the corresponding spectrum.(239)

A more severe relaxation process would facilitate the movement of surface cobalt ions into tetrahedral interstices under the surface. It is possible that both distorted and undistorted tetrahedral species could arise in this way.

On the basis of the spectroscopic evidence it is not possible to assign unequivocally the 13,900 band either to a distorted fourfold or a distorted fivefold coordination of the Co^{2+} ion; indeed both species are likely to coexist. It should be clear, however, that more than one low coordinated cobalt(II) species are responsible for the surface spectrum(*)

Spectra C and E in fig. 3.14 show that exposure of MSA and HSA oxides to the atmosphere destroys the surface spectrum and regenerates the octahedral bulk spectrum. (The absorption maximum at 7,200 cm^{-1} in spectra C and E is probably due to a water overtone[240]). This effect can be ascribed to the action of water vapour and oxygen which attack the low coordinated cobalt species.

4.1.7 Spectroscopic study of oxygen adsorption

The effects of oxygen adsorption on the UV-vis spectrum of MCo 7.5 are shown in fig. 3.15. Spectrum B was taken after allowing 2 hours of equilibration time once the oxygen was dosed. It is observed that adsorption of oxygen weakens the surface spectrum but does not destroy it so completely as in the case of samples exposed to the atmosphere. Outgassing at 1273 K regenerates the surface spectrum.

(*) Very detailed UV-vis work, which is now being carried out in the University of Bath by Mr. M.A. Trevethan, provides further evidence for the presence of more than one surface species of low coordinated Co^{2+} ions.

The fact that the surface spectrum is still remaining (band at 7,100 cm^{-1}) after dosing 260 Torr of oxygen provides some indication that the low coordinated cobalt species giving rise to this spectrum are not in the outermost surface layer but rather in deeper surface layers. It is likely that cobalt(II) tetrahedrally coordinated under the surface would be moderately stable towards oxygen adsorption. Water vapour, however, is more aggressive towards the magnesium oxide matrix and attacks the surface layers strongly. This explains why exposure of the oxide to the atmosphere completely destroys the surface spectrum (fig. 3.14).

Upon oxygen adsorption a broad absorption band develops above 12,000 cm^{-1} and extends into the UV. This band is almost certainly due to charge transfer, e.g. $O_{2(g)} + 2Co(II) \rightarrow 2O_{(ads)} + 2Co(III)$, or $O_{2(g)} + Co(II) \rightarrow O_{2(ads)} + Co(III)$. Presumably intervalence absorption ($Co(II) \rightarrow Co(III)$) also takes place.

Intervalence charge transfer is well characterized in the literature for the case of Co_3O_4[241,242] which possesses cobalt ions in both divalent and trivalent states.[243] The observed charge transfer band extends from 20,000 to 30,000 cm^{-1}. The O_2^- superoxide anion has also been well characterized on oxide surfaces.[244]

4.1.8 Final comments

Diffraction and magnetic susceptibility[196] studies have both given evidence for solid solution formation. Moreover, this is independent of the degree of subdivision of the oxide. LSA, MSA and HSA specimens all show the same linear variation of lattice parameter with cobalt concentration, and the same materials all show an octahedral magnetic moment.[196] Diffuse reflectance spectroscopy, however, gave evidence for some low coordinated cobalt ions in the surface layers of HSA, and to a smaller extent MSA, oxides. Nevertheless these results are not contradictory. They add together to give a consistent picture of the solid. The bulk of the crystals consists in all cases (LSA, MSA and HSA materials) of a true solid solution between CoO and MgO where all the cations possess sixfold octahedral coordination and the Co^{2+} ions are randomly dispersed in the diamagnetic matrix. In the surface layers, however, relaxation of the ionic close packing allows some transition metal ions to adopt lower coordination states, mainly tetrahedral. The surface relaxation increases with decreasing crystallite size and for HSA oxides the surface spectrum becomes preponderant over the bulk spectrum. This does not necessarily mean, however, that the concentration of low coordinated cobalt species are preponderant over

octahedral ones, since the non-centrosymmetric nature of the former gives rise to a much more intense absorption.

4.2 Studies on MnO-CaO and MnO-CaO-Na_2O

4.2.1 Lattice parameters in the system MnO-CaO

Fig. 3.18 shows that MnO-CaO oxides exhibit a constant decrease in lattice parameter, a_o, with increasing manganese content. This, together with the absence in the diffraction films of lines other than those corresponding to the NaCl-type phase, provides good evidence for solid solution formation. It can therefore be concluded that, under the experimental conditions of the present work, MnO and CaO form a complete series of solid solutions, with no immiscibility gaps. This is an interesting finding which not only confirms the results of previous workers who report complete solid solubility at 1423 - 1573 K,[115-118] but also extends them to a lower temperature (1273 K). It is also remarkable that despite the large difference in ionic radius between Mn^{2+} and Ca^{2+} (21.95%) MnO and CaO do show complete solid solubility.

The decrease in lattice parameter with manganese content is linear up to a manganese concentration of 50 mol % (fig. 3.18), and the observed value of $\Delta a_o = -3.7 \cdot 10^{-3}$ Å per manganese ion is exactly the

same as would be predicted by Végard's law (a_o CaO = 4.8105 Å, a_o MnO = 4.4449 Å). For [Mn] > 50 mol %, however, the a_o versus [Mn] line lies below the theoretical (Végard's law) line, the deviation reaching a maximum ($a_{o(theor)} - a_{o(observ)} = 0.0006$ Å) for [Mn] ≈ 70 mol %. On account of the large difference between the lattice parameters of MnO and CaO, a deviation from Végard's law should be expected (section 1.10.2), but, in principle, there is no apparent reason why this deviation should only occur in the high manganese content region.

An explanation for a negative deviation from Végard's law occurring only in the MnO-rich region of the MnO-CaO system could, in principle, be found in terms of some Mn^{2+} ions going into a higher oxidation state, presumably Mn^{3+}, without the formation of a separate phase. This would imply the concomitant creation of cation vacancies and it is conceivable that the overall effect would result in a decrease of the lattice parameter. It is also possible that the solubility of Mn^{3+} would increase with increasing manganese content, but, to account for the observed shape of the a_o versus [Mn] line it would be necessary to postulate that (i) the solubility of Mn^{3+} (in the NaCl-type structure) is independent of manganese content up to [Mn] ≈ 50%, and (ii) that this solubility would increase with increasing manganese content from [Mn] ≈ 50% to [Mn] ≈ 70%, to decrease then for [Mn] >

75%. It is difficult to explain this solubility pattern of the Mn^{3+} ion. However, a maximum negative deviation from Végard's law at [Mn] ~ 70% would be consistent with the formation of 'microdomains' of $CaMn_2O_4$ structure within the rock-salt structure, in analogy with the formation of Fe_3O_4 microdomains in non-stoichiometric'FeO'.[245,246] These $CaMn_2O_4$ microdomains would have 3N cations (distributed over octahedral and tetrahedral sites) for every 4N anions, as in a spinel-type structure. Thus, the corresponding parameter would presumably be smaller than for a NaCl-type structure, where there are 4N cations for every 4N anions. It seems probable that the stability of the $CaMn_2O_4$ microdomains would be greater when the overall stoichiometry is 1Ca:2Mn, i.e. at 66 mol % Mn. It must be pointed out that chemical analysis, by redox titration, of CM 75 showed no evidence for manganese in oxidation states higher than 2+. Very small amounts of Mn^{3+}, however, would escape detection.

A different working hypothesis to explain the observed shape of the a_o versus [Mn] line would be as follows: Up to [Mn] = 50% one can consider that Mn^{2+} is being introduced into the crystal lattice of CaO. The Mn^{2+} ion is smaller than the Ca^{2+} ion and therefore finds little difficulty to accomodate itself in the large octahedral sites of the host lattice. The resulting effect on the lattice parameter

is a decrease in a_o of pure calcium oxide corresponding to the amount of Mn^{2+} incorporated in the lattice. For the Mn-rich end, however, the solid solution process can be envisaged as the replacement of Mn^{2+} ions by Ca^{2+} ions in the MnO crystal lattice. Now, the octahedral sites in MnO are too small to accommodate Ca^{2+}; therefore the lattice must be expanded, as indeed happens (all solid solutions have an a_o value larger than a_o for MnO). However, although the Ca^{2+} ion forces the lattice to expand the lattice in its turn forces the Ca^{2+} ion to compress, and the equilibrium value is the balance of these opposing effects. A "compressed" Ca^{2+} ion would be less effective in expanding the MnO lattice than a Ca^{2+} ion with the ionic radius characteristic of Ca^{2+} in CaO. The experimental data indicate that the lattice parameter of CaO dissolved in MnO is no longer 4.8105 Å (as in pure CaO) but 4.7820 Å (extrapolated value in fig. 3.18). This phenomenon can alternatively be envisaged as the development of an increased covalent character in the Ca-O bond when Ca^{2+} ions are in the MnO matrix. The MnO structure is more covalent than the CaO structure. Hence Ca^{2+} ions dissolved in MnO are likely to have some delocalization of their electrons thrust upon them: this will mean an increased covalent character in the Ca-O bonds as compared with

pure (i.e. highly ionic) CaO, and hence a smaller Ca-O separation becomes possible. This is a situation made probable when Ca^{2+} ions are no longer surrounded by other Ca^{2+} ions, i.e. in Mn-rich solid solutions. The shortened interionic distance between Ca^{2+} and O^{2-} ions (as compared to parent CaO) would be reflected in a smaller lattice parameter. Experimental verification of this hypothesis will have to await the development of some technique for accurate determination of the degree of covalency in the Ca-O bond.

4.2.2 Lattice parameters in the system MnO-CaO-Na_2O

Fig. 3.19 shows the variation of lattice parameter with increasing Na/Mn ratio for samples with total manganese content of 3 mol %. A linear decrease in lattice parameter with increasing Na/Mn ratio is observed up to Na/Mn = 2. Larger concentrations of Na_2O, however, do not produce a further decrease in a_o, which remains at the constant value of a_o = 4.8098 Å. It must be borne in mind that the quoted Na/Mn ratios are those corresponding to the initial mixture. The firing process (1273 K for 15 hours, in air) will no doubt cause volatilization of significant amounts of Na_2O (sublimation point 1548 K). A significant amount of $CaMn_2O_4$ was always present

together with the Mn-doped CaO phase; thus it is clear that in no case did all the manganese enter into the CaO lattice. The presence of the $CaMn_2O_4$ phase is easily detectable from the brown coloration of the samples, and also from the X-ray diffraction films. A sample with [Mn] = 0.1 mol % and initial ratio Na/Mn = 4 (0.1N 4) showed a white colour, whilst another sample prepared from the same coprecipitated carbonates, but without sodium showed a brown colour indicative of the formation of $CaMn_2O_4$.

Considering the a_o values quoted in Table 3.12, these results can be rationalized as follows:

1. The a_o value for sample 3N 0 (no sodium) is 4.8108 Å, larger than a_o for pure calcium oxide (4.8105 Å). This discrepancy, however, can be assigned to the formation of a surface layer of calcium hydroxide(*) which would impose a dilatant volume strain on the crystal interior.[192,247]

2. The a_o value for sample 0.1N 4 is 4.8105 Å, thus showing a decrease of $3 \cdot 10^{-4}$ Å with respect to 3N 0. This would imply that $\Delta a_o = -3 \cdot 10^{-3}$ Å per manganese ion, if it assumed that all the manganese has entered the CaO lattice (no traces of brown colour).

(*) All samples in the system $MnO-CaO-Na_2O$ have been fired in air, and no precaution was taken to avoid exposure to the atmosphere during the preparation of the specimens for X-ray studies.

3. Samples 3N 1 and 3N 2 show a_o values of 4.8102 Å and 4.8098 Å respectively. Since the ionic radius of Na^+ (1.02 Å) is larger than that of Ca^{2+} (1.00 Å), the decrease in a_o from 4.8102 to 4.8098 Å cannot be ascribed to the incorporation of an excess of Na^+ ions in sample 3N 2. This sample must also contain more manganese ions than 3N 1. Presumably the amount of Na^+ left in 3N 1 after the firing process was not enough to match all the Mn^{n+} ($n > 2$) ions that could be taken into solid solution.

4. Samples 3N 4 and 3N 8 show the same value of a_o (within experimental error) as 3N 2, therefore indicating that the solubility limit has been attained.

The main conclusions to be drawn are:

A In the absence of sodium there is no appreciable solubility of manganese oxides in calcium oxide, for samples heated in air. This follows from the fact that, whilst all Mn^{n+} ions are smaller than Ca^{2+}, a_o for 3N 0 is not smaller than a_o for CaO. This conclusion is consistent with the fact that MnO is not stable at 1273 K in air (fig. 3.16). The introduction of Mn^{n+} ($n > 2$) ions in CaO, on the other hand, would imply the simultaneous creation of cation vacancies in the lattice.

The excess energy required, together with that associated with the strains caused by cationic replacement, renders the solution unstable.

B Na^+ ions are able to induce solubility of manganese in CaO. It is clear that the transition metal cationic species which has been dissolved is not Mn^{2+}. In principle either Mn^{3+} or Mn^{4+} (or both) could replace Ca^{2+} in CaO if simultaneously 1 or 2 Na^+ ions were taken into the structure to preserve charge balance. Ionic size arguments favour Mn^{3+} rather than Mn^{4+} and ESR spectroscopy (sections 3.2.5e and 4.2.5) gave no evidence for Mn^{4+}. It is therefore concluded that the reduction in lattice parameter in the system $MnO-CaO-Na_2O$ corresponds to the replacement of calcium ions by equal amounts of Mn^{3+} and Na^+ ions.

C Considering the above-mentioned value of $\Delta a_o = -3 \cdot 10^{-3}$ Å per manganese ion (couple Mn^{3+} plus Na^+) the solubility limit is established at 0.35 mol % Mn^{3+}. It must be pointed out that the value $\Delta a_o = -3 \cdot 10^{-3}$ Å per manganese ion is possibly subject to considerable experimental error. However, it is consistent with the value of $\Delta a_o = -3.7 \cdot 10^{-3}$ Å per manganese ion found

for MnO-CaO solid solutions, since although the Mn^{3+} ion is smaller than Mn^{2+} there is a compensation effect from the Na^{+} ion which is larger than Ca^{2+} (Table 1.3).

No data on the system MnO-CaO-Na_2O exist in the literature. However, Cimino et al[248] have made a detailed study of the similar system MnO-MgO-Li_2O, in the range 0 to 5 mol % manganese. They found that in the samples without lithium most of the manganese ions did not dissolve in MgO, but formed a new phase: Mg_6MnO_8. Addition of lithium results in the incorporation of all the manganese into the MgO lattice, either as Mn^{3+} or Mn^{4+} depending on whether [Li]/[Mn] = 1 or [Li]/[Mn] = 2. The much more limited solubility found in the present study is presumably due to the much larger difference in ionic radius between Ca^{2+} and Mn^{3+} (72.4%) in comparison with the difference between Mg^{2+} and Mn^{3+} or Mn^{4+} (24.1% and 31.0% respectively). The same argument can be used to explain the fact that Mn^{4+} was not observed in the present study.

4.2.3 ESR spectrum of isolated Mn^{2+} ions in CaO

As shown in figs 3.21-3.25, the ESR spectrum of isolated Mn^{2+} ions displays the characteristic set of six lines corresponding to the hyperfine interaction of the $m_S = +\frac{1}{2} \leftrightarrow m_S = -\frac{1}{2}$ line with the

^{55}Mn nuclei which have nuclear spin 5/2. As pointed out in section 3.2.5, the other 24 allowed transitions will have a considerable angular dependence, and will not usually be observed in the spectrum from a powder where the direction of the axial symmetry axis is distributed at random relative to the external field, thus causing the outer Zeeman transitions to smear out.

The average value of g (g = 2.0069) is close to the free spin value as might be expected for a S-state ion where orbital caontributions are very limited (Section 2.4.5). It is also in good agreement with the value g = 2.0064 found by Derouane and Indovina[249] for Mn^{2+} in polycrystalline magnesium oxide.

The ESR signal is nearly isotropic and the line-width, 0.5 gauss for the sample fired at 1523 K, is the same as found for Mn^{2+}-doped single crystals of MgO,[250] therefore confirming that the local crystal field has cubic symmetry to a high degree of accuracy, and that no appreciable interactions exist between the transition metal ions, i.e. Mn^{2+} ions are well dispersed in the diamagnetic matrix. The main conclusion to be drawn is that, despite the large difference in ionic radius between Mn^{2+} and Ca^{2+} ions (21.95%), the former substitute the latter at their lattice sites in CaO without appreciable distortion of the local symmetry. It must be

pointed out that the spectra show a slight increase of the hyperfine splitting constant with increasing magnetic field; however, this increase in A does not presuppose a lowering of the crystal field symmetry since it can be explained as a consequence of second order terms, proportional to A^2/H_o, in the spin Hamiltonian,[251] which arise even for a cubic field.

An additional feature of the spectra shown in figs. 3.21-3.25 is the presence of ten weak absorption lines appearing in groups of two between the main lines. These weak absorptions correspond to the forbidden transitions $\Delta m_S = \pm 1$, $\Delta m_I = \pm 1$ and have also been observed in the ESR spectrum of Mn^{2+} in polycrystalline magnesium oxide.[251]

The variations of line width with firing temperature, and exposure of the samples to air, are of considerable interest. As shown in Table 3.14 the line-width for a sample with [Mn] = 0.01 mol %, fired at 1523 K, is 0.5 gauss. However, the vacuum spectrum of a sample with the same manganese content, but fired at 1273 K, shows a line-width of 5 gauss which narrows to 2.5 gauss upon exposure to air. A sample with [Mn] = 0.1 mol % again exhibits the same behaviour, i.e. line-width for the spectrum recorded in vacuum: 5 gauss; line-width after exposure to air: 2.5 gauss. The increased line-width of the vacuum

spectra of samples fired at 1273 K (low temperature samples) compared with that of the sample fired at 1523 K (high temperature sample), can be explained in terms of surface Mn^{2+} ions having an incomplete coordination (surface unsaturation) which will cause a lowering of the local crystal field symmetry, therefore widening the resonance lines. It is clear that surface transition metal ions will also be present in the high temperature sample, but, presumably, their contribution to the ESR spectrum would be vanishingly small compared with the contribution from the ions in the bulk on account of the much smaller surface area. In low temperature samples, however, the role of the paramagnetic surface ions is greater; firstly because the ratio surface to bulk is greater, and secondly because there is likely to be appreciable surface segregation of the manganese ions. Upon exposure of the samples to the atmosphere the unsaturation of coordination will be removed (at least partially), therefore restoring the cubic symmetry and consequently narrowing the ESR absorption lines. A more detailed study of variations in line-width upon controlled adsorption of different gases could presumably give further information about surface structure and coordination.

4.2.4 ESR spectrum as a function of concentration

ESR spectra of samples with [Mn] = 0.01 and [Mn] = 0.1 mol % show the hyperfine structure sextet

corresponding to the spectrum of isolated Mn^{2+} ions to be clearly resolved. When the concentration of manganese in solid solution increases, the ESR spectrum is gradually modified, revealing the development of interactions between neighbouring Mn^{2+} ions which produce first a broadening of the isolated ion spectrum (Figs. 3.26 and 3.27) and then a new spectrum without hyperfine structure (Fig. 3.29). The total width of the ESR signal is as shown in Table 4.2.

Table 4.2

Sample	[Mn] (mol %)	Total width (gauss)
CM 0.01	0.01	425
CM 0.1	0.1	425
CM 1	1	475
CM 2	2	500
CM 5	5	300

It is observed that the total width increases first from 425 to 500 gauss to decrease then from 500 to 300 gauss. This pattern can be explained in terms of two different mechanisms of spin-spin interaction, namely:

(i) Magnetic dipole interaction

(ii) Exchange interaction

Magnetic dipole interaction arises from the influence of the magnetic field of one paramagnetic ion on the dipole moments of neighbouring paramagnetic ions and it causes a linear increase in line-width with concentration of paramagnetic ions.[252] Exchange interactions,[*] on the other hand, depend on the overlap of the orbitals of the unpaired electrons and cause very rapid fluctuations of the local fields so that they become less efficient in broadening the absorption signal.[253] The result is that the width at half maximum intensity is reduced. If the distance between the paramagnetic ions is short enough and their positions suitable, the exchange interaction may be greater than the Zeeman interaction. In such case all the paramagnetic ions will behave as a single unit giving an ESR signal with the same g-value as the isolated ions but showing exchange narrowing.

(*) There are two types of exchange interaction: isotropic interaction and anisotropic interaction. Isotropic interaction causes a narrowing of the absorption line in the centre and an extension of the wings. Anisotropic interaction, on the other hand, results in a broadening of the absorption line. However, when the g-tensor is isotropic, only isotropic interaction is to be expected.[253]

The observed spectra for samples with [Mn] = 0.01 mol % and [Mn] = 0.1 mol % (figs. 3.21 - 3.25; total width = 425 gauss) do not show either dipole or exchange interaction, and can be assigned to isolated Mn^{2+} ions. When [Mn] = 1 mol % the spectrum (fig. 3.26) shows considerable broadening of the hyperfine structure lines, this broadening is even more pronounced for [Mn] = 2 mol % (fig. 3.27), and there is a parallel increase in the total width (from 425 to 475 and finally 500 gauss). Therefore, it may be concluded that in this concentration range the distance between Mn^{2+} ions becomes small enough for dipole interactions to take place, but not so close as to allow exchange interaction. When [Mn] = 5 mol % a single line showing exchange narrowing (peak to peak width = 300 gauss) is observed, thus showing that, at this manganese concentration, the average interionic distance between Mn^{2+} ions has been so reduced as to allow exchange interaction to become dominant over dipolar interaction. Moreover, since only a single signal is observed, it may be concluded that at [Mn] = 5 mol % no electronically isolated Mn^{2+} ions are left. The interpretation of the spectrum in fig. 3.28, corresponding to a [Mn] = 3 mol % is not so clear-cut, but it is likely that this spectrum is the resultant of two signals,

namely an internal one with 300 gauss width, and an outer one with 500 gauss width. This interpretation would imply that for [Mn] = 3 mol % some of the Mn^{2+} ions are already close enough to allow the onset of exchange interactions, whilst the remaining Mn^{2+} ions are still at a larger interionic distance.

Pairs of manganese ions have been detected in Mn-doped MgO by Coles et al,(254) using ESR spectroscopy. Two Mn^{2+} ions in a pair would produce an ESR signal with a hyperfine structure consisting of eleven lines, corresponding to the allowed values of the total nuclear magnetic quantum number M_I = 5, 4, ..., -5.. The relative intensities of these lines would be 1:2:3:4:5:6:5:4:3:2:1 corresponding to the different ways of building up each M_I value. Such a spectrum, however, has never been observed in the present work.

4.2.5 ESR spectrum of MnO-CaO-Na_2O specimens

The ESR spectra of 0.1N 4 and 3N 1 are shown in figs. 3.30 and 3.31 respectively. These spectra show a set of six hyperfine structure lines centred at a g-value of 2.0067 which makes it clear that the ESR signal is arising from Mn^{2+}. It must therefore be concluded that some Mn^{2+} ions are still present in the CaO lattice even for samples

heated in air. The concentration of Mn^{2+}, however, need not be very high, since it is known[249] that even 10 ppm of Mn^{2+} are enough to produce a strong ESR signal.

The most remarkable feature of the spectra shown in figs. 3.30 and 3.31 is the splitting of the hyperfine structure lines in two components which are clearly resolved in the outer lines of the spectra. This effect cannot be due to a contribution from an Mn^{3+} signal, since it is known that Mn^{3+} does not give a well-resolved ESR spectrum in powdered samples[249] presumably because of a short relaxation time, together with the possibility of a decrease in the site symmetry by Jahn-Teller distortion.[255] (Compare with the ESR spectrum of $CaMn_2O_4$ shown in fig. 3.32). A possible contribution from Mn^{4+} must also be ruled out because the ESR spectrum of Mn^{4+} would appear at $g = 1.995$[249,256] and therefore the absorption lines from Mn^{2+} and Mn^{4+} would not be exactly superimposed in the ESR spectrum. In view of these arguments it is tentatively concluded that the Mn^{2+} ions are always very close to Mn^{3+} ions, or Na^{+} ions, in the CaO lattice, and that the distortion of the local symmetry produced by the latter ions causes the Mn^{2+} ESR signal to split in the observed way.

The absence of an Mn^{4+} ESR signal allows one to conclude that these ions are not present. This is not unexpected, because the difference in ionic radius between Mn^{4+} and Ca^{2+} (85.2%) makes it very unlikely that Mn^{4+} could replace Ca^{2+} in the CaO lattice, even with the corresponding introduction of two Na^{+} per Mn^{4+} ion.

4.3 Studies on $Cu_xCd_{1-x}In_2O_4$

4.3.1 The crystal structure of $CdIn_2O_4$

As pointed out in section 1.13. the crystal structure of cadmium indate ($CdIn_2O_4$) has given rise to some controversy. Thus, while Passerini[122] has indexed the X-ray reflections in a tetragonal system with a = 8.650 Å and C = 9.875 Å, Skribljak et al[123] report the structure to be cubic, spinel-type, with a_o = 9.115 Å. In the present work it was found that all lines appearing on the X-ray powder films could be indexed in a cubic system with a_o = 9.1653 Å (for the compound prepared in air). The agreement between interplanar spacings, d, observed and calculated was very good, as can be appreciated from Table 4.3 which lists the values for reflections occurring at high angles.

Table 4.3

Reflection	d observed (Å)	d calculated (Å)
931	0.9604	0.9608
844	0.9351	0.9354
$\underline{1}020$	0.8985	0.8987
951	0.8857	0.8860
$\underline{1}022$	0.8817	0.8819
$\underline{1}042$	0.8366	0.8367
$\underline{1}111$	0.8263	0.8264
880	0.8100	0.8101
$\underline{1}131$	0.8007	0.8008
$\underline{1}060$	0.7859	0.7859
$\underline{1}133$	0.7774	0.7774
$\underline{1}062$	0.7746	0.7746

Systematic extinctions were consistent with a spinel-type structure, space group Fd3m, whose symmetry imposes the conditions[1]

hkl: h+k, k+l, l+h = 2n

hhl: l+h = 2n

0kl: (k, l = 2n); k+l = 4n

on the allowed reflections. As can be appreciated from Table 3.17 these conditions were fulfilled by all the reflections present in the diffraction pattern of $CdIn_2O_4$. It is therefore concluded that, under the present conditions of preparation, cadmium indate has a non-distorted cubic, spinel-type, crystal structure.

4.3.2 Lattice parameter of $CdIn_2O_4$

a) Samples prepared in air

Table 3.18 shows that the value of the lattice parameter for cadmium indate prepared in air was a_o = 9.1653 Å regardless of the temperature of preparation (between 1073 and 1323 K), and fig. 3.39 shows that there are no discontinuities in the a_o value from room temperature up to 1390 K. It can therefore be concluded that there is only one polymorph of $CdIn_2O_4$ in this range of temperature, and at atmospheric pressure.

The value of a_o found in the present work is not in very good agreement with that reported

by Skribljak et al,[123] who also prepared $CdIn_2O_4$ by solid state reaction between CdO and In_2O_3 at 1073 K in air, and found the lattice parameter to be a_o = 9.115 Å. It is likely, as will be discussed later, that small deviations from stoichiometry (anion deficiency) can produce substantial changes in the lattice parameter. However, the fact that Skribljak et al prepared the compound in conditions very similar to those used in the present work makes it unlikely that the final stoichiometries were significantly different. A critical analysis of the work of Skribljak et al revealed that they have computed the lattice parameter from Debye-Scherrer diffraction lines occurring at low angles. They have used Mo Kα radiation and have observed diffraction lines only up to $\theta = 22.4^o$. As discussed in section 2.1, the use of only low angle reflections to compute lattice parameters from Debye-Scherrer films can lead to considerable inaccuracies; these could possibly account for the observed discrepancies in the a_o value for $CdIn_2O_4$. Confirmation was obtained from a Debye-Scherrer film of $CdIn_2O_4$ taken with Mo Kα radiation; the lattice parameter computed from the low angle reflections (the only ones appearing on the film) was a_o = 9.137 Å, thus closer to the value reported by Skribljak et al.

It must be emphasized that cadmium indate is highly absorbent for X-rays and therefore values of a_o computed from low angle reflections will always be substantially smaller than the true value (Section 2.1.5(b)). Finally, it should be added that Esveldt[257] gives for the lattice parameter of $CdIn_2O_4$ the value a_o = 9.167 Å which is in good agreement with the value found in the present work. No details are available on Esveldt's work.

b) Samples prepared in oxygen

As shown in Table 3.18 the value of the lattice parameter of $CdIn_2O_4$ prepared in oxygen at 1323 K was a_o = 9.1635 Å, which is significantly smaller than the value for the sample prepared in air at the same temperature (a_o = 9.1653 Å). Some indication on the possible reasons for this discrepancy can be derived from the results of the chemical analysis shown in Table 3.16. It can be observed that the chemical analysis of a sample prepared in air showed it to be oxygen deficient (experimental values for [Cd] and [In] greater than those required by stoichiometry). The sample prepared in oxygen, however, showed little anion deficiency, if any, since the discrepancies between experimental and theoretical values are here within experimental error.

According to Cimino and Marezio[258] pure cadmium oxide is usually oxygen deficient and shows a lattice parameter which is greater than that corresponding to stoichiometric CdO. This is probably due to the presence in the nonstoichiometric oxide of Cd^+ ions, or even Cd atoms, which cause an expansion of the crystal lattice. Since $CdIn_2O_4$ prepared in air was found to be slightly oxygen deficient, it is reasonable to assume that it also possesses some cations in low oxidation state which produce a small lattice dilation that is absent in the specimen prepared in oxygen. This would explain the above-mentioned differences in a_o.

4.3.3 Lattice parameters of $Cu_xCd_{1-x}In_2O_4$

a) Low temperature (LT) samples

$Cu_xCd_{1-x}In_2O_4$ specimens prepared at 1173 K in air show a linear decrease in lattice parameter with increasing copper content up to [Cu] = 2.4 mol % (fig. 3.41), the change in a_o being $\Delta a_o = -2 \cdot 10^{-3}$ Å per copper ion. This is the effect which would be expected for a replacement of Cd^{2+} by Cu^{2+} in $CdIn_2O_4$. It is, in principle, possible that such a replacement could cause a simultaneous change of cation distribution in the spinel, i.e. it is possible that Cu^{2+} would enter octahedral sites, whilst Cd^{2+} could have been at tetrahedral sites,

or viceversa (thus implying a change in the degree of inversion), but, in any case, a reduction of a_o should be expected. This follows from the fact that the ionic radius of Cu^{2+} in either tetrahedral or octahedral coordination is smaller than the radius of Cd^{2+} in any of these coordinations (Table 1.3). Thus, the observed decrease in a_o with increasing copper content can be assumed to indicate solid solution formation.

For specimens with [Cu] > 2.4 mol %, samples CICu 4(LT) and CICu 10(LT), the lattice parameter remains at the constant value of a_o = 9.1603 Å, therefore showing that the limit of solubility has been attained. The cupric oxide in excess reacts with indium oxide to form $Cu_2In_2O_5$ whose characteristic X-ray diffraction lines are observable in the diffraction pattern of CICu 10(LT) after long exposure. The separate phase $Cu_2In_2O_5$ gives to the samples a green shade which is easily distinguishable even when the amount of the compound is not enough to show up in the diffraction films. As already stated in section 1.13, $Cu_2In_2O_5$ is the only compound which has been found to form by direct solid state reaction between CuO and In_2O_3.

b) Medium temperature (MT) samples

Increase of the firing temperature from 1173 to 1223 K results in an increase in solubility

from 2.4 to 2.9 mol % Cu (fig. 3.41). This is an expected result since, as has been discussed in section 1.10.6, the entropic contribution to the free energy results in a greater stability of solid solutions at higher temperatures.

c) High temperature (HT) samples

The lattice parameter of $Cu_xCd_{1-x}In_2O_4$ specimens prepared at 1323 K in oxygen also shows a linear decrease with increasing copper content up to [Cu] = 5.2 mol %. The a_o versus [Cu] line (fig. 3.41), however, lies below the corresponding line for LT and MT specimens. This is due to the fact already commented upon that the lattice parameter of pure $CdIn_2O_4$ prepared in oxygen is smaller than the corresponding value for the compound prepared in air. It should be noticed that, although the a_o versus [Cu] lines for specimens prepared in air and oxygen do not coincide, they do have the same slope, i.e. $\Delta a_o = -2 \cdot 10^{-3}$ Å per copper ion in both cases. This suggests that the distribution of Cu^{2+} ions between octahedral and tetrahedral sites is not appreciably changed by differences in either temperature or other experimental factors in the range investigated.

It must be added that a long-exposure (24 hours) X-ray film of sample CICu 4(HT) did not show lines other than those corresponding to

the crystalline phase with the spinel-type structure, thus providing further evidence of solid solution formation. Sample CICu 15(HT), however, gave a diffraction pattern in which lines from both the spinel and the $Cu_2In_2O_5$ phase were present. On the other hand, solid state reaction between CuO and In_2O_3 at 1323 K in oxygen resulted in the formation of $Cu_2In_2O_5$ as the only new compound.

A relevant result of the present work is the finding that although $CuIn_2O_4$ does not form as an individual compound (section 1.13), it does act as a hypothetical end member for the solid solution series $CuIn_2O_4$ - $CdIn_2O_4$. The limit of solubility, however, is small (5.2 mol % at 1323 K). Any CuO in excess reacts with In_2O_3 to form $Cu_2In_2O_5$ as a separate phase.

4.3.4 Cation distribution

The cation distribution in $CdIn_2O_4$ is not known and it is very difficult to predict on theoretical grounds. Both cations have the $4d^{10}$ configuration in the ground state and should therefore show a pronounced preference for tetrahedral sites (sections 1.4.4, 1.4.6 and 1.6). Indeed, in all cases where the cation distribution is known, indates with the spinel structure have always been found to possess the inverse distribution,[42]

whilst cadmium spinels were always found to be normal,[42] i.e., both Cd^{2+} and In^{3+} have a strong tetrahedral preference. It is clear that a competition for the available tetrahedral sites in $CdIn_2O_4$ will take place, and yet it is remarkable that the compound forms at very low temperatures when compared with other indates. Thus, whilst $CdIn_2O_4$ forms readily at 1123 K (and even at lower temperatures), the corresponding magnesium compound, $MgIn_2O_4$, does not form appreciably at temperatures lower than 1673 K.[119]

The determination of cation distribution in $CdIn_2O_4$ is therefore interesting from a theoretical point of view, but the problem poses some experimental difficulties. X-ray diffraction methods are not usable because the X-ray scattering factors for Cd^{2+} and In^{3+} are identical (same number of electrons) and the same is true of electron diffraction. UV-vis spectroscopy is also of no value because the d^{10} configuration of both cations precludes any d-d transition. Neutron diffraction is probably the best alternative although the high cross section of both nuclei may give rise to some technical difficulties. It is also possible that some information could be gathered by infrared spectroscopy (Section 1.7.3).

UV-vis spectroscopy provides some information on the distribution of copper ions in $Cu_xCd_{1-x}In_2O_4$. Figure 3.42 shows the UV-vis spectra of specimens with different copper content, along with the spectra of pure $CdIn_2O_4$ and pure $CuGa_2O_4$. The latter compound is known to have the spinel structure with a partially inverse cation distribution.(119) Its UV-vis spectrum shows two absorption maxima at about 11,300 and 5,800 cm^{-1} which correspond to the $^2E_g \rightarrow {}^2T_{2g}$ and $^2T_2 \rightarrow {}^2E$ transitions of octahedrally and tetrahedrally coordinated copper respectively.(119) The spectra of CICu 1 (LT) and CICu 2 (LT) do not show any distinctive features apart from the intense absorption bands at $\bar{\nu} > 20{,}000$ cm^{-1} and $\bar{\nu} < 8{,}000$ cm^{-1} which are also present in the spectrum of $CdIn_2O_4$. However, the spectrum of CICu 4 (HT) shows a slight shoulder at 11,000 cm^{-1} which is the expected region for the $^2E_g \rightarrow {}^2T_{2g}$ transition of copper(II) in octahedral coordination. This provides some indication that at least part of the Cu^{2+} ions occupy octahedral sites in $Cu_xCd_{1-x}In_2O_4$. The strong absorption band developing at $\bar{\nu} < 8000$ cm^{-1} in the parent $CdIn_2O_4$ makes it impossible to conclude whether some tetrahedrally coordinated Cu^{2+} ions are also present.

REFERENCES

1. H.F.M. HENRY and K. LONSDALE (Ed.), International Tables for X-ray Crystallography, Kynoch Press (1965).

2. H.E. SWANSON and R.K. FUYAT, Natl. Bur. Stand. 539, 41 (1953).

3. M. BORN and J.E. MAYER, Z. Physik. 75, 1 (1932).

4. J.S. KASPER and J.S. PRENNER, Acta. Cyst. 7, 246 (1954).

5. A. CIMINO, M. LO JACONO, P. PORTA and M. VALIGI, Z. Phys. Chem. NF 59, 134 (1968).

6. W.H. BRAGG, Nature 95, 561 (1915).

7. W.H. BRAGG, Phil. Mag. 30, 305 (1915).

8. S. NISHIKAWA, Proc. Maths. Phys. Soc. (Tokyo) 8, 199 (1915).

9. T.F.W. BARTH and E. POSNJAK, Z. Krist. 82, 325 (1932).

10. L.V. AZAROFF, Introduction to Solids. McGraw-Hill (1960).

11. W. NOWACKI, ACA Monograph No. 6, Amer. Crystallogr. Assoc. (1967).

12. R.W.G. WYCKOFF, Crystal Structures. Interscience (1963).

13. E.W. GORTER, Philps Res. Rep. 9, 295, 321 & 403 (1954).

14. F.S. STONE and R.J.D. TILLEY, Proc. 7th Intern. Symp. React. Solids. Bristol 1972.

15. T.F.W. BARTH and E. POSNJAK, J. Wash. Acad. Sci. 21, 255 (1931).

16. N.N. GREENWOOD, Ionic Crystals, Lattice Defects and Nonstoichiometry. Butterworths (1968).

17. E.J.W. VERWEY and E.L. HEILMAN, J. Chem. Phys. 15, 174 (1947).

18. E.J.W. VERWEY, F. de BOER and J.H. VAN SANTEN, J. Chem. Phys. 16, 1091 (1948).

19. Y. SAKAMOTO and U. TAKAHASHI, J. Sci. Hiroshima Univ., Ser. A-II 26, 1 & 67 (1962).

20. L. HERMANS, J. WEENK and W. Van GOOL, Z. Phys. Chem. NF. 88, 15 (1974).

21. F. de BOER, J.H. Van SANTEN and E.J.W. VERWEY, J. Chem. Phys. 17, 1032 (1950).

22. H. BETHE, Ann. Physik. 3, 133 (1929).

23. L.E. ORGEL, An Introduction to Transition Metal Chemistry. Methuen (1967).

24. H.A. JAHN and E. TELLER, Proc. Roy. Soc. (London) A161, 220 (1937).

25. W.L. CLINTON and B. RICE, J. Chem. Phys. 30, 542 (1959).

26. J.D. DUNITZ and L.E. ORGEL, J. Phys. Chem. Solids 3, 20 (1957).

27. J.D. DUNITZ and L.E. ORGEL, J. Phys. Chem. Solids 3, 318 (1957).

28. D.S. McCLURE, J. Phys. Chem. Solids 3, 311 (1957).

29. A. MILLER, J. Appl. Phys. 30, 24S (1959).

30. J.B. GOODENOUGH and A.L. LOEB, Phys. Rev. 98, 391 (1955).

31. L. PAULING, The Nature of the Chemical Bond. Oxford Univ. Press (1963).

32. E.W. GORTER, Nature 165, 798 (1950).

33. E. PRINCE, Phys. Rev. 102, 674 (1956).

34. E. PRINCE and R.G. TREUTING, Acta Cryst. 9, 1025 (1956).

35. M. BALANDA, A. SZYTULA, Z. DIMITRIJEVIC and J. TODOROVIC, Phys. Status Solidi 32, K91 (1969).

36. E. JAROCKI, W. KUBEL and J. WENDA, Phys. Status Solidi 34, K17 (1969).

37. D.P. MELLOR and D.P. CRAIG, Proc. Roy. Soc. (N.S. Wales) 75, 27 (1941).

38. A.F. WELLS, Structural Inorganic Chemistry. Clarendon Press (1975).

39. J. SMIT, F.K. LOTGERING and R.P. Van STAPELE, J. Phys. Soc. Japan 17, 268 (1962).

40. J. SMIT, Solid State Comm. 6, 745 (1968).

41. J. FLAHAUT, L. DOMAGE, M. OURMITCHI and J. KAM SU KAM, Bull. Soc. Chim. Fr. 2382 (1961).

42. G. BLASSE, Philips Res. Rep. Suppl. 3, (1964).

43. J.H. Van VLECK, J. Chem. Phys. 3, 803 (1935).

44. H. SCHMALZRIED, Z. Phys. Chem. FA 28, 203 (1961).

45. F.A. KRÖGER, The Chemistry of Imperfect Crystals. North-Holland (1974).

46. C.J. KRIESSMAN, Phys. Rev. 103, 857 (1956).

47. N. SAKAMOTO, T. ASAKI and S. MIYAHARA, J. Phys. Soc. Japan 8, 677 (1953).

48. R.L. MOZZI and A.E. PALADINO, J. Chem. Phys. 39, 435 (1963).

49. H. ONISHI and T. TERANISHI, J. Phys. Soc. Japan 16, 35 (1961).

50. J.M. ROBERTSON, Solid State Comm. 4, 257 (1966).

51. A. NAVROTSKY and O.J. KLEPPA, J. Inorg. Nucl. Chem. 29, 2701 (1967).

52. A.N. MEN', Fiz. Tverd. Tela 3, 1054 (1961).

53. A.N. MEN', Izv. Akad. Nauk SSSR, Ser. Fiz. 25, 1385 (1961).

54. A.N. MEN', Soviet Phys., Solid State 4, 653 (1962).

55. E.F. BERTAUT, C.R. Acad. Sci. Paris 230, 213 (1950).

56. E.F. BERTAUT, J. Phys. Radium 12, 252 (1951).

57. M. HUBER, J. Chim. Phys. 57, 202 (1960).

58. H. FURUHASHI, M. INAGAKI and S. NAKA, J. Inorg. Nucl. Chem. 35, 3009 (1973).

59. G.E. BACON, Neutron Diffraction. Clarendon Press (1967).

60. C.G. SHULL, Trans. Amer. Crystallogr. Assoc. 3, 1 (1967).

61. Y. TANABE and S. SUGANO, J. Phys. Soc. Japan 9, 753 (1954).

62. F.S. STONE, Bull. Soc. Chim. Fr. 3, 819 (1966).

63. F.S. STONE and R.J.D. TILLEY, Proc. 5th Intern. Symp. React. Solids, Munich 1964.

64. P. PORTA, F.S. STONE and R.G. TURNER, J. Solid State Chem. 11, 135 (1974).

65. O. SCHMITZ-DUMONT, Bull. Soc. Chim. Fr. 4, 1099 (1965).

66. R.D. WALDRON, Phys. Res. 99, 1727 (1955).

67. W.B. WHITE and B.A. DeANGELIS, Spectrochim. Acta 23A, 985 (1967).

68. S. HAFNER, Z. Krist. 115, 331 (1961).

69. J. PREUDHOMME and P. TARTE, Spectrochim. Acta 27A, 961 (1971).

70. P. TARTE, Acta Cryst. 16, 228 (1963).

71. N.W. GRIMES, Spectrochim. Acta 28A, 2217 (1972).

72. J. PREUDHOMME and P. TARTE, Spectrochim. Acta 27A, 845 (1971).

73. W. JOST, Diffusion in Solids, Liquids and Gases. Academic Press (1960).

74. J. CRANK, Mathematics of Diffusion. Oxford Univ. Press (1956).

75. W.D. KINGERY, Kinet. High Temp. Processes. Dedham, Mass. (1958).

76. R.J. FRIAUF, Phys. Rev. 105, 843 (1957).

77. C. ZENER, Acta Cryst. 3, 346 (1950).

78. S.A. RICE, Phys. Rev. 112, 804 (1958).

79. J.S. ANDERSON, Proc. Chem. Soc. (London) 1964, 166 (1964).

80. J.S. ANDERSON, NBS, Special Publ. No. 364, p. 295 (1972).

81. H.D. MEGAW, Crystal Structures. Saunders (1973).

82. R. FOWLER and E.A. GUGGENHEIM, Statistical Thermodynamics. Cambridge Univ. Press (1965).

83. E.A. GUGGENHEIM, Mixtures. Oxford Univ. Press (1952).

84. W. HUME-ROTHERY and G.V. RAYNOR, The Structure of Metals and Alloys. Institute of Metals (1962).

85. R.D. SHANNON and C.T. PREWITT, Acta Cryst. 825, 925 (1969).

86. R.D. SHANNON and C.T. PREWITT, Acta Cryst. 826, 1046 (1970).

87. L. VEGARD, Z. Physik. 5, 17 (1921).

88. L. VEGARD and H. DALE, Z. Krist. 67, 148 (1928).

89. G.S. ZHDANOV, Crystal Physics. Oliver & Boyd (1965).

90. E. an ZEN, Amer. Mineralog. 41, 523 (1956).

91. J. FRIEDEL, Phil. Mag. 46, 514 (1955).

92. D.M. ROY and E.F. OSBORN, J. Amer. Ceram. Soc. 36, 149 (1953).

93. H.P. ROOKSBY, in X-ray Identification and Crystal Structure of Clay Minerals, ed. by G. Brown. Mineralogical Society (London) (1961).

94. E.J.W. VERWEY, P.W. HAAYMAN, F.C. ROMEJN and G.W. Van OOSTERHOUT, Philips Res. Rep. 5, 173 (1950).

95. A. CIMINO, M. SCHIAVELLO and F.S. STONE, Disc. Faraday Soc. 41, 350 (1966).

96. R.I. BICKLEY and F.S. STONE, Proc. Symp. Electronic Phenomena in Chem. and Catal. on Semiconductors, ed. by K. Hauffe and Th. Wolkenstein, Moscow (1968). DeGruyter, Berlin (1969).

97. H. WELKER, Z. Naturforsch 7a, 744 (1952).

98. O.G. FOLBERTH and E. SCHILLMANN, Z. Naturforsch 12a, 943 (1957).

99. J.T. EDMOND, Proc. Phys. Soc. (London) 73, 622 (1959).

100. C. KOLM, S.A. KULIN and B.A. AVERBACH, Phys. Rev. 108, 965 (1957).

101. E.M. RHODERICK, J. Phys. Chem. Solids 8, 498 (1959).

102. J.M. WHELAN, J.D. STRUTHERS and J.A. DITZENBERGER, Proc. Intern. Conf. Semiconductor Phys. Prague 1960.

103. E. SCHILLMANN, Z. Naturforsch 11a, 463 (1956).

104. R. RIGAMONTI, Atti accad. nazl. Lincei, Classe sci. fis. mat. e nat. 2,487 (1947).

105. C. DELORME, Bull. Soc. Franc. Minér. Cryst. 81, 19 (1958).

106. F.H. CHAPPLE and F.S. STONE, Proc. Brit. Ceram. Soc. 1, 45 (1964).

107. N.G. SCHMAHL and G.F. EIKERLING, Z. Phys. Chem. FM 62, 268 (1968).

108. J.D.H. DONNAY (ed.), ACA Monograph No. 5, Amer. Crystallogr. Assoc. (1963).

109. H.E. SWANSON, NBS Circular 539, 9 (1959).

110. J. ROBIN, Ann. Chim. 10, 389 (1955).

111. A. CIMINO, M. LO JACONO, P. PORTA and M. VALIGI, Z. Phys. Chem. NF 70, 166 (1970).

112. H.E. SWANSON, NBS Circular 539, 45 (1959).

113. H.E. SWANSON and E. TAGTE, J.C. Fel. Rep. NBS (1950).

114. G. NATTA and L. PASSERINI, Gazz. chim. ital. 59, 129 (1929).

115. A.H. JAY and K.W. ANDREWS, Nature 154, 116 (1944).

116. A.H. JAY and K.W. ANDREWS, J. Iron and Steel Inst. 152, 15 (1945).

117. F.P. GLASSER, J. Amer. Ceram. Soc. 45, 242 (1962).

118. H. SCHENK, M.G. FROHBERG and R. NUNNINGHOFF, Arch. Eisenhuettenw. 35, 269 (1964).

119. R.J.D. TILLEY, PhD Thesis. Bristol (1966).

120. O. SCHMITZ-DuMONT and H. KASPER, Monatsh. Chem. 96, 506 (1965).

121. G. BERGERHOFF and H. KASPER, Acta Cryst. 24B, 386 (1968).

122. L. PASSERINI, Gazz. chim. ital. 60, 754 (1930).

123. M. SKRIBLJAK, S. DASGUPTA and A.B. BISWAS, Acta Cryst. 12, 1049 (1959).

124. F.R. CRUICKSHANK, D. McK. TAYLOR and F.P. GLASSER, J. Inorg. Nucl. Chem. 26, 937 (1964).

125. E.F. BERTAUT and C. DELORME, C.R. Acad. Sci. Paris 239, 504 (1954).

126. P.P. BUDNIKOV and A.M. GINSTLING, Principles of Solid State Chemistry. Maclaren (1968).

127. e.g. R.W. JAMES, The Optical Principles of the Diffraction of X-rays. G. Bell & Sons (1962).

M.J. BUERGER, X-ray Crystallography. John Wiley & Sons (1966).

A.J.C. WILSON, X-ray Optics. Methuen (1962).

128. L.V. AZAROFF and M.J. BUERGER, The Powder Method in X-ray Crystallography. McGraw-Hill (1958).

129. W. FRIEDRICH, P. KNIPPING and M.v.LAUE, Ann. Physik. 41, 971 (1912).

130. P. DEBYE and P. SCHERRER, Phys. Z. 17, 237 (1916).

131. P. DEBYE and P. SCHERRER, Phys. Z. 18, 291 (1917).

132. A.W. HULL, Phys. Rev. 9, 84, 564 (1917).

133. A.W. HULL, Phys. Rev. 10, 661 (1917).

134. H. EKSTEIN and S. SIEGEL, Acta Cryst. 2, 99 (1949).

135. A.J. BRADLEY and A.H. HAY, Proc. Phys. Soc. (London) 44, 563 (1932).

136. M.E. STRAUMANIS and A. IEVINS, Z. Physik 98, 461 (1936).

137. A.J.C. WILSON, Elements of X-ray Crystallography. Addison-Wesley (1970).

138. A. TAYLOR and H. SINCLAIR, Proc. Phys. Soc. (London) 57, 126 (1945).

139. J.B. NELSON and D.P. RILEY, Proc. Phys. Soc. (London) 57, 160 (1945).

140. M.U. COHEN, Rev. Sci. Instr. 6, 68 (1935).

141. E.R. JETTE and F. FOOTE, J. Chem. Phys. 3, 605 (1935).

142. M.U. COHEN, Rev. Sci. Instr. 7, 155 (1936).

143. M.U. COHEN, Z. Kristallogr. 94A, 288, 306 (1936).

144. J.B. HESS, Acta Cryst. 4, 209 (1951).

145. J.I. LANGFORD and A.J.C. WILSON, J. Appl. Cryst. 6, 197 (1973).

146. N.C. KHANDURI, J. Appl. Cryst. 6, 408 (1973).

147. C.G. DARWIN, Phil. Mag. 27, 315, 675 (1914).

148. P.P. EWALD, Ann. Phys., Lpz. 54, 519 (1918).

149. P.P. EWALD, Z. Phys. 2, 332 (1920).

150. P.P. EWALD, Z. Phys. 30, 1 (1924).

151. A.J.C. WILSON, Proc. Camb. Phil. Soc. 36, 485 (1940).

152. M.E. STRAUMANIS, Acta Cryst. 8, 654 (1955).

153. L. De BROGLIE, Phil. Mag. 47, 446 (1924).

154. C. DAVISSON and L.H. GERMER, Phys. Rev. 30, 705 (1927).

155. G.P. THOMSON and A. REID, Nature 119, 890 (1927).

156. A.W. AGAR, Brit. J. Appl. Phys. 11, 185 (1960).

157. R. PHILLIPS, Brit. J. Appl. Phys. 11, 504 (1960).

158. R.H. ALDERSON and J.S. HALLIDAY, in Techniques for Electron Microscopy, Ed. by D.H. Kay. Blackwell (1965).

159. D.T. KEATING and B.E. WARREN, Rev. Sci. Instr. 23, 519 (1952).

160. L. ALEXANDER, J. Appl. Phys. 21, 126 (1950).

161. P. SCHERRER, Gött. Nachr. 2, 98 (1918).

162. A. GUINIER, X-ray Diffraction. Freeman (1963).

163. I. WALLER, Nova Acta Reg. Soc. Sc. Upsala, IV 7, 11 (1939).

164. J. BOUMAN and P.M. de WOLFF, Physica 9, 833 (1942).

165. A.R. STOKES and A.J.C. WILSON, Proc. Camb. Phil. Soc. 40, 197 (1943).

166. F. FERGUSON, A.E.R.E. R3795 (1960).

167. A.R. STOKES and A.J.C. WILSON, Proc. Phys. Soc. (London) 56, 174 (1944).

168. R.C. SPENCER, J. Appl. Phys. 20, 413 (1949).

169. A.R. STOKES, Proc. Phys. Soc. (London) 61B, 382 (1948).

170. R.J. de ANGELIS, Proc. Symp. Local Atomic Arrangements; Ed. by J.B. Cohen and J.E. Hilliard. Chicago (1965).

171. M.S. PATERSON, Proc. Phys. Soc. (London) 63A, 477 (1950).

172. S. ERGUN, J. Appl. Cryst. 1, 19 (1968).

173. F.R.L. SCHOENING, Acta Cryst. 18, 975 (1965).

174. F.W. JONES, Proc. Roy. Soc. (London) 166A, 16 (1938).

175. W.M. DuMOND and H.A. KIRKPATRICK, Phys. Rev. 37, 136 (1931).

176. W.A. RACHINGER, J. Sci. Instr. 25, 254 (1948).

177. R.S. PEASE, J. Sci. Instr. 25, 353 (1948).

178. H.A. KRAMERS, Proc. Amsterdam Acad. Sci. 33, 959 (1930).

179. H.A. KRAMERS, Quantum Mechanics. North-Holland (1957).

180. B. BLEANEY, Hyperfine Interactions Ed. by A.J. Freeman and R.B. Frankel. Academic Press (1967).

181. G.E. PAKE, Paramagnetic Resonance. Bejamin Inc. (1962).

182. R.S. ALGER, Electron Paramagnetic Resonance. Interscience (1968).

183. N.M. ATHERTON, Electron Spin Resonance. John Wiley (1973).

184. J.A. GIORDMAINE, L.E. ALSOP, F.R. NASH and C.H. TOWNES, Phys. Rev. 109, 302 (1958).

185. W. LOW, Paramagnetic Resonance in Solids, in Solid State Physics, Suppl. 2; F. Seitz and D. Turnbull (ed.). Academic Press (1960).

186. W.H. SHIPMAN and J.R. LAI, Anal. Chem. 28, 1151 (1956).

187. T.S. WEST, Complexiometry with EDTA and Related Reagents. BDH Chemicals (1969).

188. S. BRUNAUER, P.H. EMMETT and E. TELLER, J. Amer. Chem. Soc. 60, 309 (1938).

189. P.H. EMMETT, in Advances in Colloid Science, Vol. 1. Interscience (1942).

190. S. BRUNAUER, The Adsorption of Gases and Vapors, Vol. 1. Princeton University Press (1945).

191. T.B. RYMER, Nuovo Cimento 6, 294 (1957).

192. A. CIMINO, P. PORTA and M. VALIGI, J. Amer. Ceram. Soc. 49, 152 (1966).

193. K.W. ANDREWS, D.J. DYSON and S.R. KEOWN, Interpretation of Electron Diffraction Patterns. Hilger (1971).

194. J.C. LODDER and K.G. BERG, J. Microscopy 100, 93 (1974).

195. W.B. PEARSON, Handbook of Lattice Spacings and Structures of Metals and Alloys. Pergamon (1967).

196. A.P. HAGAN, PhD Thesis. Bristol (1974).

197. A. ZECCHINA, M.G. LOFTHOUSE and F.S. STONE, J.C.S. Faraday I, 71, 146 (1975).

198. K. KLIER, Catal. Rev. 1, 207 (1967).

199. G. KORTÜM, Reflectance Spectroscopy. Springer-Verlag (1969).

200. W. LOW, Phys. Rev. 109, 256 (1958).

201. A. CIMINO, M. LO JACONO and A. SGAMELLOTI, Z. Phys. Chem. NF 70, 179 (1970).

202. R. PAPPALARDO, D.L. WOOD and R.C. LINARES, J. Chem. Phys. 35, 2041 (1961).

203. J.R. GOLSMITH and D.L. GRAF, Geochim, Cosmochim. Acta 11, 310 (1957).

204. H. TOUSSAINT, Rev. Chim. Minerale 1,141 (1964).

205. P.B. AYSCOUGH, Electron Spin Resonance in Chemistry. Methuen (1967).

206. E. SIMANEK and K.A. MÜLLER, J. Phys. Chem. Solids 31, 1027 (1970).

207. A. ABRAGAM, Phys. Rev. 79, 534 (1950).

208. A. ABRAGAM, J. HOROWITZ and M.H.L. PRYCE, Proc. Roy. Soc. (London) A230, 169 (1955).

209. M.P. STOMBLER, H.A. FARCH and C.P. POOLE, Phys. Rev. B6, 40 (1972).

210. D.J.E. INGRAM, Spectroscopy at Radio and Microwave Frequencies. Plenum Press (1967).

211. L. VAN GERVEN, J. TALPE and A. VAN ITTERBEEK, Physica 33, 207 (1967).

212. A.I. BUSEV, The Analytical Chemistry of Indium. Pergamon (1962).

213. K.L. CHENG and R.H. BRAY, Anal Chem. 27, 782 (1955).

214. K.L. CHENG, Anal. Chem. 27, 1582 (1955).

215. A.M.M. GADALLA and J. WHITE, Trans. Brit. Ceram. Soc. 63, 119 (1964).

216. R. LINDNER and G.D. PARFITT, J. Chem. Phys. 26, 182 (1957).

217. B.J. WUENSCH and T. VASILOS, J. Chem. Phys. 36, 2917 (1962).

218. R.M. DELL and S. WELLER, Trans. Faraday Soc. 55, 2203 (1959).

219. P.J. ANDERSON and R.F. HORLOCK, Trans. Faraday Soc. 58, 1993 (1962).

220. P.J. ANDERSON and P.L. MORGAN, Trans Faraday Soc. 60, 930 (1964).

221. G.V. SAMSONOV (Ed.), The Oxide Handbook. Plenum (1973).

222. R. PAMPUCH and Z. LIBRANT, Zesz. Nauk. Gorn.-Hutn. Krakow, Ceram. 11, 45 (1969).

223. I. CUTTER and R. McPHERSON, Phil. Mag. 20, 489 (1969).

224. K. HUANG, Proc. Roy. Soc. (London) A190, 102 (1947).

225. M.M. NICOLSON, Proc. Roy. Soc. (London) A228, 490 (1955).

226. D.H. EVERETT, in The Solid-Gas Interface, Vol. II, ed. by E.A. Flood. Edward Arnold (1967).

227. J.E. LENNARD-JONES and L. DENT, Proc. Roy. Soc. (London) 121, 247 (1928).

228. J.E. LENNARD-JONES, Z. Krystallogr. 75, 215 (1930).

229. P.J. ANDERSON and A. SCHOLZ, Trans. Faraday Soc. 64, 2937 (1968).

230. F.A. COTTON and G. WILKINSON, Advanced Inorganic Chemistry. Interscience (1968).

231. P.L. ORIOLI, M. Di VAIRA and L. SACCONI, Chem. Comm. 103, 590 (1965).

232. L. SACCONI, P.L. ORIOLI and M. Di VAIRA, J. Amer. Chem. Soc. 87, 2059 (1965).

233. P. PAULING, G.B. ROBERTSON and G.A. RODLEY, Nature 207, 73 (1965).

234. M. CIAMPOLINI and I. BERTINI, J. Chem. Soc. A, 2241 (1968).

235. J. HABER and F.S. STONE, Trans. Faraday Soc. 59, 192 (1963).

236. H.A. WEAKLIEM and D.S. McCLURE, J. Appl. Phys., Suppl. No. 1, 33, 347 (1962).

237. F. LIONS, I.G. DANCE and J. LEWIS, J. Chem. Soc., A, 565 (1967).

238. M. CIAMPOLINI, Structure and Bonding 6, 52 (1969).

239. K. KLIER, R. KELLERMAN and P.J. HUTTA, J. Chem. Phys. 61, 4224 (1974).

240. A.J. TENCH and D. GILES, J.C.S. Faraday Trans. 1, 193 (1972).

241. J.H. ASHLEY and P.C.H. MITCHELL, J. Chem. Soc., A, 1821 (1968).

242. J.H. ASHLEY and P.C.H. MITCHELL, J. Chem. Soc. A, 2730 (1969).

243. W.L. ROTH, J. Phys. Chem. Solids 25, 1 (1964).

244. J.H. LUNSFORD, Catal. Rev. 8, 135 (1973).

245. J.S. ANDERSON, Adv. Chem. Ser. 39, 1 (1963).

246. W.L. ROTH, Acta Cryst. 13, 140 (1960).

247. I.F. GUILLIATT and N.H. BRETT, J. Mater. Sci. 5, 615 (1970).

248. A. CIMINO, M. LO JACONO, P. PORTA and M. VALIGI, Z. Phys. Chem. NF 59, 134 (1968).

249. E.G. DEROUANE and V. INDOVINA, Bull. Soc. Chim. Belg. 82, 645 (1973).

250. P. AUZINS, J.W. ORTON and J.E. WERTZ, Proc. 1st Intern. Conf. Paramagnetic Resonance, Jerusalem (1962).

251. D. CORDISCHI, R.L. NELSON and A.J. TENCH, Trans. Faraday Soc. 65, 2740 (1969).

252. P.W. ANDERSON and P.R. WEISS, Rev. Mod. Phys. 25, 269 (1953).

253. A. ABRAGAM and B. BLEANEY, Electron Paramagnetic Resonance of Transition Ions. Clarendon Press, Oxford (1970).

254. B.A. COLES, J.W. ORTON and J. OWEN, Phys. Rev. Lett. 4, 116 (1960).

255. H.J. GERRITSEN and E.S. SABISKY, Phys. Rev. 132, 1507 (1963).

256. Y. GRENIE and G. VIGNAUD, C.R. Hebd. Sean. Acad. Sci. 274B, 488 (1972).

257. C.J. ESVELDT, quoted by G. Blasse (c.f. 42).

258. A. CIMINO and M. MAREZIO , J. Phys. Chem. Solids 17, 57 (1960).

259. J.B. PRICE and J.B. WAGNER, J. Electrochem. Soc. 117, 242 (1970).